Higgs Boson Production Cross-Section Measurements in the Di-Tau Final State at ATLAS

Dissertation
zur
Erlangung des Doktorgrades (Dr. rer. nat.)
der
Mathematisch-Naturwissenschaftlichen Fakultät
der
Rheinischen Friedrich-Wilhelms-Universität Bonn

von
Michael Hübner
aus
Troisdorf

Bonn, November 2021

Angefertigt mit Genehmigung der Mathematisch-Naturwissenschaftlichen Fakultät der Rheinischen Friedrich-Wilhelms-Universität Bonn

1. Gutachter:	Prof. Dr. Klaus Desch
2. Gutachter:	Prof. Dr. Jochen Dingfelder
Tag der Promotion:	04.02.2022
Erscheinungsjahr:	2022

Abstract

The origin of masses for massive elementary particles in the Standard Model (SM) is explained by the Higgs mechanism. With the discovery of a SM-like Higgs boson resonance in 2012 a variety of measurements have been conducted to determine its exact nature. Properties like the spin and other quantum numbers are measured to ascertain whether the resonance resembles the Higgs boson predicted by the SM or another Higgs boson predicted by theories beyond the SM.

One of the Higgs boson's main characteristics is its coupling to elementary particles that grows proportional to the particle's mass. Deviations within this coupling structure could indicate hints of effects originating from physics beyond the SM. This thesis presents a measurement of the Higgs boson production cross-sections in the decay to two τ-leptons, $H \rightarrow \tau\tau$. The measurement uses the proton-proton collision dataset of 139 fb^{-1} collected by the ATLAS experiment during Run II in the years 2015 to 2018 of the Large Hadron Collider (LHC). As the τ-lepton itself is not a stable particle and decays before interacting with the detector material, which always involves particles that cannot be measured at ATLAS, it is challenging to measure this decay channel. However, studying the $H \rightarrow \tau\tau$ decay is worthwhile the efforts because it allows to deduce information on the Higgs boson's coupling to fermions in the Yukawa sector.

The measurement's final discriminating observable reconstructs the invariant mass of the two τ-lepton system and incorporates the knowledge about the produced τ-lepton-neutrinos that escape detection. Detailed studies regarding this algorithm have been performed that ultimately lead to a speedup by a factor of roughly two to four, depending on the τ-lepton decay. Multiple Higgs production cross-sections are measured, ranging from the inclusive production to the more detailed Simplified Template Cross Sections (STXS). Therefore, a complex fit model is needed to extract these information from the data. Validation methods for such complex models are discussed. In this context, a novel technique that is able to predict the behaviour of nuisance parameters and to provide an assessment of the overall agreement of the model with respect to the data is introduced. The measured cross-sections are in agreement with the SM predictions and provide the currently most precisely measured values in the $H \rightarrow \tau\tau$ channel in an ATLAS standalone measurement. As an example, the inclusive Higgs production cross-section is measured to be $2.90 \pm 0.21\,(\text{stat})\,^{+0.37}_{-0.32}\,(\text{syst})$ pb which agrees with the SM prediction of 3.15 ± 0.09 pb within the uncertainties. The vector-boson fusion production is observed with a significance of 5.3σ and there is evidence for gluon-gluon fusion production with a significance of 3.9σ.

Contents

CHAPTER 1

Introduction

Curiosity regarding their surroundings and what lies beyond is arguably one of the defining trademarks of human nature. A vast landscape of scientific fields evolved over centuries, often sparked by discoveries demanding detailed exploration. In the field of physics this lead to studying the very large scales in for example, the field of cosmology but also the very small scales of atoms and even smaller particles.

The smallest known particles as well as three out of four fundamental known interactions are summarised in the Standard Model of particle physics (SM). Only three types of these particles, namely the up- and down quarks as well as electrons, are needed to describe all known visible matter, even on very large scales such as stars. While the interactions that are part of the SM are able to describe how these particles are bound into larger structures, decay and interact over great distances, the possibly most intuitive interaction, gravity, is not part of this theoretical framework, thus hinting towards an incomplete description of the world by the SM. It has to be stressed, though, that this theory shows remarkable success in describing observations in particle physics experiments as well as predicting e.g. new particles such as the Higgs boson which was discovered in 2012 [1, 2].

In order to probe small scales, machines have been built allowing to access ever increasing energy frontiers. Increasing energies allow to resolve smaller structures that, for example, lead to the discovery of structure within atoms now known as protons and neutrons and ultimately revealing even smaller structures within for example protons. Furthermore, pushing the energy frontier in particle physics resulted in the discovery of new and increasingly heavy particles. The currently most powerful particle collider, reaching the highest collision energies, is the circular Large Hadron Collider (LHC) at CERN [3, 4]. It has been operating since 2008 [5] and collides protons from two beams circulating in opposite directions with energies of up to $\sqrt{s} = 13\,\text{TeV}$ [6]. Multiple experiments record the results of these collisions using intricate detectors built for specific research goals. The two experiments ATLAS and CMS are sometimes referred to as “multi-purpose detectors”, as they intend to cover a broad physics programme, reaching from precision measurements of known processes to the search of new phenomena. Due to the complexity of the design, construction, operation and data analysis from the acceleration of the protons to the final measurements, virtually all these aspects are parts of large collaborative efforts.

Ultimately, both types of measurements, precision measurements as well as direct searches for new particles, can serve a common goal to discover hints of physics beyond the known Standard Model. The discovery of new particles that are not predicted by the SM are a clear sign for new physics

phenomena. Out of the two measurement types, this type probably has the more obvious relation to the aforementioned goal. However, statistically significant deviations from the expectations predicted by the SM are just as clear a sign for new particle physics phenomena, albeit not as determining of one theoretical explanation in case of such an observation. With the Higgs boson being the most recent addition to the confirmed SM particles, it offers a wide range of possible measurements, either confirming the SM or providing new paths to explore possible deviations. The Higgs boson is the particle arising from the mechanism that explains the masses of elementary particles within the SM, except for neutrinos. Thus, it couples to all particles, direct or indirect, depending on whether the particle is massive or not. Due to the Higgs boson's coupling to all massive particles (except for neutrinos), it opens the possibility for new endeavours searching for new particles beyond the Standard Model that might also couple to the Higgs boson.

The presented thesis focusses on the measurement of the Higgs boson coupling to the heaviest known lepton, the τ-lepton, which is effectively a heavier copy of the electron. Due to its mass, the τ-lepton is not stable and typically decays before it interacts with the detector material at ATLAS. Thus, only its decay products can be measured. To utilise the largest possible dataset almost all possible τ-lepton decay product combinations have been considered in the coupling measurement of the $H \rightarrow \tau\tau$ process. As stated before, deviations in this coupling with respect to the SM prediction would be a direct hint for new physics. Instead of measuring the coupling directly, the production cross-section of the $H \rightarrow \tau\tau$ process is measured, which indirectly relates to the coupling. By measuring this cross-section for individual Higgs boson production processes and in unique phase spaces, the sensitivity to possible new phenomena can be increased. Some models predict, for example, a change of the cross-section for highly boosted Higgs bosons, i.e. with large transverse momentum. Additionally, more specific information about the SM are extracted if no deviations are observed. These detailed measurements are made possible by the increased available statistics compared to the previous measurement of the $H \rightarrow \tau\tau$ process [7].

This work is part of a not yet peer-reviewed publication [8] of the ATLAS collaboration. Material taken from this publication will be marked as such. After a brief introduction of the Standard Model of particle physics and the most important theoretical concepts in the context of this thesis in Chapter 2, the experimental environment of the LHC and ATLAS will be introduced in Chapter 3. This experimental environment includes a brief description of the collaborative efforts of reconstructing physics objects as well as their calibrations and associated uncertainties. The measurement's discriminating observable is the invariant mass of the two τ-leptons into which the Higgs boson decays. Detailed studies of this observable, aiming to improve it, have been performed in the context of this thesis which are documented in Chapter 4. Since the presented $H \rightarrow \tau\tau$ measurement is a collaborative work, its overall design which comprises e.g. the event selection and background estimations is briefly summarised Chapter 5. The statistical analysis implemented in the measurement follows in Chapter 6. Several studies validating the statistical model have been performed. In this context, a new approach of validating complex models such as the one implemented in this measurement has been developed, see Chapter 7. Finally, the measurement results are summarised in Chapter 8, yielding observations that are in agreement with the Standard Model. Conclusions of the measurement are given in Chapter 9.

CHAPTER 2

The Standard Model and the Higgs-Brout-Englert Mechanism

The Standard Model (SM) of particle physics has been developed over decades and shows remarkable success in predicting particle interactions and properties over a wide range of scales[1]. Starting from the 1950s with the extension of the back then model to include strong interactions [9], more and more aspects were added over time to form the SM as we know it today. It describes all known elementary particles as well as their interactions. The only known force that is not part of this theoretical framework is the gravitational force, which is orders of magnitudes smaller than the other forces in the microscopic world. This chapter will give an overview of the most important concepts relevant to the measurement that will be discussed in this thesis. A more detailed description of the theoretical background of the SM is given in the references that were consulted for this chapter, see References [10–12]. Throughout this thesis natural units will be used as described in Reference [13].

2.1 Overview

The Standard Model is a quantum field theory describing all known elementary particles and three out of four known forces between them. A comprehensive overview of all particles associated to the SM is given in Figure 2.1. Although not explicitly shown in the figure, the SM also includes anti-particles which have the same masses but opposite (electromagnetic, weak and strong) charges with respect to their partner particle.

Commonly referred to as building blocks of matter are the fermions with half-integer spin. They are subdivided into three generations with the first three columns in Figure 2.1 representing the generations. The fermions of the first generation are the constituents of all stable known matter such as hydrogen and other atoms as well as molecules. With respect to their quantum numbers the fermions of the second and third generation can be interpreted as copies of the first generation's fermions with increasing masses. Fermions carrying colour charge, c.f. Section 2.1.3, are called quarks, while fermions without colour charge are referred to as leptons.

Interactions are mediated by the gauge bosons in the fourth column, while the massive particles acquire their mass through the Higgs mechanism with its associated Higgs boson. The fermions'

[1] In the context of particle physics "scales" refer to energy regimes of interactions.

quantum numbers determine the interactions, which arise from local gauge invariances, they participate in.

While the SM is considered a great success, since it e.g. predicted the existence of particles before their discovery[2], there are also some more and some less obvious shortcomings. Some of the more obvious shortcomings are the missing quantum field description of gravitation within the SM and the missing source of matter-antimatter asymmetry to explain this effect's order of magnitude observed in the universe. Other discrepancies with respect to experimental observations only arise at high precisions such as a 4.2σ tension between theory and experiment of the muon's anomalous magnetic moment [14, 15]. High precision measurements enable tests of higher-order SM predictions that may be modified by physics beyond the SM at higher energy scales.

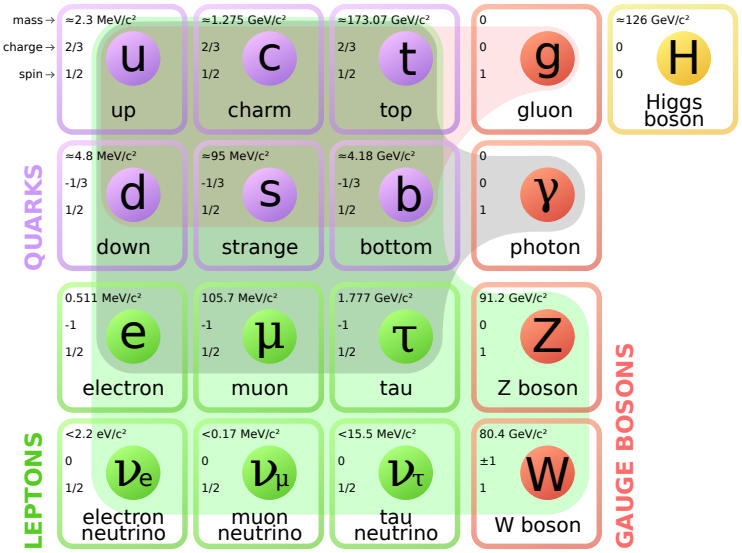

Figure 2.1: Overview of all particles and force carriers that are part of the Standard Model of particle physics. Their masses, spins and electric charges are quoted. Connections between the force carriers and quarks/leptons indicate the type of interaction they participate in. Taken from Reference [16].

2.1.1 The Electromagnetic Force

In the context of the Standard Model, the electromagnetic force is introduced by a local gauge transformation. Generally, a free fermion field's Lagrangian[3], given by [11]

$$\mathcal{L} = \bar{\psi}(i\gamma^{\mu}\partial_{\mu} - m)\psi\,, \tag{2.1}$$

is invariant under global $U(1)$ phase transformations [11]

$$\psi(x) \rightarrow \psi'(x) = e^{ia}\psi(x)\,, \tag{2.2}$$

[2] Such as the W-boson, Z-boson, Higgs boson and top quark.
[3] Using the partial derivative ∂_{mu} and the Dirac matrices γ^{μ}.

where the fermion field is denoted with $\psi(x)$ and the transformation can be any real number a in the exponent. However, this Lagrangian only describes the free propagation of fermions and no electromagnetic interactions. By replacing the real number a of the global transformation with a localised real function $a(x)$ these interactions can be included in the Lagrangian. In case of the localised function $a(x)$ the Lagrangian is not invariant under the aforementioned transformation any more. Thus, new transformations, introducing the photon field A_μ, are defined for the partial derivative ∂_μ and the photon field itself [10]

$$\partial_\mu \rightarrow D_\mu = \partial_\mu + iqA_\mu \,, \tag{2.3}$$

$$A_\mu(x) \rightarrow A'_\mu(x) = A_\mu(x) - \frac{1}{q}\partial_\mu a(x) \,. \tag{2.4}$$

The new covariant derivative D_μ implies that only electrically charged particles with non-zero q take part in the electromagnetic interaction. Usually, the fine structure constant α_{em} is used to characterise the coupling of particles to the photon field which is given by $\alpha_{\text{em}} = \frac{q^2}{4\pi}$ [17]. Finally, the field A_μ needs to obey its own dynamics, otherwise it would be possible to find a transformation under which it vanishes. This dynamic is given by the Maxwell equations and can be written in terms of a Lagrangian using the electromagnetic field tensor $F_{\mu\nu}$ [11]

$$\mathcal{L} = -\frac{1}{4}F_{\mu\nu}F^{\mu\nu} \,. \tag{2.5}$$

Modifying the free fermion field's Lagrangian from Equation 2.1 with the aforementioned transformations and photon field dynamics leads to the final Lagrangian of the electromagnetic force in the SM formalism, also called Quantum Electrodynamics (QED) [10]

$$\mathcal{L}_{\text{em}} = \bar{\psi}(i\gamma^\mu D_\mu - m)\psi - \frac{1}{4}F_{\mu\nu}F^{\mu\nu}. \tag{2.6}$$

2.1.2 The Weak Force

The weak force is part of the $SU(2)_L \times U(1)_Y$ group in the Standard Model, also known as Glashow-Weinberg-Salam theory [18–20]. Its non-Abelian $SU(2)_L$ group describes weak interactions and is unique in the sense that it distinguishes between left-handed and right-handed fermion fields that are projections using the operators[4] [11]

$$\psi_L = \frac{1-\gamma_5}{2}\psi, \qquad \psi_R = \frac{1+\gamma_5}{2}\psi \,. \tag{2.7}$$

Left-handed fermion fields appear as weak isospin I doublets and right-handed fields as isospin singlets. Given the Pauli matrices σ^i, the doublets transform under the matrix [11]

$$U = e^{ia^i\sigma^i/2} \,, \tag{2.8}$$

[4] The projection operators are based on the Dirac matrix $\gamma_5 = i\gamma_0\gamma_1\gamma_2\gamma_3$.

giving rise to the transformation of the doublets into the $U(1)_{\text{em}}$ group of Section 2.1.1 [11]

$$U_{SU(2)_L \times U(1)_Y \to U(1)_{\text{em}}} = e^{ia\sigma_3/2} e^{iaY/2} . \tag{2.9}$$

The weak hypercharge Y is related to the electric charge of the fermions and their weak isospin's third component via [11]

$$Q = I_3 + \frac{Y}{2} . \tag{2.10}$$

Following the same recipe as in Section 2.1.1, the electroweak gauge fields can be written as [11]

$$W^a_{\mu\nu} = \partial_\mu W^a_\nu - \partial_\nu W^a_\mu + g_2 \epsilon^{abc} W^b_\mu W^c_\nu \tag{2.11}$$

$$B_{\mu\nu} = \partial_\mu B_\nu - \partial_\nu B_\mu , \tag{2.12}$$

with three $W^a_{\mu\nu}$ fields and the weak coupling strength g_2. In detail, the recipe demands to identify the global symmetry of the free Lagrangian, generalise it to a local symmetry with the corresponding covariant derivative and adding a kinetic term for the newly introduced field(s) [11]. The dynamics of the electroweak fields, similarly to the electromagnetic dynamics, are [11]

$$\mathcal{L} = -\frac{1}{4} W^a_{\mu\nu} W^{\mu\nu,a} - \frac{1}{4} B_{\mu\nu} B^{\mu\nu} . \tag{2.13}$$

The physical bosons (photon, W-boson, Z-boson) are results of a rotation of these fields with the weak mixing angle $\cos\theta_W = \frac{g_2}{\sqrt{g_2^2 + g_1^2}}$ which also relates the weak hypercharge coupling g_1 and the electromagnetic charge $e = g_1 \cos\theta_W$ [11].

The final fermion Lagrangian does not contain explicit mass terms for neither the fermions nor the bosons as they would break the gauge symmetry: [11]

$$\begin{aligned} \mathcal{L} = &\sum_{j=1}^{6} \bar{\psi}^j_L i\gamma^\mu \left(\partial_\mu - i g_2 \frac{\sigma^a}{2} W^a_\mu + i g_1 \frac{Y}{2} B_\mu \right) \psi^j_L \\ &+ \sum_{j=1}^{9} \bar{\psi}^j_R i\gamma^\mu \left(\partial_\mu + i g_1 \frac{Y}{2} B_\mu \right) \psi^j_R . \end{aligned} \tag{2.14}$$

However, fermion masses as well as W-boson and Z-boson masses are experimentally confirmed to be non-zero [21–25]. The mechanisms by which these particles acquire their mass will be introduced in Section 2.2.1 and 2.2.2.

2.1.3 The Strong Force

Applying the recipe of Section 2.1.1 to more general non-Abelian groups $SU(N)$ gives rise to the Yang-Mills theory [9, 11]. In case of the strong force, the SM formalism is using the $SU(3)_C$ group and is called Quantum Chromodynamics (QCD). The free fermion fields occur as colour triplets q_i with $i = 1, 2, 3$ where each quark flavour has its own field. These colour states are the quantum number of the strong interaction and are only non-zero for quarks and gluons. Eight individual gauge fields

G^a_μ, associated to the gluons [10], arise from the covariant derivative [11]

$$D_\mu = \partial_\mu - ig_s \frac{\lambda^a}{2} G^a_\mu \,, \tag{2.15}$$

with the strong coupling coupling constant g_s and the Gell-Mann matrices λ^a. Each gauge field carries a combination of the colour states introduced for the fermions. The dynamics of QCD are encoded in its Lagrangian [11]

$$\mathcal{L} = \sum_q \bar{q}(i\gamma^\mu \partial_\mu - m_q)q - \sum_q -g_s \bar{q}\gamma^\mu \frac{\lambda^a}{2} q G^a_\mu - \frac{1}{4} G^a_{\mu\nu} G^{a,\mu\nu} \tag{2.16}$$

with the gluon field strengths using the structure constants f^{abc} [11]

$$G^a_{\mu\nu} = \partial_\mu G^a_\nu - \partial_\nu G^a_\mu + g_s f^{abc} G^b_\mu G^c_\nu \,. \tag{2.17}$$

From this Lagrangian arise triple and quartic gluon self-interactions. Since the gluons carry colour charge, these self-interactions result in an anti-screening effect which ultimately leads to the strong force decreasing with increasing momentum Q^2 and increasing with distance [26]. Thus, only colour neutral bound states can be observed freely, which is also referred to as confinement.

This variation of the strong force can be interpreted as a variation of the strong coupling constant $g_s = \sqrt{4\pi\alpha_s}$ [11] with momentum Q^2. Since the theory is renormalisable, divergences introduced by high momentum loops[5] are absorbed into the coupling by introducing a cut-off scale μ_R [11]. A similar effect can be observed for the coupling constant of QED, α_{em}, which consequently also varies as a function of the momentum Q^2. However, the structure of the variation is different since the photon does not self-interact as opposed to the gluon.

2.2 Higgs Physics

All fermions[6] and massive bosons acquire their mass through their interaction with the Higgs field. While the interaction with the Higgs field is common for massive particles, the interaction structure and motivation differs for fermions and bosons. Naive mass terms in the fermion Lagrangian would result in a mixing of left-handed and right-handed fields, breaking the gauge symmetry introduced in the electroweak formulation of the SM. Introducing mass terms for the massive bosons directly breaks the gauge symmetry, thus interactions with the Higgs field are needed for both particle categories. Although the mechanism is named after Peter Higgs, it was proposed by three author groups independently, Higgs [27], Englert and Brout [28] and Guralnik, Hagen and Kibble [29]. The boson masses are generated by the spontaneous symmetry breaking in the coupling to a complex scalar field. This broken symmetry manifests itself in a non-zero vacuum expectation value (vev) or ground state of the field. A detailed description of the mechanism is given in References [10–12], which were consulted for this section.

[5] Loops are closed internal propagators in Feynman graphs. As explained in Reference [13] Feynman diagrams represent computations of particle physics processes graphically.

[6] Except for neutrinos which are massless in the SM.

2.2.1 Electroweak Symmetry Breaking

The electroweak symmetry discussed in Section 2.1.2 is spontaneously broken by the introduction of a complex scalar field [11]

$$\phi(x) = \begin{pmatrix} \phi(x)^+ \\ \phi(x)^0 \end{pmatrix} . \tag{2.18}$$

Since the goal is to determine mass terms for the massive weak bosons, this field should be an isospin doublet with weak hypercharge $Y = 1$ leading to the covariant derivative [11]

$$D_\mu = \partial_\mu - ig_2 \frac{\sigma^a}{2} W_\mu^a + ig_1 \frac{1}{2} B_\mu , \tag{2.19}$$

which is the same covariant derivative as the one used for the fermion Lagrangian in Equation 2.14. Consequently, the Lagrangian of the scalar Higgs field is given by [11]

$$\begin{aligned} \mathcal{L}_H &= (D_\mu \phi)^\dagger (D^\mu \phi) - V(\phi) , \\ \text{with} \quad V(\phi) &= -\mu^2 \phi^\dagger \phi + \frac{\lambda}{4} (\phi^\dagger \phi)^2 = \frac{\lambda}{4} (\phi^\dagger \phi - \frac{2\mu^2}{\lambda})^2 - \frac{\mu^4}{\lambda} . \end{aligned} \tag{2.20}$$

The potential $V(\phi)$'s minima are given by $v^2 = \phi^\dagger \phi = \frac{2\mu^2}{\lambda} = (246.22\,\text{GeV})^2$ if μ^2 and λ are positive [11]. This leads to a shape for the potential as it is shown in Figure 2.2. For the photons to

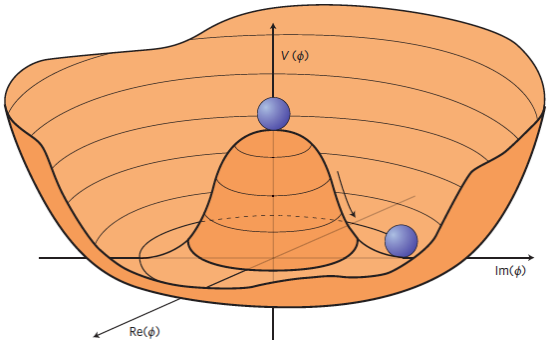

Figure 2.2: Sketch of the Higgs potential's shape for positive values of μ^2 and λ. Taken from Reference [30].

remain massless a field configuration for the vacuum is chosen[7] where the electrically charged field component vanishes [11]

$$<\phi> = \frac{1}{\sqrt{2}} \begin{pmatrix} 0 \\ v \end{pmatrix} \tag{2.21}$$

as the electrically neutral component is always invariant under $U(1)$. However, this configuration is not invariant under the transformation introduced in Equation 2.8 nor a phase shift of $e^{iaY/2}$ which breaks the electroweak symmetry [11].

Excitations of the field close to its minimum correspond to particles. Thus, small deviations,

[7] Using an appropriate gauge such that SM interactions are "easy" to identify.

introducing the real fields H, χ, ϕ_1 and ϕ_2, can be written as [11]

$$\phi(x) = \frac{1}{\sqrt{2}} \begin{pmatrix} \phi_1(x) + i\phi_2(x) \\ v + H(x) + i\chi(x) \end{pmatrix} . \tag{2.22}$$

The potential introduced in Equation 2.20 yields a term proportional to $\mu^2 H^2$ using this representation of the Higgs field. Hence, the Higgs boson mass is given by $m_H = \sqrt{2}\mu$ [11]. The other real fields in this representation do not correspond to physical fields as they can be gauged away using an appropriate gauge resulting in [11]

$$\phi(x) = \frac{1}{\sqrt{2}} \begin{pmatrix} 0 \\ v + H(x) \end{pmatrix} , \tag{2.23}$$

which gives rise to the self-coupling terms of the Higgs boson in its potential. Finally, the physical fields of the electroweak sector's bosons are obtained by using Equation 2.22 in the Lagrangian defined in Equation 2.20. Together with the application of the gauge used to eliminate the non-physical fields in Equation 2.23, the physical boson fields are a rotation of the original W^a_μ and B_μ fields: [11]

$$W^\pm_\mu = \frac{1}{\sqrt{2}}(W^1_\mu \mp iW^2_\mu) , \quad \begin{pmatrix} Z_\mu \\ A_\mu \end{pmatrix} = \begin{pmatrix} \cos\theta_W & \sin\theta_W \\ -\sin\theta_W & \cos\theta_W \end{pmatrix} \begin{pmatrix} W^3_\mu \\ B_\mu \end{pmatrix} . \tag{2.24}$$

This representation of the fields leads to the following mass terms in the Lagrangian: [11]

$$m^2_W W^+_\mu W^{-\mu} + \frac{1}{2}(Z_\mu, A_\mu) \begin{pmatrix} m^2_Z & 0 \\ 0 & 0 \end{pmatrix} \begin{pmatrix} Z^\mu \\ A^\mu \end{pmatrix} . \tag{2.25}$$

Hence, the masses of the massive weak gauge bosons are obtained from the relation to the original W^a_μ and B_μ fields and are given by: [11]

$$m_W = \frac{g_2}{2} v , \quad m_Z = \frac{\sqrt{g_1^2 + g_2^2}}{2} v . \tag{2.26}$$

The non-physical fields χ, ϕ_1 and ϕ_2, also referred to as Goldstone bosons in this context, have been absorbed into mass terms for the massive gauge bosons. Additionally, the Lagrangian's mass terms show that the choice of the vacuum field configuration in Equation 2.21 retains a massless physical photon field A_μ.

2.2.2 Yukawa Couplings

Fermion masses are achieved through the introduction of Yukawa interactions. This type of interaction generally describes the coupling of a scalar field to fermion fields [31]. In the SM, the Higgs field, which was motivated by the non-zero masses of the weak gauge bosons, is chosen as the scalar field. It has to be noted though, that these two mechanisms are not fundamentally related, i.e. the scalar field in the Yukawa interactions could in principal be another field. The corresponding Lagrangian for one generation of fermions, with the Higgs field being the scalar field, takes the form [11]

$$\mathcal{L}_Y = -Y_l \bar{L}_L \phi l_R - Y_d \bar{Q}_L \phi d_R - Y_u \bar{Q}_L \phi^c u_R + \text{h.c.} , \tag{2.27}$$

with L_L and Q_L being the left-handed isospin lepton and quark doublets and ϕ^c being the charge conjugate of the Higgs doublet $\phi^c = i\sigma_2\phi^*$ [11]. Since both the fermion and the scalar fields are isospin doublets, their product transforms as an isospin singlet [12]. Consequently, the product of the two doublets and the right-handed singlets do not violate gauge invariance any more and mass terms are possible in the Lagrangian. Using the gauge of Equation 2.23, the Lagrangian can be rewritten as [11]

$$\mathcal{L}_Y = -\sum_{f=l,d,u} (m_f \bar{\psi}_f \psi_f + \frac{m_f}{v} H \bar{\psi}_f \psi_f), \tag{2.28}$$

with the fermion mass terms $m_f = Y_f \frac{v}{\sqrt{2}}$ and interaction terms of the fermions with the Higgs field. Given the fermion mass relation, the coupling of the fermions to the Higgs field is proportional to the fermion mass. Even though the mechanisms by which fermions and bosons acquire their masses are different, both their mass terms are proportional to the vacuum expectation value v.

When all three fermion generations are considered in the Lagrangian introduced in Equation 2.27, terms arise that mix different fermion generations. The weak eigenstates and the mass eigenstates of the fermions are not the same.[8] Using the mass eigenstates in the electroweak Lagrangian shown in Equation 2.14 results in a modification of the fermion interactions with the W-boson [11]. This leads to a mixing of fermion generations which is generally described by a unitary matrix. In the lepton sector this matrix is an identity matrix as long as the neutrinos are massless [11]. For quarks this matrix is known as the Cabibbo-Kobayashi–Maskawa (CKM) matrix [32, 33] and describes the mixing of quark flavours. The unitary CKM matrix takes the form [34]

$$V_{\text{CKM}} = \begin{pmatrix} V_{ud} & V_{us} & V_{ub} \\ V_{cd} & V_{cs} & V_{cb} \\ V_{td} & V_{ts} & V_{tb} \end{pmatrix}, \tag{2.29}$$

with decreasing values the more off-diagonal the element is. Thus, transitions taking place on off-diagonal matrix elements are called Cabibbo-suppressed.

Additionally, the CKM matrix is accompanied by a complex phase which, if non-vanishing, results in a violation of the combined charge conjugation and parity (CP) symmetry. Since thus far the only observation of CP violation in the SM is related to the fermion sector, such as seen in measurements by BaBar [35], Belle [36] and possibly future analyses at Belle II [37], all known CP violating effects are related to the Higgs sector via Yukawa interactions. Hence, the Higgs boson provides an additional path to search for CP violating effects. The process measured in this thesis, i.e. $H \to \tau\tau$, is a promising channel to study the CP properties in the Higgs sector as described in References [38, 39]. Several studies have been performed in preparation for such a measurement at ATLAS [40–42] and a first result has been published by CMS [43]. A certain amount of CP violation is an important component of the Sakharov conditions [44] that were formulated trying to find conditions under which the observed baryon asymmetry in the universe can be explained.

[8] Even if the fermions and bosons were massless, the mass eigenstates would not necessarily be the same as the weak eigenstates.

2.2.3 Production and Decay

The Higgs field couples to all massive fermions and bosons and subsequently so does the Higgs boson which can be interpreted as an excitation of said field. This opens the possibility to produce the Higgs boson in a number of different processes. Since the measurement presented in this thesis utilises data taken at the Large Hadron Collider (LHC), the most relevant production modes in this context involve either gluons or quarks. The massless gluons do not couple directly to the Higgs but rather through quark loops with larger contributions from more massive quarks due to the coupling structure of the Higgs. Some of the leading Feynman diagrams of the most common production modes in proton-proton collisions are shown in Figure 2.3. The production cross-sections calculated

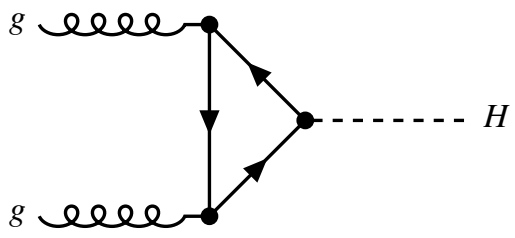

(a) Gluon-gluon fusion with an intermediate quark loop that couples to the Higgs boson (ggH).

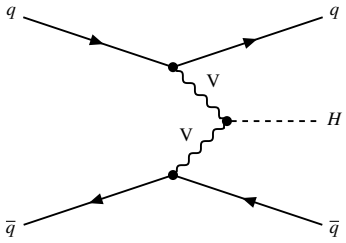

(b) Vector-boson fusion where the bosons are radiated off of quarks (VBFH).

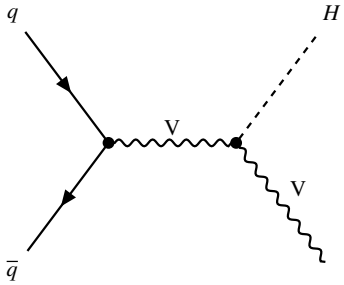

(c) Higgs-Bremsstrahlung where the Higgs boson is radiated off of a vector boson (VH).

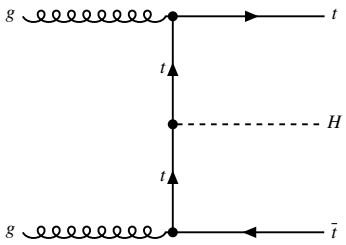

(d) Associated production of the Higgs boson with two top quarks ($t\bar{t}H$).

Figure 2.3: Examples of the leading Feynman diagrams of the targeted Higgs boson production modes.

for the LHC at $\sqrt{s} = 13\,\text{TeV}$ and an assumed Higgs mass of $m_H = 125\,\text{GeV}$ are listed in Table 2.1. Depending on the production mode, the cross-sections are calculated to higher orders of perturbation theory. These higher orders are denoted by NLO (next-to-leading order), NNLO or N3LO.

Gluon-gluon fusion processes (ggH) with an intermediate quark loop provide the highest production cross-section, followed by vector-boson fusion (VBFH). The next highest cross-section is given by the Higgs-Bremsstrahlung process (VH) where the Higgs is radiated off of a vector boson which can either be a W-boson or a Z-boson. Thus, in the $H \to \tau\tau$ measurement, the VH production comprises both WH and ZH production. The leading production modes up to the associated production of the Higgs with two top quarks ($t\bar{t}H$) are targeted while it is not attempted to measure the associated production with two b-quarks ($b\bar{b}H$) and smaller cross-sections. Even though $b\bar{b}H$ and $t\bar{t}H$ production cross-sections are of similar size, $b\bar{b}H$ is more difficult to identify in the detector which will be discussed in more detail in Section 5.2 together with the detector signatures associated to each targeted production mode. However, the $b\bar{b}H$ production mode is included in the measurement but its

cross-section is fixed to the Standard Model prediction. The production cross-section for $b\bar{b}H$ has been computed in the 4 flavour-scheme (4FS) and the 5 flavour-scheme (5FS), where no b-quarks are allowed in initial states in the 4FS [45]. Associated production with a single top quark tH is not measured in the presented analysis due to its small cross-section. Nevertheless, it is included in the measurement with its cross-section fixed to the Standard Model prediction.

Production mode	Cross-section in pb	Comments
ggH	48.58	N3LO
VBFH	3.782	(approx.) NNLO QCD and NLO EW accuracies
WH	1.373	NNLO QCD and NLO EW accuracies
ZH	0.884	NNLO QCD and NLO EW accuracies
$t\bar{t}H$	0.507	NLO QCD and NLO EW accuracies
$b\bar{b}H$	0.488	Santander matched numbers with 5FS (NNLO) and 4FS (NLO). No EW corrections
tH (t-channel: $qb \to tHq$)	0.074	NLO QCD accuracy in 5FS. No EW corrections
tH (s-channel: $qq \to tHb$)	0.003	NLO QCD accuracy in 5FS. No EW corrections

Table 2.1: Higgs production cross-sections at $\sqrt{s} = 13\,\text{TeV}$ for $m_H = 125\,\text{GeV}$. The uncertainties on the cross-sections are not shown since this table intends to illustrate the order of magnitude of the individual production modes. Numbers and perturbation theory accuracy for each process are taken from References [45, 46].

Due to the coupling of the Higgs boson it can (indirectly) decay into all known SM particles. Similar to the production modes, the decay into massless particles occurs via loops of massive fermions. The most common branching ratios are shown in Figure 2.4 as a function of m_H. Relevant for this measurement is a mass of $m_H = 125\,\text{GeV}$ which is used for the simulation of the Higgs signal. The focus lies on the decay $H \to \tau\tau$[9] with a branching ratio of roughly 6.3% [45]. With the τ-lepton being the heaviest lepton, this decay gives access to the Yukawa interaction of the Higgs. The other fermionic decays with large branching ratios such as $H \to b\bar{b}$ are more difficult to measure at the LHC because of the hadronic activity in the environment of proton-proton collisions. A multitude of measurements are performed in order to determine whether the resonance at 125 GeV first observed in 2012 [1, 2] is the SM Higgs boson or possibly a Higgs boson of a theory beyond the SM. These measurements target specific properties of the resonance such as its quantum numbers, see e.g. References [47–49] measuring its spin as well as charge conjugation and parity properties. Thus far all observed properties are in agreement with the Standard Model predictions for the Higgs boson.

The presented measurement of the $H \to \tau\tau$ production cross-sections is sensitive to possible deviations from the SM in multiple ways. Differential cross-section modifications are targeted by the Simplified Template Cross Sections [45], as discussed in Section 5.1. Overall modifications of the

[9] The charges of the decay products are omitted in this notation for electrically neutral mother particles as the charges commute.

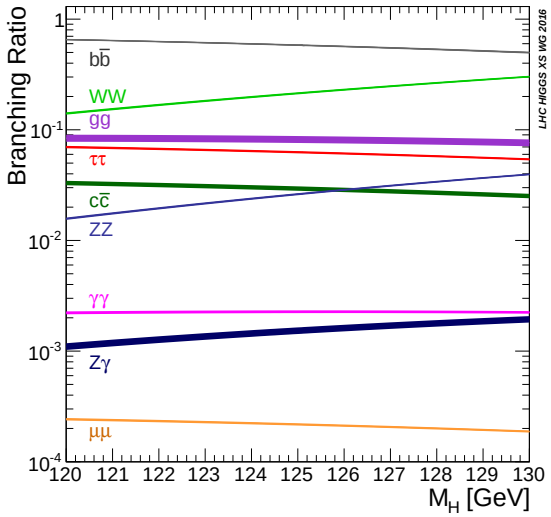

Figure 2.4: Branching ratios of the Higgs boson decay versus the Higgs mass. Taken from Reference [45].

$H \to \tau\tau$ rate would be observed in the inclusive cross-section measurement which is introduced in Section 6.2. If new particles were to couple to the Higgs boson and modify e.g. its branching ratio into particles that are invisible to the LHC experiments, this would indirectly modify its branching ratio into a pair of τ-leptons. Thus, the presented measurement aims to achieve multiple goals. An as precise as possible measurement of the $H \to \tau\tau$ production cross-sections and consequently searching for indirect hints of physics effects beyond the Standard Model.

2.3 τ-leptons

Since the presented measurement involves a Higgs boson decaying into a pair of τ-leptons[10], it is noteworthy to discuss this lepton in more detail. Being the heaviest lepton known to the SM with a mass of $m_\tau = 1.777\,\text{GeV}$ [25], its properties differ from the lighter known leptons. Due to its invariant mass, the τ-lepton can either decay into an electron or muon and their associated neutrino or even into hadrons.[11] All decays occur via a virtual W-boson. In the following, decays into either electrons or muons will be referred to as leptonic decays and denoted with τ_{lep} while decays into hadrons will be referred to as hadronic decays and denoted with τ_{had}. Since the kinematics allow for a variety of possible decays, the τ-lepton's lifetime is rather short, $\tau_\tau = 290 \times 10^{-15}\,\text{s}$ [25]. It is possible to derive a leading order estimate of the τ-lepton's lifetime as done in Reference [50] by assuming zero mass for all produced fermions:

$$\tau_\tau \equiv \frac{1}{\Gamma(\tau)} = \left(\Gamma(\mu) \left(\frac{m_\tau}{m_\mu} \right)^5 \left[2 + N_C \left(|V_{ud}|^2 + |V_{us}|^2 \right) \right] \right)^{-1} \approx 330 \times 10^{-15}\,\text{s}\,. \tag{2.30}$$

[10] To be more precise, the decay involves a τ-lepton and an anti-τ-lepton. Particles and anti-particles will not be differentiated in the following.

[11] Each decay always involves a τ-lepton neutrino.

At the same time, this equation motivates the leading order branching ratios of the τ-lepton's final states. The number of colours accessible in the strong interaction, $N_C = 3$, makes decays into hadrons more likely than decays into leptons. Roughly 20% of the τ-lepton decays are expected to be electrons or muons each and the other 60% are expected to be hadrons, as can be seen from Equation 2.30. In principle, all up-type and down-type quarks couple to the virtual W-boson but due to the τ-lepton's invariant mass the decay mostly involves up-, down- and strange quarks. Thus, the final hadronic decay products are mainly composed out of charged and neutral pions and, to a lesser extent, kaons.[12] Some of these decays happen via intermediate resonances such as the decay into one charged and one neutral pion via the ρ^- meson. The most relevant resonances are given in Table 4.2 in Section 4.3.2 in the context of the di-τ mass reconstruction. An overview of all possible final states with the categorisation used in ATLAS is given in Figure 2.5. Only decay modes involving pions are classified into the shown categories, i.e. decays involving kaons are grouped into "Others". The τ-lepton decay mode classification will be discussed briefly in Section 3.3.4. It distinguishes the number of charged hadronic decay products (X) and neutral hadronic decay products (Y), resulting in the short-hand notation XpYn.[13]

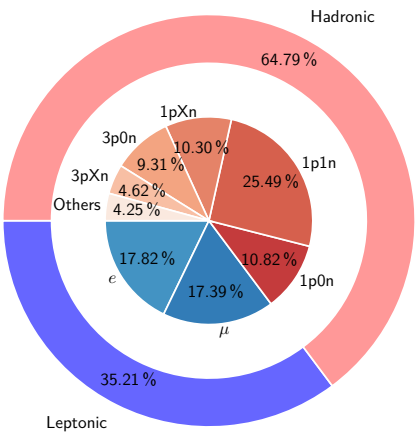

(a) Branching ratios of the τ-lepton decay.

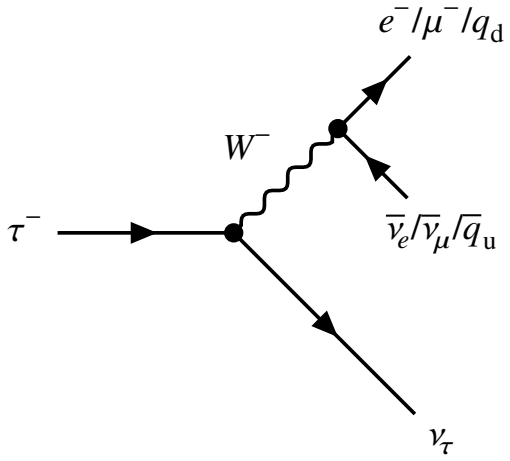

(b) Feynman diagram of the τ-lepton decay.

Figure 2.5: Feynman diagram of the τ-lepton decay and overview of the measured branching ratios. Decay modes involving kaons are grouped into "others". Values are taken from Reference [25]. XpYn denotes the number of charged hadronic decay products (X) and neutral hadronic decay products (Y).

Using special relativity, the boost and, thus, energy dependent decay length of the τ-lepton can be approximated to

$$L = \gamma\beta c\tau = \frac{\left|\overrightarrow{p}_\tau\right|}{m_\tau} c\tau \approx 49\,\mu\text{m} \cdot p_\text{T}[\text{GeV}]. \tag{2.31}$$

Hence, they typically do not interact with the detector material themselves, only their decay products do. Even though τ-leptons can travel macroscopic distances with energies easily accessible at the

[12] Decays into kaons are Cabibbo suppressed by $|V_{us}|$.

[13] The short-hand notation XpYn is motivated by the colloquial term for charged decay products producing tracks, prong (p), and the neutral (n) decay products.

LHC, they already need a transverse momentum of $p_{\mathrm{T},\tau} > 674\,\mathrm{GeV}$ to reach the innermost layer of the detector at 33 mm [51]. This effect can be neglected in this measurement due to the typical τ-lepton energy ranges for the considered processes, see Figure 5.7(a) in Section 5.3.2.

In cases where τ-leptons are produced in pairs as the result of a decaying resonance, the spin of the resonance plays an important role in the momentum distributions of the τ-lepton decay products. Since the τ-lepton decays via the weak interaction and (anti-)neutrinos are (right-)left-handed, the decay products' resulting momenta depend on the helicity[14] of the individual τ-lepton. Generally, events with τ-leptons, e.g. originating from decaying resonances, can be classified into three main categories according to the aforementioned decay classes. These categories are fully leptonic decays ($\tau_{\mathrm{lep}}\tau_{\mathrm{lep}}$), semi-leptonic or semi-hadronic decays ($\tau_{\mathrm{lep}}\tau_{\mathrm{had}}$) and fully hadronic decays ($\tau_{\mathrm{had}}\tau_{\mathrm{had}}$). Since the measurement only targets fully leptonic decays with different lepton flavours as explained in Section 5.2, these decays are also referred to as $\tau_e\tau_\mu$.

[14] The helicity is the projection of a particle's spin onto its momentum.

CHAPTER 3

Data, Event Reconstruction and Simulation

The proton-proton collision data analysed in the $H \rightarrow \tau\tau$ measurement presented in this thesis corresponds to the full Run II dataset provided by the LHC and recorded by ATLAS. Run II comprises the data taking periods in the years of 2015 until 2018. In this section, a short overview of the LHC and ATLAS will be given, followed by a description of the object reconstruction and calibration techniques applied at ATLAS. Finally, the simulated datasets utilised in the measurement will be introduced.

3.1 LHC

The data collected by the ATLAS experiment are provided by the Large Hadron Collider located at the Swiss-French border at CERN. While ATLAS records the results of deep inelastic scattering (DIS) processes, the LHC is responsible for bringing particles to collision. Detailed descriptions of the LHC are given in References [3, 4] on which this section is based on.

It is possible to operate the LHC with different particle types colliding. These particles are either protons or lead ions ($^{208}\mathrm{Pb}^{82+}$) [4].[1] The data analysed in this measurement are the result of proton-proton collisions. However, the basic principles behind the acceleration and steering of the particle beams is the same for both types. Superconducting cavities are used to generate electric fields in which the particles can be accelerated while superconducting dipole and quadrupole magnets are used to steer and focus the beams. The superconductivity is important to reach the required field strengths of e.g. magnetic fields up to 8.33 T [4]. Since the LHC is designed to accelerate protons to energies of up to 7 TeV per beam at a bunch frequency of 40 MHz, involved machine designs are necessary to achieve these goals [4]. An overview of the various pre-accelerator stages and the major experiments is shown in Figure 3.1. One possible measure to quantify the performance of the LHC accelerator complex is the luminosity. It relates the number of events generated per second for a specific process to machine specifications, like the number of protons or the emittance of the beams. Given the process' cross-section the number of events per second can be calculated via [4]:

$$N_{\text{event}} = L\sigma_{\text{event}}\,, \tag{3.1}$$

with the LHC's original design peak instantaneous luminosity being $L = 1 \times 10^{34}\,\mathrm{cm}^{-2}\,\mathrm{s}^{-1}$.

[1] For one day in 2017 xenon ions were brought to collision [53].

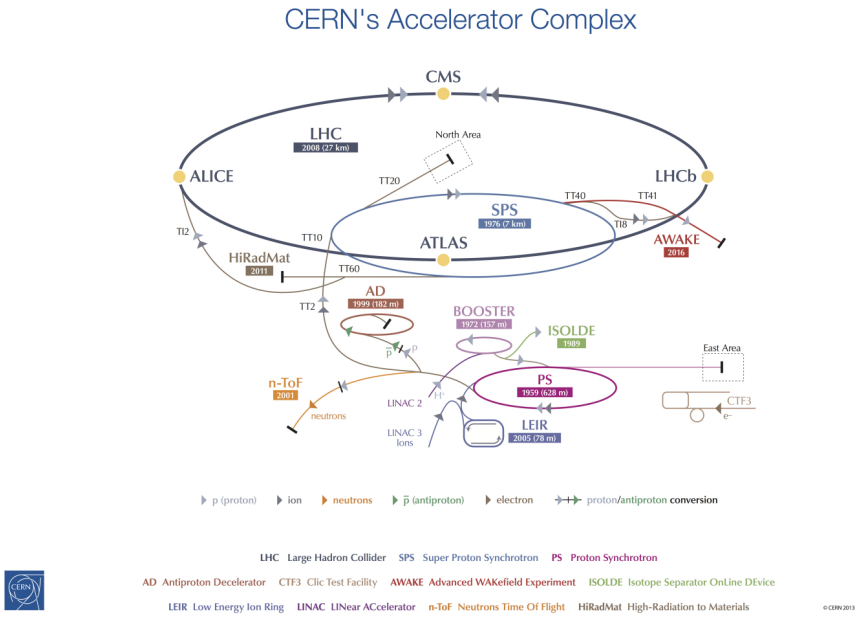

Figure 3.1: Overview of the CERN accelerator complex including all accelerators and major experiments like ATLAS. Taken from Reference [52].

Due to different effects, such as the beams colliding at the interaction points of different experiments or residual gas in the beam lines, the luminosity is not constant over the course of one LHC fill.[2] This effect is shown in Figure 3.2 for one fill where the instantaneous luminosity is measured by counting reconstructed $Z \rightarrow \mu\mu$ events. It also shows that the achieved instantaneous luminosity surpassed the design luminosity by roughly a factor of 2.

3.2 ATLAS

ATLAS is the biggest detector at the LHC, albeit not the heaviest, with a length of 46 m, a diameter of 25 m and a weight of 7 000 t [55].[3] The following section is based on the detailed description of ATLAS in Reference [57]. Its cylindrical design and detector components reflect the goal of measuring a broad physics spectrum unlike e.g. the LHCb detector [58] which specifies in b-quark physics. Thus, the ATLAS detector's components cover as much as possible of the solid angle around the nominal interaction point in its centre.[4] This design is reflected in the distinction of a barrel region of the detector and a forward region with individual components of the same detector subsystems. The interaction point functions as the origin of the right-handed coordinate system that is used with the x-axis pointing towards the centre of the LHC, the y-axis pointing upwards and the z-axis going along the beam pipe [8]. Due to the detector's geometry, a spherical representation is typically used

[2] The LHC is filled with protons for both beams once. Afterwards, these beams are stored in the rings and collided during each revolution until the luminosity has degraded so that a refill becomes necessary.

[3] The heaviest detector is the CMS detector with roughly 14 000 t [56].

[4] The actual interaction point, where the two proton beams collide, can slightly deviate from the detector's centre.

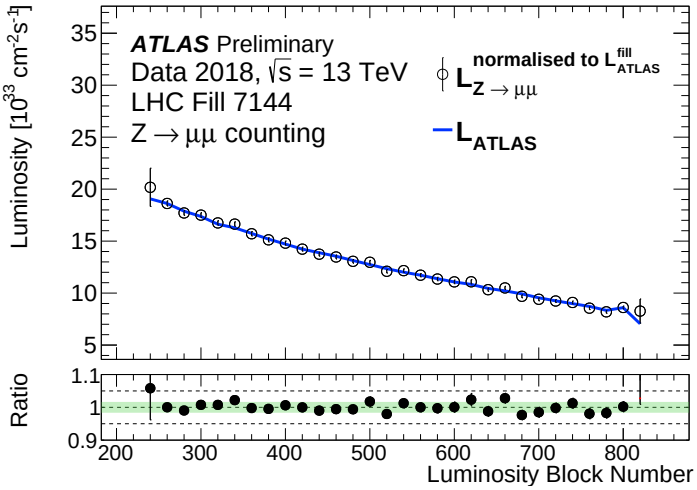

Figure 3.2: Instantaneous luminosity measured by ATLAS in $Z \to \mu\mu$ events for one fill of the LHC. The ratio of the instantaneous luminosity measurements in $Z \to ee$ and $Z \to \mu\mu$ events is shown. Taken from Reference [54].

with the pseudorapidity η replacing the polar angle θ and subsequently using ΔR to measure angular distances [8]

$$\eta = -\ln\tan\frac{\theta}{2}, \quad \Delta R = \sqrt{(\Delta\eta)^2 + (\Delta\phi)^2}\,. \tag{3.2}$$

The advantage of η with respect to θ is that differences in η are invariant under Lorentz transformations along the beam pipe.

In the $H \to \tau\tau$ measurement discussed in this thesis the full Run II dataset which has been declared "good for physics" [6] is used, resulting in a dataset of the size $(139.0 \pm 2.4)\,\text{fb}^{-1}$ [8, 59, 60]. The recorded data have to fulfill quality criteria to be labelled "good for physics" such as proper working conditions of the detector subsystems.

3.2.1 Detector Components

In order to detect as many particle types as possible, the ATLAS experiment is composed out of multiple subdetectors. Individual types of particles can comprise electrically charged or neutral particles, particles interacting strongly or electromagnetically etc. An overview of ATLAS and its various subdetectors is shown in Figure 3.3. Typically the components are arranged cylindrically in layers, following the general ATLAS design. Toroid and Solenoid magnets place the individual subdetectors in magnetic fields that force electrically charged particles on a bent trajectory via the Lorentz force. The resulting curvature can be used to determine a particle's momentum.

Tracking Detectors

The innermost layers consist of multiple components that can be grouped into tracking detectors and is called Inner Detector (ID). Their purpose is to provide precise position and momentum measurements

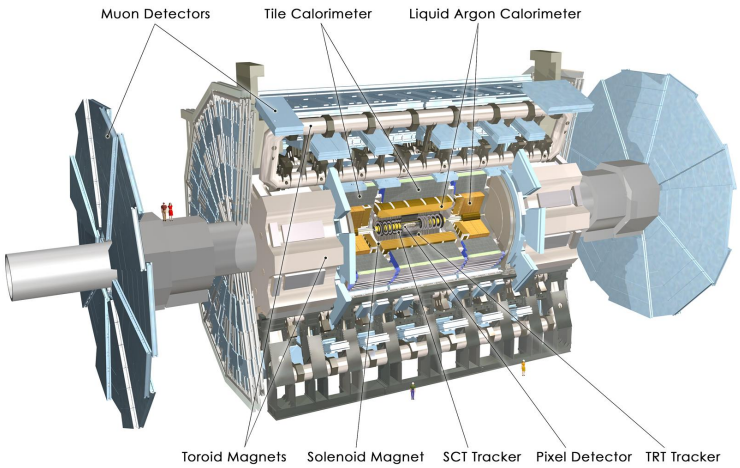

Figure 3.3: Overview of the ATLAS experiment with its detector components. The insertable B-Layer is not included in the graphic. Taken from Reference [61].

of charged particles. This is achieved in a non-destructive way[5] by measuring the particles' interaction with semiconducting material or gas. To some extent it is also possible to identify different particles based on their interactions with the detectors, e.g. to distinguish electrons and charged pions [62].

The detectors closest to the beamline are the pixel detectors. First, when going from the beamline to larger radii, is the insertable B-Layer (IBL) at a distance of only 3.3 cm which was added after Run I [63]. It provides one layer of pixel detectors covering $|\eta| < 3$ and improves the transverse impact parameter resolution by roughly 10 µm, depending on the transverse momentum of the tracks. The IBL is part of the Pixel Detector complex with overall four layers of pixel modules, covering $|\eta| < 2.5$.

Followed by the Pixel Detector is the Semi-Conducting Tracker (SCT) which consists of silicon microstrips. It is arranged in four layers and provides slightly less accurate position measurements along the beamline since the strips are aligned in that direction and larger than the pixels.

Lastly, the transition radiation tracker (TRT) covers the largest volume compared to the other subdetectors of the Inner Detector. It consists of gas-filled drift tubes that register particles through ionisation of the gas and covers $|\eta| < 2$.

Calorimeters

The calorimeters encapsulate the Inner Detector and are responsible for measuring the energies of mostly electromagnetically and strongly interacting particles. They also provide position measurements, however, with less accurate resolutions compared to the Inner Detector. Both calorimeters cover $|\eta| < 4.9$ and measure the energy in a destructive measurement, i.e. the incoming particles are supposed to be completely absorbed by the calorimeter material. Their general layout follows the principle of interaction material followed by readout material in multiple layers.

Closest to the beamline is the electromagnetic calorimeter (ECal) targeting mostly electromagnetically interacting particles. It consists of lead as interaction material and liquid argon as readout material. Its first layer shows a finer granularity compared to the following layers which helps to

[5] In this context non-destructive means that the particles do not deposit all their energy in these components.

resolve e.g. incoming closeby photons.

The hadronic calorimeter (HCal) follows the ECal. It targets mainly strongly interacting particles which is reflected in its interaction material being steel in the barrel region of the detector and copper in the endcap region. The readout materials are scintillating tiles and liquid argon, respectively. Covering the very forward region up to $|\eta| < 4.9$, modules specialised for electromagnetic and hadronic interactions are implemented with copper and tungsten as interaction material. Both forward module types use liquid argon as readout material.

Muon Detectors

The muon chambers (MS) comprise the outermost detector of ATLAS. Since muons mostly interact with the detector materials electromagnetically and Bremsstrahlung only accounts for small energy losses, they are the only particles that are able to pass the calorimeters. This detector subsystem is based on the ionising interaction of muons with gas, similar to the TRT. It covers $|\eta| < 2.7$.

3.2.2 Trigger

Due to technical limitations, it is not possible to record all events at the collision rate of 40 MHz. A final rate of 1 kHz is the goal at which events are written to permanent storage. Thus, a fast decision whether an event is of interest or not has to be made which is achieved by the ATLAS trigger system [64]. This system is able to reduce the initial rate of 40 MHz down to the desired rate of 1 kHz in two steps. First, a hardware based trigger called L1 reduces the rate to roughly 100 kHz which is then further reduced by a software trigger to the final rate written to storage.

Depending on the analysis, the definition of an interesting event may differ but typically it relates to events with small cross-sections compared to pure QCD jet production at a hadron collider. To meet these different demands of interesting events a multitude of possible trigger selections are implemented, targeting different physics objects with different kinematic properties such as the transverse momentum p_{T}. Since it is not possible to apply the full (offline) reconstruction chain at the full collision rate because of its runtime, a dedicated online reconstruction is implemented. One of the dedicated online reconstruction systems is the Fast Tracker [65] that reconstructs tracks in the Inner Detector using a hardware implementation.

The trigger signatures utilised in this measurement comprise the signatures of single isolated light leptons, i.e. electrons or muons, events with an isolated electron and an additional isolated muon as well as events with two hadronically decaying τ-leptons. To further reduce the rate an additional jet is required in events triggered with two τ_{had}. More details on the used triggers are given in Section 5.2.

3.3 Object Reconstruction & Calibration

For the events selected by the trigger system, the physical objects are reconstructed from the detector responses. Dedicated algorithms for different physics objects such as photons, muons or jets are implemented. In the following, the different algorithms will be briefly summarised. All objects, except for photons, are utilised in the $H \rightarrow \tau\tau$ measurement either for the classification of events or as an object of interest due to the various τ-lepton decay channels introduced in Section 2.3.

3.3.1 Electrons & Photons

The reconstruction of electrons and photons is combined within one workflow, see Reference [66]. Since a non-negligible portion of photons, up to 65% at $|\eta| \approx 2.3$, undergo conversion[6] the detector components involved and the general signatures compared to electrons can be very similar.

Both types of particles, electrons and photons, interact electromagnetically and, thus, with the ECal. Hence, the algorithm starts by building topological clusters (topo-clusters) [67] using the nearest-neighbour algorithm, taking into account the noise profile of individual cells. In a next step, the Inner Detector information are used to reconstruct tracks. For photons, this step also includes the finding of conversion tracks and their vertices. If conversion tracks are found, they have to be classified as electron tracks by the TRT. This classification utilises transition radiation caused by charged particles passing through the boundaries of different media for which foam is placed between the TRT's drift tubes. The final clusters are built by using the topo-clusters as seeds for a cluster finding algorithm that allows for variable sized clusters resulting in superclusters. Finally, by matching these superclusters with the tracks and possible conversion vertices, the type of particle is determined. Electrons are defined as a supercluster with a matched track while photons can either be superclusters without tracks or superclusters with conversion tracks and the corresponding conversion vertex.

The physics objects used in analyses are defined by calibrating the electrons and photons and applying particle identification. By minimising the χ^2 between data and simulation in $Z \to ee$ events using the invariant mass distribution of the two reconstructed electrons, corrections to the energy scale and resolution are measured. Residual corrections for photons are measured in $Z \to \ell\ell\gamma$ decays.[7] Overall, the electron energy scale is determined with an uncertainty of less than a percent while the identification uncertainty, also measured in $Z \to ee$ events, is in the lower percent regime.

3.3.2 Muons

Muons are the only particles taking full advantage of all subdetectors in ATLAS. Their reconstruction is described in detail in Reference [68]. Based on the involved detector components, different types of muons are defined.

If the muon produces tracks in the Inner Detector and the muon chambers, it is called a combined muon. Both tracks are combined in a common track fit. This type of muon is the best case scenario and the other types help recovering efficiency for muons where one of these tracks is not well-defined. Examples for this are muons where no track is found in the MS and the inside-out approach is applied. Tracks from the ID are extrapolated to the MS and if three or more aligned hits in the MS are found, this information is used for a combined track fit. The fact that muons are minimum-ionising particles shapes their signal in the calorimeters, typically resembling a constant energy loss. Thus, these information are utilised in cases where calorimeter information are used to define muon objects.

Just like for electrons, the muon objects are calibrated and a particle identification is applied. The associated uncertainties are measured in $Z \to \mu\mu$ and $J/\psi \to \mu\mu$ events.[8] For the muon identification an uncertainty in the small percent regime down to permille has been measured. The energy scale uncertainties have been determined to be in the range of 0.05% to 0.2% depending on the

[6] Conversion happens when photons interact with the detector material and an electron-positron pair is created $\gamma \to e^+e^-$.

[7] ℓ stands for either electrons or muons.

[8] The J/ψ meson is a bound quark state composed out of a charm quark and its antiparticle.

pseudorapidity [69] and have been validated using $\Upsilon \to \mu\mu$ events [70].[9] Overall, the reconstruction efficiency has been measured to be close to 99% [69].

3.3.3 Jets

Jets are a phenomenon caused by the confinement discussed in Section 2.1.3. Since only colour neutral bound states can exist freely, quarks and gluons produced in hard scattering processes are not observed as free quarks or gluons. Instead, a process called hadronisation takes place which results in the formation of a multitude of collimated hadrons. The collection of these hadrons is called a jet.

Typically the hadrons contained in a jet interact with the ECal and HCal, while the electrically charged hadrons also interact with the Inner Detector. In order to exploit the subdetectors with the best resolution for specific hadron interactions a particle flow algorithm is implemented for the jet reconstruction, see Reference [71] for details. After tracks and topo-clusters have been reconstructed, the tracks are matched to clusters if possible and the energy deposits extrapolated from the track are subtracted from the clusters. The possibility of particles contributing to multiple clusters is taken into account.

Finally, the jets are reconstructed from these modified topo-clusters and tracks associated to the vertex of the hard scattering process. The reconstruction uses the anti-k_t algorithm [72] with radius parameter 0.4 [71]. It is possible to distinguish different origins for jets using multivariate analysis techniques such as the neural network described in References [73, 74] used to identify jets originating from b-quarks. This kind of algorithm is often referred to as a tagger. Different working points are defined as the background rejection usually varies as a function of the signal (tagging) efficiency. Depending on the measurement utilising the tagger, the requirements of rejecting more background events or achieving a higher purity of tagged jets may have to be adapted. Thus, tagger working points are usually defined via the achieved signal efficiency.

A transverse momentum resolution of roughly 14% is achieved for jets with $p_{\mathrm{T}} \approx 50\,\mathrm{GeV}$, with an improving resolution for jets with increasing transverse momentum. The jet energy scale uncertainties are at the order of $1 - 5\%$ while the resolution uncertainty is roughly 1% [75].

3.3.4 τ-leptons

As described in Section 2.3 τ-leptons can decay into either leptons or hadrons always with at least one neutrino involved. The τ-lepton reconstruction focuses on hadronically decaying τ_{had} since it is difficult to distinguish prompt leptons[10] and leptons from τ-lepton decays. Thus, leptonically decaying τ-leptons are reconstructed as electrons or muons. A detailed description of the τ_{had} reconstruction is given in References [76, 77].

As hadronic τ-lepton decays involve collimated hadrons, just like jets, their reconstruction is seeded by reconstructed topo-cluster jets with a transverse momentum of at least 10 GeV, using the anti-k_t algorithm with radius parameter 0.4 [78]. Due to its lifetime, a dedicated τ-lepton vertex is reconstructed from the reconstructed tracks associated to the τ-lepton candidate. These tracks are classified according to how likely they are to be produced by charged τ_{had} decay products using a multivariate discriminant [8]. Similarly to jets, a particle flow approach is implemented for the τ_{had} candidates, see Reference [77]. The goal is to reconstruct the individual hadrons of the candidate's

[9] Similar to the J/ψ meson, the Υ meson is a bound state of a bottom quark and its antiparticle.

[10] Prompt leptons are for example the ones in a $Z \to \mu\mu$ decay as opposed to $Z \to \tau\tau \to \mu\mu$.

decay emphasising the detector components with the superior resolution. Thus, energy deposits from charged pions in the ECal have to be identified and subtracted using e.g. track information. With the reconstruction of the individual τ-lepton decay constituents it is possible to classify the τ_{had} into one of the categories defined in Section 2.3. Boosted decision trees are implemented for the final classification improving the counting of neutral pions in the decay.

The final τ-lepton object is defined by the sum of its constituents of the particle flow reconstruction which are calibrated using a boosted regression tree [78]. A transverse momentum resolution of roughly $5-7\%$ [78] is achieved with an uncertainty on the energy scale between $1-4\%$ [8]. In the context of this thesis, studies towards a more precise tau energy scale measurement have been performed. The idea behind this measurement is discussed in Appendix A. The particle identification is based on a neural network [79] with uncertainties around $2-6\%$ [8]. An extensive overview of the measurement techniques used to derive the uncertainties is given in Reference [78]. Depending on the targeted τ-lepton transverse momentum range and measured quantity, different processes are used for the individual tag-and-prove measurements performed. For instance, the $Z \to \tau\tau$ process, with one τ-lepton decaying into a muon that is tagged and the other decaying hadronically which is probed, is used to measure the energy scale. Typically, a minimal transverse momentum of $p_{\text{T},\tau} > 20\,\text{GeV}$ [77] is required in these measurements.

3.3.5 Missing Transverse Energy

The missing transverse energy $E_{\text{T}}^{\text{miss}}$ takes a special role in the event reconstruction at ATLAS as it is only defined for the whole event and the only estimate for particles not interacting with the detector such as neutrinos[11]. It relies on the fully reconstructed and calibrated objects of all previously described particles and, therefore, indirectly utilises the whole detector, see Reference [80] for details. As it is not possible to know the initial boost along the beamline in a hadron collider[12], the $E_{\text{T}}^{\text{miss}}$ reconstruction focuses on the transverse plane. The idea is to utilise that the incoming protons' initial transverse momenta are roughly zero. Thus, its components are defined by [80]

$$E_{\text{T,x/y}}^{\text{miss}} = -\sum_{i\in(\text{hard objects})} p_{x/y,i} - \sum_{j\in(\text{soft signals})} p_{x/y,j}\,. \tag{3.3}$$

The hard objects are defined by the calibrated objects of the other reconstruction algorithms while the soft signals are the remaining charged tracks in the Inner Detector that are not associated to any of the calibrated objects. These tracks have to originate from the vertex of the hard scattering process of the event [81]. Since the calibrated objects rely on particle identification and their signals in the detector are thus only known to stem from a certain particle with a given probability, it is possible that the same detector signal is used for multiple reconstructed objects. Hence, within the $E_{\text{T}}^{\text{miss}}$ reconstruction, an overlap removal is applied that prevents detector signals from being counted multiple times. In terms of priority, the particles are typically ordered as electrons being first, then photons, hadronically decaying τ-leptons and jets [80]. A similar procedure is applied to all events in general to avoid double-counting of any physics object.

Using $Z \to \mu\mu$ events the $E_{\text{T}}^{\text{miss}}$ resolution can be measured in data as no real $E_{\text{T}}^{\text{miss}}$ is expected

[11] This is generally true for particles not interacting strongly or electromagnetically.

[12] Only the incoming proton energies are known but the hard scattering process happens among the proton's constituents and their momenta are distributed according to the proton's PDFs.

in these events. The resolution depends on a number of effects like pile-up[13], the presence of jets and detector resolutions for different energies and is found to be roughly in the range of $5 - 10\,\text{GeV}$. Associated uncertainties are at the order of 10%.

3.4 Simulation

A general overview of the most important concepts utilised in Monte Carlo (MC) simulations of particle physics processes is given in References [26, 82]. Some of the most important concepts, at least in the context of hadron colliders, are related to QCD. In addition to the renormalisation scale μ_R introduced in Section 2.1.3, a factorisation scale μ_F can be defined. This scale represents the energy at which hard scattering processes and strong interactions inside and between protons can be separated. The idea behind this concept of factorisation is that the hard scattering processes can be calculated using perturbation theory since α_s will be small while this is not possible for the other processes with large α_s. Thus, the cross-section for a process creating hadron(s) X resulting from a proton proton collision can be written as [26]

$$\begin{aligned}\sigma_{pp\to X} = \sum_{ijk} \int \mathrm{d}x_1 \mathrm{d}x_2 \mathrm{d}z f_i(x_1, \mu_F) f_j(x_2, \mu_F) \\ \times \hat{\sigma}_{ij\to k}(x_1, x_2, z, Q^2, \alpha_s(\mu_R), \mu_R) D_{k\to X}(z, \mu_F)\,,\end{aligned} \tag{3.4}$$

with Q^2 being the momentum transfer and the integration scale z. Phenomenological knowledge about the parton distribution functions (PDFs) of the protons, which effectively break down the fraction x_i of the proton momentum carried by its constituents, is encoded in the functions $f_{i/j}$. The hard scatter process $\hat{\sigma}_{ij\to k}$ is factorised and can be calculated perturbatively. Finally, the function $D_{k\to X}$ describes the showering from the hard scattered parton(s) k to the final particle(s) X. Often the factorisation scale is chosen to be equal to the renormalisation scale $\mu = \mu_R = \mu_F$. The order of α_s that is used in the calculation defines the notation usually used for MC simulations, i.e. leading order (LO), next-to-leading order (NLO) etc. In order to model physics processes accurately in the phase space regions of interest, a sufficient amount of MC statistics have to be generated. Thus, the generation is sometimes split into bins of some quantity.

Multiple generators are used for the MC samples included in the measurement presented in this thesis, e.g. Sherpa [v2.2.1] [91] or Powheg Box v2 [v2] [92–96] for the matrix element (ME) and Pythia 8 [97] for the parton showering (PS). The details of all generators and the tunes applied are given in Reference [8] while a short overview is given in Table 3.1. Simulated samples are generated for the signal processes introduced in Section 2.2.3 and background processes comprising vector boson production in association with jets, $t\bar{t}$ production, single top quark production and the production of two vector bosons. A Higgs boson mass of $m_H = 125.09\,\text{GeV}$ is used to calculate cross-sections and for the $H \to \tau\tau$ branching ratio [8]. Spin correlations and decays of τ-leptons are modelled by Sherpa and Powheg [98], respectively. For Powheg they have been validated against Tauola [99] [8]. The simulation of the ATLAS detector responses is based on Geant4 [8, 100, 101].

Multiple corrections to the simulations have to be applied in the final measurement. Differences between data and MC for reconstruction specific quantities like efficiencies and energy scales

[13] Pile-up refers to the fact that multiple protons collide in each bunch crossing leading to additional (soft) interactions.

Process	Generator		PDF set		Tune	Order
	ME	PS	ME	PS		
Higgs boson						
ggF	Powheg Box v2 [v2]	Pythia 8	PDF4LHC15nnlo [83]	CTEQ6L1 [84]	AZNLO [85]	N^{3}LO QCD + NLO EW
VBF	Powheg Box v2 [v2]	Pythia 8	PDF4LHC15nlo	CTEQ6L1	AZNLO	NNLO QCD + NLO EW
VH	Powheg Box v2 [v2]	Pythia 8	PDF4LHC15nlo	CTEQ6L1	AZNLO	NNLO QCD + NLO EW
$t\bar{t}H$	Powheg Box v2 [v2]	Pythia 8	NNPDF3.0nnlo [86]	NNPDF2.3lo [87]	A14 [88]	NLO QCD + NLO EW
tH	MadGraph5_aMC@NLO [90]	Pythia 8	CT10 [89]	NNPDF2.3lo	A14	NLO
Background						
V + jets (QCD/EWK)	Sherpa [v2.2.1]		NNPDF3.0nnlo		Sherpa	NNLO for QCD, LO for EWK
$t\bar{t}$	Powheg Box v2 [v2]	Pythia 8	NNPDF3.0nnlo	NNPDF2.3lo	A14	NNLO + NNLL
Single top	Powheg Box v2 [v2]	Pythia 8	NNPDF3.0nnlo	NNPDF2.3lo	A14	NLO
Diboson	Sherpa [v2.2.1]		NNPDF3.0nnlo		Sherpa	NLO

Table 3.1: Monte Carlo generators with their tunes and the utilised matrix element (ME) and parton showering (PS) configurations for all simulated samples. The respective proton PDFs are also given as well as the order of perturbation theory used to calculate the cross-section normalisation. Taken from Reference [8].

are measured and centrally provided as scale factors by the ATLAS collaboration. Some of the corresponding uncertainties are discussed in Section 3.3. Additionally, the pile-up distribution assumed during the MC event generation is a best guess. The mean number of interactions per bunch crossing is used as a measure for the pile-up [102]

$$<\mu> = \frac{L_{\text{bunch}}\sigma_{\text{inel}}}{f_r}\,, \tag{3.5}$$

with the LHC revolution frequency f_r, the instantaneous luminosity per bunch L_{bunch} and the inelastic cross-section σ_{inel}. This distribution has to be corrected to match the actual measured distribution shown in Figure 3.4.

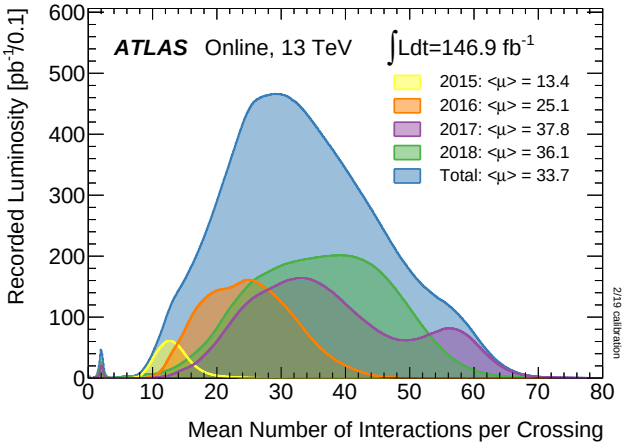

Figure 3.4: Pile-up distribution as measured by the ATLAS experiment for all years of the Run II data taking. Taken from Reference [102].

CHAPTER 4

Di-τ Mass Reconstruction

As briefly motivated in Section 2.2.3, the goal of the measurement in this thesis is to measure the production cross-section(s) of the $H \to \tau\tau$ process. While being an intriguing process, the task of the measurement is equally challenging. The difficulties arise from the τ-lepton decay, which is described in more detail in Section 2.3, involving always at least one neutrino per decay. Reconstructing the invariant di-τ mass, $m_{\tau\tau}$, is one of the most powerful tools to separate the signal, $H \to \tau\tau$, from one of the major backgrounds, $Z \to \tau\tau$. As both are electrically neutral bosons with similar invariant masses of roughly $m_Z = 91\,\text{GeV}$ [25] and $m_H = 125\,\text{GeV}$ [25], their signatures in the detector are alike. Theoretically, the invariant mass reconstruction can be done using basic 4-momentum algebra:

$$m_{\tau\tau}^2 = \left(\mathbf{p}_{\tau_1} + \mathbf{p}_{\tau_2}\right)^2 \tag{4.1}$$

$$= \left(\mathbf{p}_{\tau_1^{\text{vis}}} + \mathbf{p}_{\tau_1^{\nu}} + \mathbf{p}_{\tau_2^{\text{vis}}} + \mathbf{p}_{\tau_2^{\nu}}\right)^2 . \tag{4.2}$$

The neutrinos of the τ-lepton decays enter the calculation of the invariant mass in Equation 4.2. Since they cannot be measured directly and at least two neutrinos are always present, see Section 3.3.5, it is not possible to analytically calculate $m_{\tau\tau}$.

This chapter explains different approaches and approximations to estimate the invariant di-τ mass. After a short introduction of analytical mass estimation techniques, the Missing Mass Calculator (MMC) will be discussed in more detail, including studies on improving its performance and a detailed description of the final setup. The MMC provides the mass estimate used as the final observable in the measurement.

In the following, the two neutrinos involved in leptonic τ-lepton decays will be considered as a single neutrino system. The treatment as a neutrino system has the advantage that no distinction of leptonic and hadronic τ-lepton decays in the equations is necessary due to different amounts of undetected particles involved. Treating the two neutrinos of leptonic decays separately quickly increases the degrees of freedom in the determination of $m_{\tau\tau}$ which already is an underconstrained problem. Another motivation for this is the fact that only very limited reconstructed information about neutrinos in an event are available, namely information related to $E_{\text{T}}^{\text{miss}}$. Lastly, for the typical boosts of τ-leptons in this analysis the neutrinos originating from leptonically decaying τ-leptons are strongly collimated. Thus, minimising the inaccuracy of the assumption as the angular separation of the two neutrinos decreases with increasing boost.

4.1 Standard Techniques

To provide more context to the technique that will be used for the final observable of the fit, other techniques to estimate $m_{\tau\tau}$ will be discussed first. All methods have their knowledge of the missing information of the neutrinos in the event in common. The standard approaches discussed in this section try to solve the problem analytically and incorporate assumptions on the neutrinos in the $m_{\tau\tau}$ estimate to a varying extent.

4.1.1 Visible Mass

The easiest approach to estimate $m_{\tau\tau}$ is to neglect the neutrinos in the τ-lepton decays altogether. This simplifies Equation 4.2 to the following approximation:

$$m_{\tau\tau} \approx m_{\tau\tau}^{\text{vis}} = \left(\mathbf{p}_{\tau_1^{\text{vis}}} + \mathbf{p}_{\tau_2^{\text{vis}}}\right)^2 .$$

Depending on the analysis, this estimate of $m_{\tau\tau}$ can already provide sufficient information. While the neutrino information are missing in this estimator, it is also agnostic to resolution effects related to $E_{\text{T}}^{\text{miss}}$, which can be quite sizeable as discussed in Section 3.3.5. Figure 4.1 shows the $m_{\tau\tau}^{\text{vis}}$ distribution

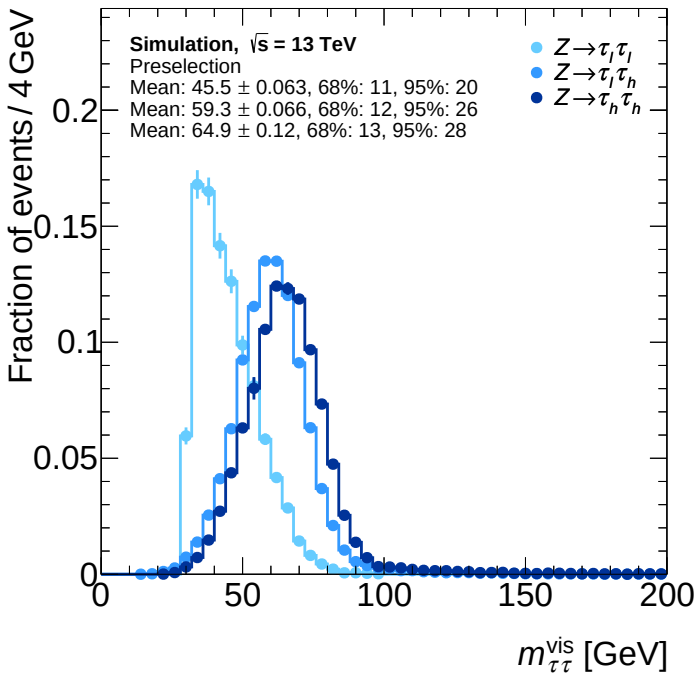

Figure 4.1: Visible mass, $m_{\tau\tau}^{\text{vis}}$, of the di-$\tau$ system for the fully leptonic, semi-leptonic and fully hadronic decay channels of the $Z \to \tau\tau$ process. The channels' respective preselections used in the final measurement are applied. The means of the distributions and their 68% and 95% quantiles are quoted in GeV.

of the $Z \to \tau\tau$ process for all di-τ decay channels considered in this analysis, i.e. the fully leptonic, the semi-leptonic and the fully hadronic decay channels. Their respective preselection listed in

Table 5.2 is applied. The cut-off towards smaller $m_{\tau\tau}$ values in the fully leptonic channel is likely caused by minimum requirements on the τ-lepton momenta in the preselection. With an increasing number of total neutrinos involved in the τ-lepton decays, the mean of the distribution shows an increasing shift with respect to the expected $Z \to \tau\tau$ mass peak at roughly 91 GeV [25]. Since only the visible decay products of the individual τ-leptons are taken into account for this estimator, it is their resolution that defines the resolution of the $m_{\tau\tau}$ distribution. Typically, the momentum and angular resolution of leptonically decaying τ-leptons is smaller than for hadronically decaying τ-leptons, also see Section 3.3.4. This results in an increasing 68% (95%) quantile width of the $m_{\tau\tau}^{\text{vis}}$ distribution with an increasing number of hadronically decaying τ-leptons in the decay chain.

For an application in the measurement discussed in this thesis, the resolution of $m_{\tau\tau}^{\text{vis}}$ would suffice to separate $Z \to \tau\tau$ and $H \to \tau\tau$ processes. However, the dependence of the mean of this estimator on the number of neutrinos involved diminishes the separation power. Thus, a different estimator with a more robust expectation value of the reconstructed di-τ mass is used.

4.1.2 Collinear Approximation

A more reliable estimator of the di-τ mass when it comes to the expectation value of the distribution is given with the Collinear Approximation as introduced in Reference [103]. This method includes the only available reconstructed information about the neutrinos in its estimate, namely $E_{\text{T}}^{\text{miss}}$. The estimated mass, $m_{\tau\tau}^{\text{coll}}$, is given by the solution to a set of equations that can only be solved analytically by imposing a set of assumptions on the event kinematics.

First and foremost, it is assumed that all $E_{\text{T}}^{\text{miss}}$ in the event is produced by the neutrinos of the τ-lepton decays, not taking into account detector effects, reconstruction efficiencies, etc. The second assumption gives the estimate its name. By considering the boost of the τ-lepton system, originating from the mass of its mother particle, i.e. $m_{Z/H} \gg m_{\tau}$, the τ-lepton's decay products are found to be strongly collimated or even collinear. Any possible deviations from perfect collinearity are neglected in this ansatz. With these assumptions it is possible to define the following set of equations: [104]

$$\begin{aligned} E_{\text{T,x}}^{\text{miss}} &= p_{\text{mis},1} \sin\theta_{\text{vis},1} \cos\phi_{\text{vis},1} + p_{\text{mis},2} \sin\theta_{\text{vis},2} \cos\phi_{\text{vis},2} \\ E_{\text{T,y}}^{\text{miss}} &= p_{\text{mis},1} \sin\theta_{\text{vis},1} \sin\phi_{\text{vis},1} + p_{\text{mis},2} \sin\theta_{\text{vis},2} \sin\phi_{\text{vis},2} \,, \end{aligned} \tag{4.3}$$

$$x_i = \frac{p_{\text{vis},i}}{p_{\text{vis},i} + p_{\text{mis},i}} \,, \tag{4.4}$$

$$m_{\tau\tau}^{\text{coll}} = \frac{m_{\tau\tau}^{\text{vis}}}{\sqrt{x_1 x_2}} \,, \tag{4.5}$$

where $p_{\text{mis},i}$ denote the three-momenta of the invisible decay products, i.e. neutrinos, and $p_{\text{vis},i}$ denote the three-momenta of the visible decay products, i.e. mostly pions. An estimation of the visible decay products' energy fraction with respect to the total τ-lepton energy is given by x_i. Thus, the mass estimation in Equation 4.5 incorporates an approximation of the energy carried by the neutrinos. Overall, these equations lead to another restriction: if the two τ-leptons are emitted with an angle of $\Delta\phi = \phi_{\text{vis},2} - \phi_{\text{vis},1} = 0°$, this set becomes degenerate [104]. Since this measurement targets boosted Higgs bosons as described in Section 5.2, it is less likely that the τ-leptons are subject to this limitation. The $m_{\tau\tau}^{\text{coll}}$ distribution is shown in Figure 4.2 for the fully leptonic, the semi-leptonic and the fully hadronic $Z \to \tau\tau$ decay channels in their respective preselection, c.f. Table 5.2. The used

implementation further simplifies Equation 4.3 by moving the calculation into the transverse plane. By incorporating information on the neutrinos, the mean of the estimator becomes more robust with respect to the number of overall neutrinos as shown by the similar values for all decay channels. On the other hand, the resolution of $m_{\tau\tau}^{\text{coll}}$ suffers in comparison to the resolution of $m_{\tau\tau}^{\text{vis}}$, manifesting in increased quantile widths. This is a direct result of the $E_{\text{T}}^{\text{miss}}$ resolution entering in Equation 4.3. Another characteristic of this estimator is the tendency to overestimate the di-τ mass which presents as asymmetric tails of the distribution. The increased resolution and the tendency to overestimate $m_{\tau\tau}$, especially the high mass tails, both make the Collinear Approximation not the ideal di-τ mass estimator to separate $Z \to \tau\tau$ and $H \to \tau\tau$.

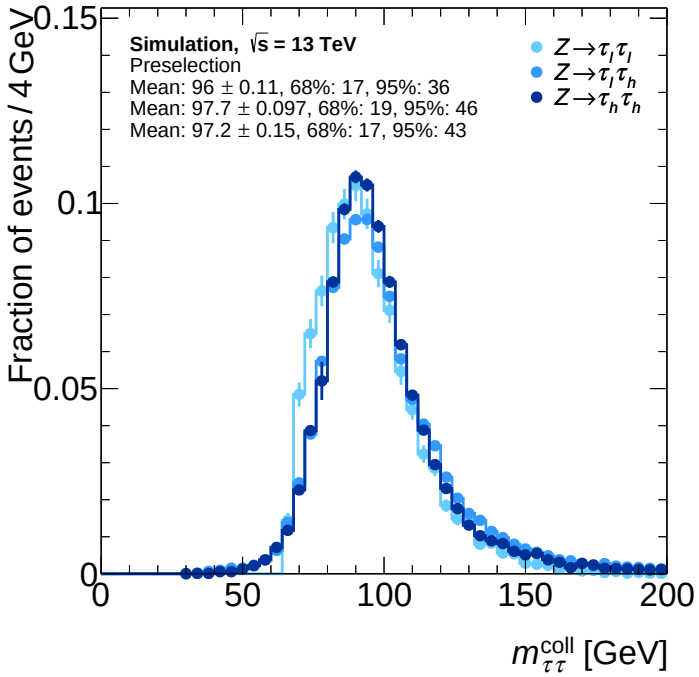

Figure 4.2: Di-τ mass estimated using the Collinear Approximation, $m_{\tau\tau}^{\text{coll}}$. It is shown for the fully leptonic, semi-leptonic and fully hadronic decay channels of the $Z \to \tau\tau$ process. The channels' respective preselections used in the final measurement are applied. The means of the distributions and their 68% and 95% quantiles are quoted in GeV.

4.1.3 Further Techniques

Beside the mass reconstruction techniques described in Section 4.1.1 and 4.1.2 as well as the one actually used in the measurement, described in more detail in Section 4.2, there are many more techniques incorporating information of the neutrinos in the event to varying extent and imposing different assumptions. However, most of these estimators are constructed for a specific purpose such as the Transverse Mass, m_T [21, 25], which is a powerful discriminator against backgrounds for analyses targeting W-bosons. In contrast to this measurement primarily focusing on $Z \to \tau\tau$ and $H \to \tau\tau$ processes, the advantage of the Transverse Mass for $W^{\pm}$ analyses lies in the single neutrino in the

event in case of hadronic $W^{\pm}$ decays, or one collimated neutrino system in case of leptonic $W^{\pm}$ decays. Further techniques are described, for example, in Reference [105].

4.2 The Missing Mass Calculator

The Missing Mass Calculator (MMC) is the mass estimator of choice for the measurement discussed in this thesis. Originally developed by the CDF collaboration at the Tevatron [104], it was adapted by the ATLAS collaboration for $H \rightarrow \tau\tau$ measurements [106]. Since its early application in ATLAS in Reference [106], the MMC has been extended and improved numerical methods have been implemented. Nevertheless, the underlying ideas and mathematical model remain unchanged with respect to the original publication of this method in Reference [104].

In this section, the underlying concepts will be introduced and the aforementioned changes will be highlighted. As outlined in Section 4.1, incorporating information on the neutrinos in the di-τ decay chain is crucial to achieve a robust mass estimate for $m_{\tau\tau}$. In this context, a robust estimate would provide invariant mass distributions of the investigated resonances that resemble the generated mass distributions as closely as possible. Taking the $Z \rightarrow \tau\tau$ process as an example, the mean of the estimated mass should be close to 91 GeV [25] for all possible di-τ decay channels. Furthermore, it is important that the width of the $m_{\tau\tau}$ distribution is as narrow as possible, taking into account detector and object resolution effects that impose a lower bound on the achievable mass resolution. All of these considerations ensure that the $H \rightarrow \tau\tau$ and $Z \rightarrow \tau\tau$ processes can be distinguished via $m_{\tau\tau}$.

Just like the Collinear Approximation, the MMC presumes that the resonance's mass is larger than the τ-lepton mass, i.e. $m_{Z/H} \gg m_{\tau}$, and that the missing transverse energy in the event is solely produced by the neutrinos in the di-τ decay. In contrast to the Collinear Approximation, the resulting boosts of the individual τ-leptons do not lead to a vanishing separation between the visible and invisible decay products. Instead, the MMC takes this small but non-zero angle $\theta_{3\mathrm{D},i}$ into account, which will be described in more detail in Section 4.2.2. Similarly, the assumption on the neutrinos being the only source of $E_{\mathrm{T}}^{\mathrm{miss}}$ in the event is taken further in the MMC. The resolution of $E_{\mathrm{T}}^{\mathrm{miss}}$ is incorporated into the algorithm as explained in Section 4.2.1 and 4.2.2, allowing for more possible neutrino momenta in the numerical evaluation. However, neutrinos are considered the sole physics origin.

With these assumptions, the following two sets of equations can be formulated to describe the problem: [104]

$$\begin{aligned} E_{\mathrm{T,x}}^{\mathrm{miss}} &= p_{\mathrm{mis},1}\sin\theta_{\mathrm{mis},1}\cos\phi_{\mathrm{mis},1} + p_{\mathrm{mis},2}\sin\theta_{\mathrm{mis},2}\cos\phi_{\mathrm{mis},2}\,, \\ E_{\mathrm{T,y}}^{\mathrm{miss}} &= p_{\mathrm{mis},1}\sin\theta_{\mathrm{mis},1}\sin\phi_{\mathrm{mis},1} + p_{\mathrm{mis},2}\sin\theta_{\mathrm{mis},2}\sin\phi_{\mathrm{mis},2}\,, \end{aligned} \tag{4.6}$$

$$\begin{aligned} m_{\tau,1}^2 = {} & \mathrm{M}\Big(\sum_i \nu_i^{\tau_1^1}\Big)^2 + m_{\mathrm{vis},1}^2 + 2\cdot\sqrt{\vec{p}_{\mathrm{vis},1}^{\,2} + m_{\mathrm{vis},1}^2}\cdot\sqrt{\vec{p}_{\nu,1}^{\,2} + \mathrm{M}\Big(\sum_i \nu_i^{\tau_1^1}\Big)^2} \\ & - 2\cdot\left|\vec{p}_{\mathrm{vis},1}\right|\left|\vec{p}_{\nu,1}\right|\cos\theta_{\mathrm{3D},1}\,, \\ m_{\tau,2}^2 = {} & \mathrm{M}\Big(\sum_i \nu_i^{\tau_1^2}\Big)^2 + m_{\mathrm{vis},2}^2 + 2\cdot\sqrt{\vec{p}_{\mathrm{vis},2}^{\,2} + m_{\mathrm{vis},2}^2}\cdot\sqrt{\vec{p}_{\nu,2}^{\,2} + \mathrm{M}\Big(\sum_i \nu_i^{\tau_1^2}\Big)^2} \\ & - 2\cdot\left|\vec{p}_{\mathrm{vis},2}\right|\left|\vec{p}_{\nu,2}\right|\cos\theta_{\mathrm{3D},2}\,. \end{aligned} \tag{4.7}$$

Equations 4.6 only differ by the angles used from the equations of the Collinear Approximation, c.f. Equation 4.3. The MMC assumes a non-vanishing angle between the visible and invisible τ-lepton decay products. This is reflected by the angles in Equation 4.6 being the ones of the actual invisible decay products' three-momenta and not the ones of the visible decay products as in Equation 4.3[1]. Consequently, the set of equations in 4.6 is underconstrained as only two of the quantities, namely $E_{\mathrm{T,x}}^{\mathrm{miss}}$ and $E_{\mathrm{T,y}}^{\mathrm{miss}}$, can be measured and the other six are to be determined. Hence, the other set of equations is introduced in 4.7 helping to constrain the system by utilising the constraint of the invariant τ-lepton mass m_τ. The mass m_τ is calculated by squaring the sum of the invisible and visible decay products' four-momenta. Depending on the di-τ decay channel, up to two additional unknowns are introduced, the invariant masses of the neutrino system in leptonic decays, $\mathrm{M}(\sum_i \nu_i^{\tau_{\mathrm{l}}^j})$. For each leptonically decaying τ-lepton there are two neutrinos associated to the decay. These two neutrinos are treated as a single neutrino system as described in the introduction of this chapter. As a direct consequence, an invariant mass of the neutrino system can be defined which will be non-zero, even though the neutrino mass itself can be approximated with $m_\nu \approx 0\,\mathrm{GeV}$. The angular differences between the visible and invisible decay products of the respective τ-lepton decay, $\theta_{\mathrm{3D},1}$ and $\theta_{\mathrm{3D},2}$, can be expressed in terms of quantities already defined in Equations 4.6. Overall, six to eight unknowns have to be determined from the set of four equations given in Equations 4.6 and 4.7.

Since the problem is thus underconstrained and therefore cannot be solved analytically, numerical methods have to be applied which will be described in Section 4.2.1 and 4.2.2. The methods scan a physically motivated region of phase space for valid solutions of the introduced equations. These solutions represent neutrino four-momenta, assuming $m_\nu = 0\,\mathrm{GeV}$, and are evaluated in a likelihood-based approach to determine the final estimate of the invariant di-τ mass. The Missing Mass Calculator's code can be found in Reference [107].

4.2.1 Markov Chain & Metropolis Algorithm

Before evaluating possible solutions of Equations 4.6 and 4.7 based on their likelihood or probability, see Section 4.2.2, these solutions have to be numerically found by scanning the phase space of said equations. The unknowns are reformulated for this scan to simplify the implementation. All angular components are reparameterised in terms of the azimuthal angles of the neutrinos, $\phi_{\nu,1}$ and $\phi_{\nu,2}$. Instead of directly scanning the individual neutrino momentum components, $E_{\mathrm{T}}^{\mathrm{miss}}$ is varied within its given resolution. This automatically incorporates the assumption that $E_{\mathrm{T}}^{\mathrm{miss}}$ is an experimentally measured event quantity with an associated uncertainty due to detector resolution effects, jet counting effects, etc. The neutrino momenta are then calculated using Equations 4.6 and 4.7 with the angles $\phi_{\nu,1}$ and $\phi_{\nu,2}$ as well as the components $E_{\mathrm{T,x}}^{\mathrm{miss}}$ and $E_{\mathrm{T,y}}^{\mathrm{miss}}$ of a given phase space point that is to be tested. Since the overall task of finding the neutrino momenta is underconstrained, there are generally two possible solutions, differentiated by the sign of the momentum's z-component for a given point. This ambiguity will be discussed in more detail in Section 4.3.1. In case of leptonically decaying τ-leptons, the invariant mass of the neutrino system $\mathrm{M}(\sum_i \nu_i^{\tau_{\mathrm{l}}^i})$ is scanned as well. For hadronic τ-lepton decays, the visible τ-lepton mass is set to a specific decay mode dependant mass hypothesis, i.e. it is assumed to be the invariant mass of the visible decay products. Most hadronic τ-lepton decays occur via the a_1 or $\rho^\pm$ mesons[2], whose masses are consequently used in these hypotheses. Consequently, two

[1] Where the difference of these angles is presumed to vanish.

[2] The a_1 and $\rho^\pm$ mesons are both composed out of up- and down quarks [25].

hypotheses are implemented. One for decays into final states with one charged decay product with a hypothesis of 0.8 GeV based on the intermediate $\rho^{\pm}$ resonance and one for decays into final states with three charged decay products with a hypothesis of 1.2 GeV based on the intermediate a_1 resonance. It has to be noted that not all possible phase space points are guaranteed to yield physically valid solutions. Thus, the validity of a given point has to be confirmed before evaluating its probability.

Different sampling techniques were implemented in the MMC for this scan. Originally, the MMC was developed to perform a grid search over a predefined region of phase space. This is the technique described in the ATLAS MMC paper [104]. The implementation followed a simple approach of dividing each dimension of the N-dimensional parameter space, N being the number of scanned quantities as described above, into a configurable amount of equidistant points. For all of these points the validity and subsequently the likelihood was calculated. While being easy to implement and achieving robust results, this method suffers from a number of drawbacks. When using the MMC as the $m_{\tau\tau}$ estimator, its runtime quickly plays an important role in processing millions of events. For the grid search, this results in a trade-off between accuracy of the $m_{\tau\tau}$ estimate and available computing resources. With an increasing number of grid points the result generally becomes more accurate, c.f. law of large numbers [108], while the runtime simultaneously increases.

A more flexible approach of sampling phase space points was then implemented with a random sampling. Instead of dividing the N-dimensional parameter space into equidistant points, an iterative approach is chosen. For each iteration a new point is sampled using a uniform distribution. The starting point for this sampling would be the same throughout the scan as well as the ranges for each parameter. Even though this approach shows more flexibility, the general drawbacks of the grid search could not be completely alleviated.

This led to the implementation of a Markov Chain utilising the Metropolis-Hastings algorithm as the current sampling technique. The following introduction to the basics of Markov Chains and the Metropolis-Hastings algorithm are based on References [109] and [110]. Markov Chains are a widely used stochastic model for processes fulfilling the Markov property: [109]

$$\begin{aligned}\text{Prob}\left(X_{n+1} = x_{n+1} \mid X_n = x_n, X_{n-1} = x_{n-1}, ..., X_0 = x_0\right) \\ = \text{Prob}\left(X_{n+1} = x_{n+1} \mid X_n = x_n\right) \ .\end{aligned}$$

This property states that the probability of the random variables X of a given system to find themselves in state x at the time $n + 1$ only depends on the current state at time n and not on the previous states. Often, this property is also referred to as the system being memoryless.

The sampling problem posed in the MMC can be viewed in terms of Markov process properties. All of the to-be-scanned quantities discussed above can be interpreted as random variables following their own probability density functions. A given phase space point which effectively describes the states or values of the random variables' ensemble can be considered a state of the system. The sampling process itself is considered memoryless, i.e. the next sampled state only depends on the current state and not on the history of the sampling. This is realised in the MMC by using the system's current state as the sampling's starting point where the ranges in which random numbers are drawn are constant throughout all of the sampling process. Finally, the iterations represent discrete time steps of the Markov Chain.

While the time-discrete Markov Chain describes the general setting, it does not generally prescribe the probabilities for the system to transition between different states or to stay in its current state. These transition probabilities are implemented using the Metropolis-Hastings algorithm; for further

reading please refer to Reference [111]. It was originally proposed by Metropolis [112] and modified by Hastings [113]. The general idea is that a proposed state y is accepted as the new state x_{n+1} with a probability $\alpha(x, y)$ based on the target probability distribution $\pi(x)$ and the proposal probability distribution $Q(x, y)$ of the system: [111]

$$\alpha(x, y) = \min\left(1, \frac{Q(y, x)}{Q(x, y)} \cdot \frac{\pi(y)}{\pi(x)}\right).$$

In this representation, the proposal probability distribution $Q(x, y)$ is given by the combined probability density functions of the individual random variables and the target probability distribution $\pi(x)$ is given by the likelihood evaluations of the current state x and the proposed state y. By choosing symmetric proposal distributions $Q(x, y) = Q(y, x)$, the transition probability can be further simplified.

In the context of the MMC this is realised by sampling the new state according to the proposal densities of the individual random variables. All scanned quantities utilise densities that are Gaussian distributions centred around the current value with proposal widths w listed in Table 4.1. Until the

p.d.f.	Proposal density width w	Comments
$\theta_{3\mathrm{D},i}$	0.04	
$R_{\nu\tau,i}$		not explicitly scanned
$\mathrm{M}\left(\sum_i \nu_i^{\tau_1}\right)$	$1.5\,\mathrm{GeV} - m_\tau^{\mathrm{vis}}$	
$E_{\mathrm{T,x/y}}^{\mathrm{miss}}$	$N \cdot \sigma(E_{\mathrm{T}}^{\mathrm{miss}})$	N is configurable

Table 4.1: Proposal density widths of the individual probability density functions (p.d.f.s) used in the MMC's Markov Chain. The individual p.d.f.s are introduced in detail in Section 4.2.2.

first valid solution that solves the neutrino equations is found, the Gaussian distributions are replaced by uniform sampling distributions. Thus, the evaluation of the proposal densities is symmetric as only the difference in the values of the states matter. A Gaussian distribution centred around the current state x and evaluated at the proposed state y yields the same result as a Gaussian distribution centred around y and evaluated at x. Due to the symmetric proposal densities, the transition probability α is simplified to be the ratio of the likelihoods $\mathcal{P}$ of the proposed new state y and the current state x:

$$\alpha(x, y) = \min\left(1, \frac{\mathcal{P}(y)}{\mathcal{P}(x)}\right). \tag{4.8}$$

A detailed description of the likelihood's definition will be given in Section 4.2.2.

With this definition of the transition probability, a new proposed state y is always accepted as long as its likelihood is larger than it is for the current state x. If the likelihood of the proposed state y is smaller, it is still accepted with probability $\alpha(x, y)$. Otherwise, the proposed state y is rejected and a new proposed state y' will be sampled from the same current state x. This helps to avoid that the sampling process is caught in local likelihood maxima and instead gives the possibility to step out of local maxima and continue the search for more likely solutions. The distributions of the number of scanned points per event that do not yield a physically valid solution, the number of points that are rejected by the Metropolis-Hastings algorithm and the number of points with a new physically valid solution of Equations 4.6 and 4.7 are shown in Figure 4.3. They use the final MMC version that

includes the updates described in Section 4.4. While most points typically do not yield physically valid solutions, the valid solutions are more often accepted than rejected by the Metropolis-Hastings algorithm. More details on the individual distributions will be given in Section 4.4.1.

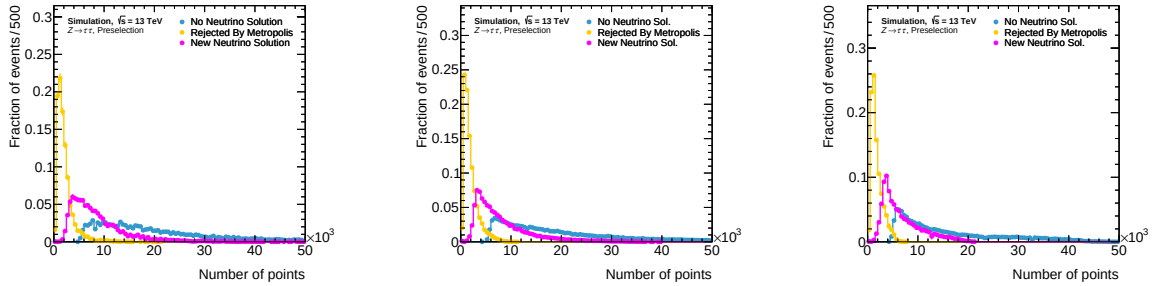

(a) $\tau_e\tau_\mu$ channel. (b) $\tau_{\text{lep}}\tau_{\text{had}}$ channel. (c) $\tau_{\text{had}}\tau_{\text{had}}$ channel.

Figure 4.3: Number of scanned points in the Markov Chain per event with no valid solution, a valid solution and a valid solution that is rejected by the Metropolis-Hastings algorithm. The distributions are shown for the $Z \to \tau\tau$ process in all decay channels used in the analysis.

4.2.2 Likelihood

The likelihoods of the states are used to define the transition probabilities of the Markov Chain as shown in Equation 4.8. These likelihoods are motivated by the kinematics of the τ-lepton decay as well as the di-τ decay and combine several individual probability density functions, p.d.f.s.

Originally, two p.d.f.s were included in the calculation of the overall likelihood, see Reference [104]. The first one being a τ-lepton specific p.d.f. which is the angular distance between the visible and invisible τ-lepton decay products. This distance was first estimated by [104]

$$\Delta R_i = \sqrt{\left(\Delta\eta_i\right)^2 + \left(\Delta\phi_i\right)^2},$$

motivated by the coordinate system introduced in Equation 3.2 in Section 3.2 and later replaced by the three-dimensional angle

$$\theta_{3\text{D},i} = \angle(\overrightarrow{p}_{\text{vis},i}, \overrightarrow{p}_{\nu,i}) = \arccos\left(\frac{\overrightarrow{p}_{\text{vis},i} \cdot \overrightarrow{p}_{\nu,i}}{\left|\overrightarrow{p}_{\text{vis},i}\right| \left|\overrightarrow{p}_{\nu,i}\right|}\right). \tag{4.9}$$

Using $\theta_{3\text{D},i}$ instead of ΔR_i puts less emphasis on the importance of the z-component of the neutrino momentum. This component is calculated using Equations 4.6 and 4.7 and consequently shows an ambiguity in its sign. The x- and y-components do not show this ambiguity due to the explicit sampling of $\phi_{\nu,i}$ as explained in Section 4.2.1. By defining the angular distance via ΔR_i the z-component enters the calculation quadratically through $\left(\Delta\eta_i\right)^2$, while the x- and y-components are combined in $\left(\Delta\phi_i\right)^2$. When using $\theta_{3\text{D},i}$ all three components enter with the same importance. Even though these two definitions do differ, the final p.d.f. is very similar because of the τ-lepton's boost which leads to collimated decay products and, thus, small angles. This is especially pronounced in the fully hadronic di-τ decay as shown in Figure 4.4(c). The slight difference between the two distance

measures in the $\tau_{\text{lep}}\tau_{\text{had}}$ channel, see Figure 4.4(b), can be attributed to a different $p_{\text{T},\tau}$ spectrum of the hadronic τ-lepton compared to the $\tau_{\text{had}}\tau_{\text{had}}$ channel. While for $\tau_{\text{had}}\tau_{\text{had}}$ the leading τ-lepton is always the lepton with the larger transverse momentum, the leading τ-lepton in the $\tau_{\text{lep}}\tau_{\text{had}}$ channel is always the hadronically decaying lepton. Consequently, the $p_{\text{T},\tau}$ spectrum also includes leptons with smaller transverse momenta, leading to less collimated decay products in comparison. In case of leptonically decaying τ-leptons, see Figure 4.4(a), an additional neutrino is produced in the decay. Since it is not possible to reliably distinguish the two neutrinos of a single leptonic τ-lepton decay, they are treated as one system. However, by doing so, the separation of visible and invisible decay products is not as clean as for hadronic decays any more. The invisible component will contain one neutrino of the direct τ-lepton decay and one from the virtual $W^{\pm}$. Since this p.d.f. strongly depends

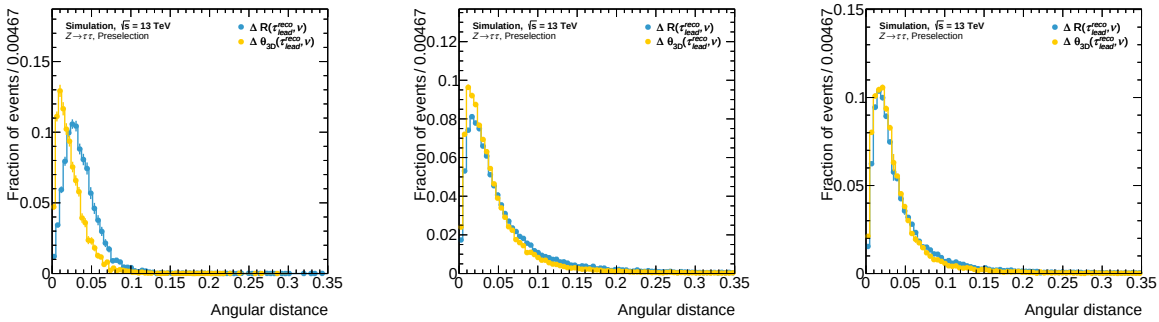

(a) $\tau_e\tau_\mu$ channel. (b) $\tau_{\text{lep}}\tau_{\text{had}}$ channel. (c) $\tau_{\text{had}}\tau_{\text{had}}$ channel.

Figure 4.4: Angular distance measures between the visible and invisible decay products of the leading τ-lepton for each decay channel used in the analysis. The leading τ-lepton in the $\tau_{\text{lep}}\tau_{\text{had}}$ channel is always the hadronic τ-lepton of the decay chain while it is the higher momentum τ-lepton in the other channels.

on the type of τ-lepton decay, leptonic or hadronic, and for hadronic decays also on the number of charged and neutral hadrons, each one of them has a separate p.d.f. version associated with them. Additionally, the boost of the τ-lepton is reflected in this angular difference, i.e. the stronger the boost the more collimated the decay products of the τ-lepton are. Thus, the p.d.f. is also parameterised in terms of different distinct $p_{\text{T},\tau_i^{\text{vis}}}$ ranges.

The other p.d.f. that was included from the first implementation in Reference [104] and is still used is the event-wide p.d.f. of the $E_{\text{T}}^{\text{miss}}$ resolution. This resolution incorporates knowledge about mismeasurements of $E_{\text{T}}^{\text{miss}}$ into the likelihood calculation. It is implemented via a Gaussian p.d.f. where $\sigma(E_{\text{T}}^{\text{miss}})$ constitutes the $E_{\text{T}}^{\text{miss}}$ resolution and $\Delta E_{\text{T,x/y}}^{\text{miss}}$ the variation of the respective $E_{\text{T}}^{\text{miss}}$ components during the sampling process with respect to the measured $E_{\text{T}}^{\text{miss}}$ of the event: [104]

$$\mathcal{P}\left(E_{\text{T,x/y}}^{\text{miss}}\right) = \exp\left(-\frac{\left(\Delta E_{\text{T,x/y}}^{\text{miss}}\right)^2}{2\sigma(E_{\text{T}}^{\text{miss}})^2}\right). \tag{4.10}$$

Since the $E_{\text{T}}^{\text{miss}}$ resolution depends the number of jets and their energy, see Section 3.3.5, the p.d.f. is parameterised as a function of the hadronic activity in the event. Furthermore, a correction term of this resolution which depends on the azimuthal angular difference between the two visible τ-leptons was introduced, see Reference [40].

Later, two additional τ-lepton specific p.d.f.s were introduced. While the angle $\theta_{3D,i}$ holds directional information about the τ-lepton decays, it does not utilise information about the magnitude of the neutrino momenta. However, this additional degree of freedom is used in the scanning process as part of the $E^{\text{miss}}_{\text{T,x/y}}$ variations described in Section 4.2.1 and the calculation of $\mathcal{P}\left(E^{\text{miss}}_{\text{T,x/y}}\right)$. In contrast to $\mathcal{P}\left(E^{\text{miss}}_{\text{T,x/y}}\right)$ which is an event-wide p.d.f., the neutrino momenta of the individual decays can provide additional τ-lepton specific information. These information are included by means of the ratio of the current state's invisible momentum $\mathbf{p}_{\tau_i^\nu}$ and the visible momentum $\mathbf{p}_{\tau_i^{\text{vis}}}$ which remains unchanged during the Markov Chain:

$$R_{\nu\tau,i} = \frac{\mathbf{p}_{\tau_i^\nu}}{\mathbf{p}_{\tau_i^{\text{vis}}}} .$$

Similarly to $\theta_{3D,i}$ each τ-lepton decay type has its own associated $R_{\nu\tau,i}$ p.d.f.. This is motivated by the expected momentum fractions carried by the invisible decay products for the different decay types. For leptonic τ-lepton decays, for example, this fraction is generally larger because of the higher number of neutrinos involved.

The last p.d.f. is specific to leptonically decaying τ-leptons. Since two neutrinos are involved in these decays and they are treated as one neutrino system, a non-zero invariant mass can be assigned to this system. This invariant mass $\text{M}\left(\sum_i \nu_i^{\tau_1}\right)$ represents a degree of freedom in the Markov Chain but also a p.d.f. by itself. In contrast to the other p.d.f.s discussed, $\text{M}\left(\sum_i \nu_i^{\tau_1}\right)$ is not further parameterised. It is a Lorentz-invariant quantity and, thus, it does not depend on the boost of the τ-leptons for example.

The final likelihood of a state y in the Markov Chain is given by the combination of all p.d.f.s:

$$\mathcal{P}(y) = \mathcal{P}\left(E^{\text{miss}}_{\text{T,x/y}}\right) \prod_i \theta_{3D,i} \cdot R_{\nu\tau,i} \cdot \text{M}\Big(\sum_i \nu_i^{\tau_1}\Big) \tag{4.11}$$

4.2.3 Mass Estimates

With the sampling process and the transition probabilities in place, the final step is to define the mass estimate provided by the MMC. In total, there are three distinct $m_{\tau\tau}$ estimates available: MAXW (maximum weight), MLM (most likely mass) and MLNU3P (most likely neutrino momenta), each one with their own advantages and disadvantages.

The most direct estimator MAXW takes the phase space point in the Markov Chain with the highest single probability $\mathcal{P}(y)$ as the solution, see Equation 4.11. Because the phase space point as a whole is considered the best solution, the MMC is able to not only provide an estimate for the di-τ mass but also a coherent estimate of the neutrino momenta. However, if the kinematics of the event, i.e. the τ-lepton kinematics and $E^{\text{miss}}_{\text{T}}$, pose a difficult configuration for the Markov Chain, it is possible that multiple phase space points show similar probabilities, which limits the reliability of this estimator.

The MLM estimator addresses this issue by utilising all of the sampled states. All $m_{\tau\tau}$ estimates are saved in a histogram which is evaluated after the Markov Chain terminates. Since the Metropolis-Hastings algorithm is used to define the transition probabilities, the entries of the histogram do not have to be weighted. If a phase space point is sampled multiple times, it will enter the histogram the same amount of times which automatically weights the entries in all bins of the histogram according to $\mathcal{P}(y)$. A state is also considered to be sampled multiple times if the proposed new state does not yield a valid solution or is rejected by the Metropolis-Hastings algorithm. Finally, the $m_{\tau\tau}$ estimate is given by the maximum of that histogram, yielding a more robust result. Two examples of the

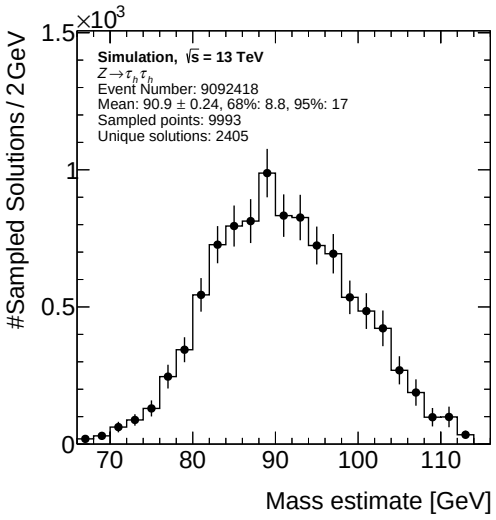

(a) Event 9092418. Number of points rejected by Metropolis-Hastings: 478. The leading τ-lepton is a 1p0n decay and the subleading τ-lepton a 1pXn decay.

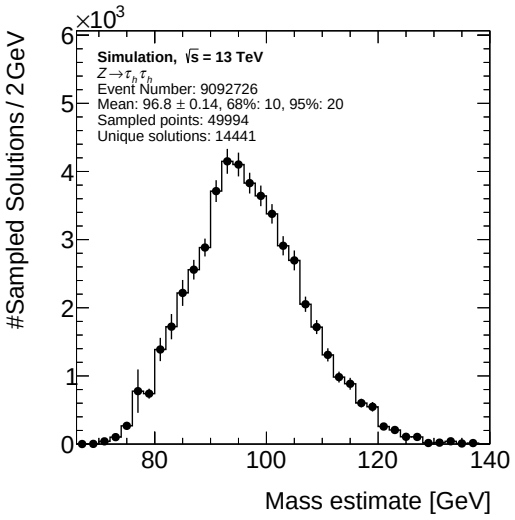

(b) Event 9092726. Number of points rejected by Metropolis-Hastings: 3270. The leading τ-lepton is a 1p1n decay and the subleading τ-lepton a 1pXn decay.

Figure 4.5: Distribution of the $m_{\tau\tau}$ estimate using the final MMC version. Two $Z \to \tau\tau$ events in the $\tau_{\text{had}}\tau_{\text{had}}$ channel are shown. The mean of the distribution together with its 68% and 95% quantiles are quoted in GeV.

$m_{\tau\tau}$ estimate distribution are given in Figure 4.5 for two individual $Z \to \tau\tau$ events in the $\tau_{\text{had}}\tau_{\text{had}}$ channel. Different measures such as the overall number of sampled points and the 68% and 95% quantiles of the distribution, providing information about the core and tail resolution, give an idea of the complexity a specific event configuration poses to the Markov Chain. As it will be explained in Section 4.4.1, the smaller the overall number of sampled points the faster the Markov Chain reaches its equilibrium. Consequently, it is easier for the MMC to find a mass estimate for event number 9092418 in Figure 4.5(a) based on these metrics. The drawback of the MLM estimate is that the final di-τ mass estimate is decoupled from the other phase space quantities. It is not possible to assign specific neutrino momenta to the mass given by the maximum of the histogram which means that no estimate of the neutrino momenta can be given.

The final estimator MLNU3P follows a similar approach as the MLM method. Instead of saving information about the di-τ mass for each Markov Chain iteration it saves information on the neutrino momenta. Following the same approach as before, the maxima of these histograms define the neutrino momentum components for each τ-lepton. These neutrino momenta can be used in Equation 4.2 to calculate the final mass estimate. Hence, MLNU3P also provides a coherent estimate for $m_{\tau\tau}$ and the neutrino momenta. However, all neutrino momentum components are treated uncorrelated which may skew the result.

Depending on the specific analyses' needs and design one of the options might be more suited than the others. For the measurement presented here the MLM estimator is chosen. The di-τ mass is the final discriminant of the statistical analysis and, thus, the most robust $m_{\tau\tau}$ estimate is used.

4.3 MMC Studies

This section describes various studies performed on the Missing Mass Calculator, e.g. parameterising the p.d.f.s, studies of the runtime, etc. To ensure a more robust reproducibility, the MAXW mass estimate is chosen to compare performances. Changes to the final MMC used in the measurement will be discussed in Subsection 4.4. All other studies did not result in improvements of the algorithm's separation power between $H \to \tau\tau$ and $Z \to \tau\tau$ and are thus not propagated. They are grouped into algorithm related efforts discussed in Subsection 4.3.1 and p.d.f. related studies shown in Subsection 4.3.2. If not stated otherwise, the studies discussed show modifications with respect to the version of the MMC used in Reference [7]. This version will be referred to as the "original" MMC version and functions as the starting point of the studies and modifications.

Part of the tools to judge the MMC's performance are Receiver-Operating-Curves (ROCs). They show the background rejection, where $Z \to \tau\tau$ is considered background, versus the signal efficiency, where $H \to \tau\tau$ is considered signal. A perfect selection algorithm would achieve a background rejection of one, i.e. no background event would be selected, while showing a signal efficiency of one, i.e. all signal events would be selected. Thus, one of the goals of the studies is to push the ROC closer to this ideal theoretical limit. In order to compare ROCs using just one number, the Area-Under-the-Curve (AUC) is used which effectively represents the integral of the curve and is exactly one in case of a perfect selection algorithm. Although the MMC is not used to select certain types of events, its performance can be judged similarly to a selection problem based on the separation power between $Z \to \tau\tau$ and $H \to \tau\tau$ using the mass estimate $m_{\tau\tau}^{\text{MMC}}$. The idea is that this quantity is the final observable in the presented measurement and the fit utilises the separation between the two processes.

4.3.1 Studies on the Algorithm

This subsection focuses on aspects regarding the implementation of the Markov Chain. It has to be noted that the used $Z \to \tau\tau$ samples for these studies are using the Powheg Box v2 [92–95, 114–119] Monte Carlo event generator. While these are not the Sherpa $Z \to \tau\tau$ samples used in the measurement, the studies are meaningful as long as they are conducted under consistent conditions within a study. The MMC is intended as a universal tool that is not specifically tailored to a certain Monte Carlo event generator or showering tool. Furthermore, the available statistics for the Powheg $Z \to \tau\tau$ samples is smaller with respect to the samples used in the measurement. This is partly due to the fact that only the Monte Carlo production campaign corresponding to the 2017 data taking period is included. Lastly, the studies shown in this subsection focus on the fully hadronic di-τ decay channel. This is motivated by the simplicity of the decay channel compared to the decay channels involving leptonic decays and, thus, a larger number of neutrinos.

Neutrino Momentum Ambiguity

For each proposed state y, two independent solutions to the neutrino equations can be found per neutrino system. From a physics point of view none of the two possible solutions is more correct than the other. Hence, the original MMC version used in Reference [7] only considers one randomly chosen solution per neutrino system in order to save computation power. To be more precise, only the randomly chosen solution is passed on to the likelihood evaluation and processed further in the

Markov Chain. The other solution is simply discarded.

In order to assess the impact of this choice on the overall performance of the MMC, a modified version evaluating all neutrino solutions has been studied. However, since multiple solutions per τ-lepton are not physically motivated, only the solution with the highest likelihood after the evaluation is used for the final result.

The effects on the runtime and the separation power are shown in Figure 4.6. As expected, the runtime is roughly doubled because the number of processed solutions increases by a factor of two. Meanwhile, the MMC's separation power is unaffected by this alternative treatment with an AUC of 0.89 for both versions. As explained before, none of the solutions stand out with respect to the other in physical meaningfulness. This seems to be emphasised by the likelihood calculations and the resulting similar performance of the MMC. Thus, the original implementation of choosing a random solution per neutrino system is retained.

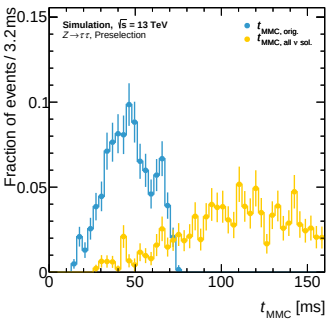

(a) Per event runtime of the MMC for the $Z \to \tau\tau$ process.

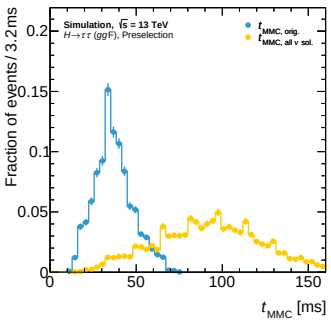

(b) Per event runtime of the MMC for the $H \to \tau\tau$ process.

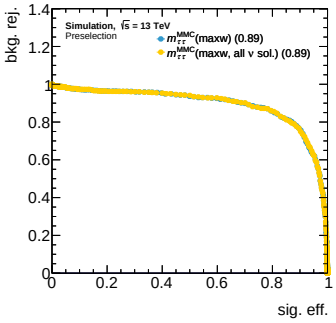

(c) Receiver-Operating-Curve with $H \to \tau\tau$ as the signal and $Z \to \tau\tau$ as the background. The area under the curve is quoted for each MMC version.

Figure 4.6: Comparison of the original MMC evaluating two randomly chosen neutrino solutions and a version evaluating all neutrino solutions. All figures show the $\tau_{\text{had}}\tau_{\text{had}}$ channel.

Markov Chain Hyperparameters

The underlying algorithm to generate new proposed states y is a Markov Chain. Within this algorithm there are several possible parameters that can be tuned and can possibly influence the overall performance of the MMC. These parameters can be classified into two categories.

The first category affects the sampling itself. Following the explanation of the Markov Chain in Section 4.2.1, the sampling process is defined by the initial values of the variables being scanned and the chosen proposal densities w. Since the initial values themselves are chosen by sampling phase space points in the vicinity of the input quantities and, thus, physically well motivated, this procedure is kept as is. The proposal densities w, however, are of a given fixed size, as summarised in Table 4.1, which makes them subject of this study.

The second category of parameters is related to the conditions under which the Markov Chain terminates. A number of different criteria are implemented in the "original" MMC such as a predefined number of successfully sampled unique solutions and a maximum number of iterations for the Markov

Chain. In practice, the criterion triggered to terminate the scan is mostly the maximum number of iterations which are given in Table 4.3 in Section 4.4.1. Hence, this parameter is also part of the studies. Due to technical reasons the runtime of the original MMC is not constant throughout the studies presented in this subsection but the conditions within a study are ensured to be consistent.

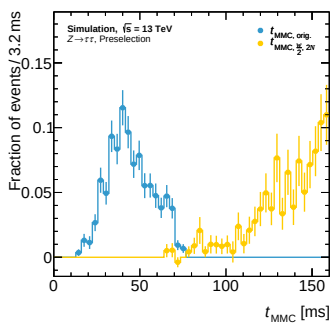

(a) Per event runtime of the MMC for the $Z \to \tau\tau$ process.

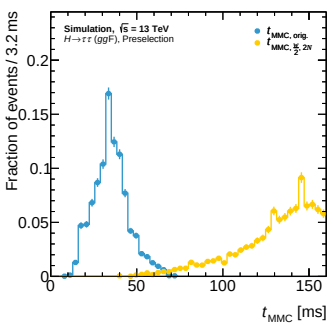

(b) Per event runtime of the MMC for the $H \to \tau\tau$ process.

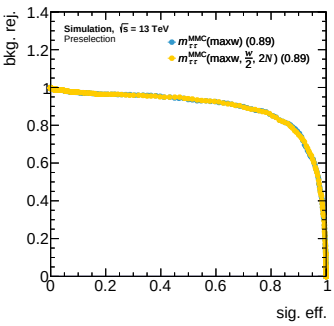

(c) Receiver-Operating-Curve with $H \to \tau\tau$ as the signal and $Z \to \tau\tau$ as the background. The area under the curve is quoted for each MMC version.

Figure 4.7: Comparison of the original MMC and a modified version with doubled number of maximum iterations and halved proposal density widths. All figures show the $\tau_{\text{had}}\tau_{\text{had}}$ channel.

Naively thought, by increasing the number of maximum iterations while simultaneously decreasing the proposal densities w, the Markov Chain's estimate of the final solution should become more accurate. Consequently, a more accurate estimate of the solution should result in a more accurate mass estimate and, finally, an improved separation power between $Z \to \tau\tau$ and $H \to \tau\tau$. A simple approach, trying to utilise this, is to increase the number of maximum iterations by a factor of two and halving the proposal densities listed in Table 4.1. This leads to a significant increase in the MMC's runtime by roughly a factor of 3, as shown in Figure 4.7(a) and (b). However, the separation power remains the same with an AUC of 0.89. Based on this, it seems that the naive expectation is not fulfilled. This can either be explained by the MMC reaching a very similar estimate of the solution with the original settings or by the MMC getting stuck in local maxima. While smaller proposal densities can increase the accuracy of the Markov Chain, it can also lead to the sampling process getting stuck in local maxima and not being able to escape those because the proposal densities are too small.

Another approach that tries to circumvent the possible issue of such local maxima is to use dynamic proposal densities w. At the start of the scan the original density widths are used and then decreased as the chain supposedly gets closer to the final estimate. This is achieved by linearly decreasing w with advancing iterations down to 20% of its original value when the maximum number of iterations is reached. The idea is that by starting with the original values the Markov Chain does not get stuck in local maxima as easily and is still able to scan the vicinity of the final estimate more thoroughly. As shown in Figure 4.8, this approach does not result in an improvement of the MMC's separation power but only increases its runtime. This suggests that it is more likely that the original values of the proposal densities give a stable estimate of the best solution rather than problems with local maxima caused by too small widths w.

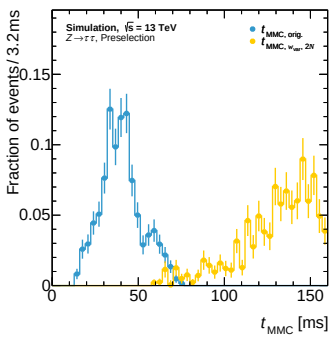

(a) Per event runtime of the MMC for the $Z \to \tau\tau$ process.

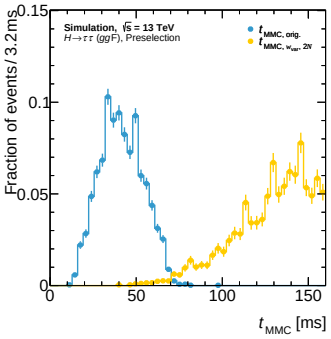

(b) Per event runtime of the MMC for the $H \to \tau\tau$ process.

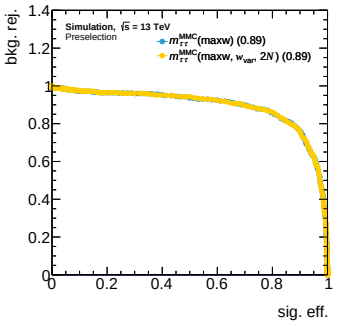

(c) Receiver-Operating-Curve with $H \to \tau\tau$ as the signal and $Z \to \tau\tau$ as the background. The area under the curve is quoted for each MMC version.

Figure 4.8: Comparison of the original MMC and a modified version with doubled number of maximum iterations and adaptive proposal density widths. All figures show the $\tau_{\text{had}}\tau_{\text{had}}$ channel.

Hence, the original values for the proposal densities w as well as the number of maximum iterations are kept. An additional termination criterion for the Markov Chain is introduced in the final version as detailed in Section 4.4.1.

Per Event Uncertainty

This section describes a first attempt at defining a per-event uncertainty on the MMC's mass estimate. Based on the implementation of the Markov Chain, a Bayesian or a Frequentist approach of defining the uncertainty estimate is possible. The Frequentist approach would not make any assumptions on the underlying p.d.f.s of the mass estimate which is one of the main advantages of this approach. Since a proper likelihood is defined for the Metropolis-Hastings algorithm, the Frequentist 1σ uncertainty estimate would correspond to $\Delta\text{NLL} = 0.5$, with NLL being the negative logarithmic likelihood. However, for a reliable uncertainty estimate this definition requires a smooth NLL distribution which is not guaranteed when projecting the multidimensional Markov Chain scan onto the final di-τ mass estimator. Hence, the Bayesian approach is chosen in the following.

In contrast to that, the Bayesian approach integrates over the underlying p.d.f.s by utilising the distribution of sampled mass estimates that is shown in Figure 4.5. Due to the MMC's methodology the underlying p.d.f.s have to be known for the Metropolis-Hastings algorithm. The final uncertainty estimate corresponding to the 1σ variation is defined by calculating the 68% quantiles of the mass estimate's distribution. Thus, it is only defined for the MAXW and MLM estimators but not for the MLNU3P estimator which does not use any information of the mass estimate's distribution. The distribution of this per-event uncertainty is shown in Figure 4.9 in the inclusive signal regions, discussed in Section 5.2, for the fully hadronic di-τ channel of the $Z \to \tau\tau$ sample using the MLM estimator. It shows the final MMC version described in Section 4.4 applied on the SHERPA $Z \to \tau\tau$ sample used in the measurement. Even though the uncertainty seems well-behaved for the ensemble of the shown events, it is not propagated to the measurement. More studies on this uncertainty's definition are required to fully understand its behaviour, stability and possible correlations with other

sources of uncertainties that enter the measurement by varying the MMC's inputs. Although the method itself provides well-defined uncertainty estimates, it has not been validated to provide reliable estimates in all phase space regions. The validity has to be verified especially for events that pose a difficult configuration of reconstructed quantities for the MMC's mass reconstruction.

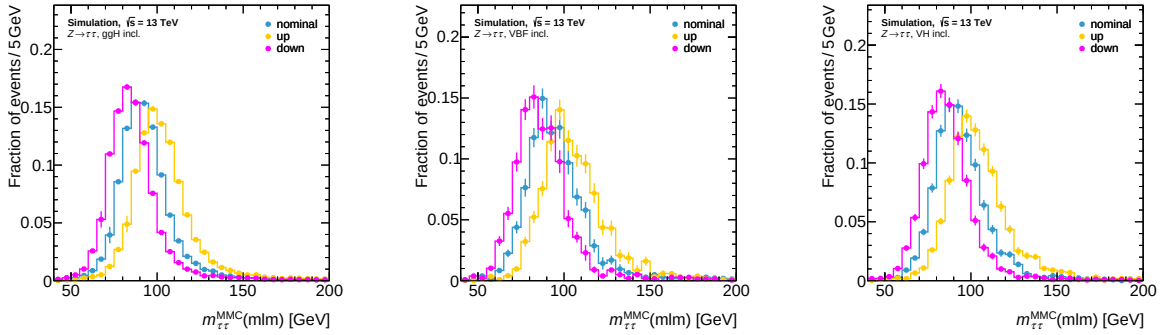

(a) Inclusive boosted signal regions. (b) Inclusive VBF signal regions. (c) Inclusive VH signal regions.

Figure 4.9: Distributions of the per-event uncertainty estimate of the MMC for the MLM estimator. All figures show the $\tau_{\mathrm{had}}\tau_{\mathrm{had}}$ channel of the $Z \to \tau\tau$ process.

4.3.2 Studies on the p.d.f.s

The second category of studies targets the p.d.f.s used to calculate the likelihood of a proposed state y in the Markov Chain. Unlike the $Z \to \tau\tau$ samples used in Section 4.3.1, the studies presented in this section use the final Sherpa $Z \to \tau\tau$ samples of the measurement. Additionally, all Monte Carlo production campaigns covering the data taking from 2015 until 2018 are used. Following the same argumentation as in the previous section, the following studies again focus on the fully hadronic di-τ decay channel because of its simplicity compared to the other channels.

Generally, the p.d.f.s define how the Markov Chain evolves since they are used in Equation 4.8 of the Metropolis-Hastings algorithm that decides whether a proposed state is accepted or rejected. Depending on the chosen mass estimator (MAXW, MLM or MLNU3P) the p.d.f.s also have a more or less direct impact on the final mass estimate. For the MAXW estimator they are used directly when computing the state with the highest likelihood, while for the other estimators they enter indirectly by shaping the histograms used for the estimate through the Metropolis-Hastings algorithm. Hence, the p.d.f. parameterisations play an important role in the performance of the MMC, possibly even a more important role than the hyperparameters of the Markov Chain discussed in Section 4.3.1. If not stated otherwise, the p.d.f. sets used in the studies are computed from simulated $Z \to \tau\tau$ events.

MET Significance

Out of all p.d.f.s used in the MMC, the $E_{\mathrm{T}}^{\mathrm{miss}}$ p.d.f. introduced in Equation 4.10 was updated the most recent for the original MMC version used in Reference [7]. This set of parameterisations was established in 2016 for the $\tau_{\mathrm{had}}\tau_{\mathrm{had}}$ channel in Reference [40]. Since then, a new tool, the MET Significance tool, became available that is able to provide a per-event estimate of the uncertainty for the reconstructed $E_{\mathrm{T}}^{\mathrm{miss}}$, c.f. Reference [120]. Utilising this per-event estimate of the $E_{\mathrm{T}}^{\mathrm{miss}}$

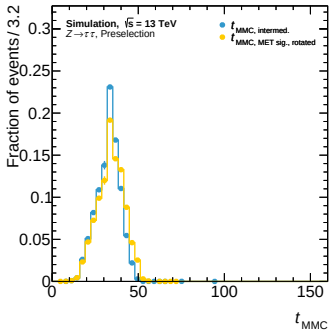

(a) Per event runtime of the MMC for the $Z \to \tau\tau$ process.

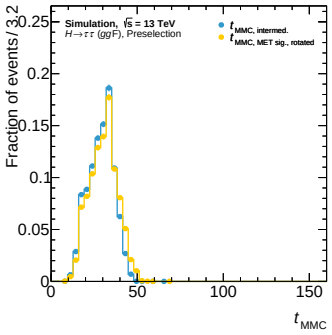

(b) Per event runtime of the MMC for the $H \to \tau\tau$ process.

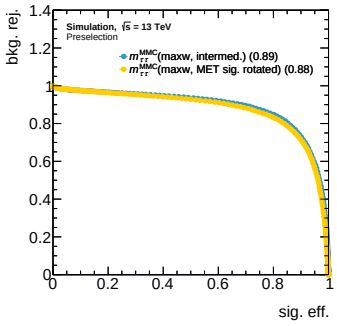

(c) Receiver-Operating-Curve with $H \to \tau\tau$ as the signal and $Z \to \tau\tau$ as the background. The area under the curve is quoted for each MMC version.

Figure 4.10: Comparison of the MMC performance using the default $E_{\text{T}}^{\text{miss}}$ p.d.f. and a modified version using the MET Significance tool for the $E_{\text{T}}^{\text{miss}}$ p.d.f. (rotated). All figures show the $\tau_{\text{had}}\tau_{\text{had}}$ channel.

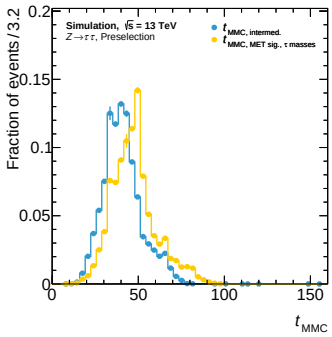

(a) Per event runtime of the MMC for the $Z \to \tau\tau$ process.

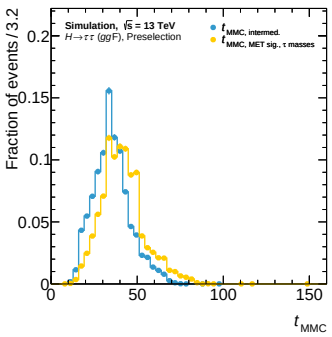

(b) Per event runtime of the MMC for the $H \to \tau\tau$ process.

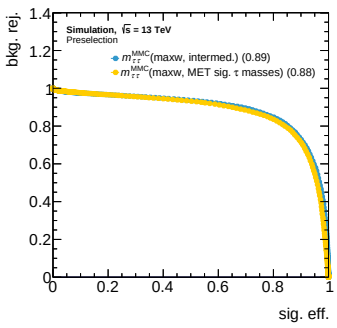

(c) Receiver-Operating-Curve with $H \to \tau\tau$ as the signal and $Z \to \tau\tau$ as the background. The area under the curve is quoted for each MMC version.

Figure 4.11: Comparison of the MMC performance using the default $E_{\text{T}}^{\text{miss}}$ p.d.f. and a modified version using the MET Significance tool for the $E_{\text{T}}^{\text{miss}}$ p.d.f. (rotated). The τ-lepton mass hypothesis of the modified version is based on the five way decay mode classification. All figures show the $\tau_{\text{had}}\tau_{\text{had}}$ channel.

uncertainty provided by an official tool could in principal result in a more accurate uncertainty than the parameterised estimate introduced in Reference [40]. As the $E_{\mathrm{T}}^{\mathrm{miss}}$ resolution inside the MMC is rotated into a system along the di-τ jet axis and the resolution is provided in Cartesian coordinates by the tool, a rotation has to be applied to match the coordinate systems. Replacing the $E_{\mathrm{T}}^{\mathrm{miss}}$ p.d.f. with the official tool's uncertainty estimate results in the performance shown in Figure 4.10. The runtime slightly increases due to the additional call of the MET Significance tool's method. In contrast to the assumptions, the MMC's separation power becomes slightly worse with an AUC of 0.88 compared to the reference value of 0.89. This is likely caused by outdated τ-lepton resolution p.d.f.s in the MET Significance tool which will be fixed in future releases. Once the τ-lepton resolution p.d.f.s have been updated, the usage of the tool should be revisited.

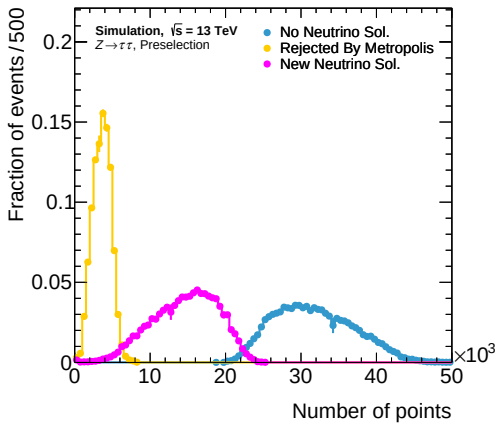

(a) Proposed state distribution using the $E_{\mathrm{T}}^{\mathrm{miss}}$ p.d.f. provided by the MET Significance tool.

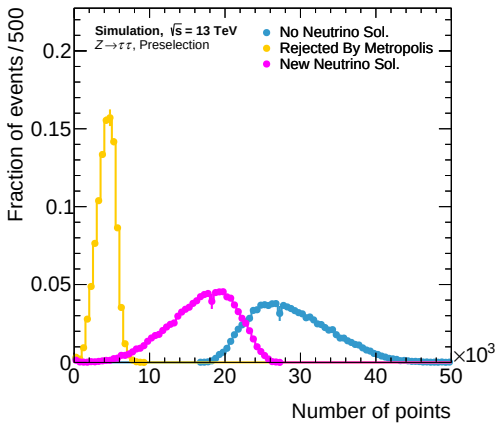

(b) Proposed state distribution using the $E_{\mathrm{T}}^{\mathrm{miss}}$ p.d.f. provided by the MET Significance tool and additionally using the five way τ-lepton mass hypotheses.

Figure 4.12: Number of proposed states with a new physically valid solution, no solution and states rejected by the Metropolis-Hastings algorithm. All figures show the $\tau_{\mathrm{had}}\tau_{\mathrm{had}}$ channel.

In the context of this study, the τ-lepton mass hypotheses entering in the solution of the neutrino equations have been re-examined. The original MMC implemented two mass hypotheses for hadronic τ-lepton decays, namely decays via the $\rho^{\pm}$ or the a_1 resonance. This classification is achieved by counting the number of tracks involved in the decay. With the exhaustive five way decay mode classification described in Section 3.3.4 a more elaborate distinction of the mass hypotheses is possible. Consequently, it is possible to assign the $\rho^{\pm}$ mass hypothesis specifically to the $\tau_{1\mathrm{p1n}}$ decay mode and a $\pi^{\pm}$ mass hypothesis to the $\tau_{1\mathrm{p0n}}$ decay mode. The individual decay modes and corresponding resonances have been collected from References [25] and [121]. A summary of the implemented mass hypothesis approximations is given in Table 4.2. As shown in Figure 4.11, the runtime further increases which hints towards a slightly larger number of physically viable proposed states inside the Markov Chain. Only physically valid states require significant computation time because they are passed on to the likelihood calculation. Comparing Figure 4.12(a) to Figure 4.12(b), the slight increase in the number of points with a new solution to the neutrino equations confirms this assumption. However, the MMC's performance in terms of separation power does not improve with respect to Figure 4.10(c) since both modified versions exhibit an AUC of 0.88. While the five way mass hypothesis does impact

Decay mode	m_τ	Comments
τ_{1p0n}	0.14 GeV	Mass of $\pi^\pm$
τ_{1p1n}	0.77 GeV	Mass of $\rho^\pm$
τ_{1pXn}	1.26 GeV	Mass of a_1 resonance decaying to τ_{1pXn}
τ_{3p0n}	1.20 GeV	Mass of a_1 resonance decaying to τ_{3p0n}
τ_{3pXn}	1.34 GeV	Mass of $a_1 + \pi^0$

Table 4.2: Invariant masses used for the more detailed m_τ hypothesis implemented in the modified MMC version. They are rough approximations based on the most common τ-lepton branching fractions [25, 121].

the Markov Chain, the additional phase space points with unique solutions do not improve the final mass estimate such that the MMC's separation power improves.

Thus, neither the usage of the MET Significance tool nor the implementation of a five way mass hypothesis is propagated to the final MMC version.

Definition of $\theta_{3D,i}$

One of the p.d.f.s applied to all τ-lepton decays is the angular distance between the neutrino and the visible τ-lepton introduced in Equation 4.9. That particular definition of the angular distance is a representation choice of the original Equations 4.6 and 4.7. Since the representation solely has to be physically motivated and well-defined, an alternative definition has been studied:

$$\theta_{3D,i} = \angle(\vec{p}_{\text{vis},i} + \vec{p}_{\nu,i}, \vec{p}_{\nu,i}) = \arccos\left(\frac{(\vec{p}_{\text{vis},i} + \vec{p}_{\nu,i}) \cdot \vec{p}_{\nu,i}}{|(\vec{p}_{\text{vis},i} + \vec{p}_{\nu,i})|\,|\vec{p}_{\nu,i}|}\right). \tag{4.12}$$

The alternative approach in Equation 4.12 defines the angular distance between the neutrino and an approximation of the τ-lepton object before its decay. Hence, the visible τ-lepton momentum in Equation 4.9 is replaced by the sum of the neutrino momentum and the visible τ-lepton momentum. Similarly to the original definition, the visible τ-lepton decay products in the p.d.f. are the reconstructed quantities. Thus, the reconstruction effects are directly folded into the p.d.f.. Comparing the two definitions for the angular distance in Figure 4.13, the alternative definition is shifted towards smaller values. This is caused by the definition of the angular distance with respect to the complete τ-lepton object rather than just the visible decay products. The neutrino and the visible decay products are not emitted in the same transverse direction with respect to the τ-lepton axis, and are thus respectively closer to the τ-lepton axis than each other.

This alternative definition of the angular distance has been tested in the MMC together with a dedicated set of p.d.f.s. More details on the procedure to derive such a p.d.f. set are given in Section 4.4.2. A very similar performance of the MMC is observed in the fully hadronic di-τ channel, c.f. Figure 4.14. While the $Z \to \tau\tau$ mass distribution is shifted towards slightly higher masses, the ROC yields compatible results with the same AUC for both approaches. Based on this result, both definitions seem equally feasible for the fully hadronic di-τ channel. However, the alternative definition puts an emphasis on the neutrino momenta as they enter the calculation twice, see Equation 4.12. While this does not seem to impact the performance for hadronic decays, it could impact the performance for

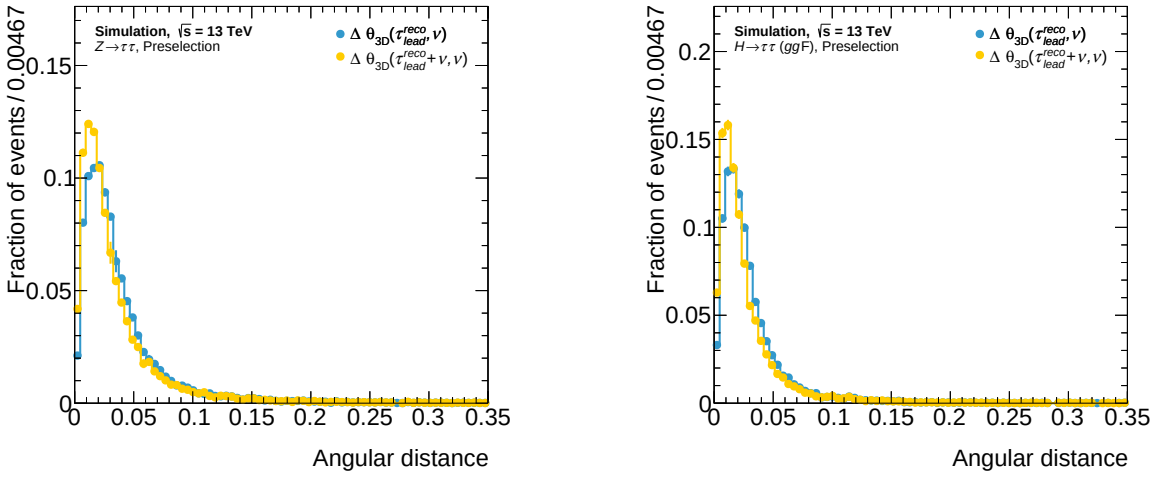

(a) $Z \rightarrow \tau\tau$ process.

(b) $H \rightarrow \tau\tau$ process.

Figure 4.13: Comparison of the default definition for $\theta_{3D,i}$ and an alternative definition where the angle is defined between the neutrino and the system of neutrino and reconstructed visible τ-lepton. All figures show the $\tau_{had}\tau_{had}$ channel.

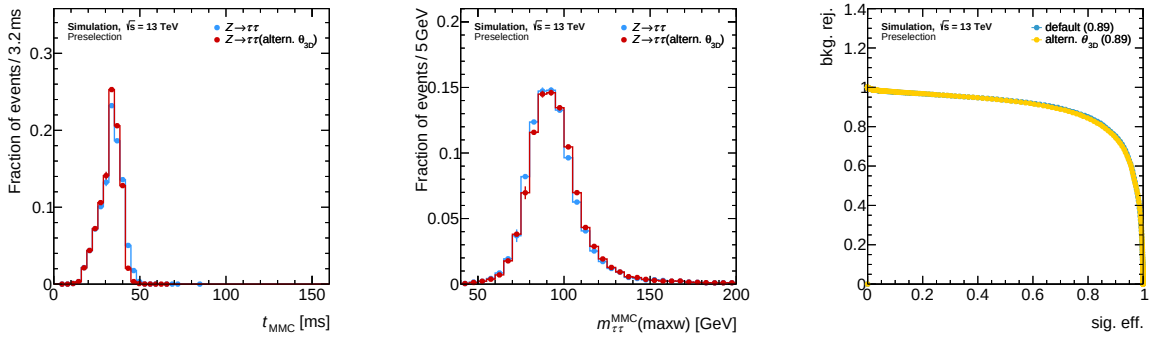

(a) Per event runtime of the MMC for the $Z \rightarrow \tau\tau$ process.

(b) MMC lineshape for the $Z \rightarrow \tau\tau$ process.

(c) Receiver-Operating-Curve with $H \rightarrow \tau\tau$ as the signal and $Z \rightarrow \tau\tau$ as the background. The area under the curve is quoted for each MMC version.

Figure 4.14: Comparison of the MMC performance using the default definition for $\theta_{3D,i}$ and an alternative definition where the angle is defined between the neutrino and the system of neutrino and reconstructed visible τ-lepton. All figures show the $\tau_{had}\tau_{had}$ channel.

leptonic decays due to the additional neutrino. Since the angular distance distribution is narrower it may be more difficult to find solutions to the neutrino equations. Thus, the definition of the angular distance introduced in Equation 4.9 is kept.

Truth Parameterisation of $\theta_{3D,i}$

In order to assess the MMC's performance limit when it comes to the $\theta_{3D,i}$ p.d.f., a p.d.f. set using only truth quantities has been studied. This effectively means that instead of reconstructed information the corresponding truth information of τ_{vis} have been used in Equation 4.9. Thus, the alternative p.d.f. does not contain any information of the τ-lepton resolution. As shown in Figure 4.15 the τ-lepton resolution only has a minor impact on the $\theta_{3D,i}$ distribution. The p.d.f. set using truth quantities was

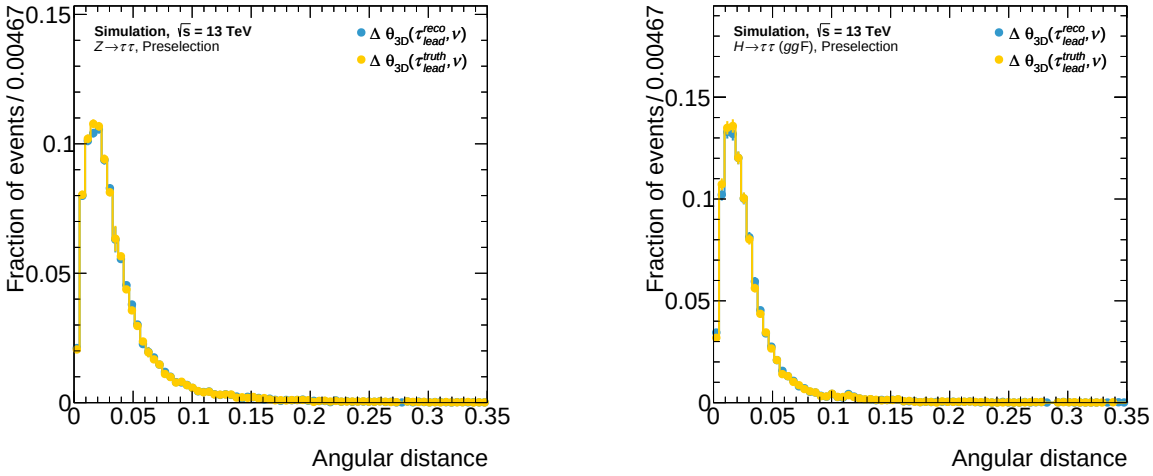

(a) $Z \rightarrow \tau\tau$. (b) $H \rightarrow \tau\tau$.

Figure 4.15: Comparison of the default definition for $\theta_{3D,i}$ and an alternative definition using only truth quantities. All figures show the $\tau_{had}\tau_{had}$ channel.

created following the same procedure described in Section 4.4.2, meaning simulated $Z \rightarrow \tau\tau$ events are used. Since the p.d.f. set uses truth quantities, the input τ-lepton quantities passed to the MMC have to utilise truth information as well and are thus not subject to resolution effects. The resulting MMC performance is shown in Figure 4.16 in comparison to a version that only differs by using reconstructed τ_{vis} quantities for the $\theta_{3D,i}$ p.d.f. set and as input to the MMC. The runtime increase in comparison to previous studies is caused by replacing hard-coded numbers for the parameterisations with a more flexible implementation encoding them in function objects, ROOT TF1s. Overall, a similar performance is achieved with both scenarios resulting in AUCs of 0.89. Thus, the MMC is more likely limited by the E_T^{miss} p.d.f. and reconstruction than the τ-lepton resolution. The E_T^{miss} p.d.f. reflects the resolution of the E_T^{miss} reconstruction. This resolution is typically twice as large as the τ-lepton resolution in the relevant energy ranges, see Sections 3.3.4 and 3.3.5. Hence, it is expected to have a larger impact on the MMC's performance.

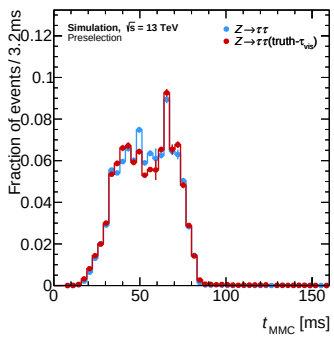

(a) Per event runtime of the MMC for the $Z \to \tau\tau$ process.

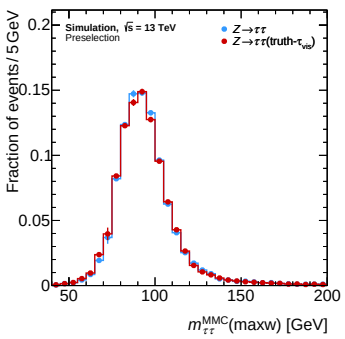

(b) MMC lineshape for the $Z \to \tau\tau$ process.

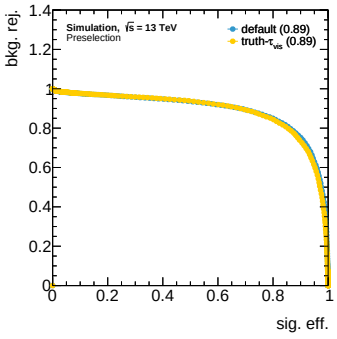

(c) Receiver-Operating-Curve with $H \to \tau\tau$ as the signal and $Z \to \tau\tau$ as the background. The area under the curve is quoted for each MMC version.

Figure 4.16: Comparison of the MMC performance using the default definition for $\theta_{3\mathrm{D},i}$ and an alternative definition using only truth quantities. All figures show the $\tau_{\mathrm{had}}\tau_{\mathrm{had}}$ channel.

Mixed Parameterisation of p.d.f.s

The MMC has to be applicable over a large $m_{\tau\tau}$ range in order to be feasible in measurements. If the tool were only well-defined in a small $m_{\tau\tau}$ range, the measurement would be limited significantly. However, it is not easily possible to provide p.d.f. sets that are optimal for all possible $m_{\tau\tau}$ values. Thus, different p.d.f. sets for different targeted $m_{\tau\tau}$ ranges are implemented in the MMC. For the measurement of the $H \to \tau\tau$ coupling those p.d.f. sets are derived from simulated $Z \to \tau\tau$ events, as it was also done in Reference [7]. Measurements targeting, for example, higher resonance masses use separate p.d.f. sets. Based on the study in Section 4.3.2, the angular distance p.d.f. using $Z \to \tau\tau$ Monte Carlo cannot be improved easily. Studying a mixture of p.d.f. sets based on $Z \to \tau\tau$ and $H \to \tau\tau$ simulations can answer two questions. Firstly, this kind of study can show whether the MMC's performance can improve beyond a pure $Z \to \tau\tau$ based p.d.f. set. Secondly, a possible bias introduced by using only $Z \to \tau\tau$ Monte Carlo would become apparent.

Hence, a mixture of p.d.f. sets based on $Z \to \tau\tau$ and $H \to \tau\tau$ has been derived according to the procedure described in Section 4.4.2. These p.d.f. sets include the $p_{\mathrm{T},\tau}$ dependent angular distance $\theta_{3\mathrm{D},i}$ parameterisation. Examples for the processed $\theta_{3\mathrm{D},i}$ distributions are shown in Figure 4.17 comparing $Z \to \tau\tau$ and $H \to \tau\tau$ for similar $p_{\mathrm{T},\tau}$ ranges. The distribution for $H \to \tau\tau$ is slightly narrower which is possibly caused by the different spins of the resonances since boost related effects are minimised by the similar $p_{\mathrm{T},\tau}$ ranges. Following a simple approach, the final p.d.f. set used per event is an admixture of the two individual p.d.f. sets for $Z \to \tau\tau$ and $H \to \tau\tau$

$$\text{p.d.f.}(m_{\tau\tau}^{\mathrm{vis}}) = \text{p.d.f.}(H \to \tau\tau) \cdot \frac{\mathrm{CDF}_{H\to\tau\tau}(m_{\tau\tau}^{\mathrm{vis}})}{\mathrm{CDF}_{Z\to\tau\tau}(m_{\tau\tau}^{\mathrm{vis}})} + \text{p.d.f.}(Z \to \tau\tau) \cdot \left(1 - \frac{\mathrm{CDF}_{H\to\tau\tau}(m_{\tau\tau}^{\mathrm{vis}})}{\mathrm{CDF}_{Z\to\tau\tau}(m_{\tau\tau}^{\mathrm{vis}})}\right) . \quad (4.13)$$

Based on the Cumulative Distribution Function (CDF) ratio of $m_{\tau\tau}^{\mathrm{vis}}$ for $Z \to \tau\tau$ and $H \to \tau\tau$, shown in Figure 4.18, the mixing is defined in Equation 4.13. Via the visible di-τ mass the final p.d.f. sets are calculated and then used in the Markov Chain. Implementing the p.d.f. sets via ROOT's

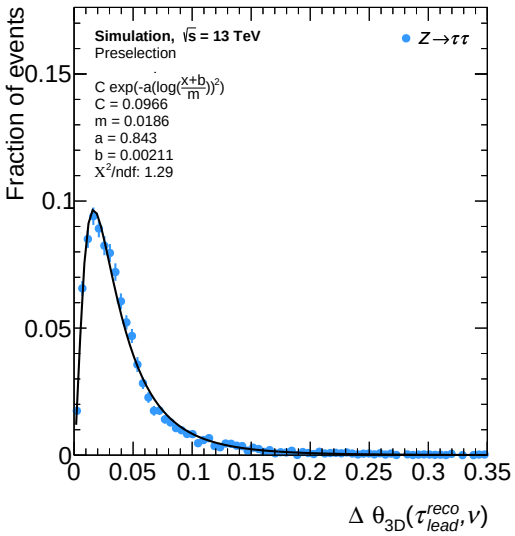

(a) $Z \to \tau\tau$ in the range of 42 GeV $< p_{\mathrm{T},\tau} <$ 47 GeV.

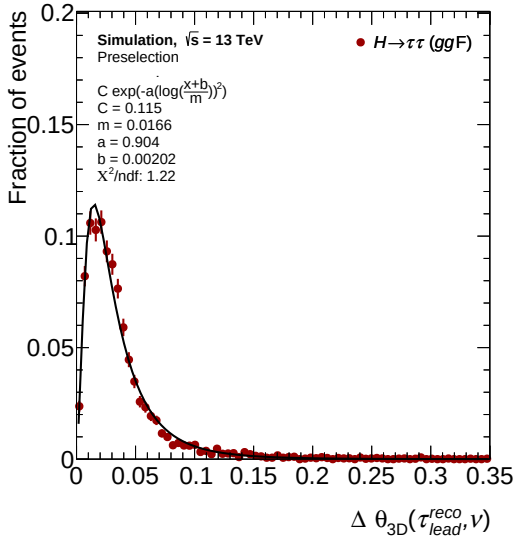

(b) $H \to \tau\tau$ in the range of 41 GeV $< p_{\mathrm{T},\tau} <$ 47 GeV.

Figure 4.17: Distribution and fit of $\theta_{3D,i}$ for the $Z \to \tau\tau$ and $H \to \tau\tau$ processes in a similar $p_{\mathrm{T},\tau}$ range. All figures show the hadronic τ_{1p1n} decay channel. The parameterisations are shown as the solid lines.

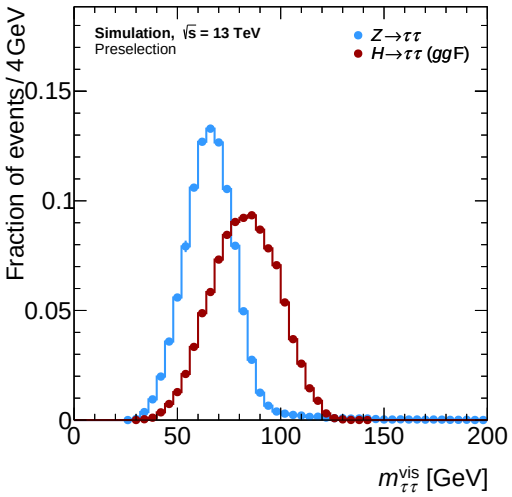

(a) Visible mass.

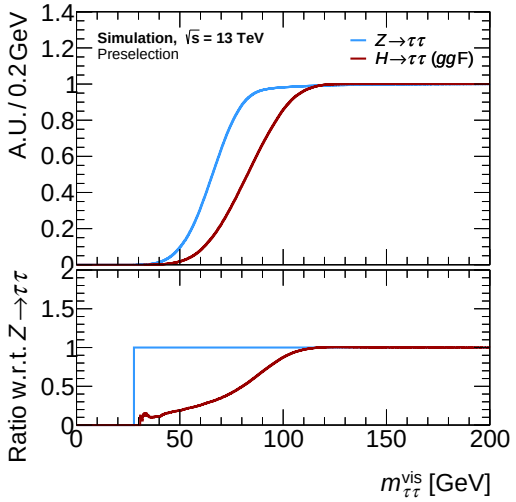

(b) CDF of $m^{\mathrm{vis}}_{\tau\tau}$ and its ratio between $H \to \tau\tau$ and $Z \to \tau\tau$.

Figure 4.18: Visible mass $m^{\mathrm{vis}}_{\tau\tau}$ and its cumulative distribution function (CDF) for the $Z \to \tau\tau$ and $H \to \tau\tau$ processes. All figures show the $\tau_{\mathrm{had}}\tau_{\mathrm{had}}$ channel.

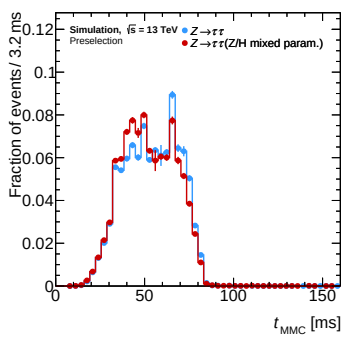

(a) Per event runtime of the MMC for the $Z \to \tau\tau$ process.

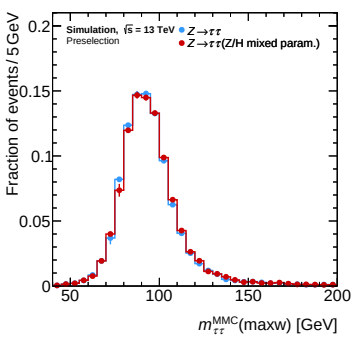

(b) MMC lineshape for the $Z \to \tau\tau$ process.

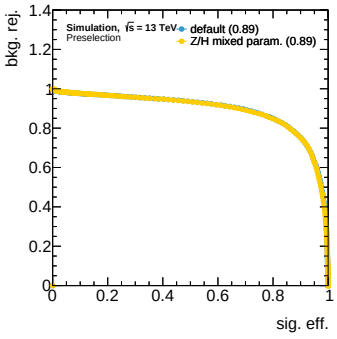

(c) Receiver-Operating-Curve with $H \to \tau\tau$ as the signal and $Z \to \tau\tau$ as the background. The area under the curve is quoted for each MMC version.

Figure 4.19: Comparison of the MMC performance using the default p.d.f. set for $\theta_{3D,i}$ and an alternative p.d.f. set mixing $Z \to \tau\tau$ and $H \to \tau\tau$ parameterisations based on $m_{\tau\tau}^{\text{vis}}$. All figures show the $\tau_{\text{had}}\tau_{\text{had}}$ channel.

TF1 function objects allows for a more flexible approach of this study but increases the runtime as explained before and shown in Figure 4.19(a). The $m_{\tau\tau}$ distribution and the separation power of the MMC are compatible with the version utilising only the $Z \to \tau\tau$ p.d.f. sets as shown in Figure 4.19(b) and 4.19(c). On the one hand, this procedure of mixed p.d.f. sets is not able to improve the MMC's performance. On the other hand, the results also suggest that no bias stemming from the $Z \to \tau\tau$ p.d.f. sets is introduced in the mass range relevant for the measurement discussed in this thesis.

Momentum Dependent $R_{\nu\tau,i}$ Parameterisation

The ratio of the neutrino momentum and the reconstructed visible τ-lepton momentum is not a Lorentz-invariant quantity. Thus, it depends on the boost of the τ-lepton and should ideally be parameterised as a function of $p_{\text{T},\tau}$. Since the neutrino system carries a larger fraction of the total τ-lepton momentum for leptonic decays this study focuses on the same. The procedure described in Section 4.4.2 is used for the $p_{\text{T},\tau}$ dependent parameterisation with eight $p_{\text{T},\tau}$ bins. To be able to adequately describe $R_{\nu\tau,i}$ in each of these bins, a different function compared to the final version has been chosen:

$$f(x) = C \cdot \exp^{\frac{(\log(m \cdot x + b) - \mu)^2}{2\sigma^2}} .$$

The resulting performances for the two decay channels involving leptonic τ-lepton decays are shown in Figure 4.20. In contrast to the other studies presented in this section, the MLM estimator was chosen for this comparison. It is the only estimator written to storage for the $\tau_{\text{lep}}\tau_{\text{lep}}$ channel because of disk space management reasons as well as the estimator used in the measurement. While the MMC shows a shift in the Receiver-Operating-Curve for the fully leptonic channel, a degradation in its performance for the semi-leptonic channel is observed with the AUC being 0.87 compared to the reference value of 0.88. Thus, the $p_{\text{T},\tau}$ independent $R_{\nu\tau,i}$ parameterisation as described in Section 4.4.2 was implemented in the final MMC.

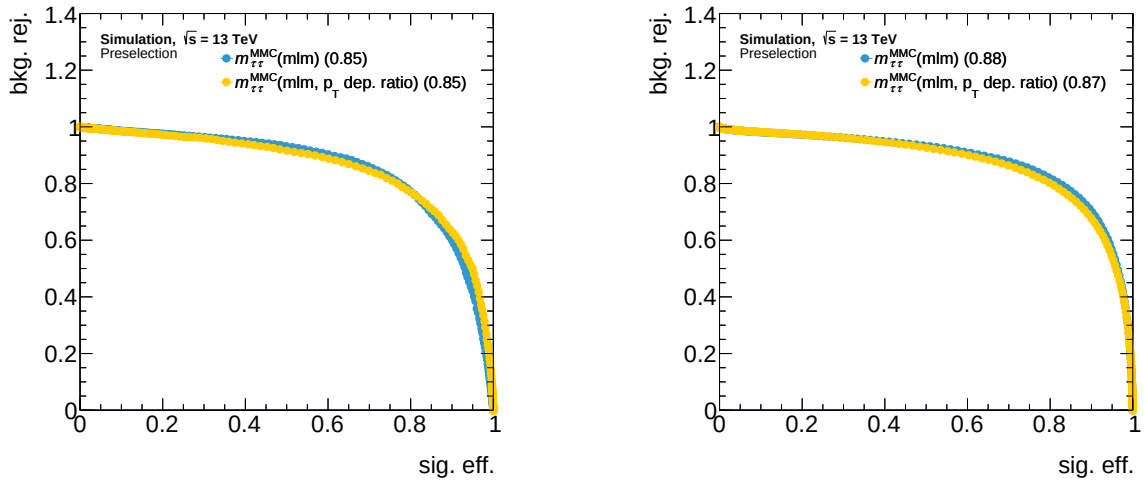

(a) $\tau_{\text{lep}}\tau_{\text{lep}}$ channel.

(b) $\tau_{\text{lep}}\tau_{\text{had}}$ channel.

Figure 4.20: Comparison of the MMC performance using the $p_{\text{T},\tau}$ dependent p.d.f. set for $R_{\nu\tau,i}$ and the inclusive p.d.f.. The Receiver-Operating-Curve with $H \rightarrow \tau\tau$ as the signal and $Z \rightarrow \tau\tau$ as the background are shown. The area under the curve is quoted for each MMC version.

4.4 Final Version

The studies discussed in this section describe modifications propagated to the final MMC version used in the measurement. As in the previous section, the reference version of the MMC is the one used in Reference [7]. Performance comparisons are mainly based on ROC, and their corresponding AUC, and the MMC distributions themselves.

Additionally to these studies and their resulting modifications, the MMC's code was refactored to increase its maintainability and improve its user interface. Changes related to the package's maintainability include the usage of modern object oriented C++ features and removal of outdated functions etc. New classes were introduced where each one takes care of one specific task such as preparing the inputs in the correct format or calculating the likelihood of a proposed state y. The p.d.f.s used in the likelihood calculation were moved from hard-coded numbers in arrays to ROOT's TF1 class. This C++ class provides a unified interface to one-dimensional functions $f(x)$ and all necessary methods to evaluate them, thus making it easier for analyses to provide p.d.f.s specific to their phase spaces. The changes to the code were carefully validated using the MAXW estimate, confirming that both code versions yield the same results with identical p.d.f.s.

4.4.1 Runtime Improvements

The MMC's runtime contributes a major part to the overall computational effort of this thesis' measurement. Studying the MMC's hyperparameters in Section 4.3.1 showed that little to no gain in the separation power is to be expected from varying these parameters. However, it was shown that they do have a significant impact on the overall runtime. Following a simple approach, the number of maximum iterations in the Markov Chain, summarised in Table 4.3 for all di-τ decay channels, was varied in order to assess this parameter's effect on the runtime and MMC performance. The impact

Decay channel	Maximum iterations
$\tau_{\text{lep}}\tau_{\text{lep}}$	200000
$\tau_{\text{lep}}\tau_{\text{had}}$	100000
$\tau_{\text{had}}\tau_{\text{had}}$	50000

Table 4.3: Number of maximum iterations set per τ-lepton decay channel for the Markov Chain.

on the runtime for the $\tau_{\text{had}}\tau_{\text{had}}$ channel in comparison to the default setting of 50×10^3 iterations is shown in Figure 4.21 and the impact on the separation power in Figure 4.22. Reducing the number of maximum iterations in the Markov Chain also decreases the MMC's overall runtime, while increasing the number of iterations also increases the runtime. Unlike the runtime, the separation power is compatible for all tested configurations. This suggests that the mass estimate does not significantly change after only a fraction of the total iterations. Thus, a substantial speedup of the algorithm is feasible without sacrificing any or only little of its performance.

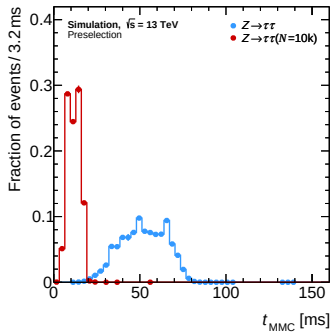

(a) A maximum of 10×10^3 iterations are used.

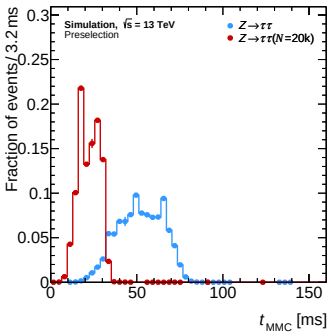

(b) A maximum of 20×10^3 iterations are used.

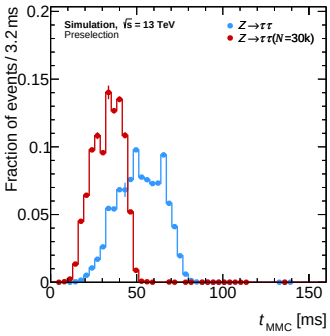

(c) A maximum of 30×10^3 iterations are used.

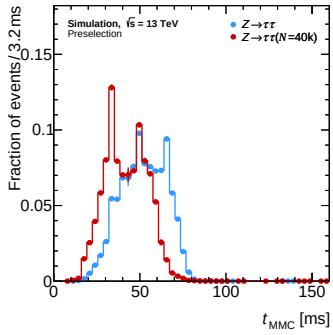

(d) A maximum of 40×10^3 iterations are used.

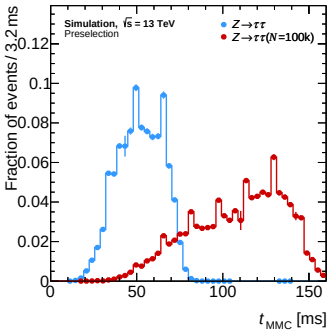

(e) A maximum of 100×10^3 iterations are used.

Figure 4.21: Per event runtime of the MMC for the $Z \rightarrow \tau\tau$ process in the $\tau_{\text{had}}\tau_{\text{had}}$ channel. Different maximum number of iterations are shown. The default configuration, shown in blue, corresponds to a maximum of 50×10^3 iterations.

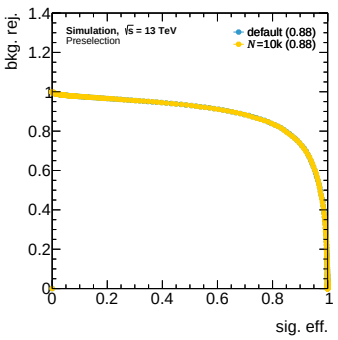

(a) A maximum of 10×10^3 iterations are used.

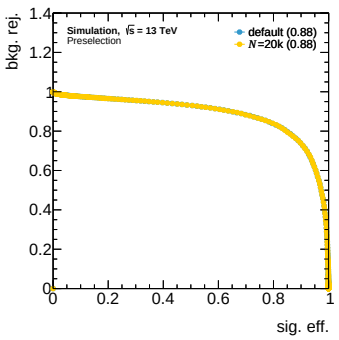

(b) A maximum of 20×10^3 iterations are used.

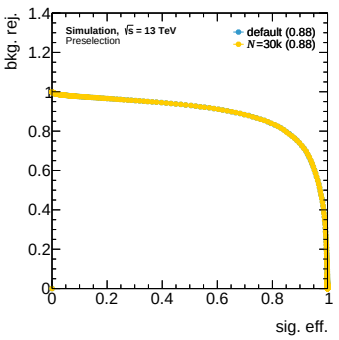

(c) A maximum of 30×10^3 iterations are used.

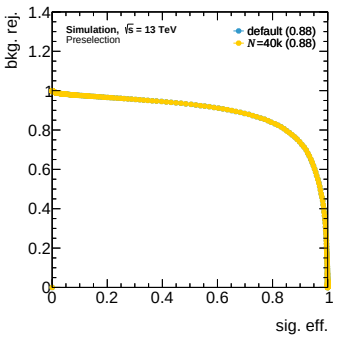

(d) A maximum of 40×10^3 iterations are used.

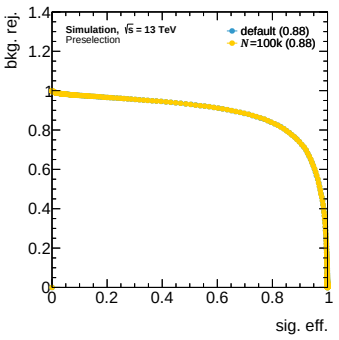

(e) A maximum of 100×10^3 iterations are used.

Figure 4.22: Receiver-Operating-Curves of the MMC in the $\tau_{\text{had}}\tau_{\text{had}}$ channel. Different maximum number of iterations are shown. The default configuration, shown in blue, corresponds to a maximum of 50×10^3 iterations.

However, the approach of simply reducing the maximum number of iterations is too simplistic to be applied in measurements. By setting this number to smaller values, a chance would be introduced that for certain events the Markov Chain terminates before a stable mass estimate is found. In order to circumvent this potential issue, a more elaborate criterion to terminate the Markov Chain has been developed. The general idea is to periodically check, every 1×10^3 iterations, the additional criterion and stop the Markov Chain once the condition is fulfilled. Motivated by Figure 4.22, showing a similar ROC for less iterations compared to the default number of iterations, the periodic check begins after the first 10×10^3 iterations. If this new condition is not triggered, the Markov Chain terminates after the already implemented maximum number of iterations. This allows to save computation power in "easy" events where the MMC finds a rather stable mass estimate early on, while being able to continue the scan in more "difficult" events that take longer to reach a stable mass estimate.

Another way to phrase this concept is that the new criterion checks if the Markov Chain has reached an equilibrium. In this context, the equilibrium is defined such that the values of the scanned quantities have become stable apart from small fluctuations due to the Metropolis-Hastings algorithm. The implementation entails splitting the proposed states for each scanned quantity randomly into two separate sets. For each set, a histogram is filled with the proposed state which allows to define an estimate of the equilibrium using the compatibility of the two histograms for a given quantity. In

order to not imply any specific assumptions on the shape of the sets' histograms, only rudimentary statistical tools are used to compute the compatibility. Two sets are considered compatible if their means agree within 5% of the first set's root mean square (RMS). The only assumption on the shapes of the histograms in this definition is that the two sets have similar shapes. Both sets are the result of a random split within the Markov Chain and, thus, shaped by the same p.d.f.s. The resulting overall

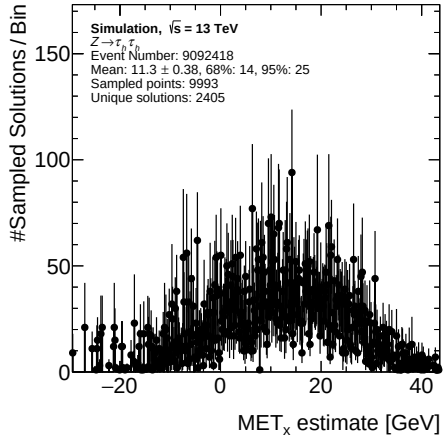

(a) Distribution of proposed $E_{\mathrm{T,x}}^{\mathrm{miss}}$ values for event 9092418.

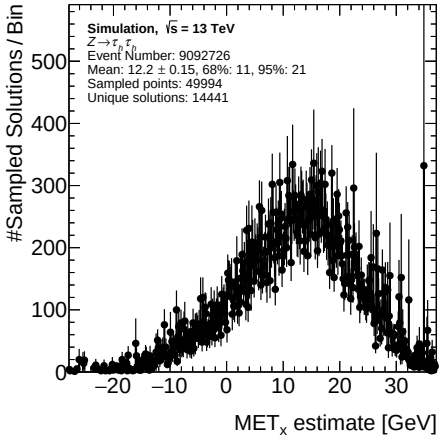

(b) Distribution of proposed $E_{\mathrm{T,x}}^{\mathrm{miss}}$ values for event 9092726.

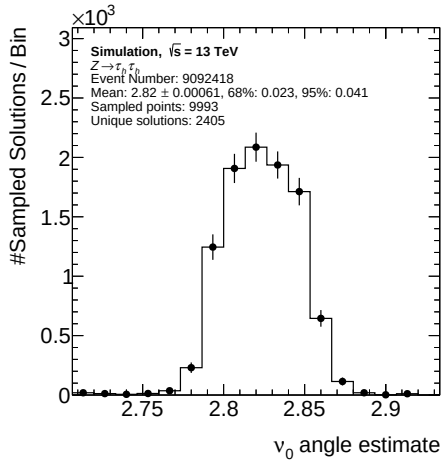

(c) Distribution of proposed $\phi_{\nu,1}$ values for event 9092418.

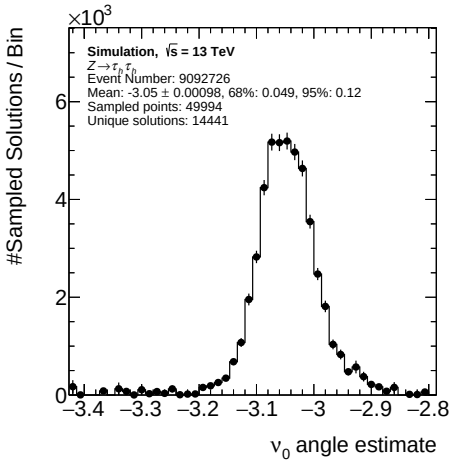

(d) Distribution of proposed $\phi_{\nu,1}$ values for event 9092726.

Figure 4.23: Distributions of proposed values for scanned quantities for two fully hadronic di-τ events of the $Z \to \tau\tau$ sample. The mean and the 68% (95%) quantiles of the distributions are quoted in GeV.

distributions for two scanned quantities are shown in Figure 4.23 for two events. In event 9092418 the equilibrium condition is already met after 10×10^3 iterations while the condition is not triggered in event 9092726 as it reaches the maximum number of 50×10^3 iterations. Generally, the less overall phase space points have been sampled, the "easier" it is for the Markov Chain to find its equilibrium and, thus, a stable mass estimate. Due to technical reasons the very first point with a valid solution to

the neutrino equations is not filled into the histograms of the scanned quantities which explains why the number of sampled points is smaller than the minimally required 10×10^3 iterations in Figure 4.23(a) and 4.23(c). After seven iterations the Markov Chain found a new valid solution. Thus, the histograms contain 9993 sampled points and for the same reason Figure 4.23(b) and 4.23(d) contain a slightly smaller number of points than the maximum number of 50×10^3 iterations. Comparing the quantiles of the distributions between the two events, the "easy" event 9092418 reaches a similar or even better accuracy after a fraction of the iterations needed for the other event. The $E_{\mathrm{T,x}}^{\mathrm{miss}}$ estimate of event 9092726 in Figure 4.23(b) shows the so-called "burn-in" on the left-hand side of the distribution. This means that the Markov Chain needs a certain number of iterations to get closer to the final estimate which is visible as a tail in the distribution. One potential reason event 9092418 reaches its equilibrium faster might be that the "burn-in" phase is not clearly visible in Figure 4.23(a) and hence, much shorter.

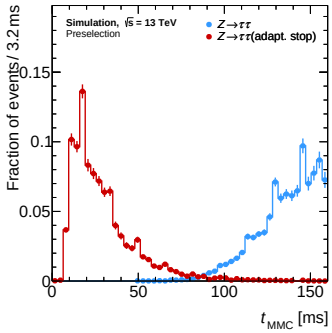

(a) Per event runtime of the MMC for the $Z \rightarrow \tau\tau$ process in the $\tau_{\mathrm{lep}}\tau_{\mathrm{lep}}$ channel.

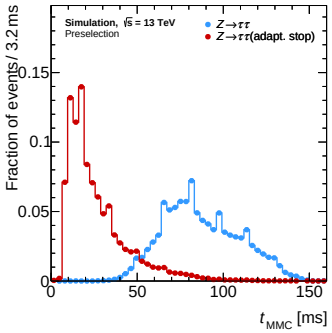

(b) Per event runtime of the MMC for the $Z \rightarrow \tau\tau$ process in the $\tau_{\mathrm{lep}}\tau_{\mathrm{had}}$ channel.

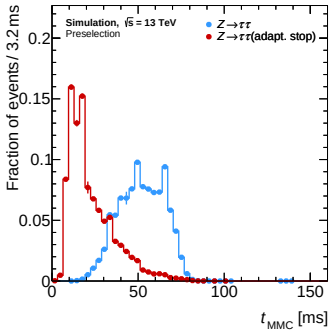

(c) Per event runtime of the MMC for the $Z \rightarrow \tau\tau$ process in the $\tau_{\mathrm{had}}\tau_{\mathrm{had}}$ channel.

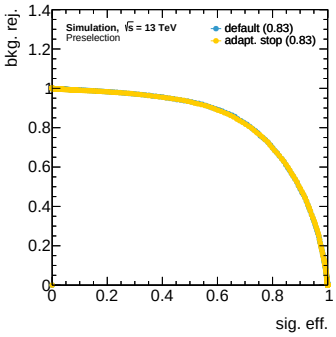

(d) Receiver-Operating-Curve of the MMC in the $\tau_{\mathrm{lep}}\tau_{\mathrm{lep}}$ channel.

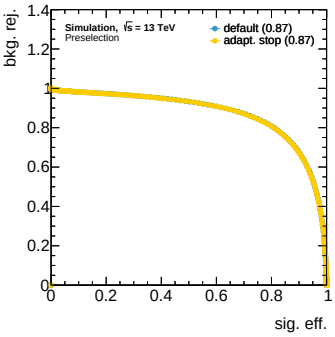

(e) Receiver-Operating-Curve of the MMC in the $\tau_{\mathrm{lep}}\tau_{\mathrm{had}}$ channel.

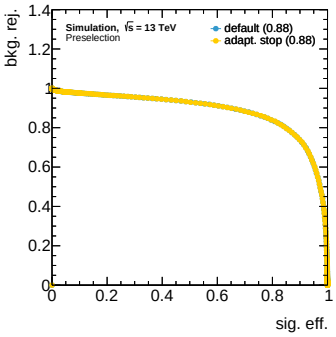

(f) Receiver-Operating-Curve of the MMC in the $\tau_{\mathrm{had}}\tau_{\mathrm{had}}$ channel.

Figure 4.24: Receiver-Operating-Curves and runtime of the MMC in all di-τ decay channels. A comparison with (adapt. stop.) and without (default) the additional equilibrium condition is shown.

The impact of this new equilibrium condition on the MMC's performance is shown in Figure 4.24 for the $\tau_{\mathrm{lep}}\tau_{\mathrm{lep}}$, the $\tau_{\mathrm{lep}}\tau_{\mathrm{had}}$ and the $\tau_{\mathrm{had}}\tau_{\mathrm{had}}$ channel. With increasing number of neutrinos in the τ-lepton decays the runtime increases without the additional criterion because the number of maximum iterations depends on the decay channel, see Table 4.3. These settings are motivated by the more complex scan for leptonic τ-lepton decays since it is only feasible to calculate the neutrino system

instead of the individual neutrinos in the Markov Chain. By introducing the additional equilibrium criterion, the mean runtime is reduced by roughly a factor of two to three for fully hadronic di-τ decays and even more significantly if leptonic decays are involved. Up to a factor of approximately five in speedup is achieved for the $\tau_{\text{lep}}\tau_{\text{lep}}$ final state. It has to be noted, though, that the comparison is conducted with the final MMC version and, thus, the runtime increase from calling the TF1 function objects is factored in. However with respect to the original MMC version, the criterion still achieves a speedup of two for the fully hadronic decay channel and up to a factor of four to five for the fully leptonic decay channel. The flexibility of this criterion is especially important for leptonic decays as can be seen by the broadened runtime distribution with increasing number of leptonic τ-leptons. Furthermore, the separation power of the MMC is unchanged with respect to the default implementation of effectively relying on the number of maximum iterations.

The impact of the additional equilibrium condition on the number of sampled phase space points with a physical solution, without a valid solution and points that are rejected by the Metropolis-Hastings algorithm is shown in Figure 4.25. Without the additional criterion most of the proposed states do not yield physical solutions while only a fraction of proposed states are rejected by the Metropolis-Hastings algorithm. With the additional criterion the Markov Chain becomes more efficient since the difference of the average number of states with and without physical solutions becomes smaller. Hence, less iterations are spent in phase space regions close to the final estimates but not yielding valid solutions due to the variation of the quantities during the scan.

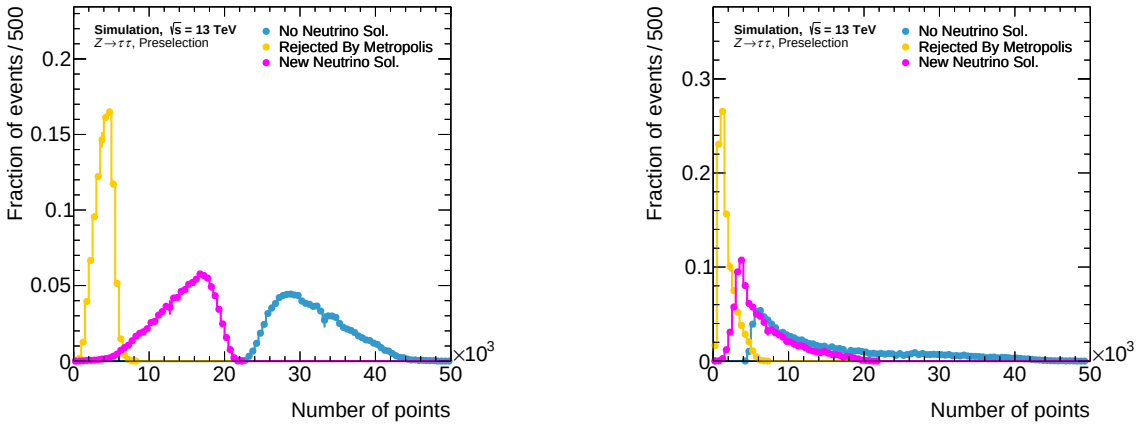

(a) Maximum number of iterations set to 50000.

(b) Additional equilibrium condition.

Figure 4.25: Number of scanned points in the Markov Chain with no valid solution, a valid solution and a valid solution that is rejected by the Metropolis-Hastings algorithm. The distributions are shown for $Z \rightarrow \tau\tau$ in the $\tau_{\text{had}}\tau_{\text{had}}$ channel.

4.4.2 Parameterisation of p.d.f.s

For all p.d.f.s discussed in Section 4.2.2 new parameterisations have been created. The only exception is the $E_{\text{T}}^{\text{miss}}$ p.d.f. which was updated for the $H \rightarrow \tau\tau$ measurement conducted in Reference [7]. In the following, the procedure implemented to derive the parameterisations will be introduced. Most functions used to mathematically describe the underlying simulated distributions are empirically

motivated. Theoretical motivations of these functions are only possible for parts of the effects included in the distributions as reconstruction effects and efficiencies introduce non-trivial alterations. All parameterisations are based on simulated $Z \rightarrow \tau\tau$ events with the τ_{had} p.d.f.s being computed using the $Z \rightarrow \tau_{\text{had}}\tau_{\text{had}}$ sample and the τ_{lep} p.d.f.s using the $Z \rightarrow \tau_{\text{lep}}\tau_{\text{had}}$ sample. The applied event selection is summarised in Table B.1 in Appendix B.1. In order to increase the available statistics when computing the p.d.f.s, a simplified selection is applied that is inspired by the $H \rightarrow \tau\tau$ measurement in Reference [7] since the selection described in Section 5.2 was still work in progress at that point.

Parameterisation of Neutrino System Mass p.d.f.s

The invariant neutrino mass p.d.f. is only relevant for leptonically decaying τ-leptons since more than one neutrino is needed to properly define it. Its Lorentz-invariance does not necessitate a further parameterisation as a function of $p_{\text{T},\tau}$ or any other quantity. Historically, a sixth order polynomial was used to describe the functional form of this distribution. As shown in Figure 4.26 this function is suitable for the new Monte Carlo simulations as well. The simulation used is a $Z \rightarrow \tau\tau$ sample in the $\tau_{\text{lep}}\tau_{\text{had}}$ decay channel as it provided the highest available statistics at that point. After the MMC's code refactoring the fitted ROOT TF1 object is directly used as the new p.d.f.. The final MMC

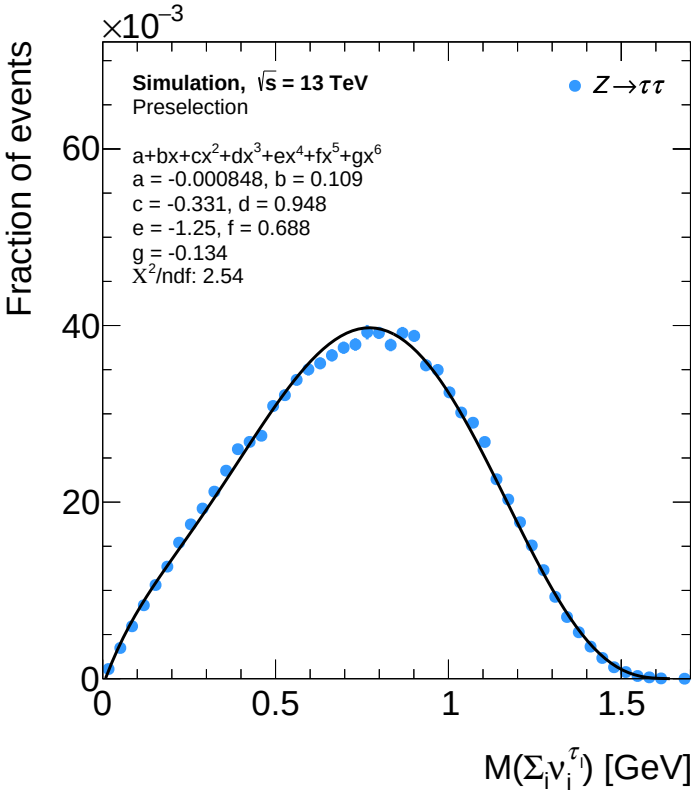

Figure 4.26: Neutrino system mass p.d.f.. A sixth order polynomial, shown as the solid line, is fitted to $Z \rightarrow \tau\tau$ Monte Carlo for leptonic τ-leptons in the $\tau_{\text{lep}}\tau_{\text{had}}$ channel.

configuration for the measurement does not include the M $\left(\sum_i \nu_i^{\tau_{\text{l}}}\right)$ p.d.f. in the likelihood evaluation.

As shown in Figure 4.27, the p.d.f.'s impact on the separation power is negligible in all inclusive signal region phase spaces for the $\tau_{\text{lep}}\tau_{\text{had}}$ channel. Since this decay channel includes leptonic decays and provides more sensitivity to the measurement than the $\tau_{\text{lep}}\tau_{\text{lep}}$ channel, the final verdict is based on the $\tau_{\text{lep}}\tau_{\text{had}}$ channel.

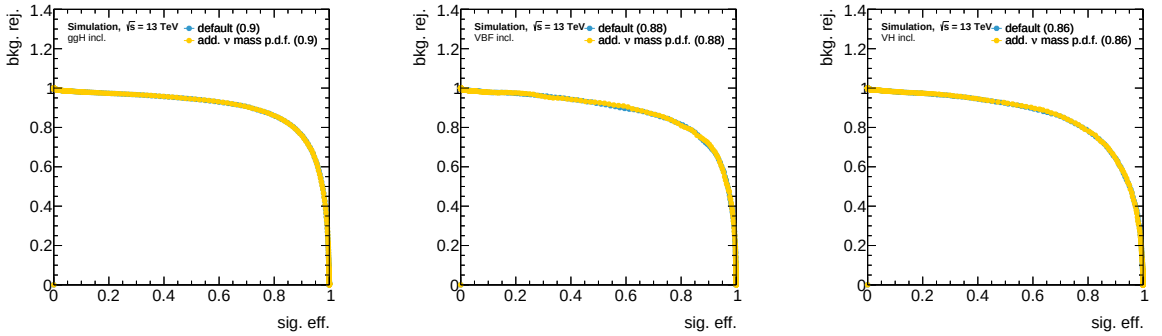

(a) Inclusive boosted signal regions. (b) Inclusive VBF-like signal regions. (c) Inclusive VH-like signal regions.

Figure 4.27: Receiver-Operating-Curves of the MMC in the $\tau_{\text{lep}}\tau_{\text{had}}$ channel comparing the final MMC configuration (default) with a setup including the M $\left(\sum_i \nu_i^{\tau_1}\right)$ p.d.f. (add. ν mass p.d.f.).

Parameterisation of Momentum Ratio p.d.f.s

The momentum ratio p.d.f. is used for both, leptonically and hadronically decaying τ-leptons. Typically, the ratio $R_{\nu\tau,i}$ is larger for leptonic τ-leptons than for hadronic τ-leptons, see Figure 4.28, due to the additional neutrino in the decay. Thus, different functions that are summarised in Table 4.4 and used as the final parameterisations are needed to describe the simulations. The additional exponential for τ_{lep} helps in modelling the rising flank of the distribution close to zero. This flank does not exist for hadronic τ-leptons and, thus, the Gaussian distribution is sufficient to describe the simulation. However, an additional dependency is introduced for hadronic τ-leptons, namely the five-way decay mode categorisation and a split into leading and subleading τ-leptons. Leading τ-leptons are defined as the higher $p_{\text{T},\tau}$ object. Since the $Z \rightarrow \tau_{\text{lep}}\tau_{\text{had}}$ sample is used for leptonic τ-leptons for the same reasons as detailed in Section 4.4.2, no split into leading and subleading τ-leptons is available for these. Momentum dependent parameterisations were studied for the semi-leptonic channel but did not yield a satisfactory MMC performance, see Section 4.3.2. All hadronic parameterisations split by decay mode and τ-lepton are shown in Appendix B.2.

Decay channel	Fit function
Leptonic	$C \cdot e^{-\frac{(x-\mu)^2}{2\sigma^2}} + e^{b+m\cdot x}$
Hadronic	$C \cdot e^{-\frac{(x-\mu)^2}{2\sigma^2}}$

Table 4.4: Chosen fit functions to parameterise the $R_{\nu\tau,i}$ p.d.f. for the different τ-lepton decay channels.

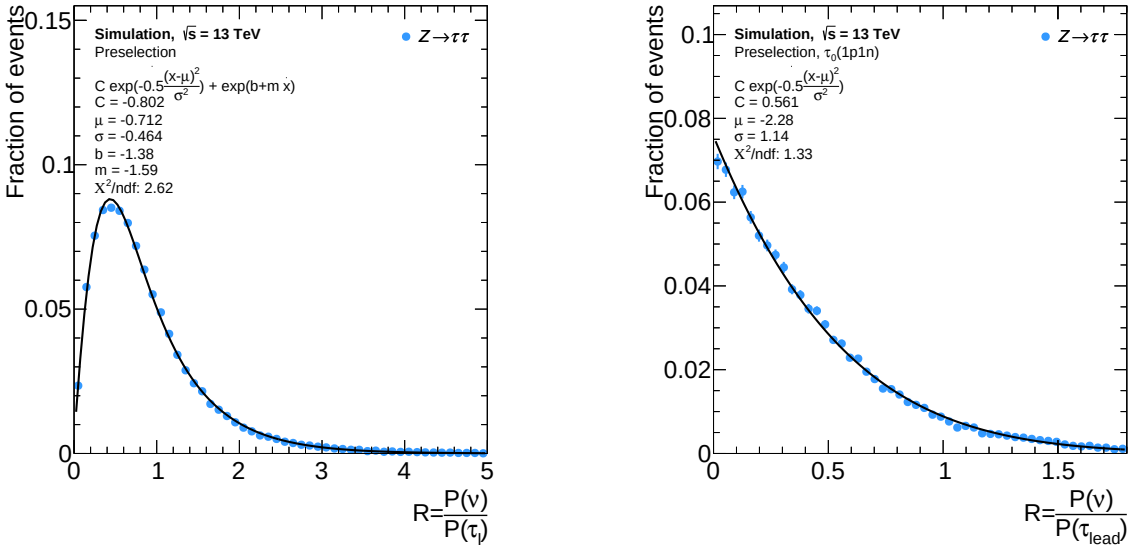

(a) Leptonic τ-lepton decays.

(b) Hadronic τ_{1p1n} decay of the leading τ-lepton.

Figure 4.28: Momentum ratio p.d.f. $R_{\nu\tau,i}$ for leptonic τ-leptons and one example for hadronic τ-leptons. The fitted functions, that are used as the parameterisations, are shown as solid lines and the fitted parameters are quoted in the figures.

Parameterisation of Angular p.d.f.s

The most complex parameterisation is implemented for the angular distance between the neutrino (system) and the visible reconstructed τ-lepton, $\theta_{3D,i}$. A $p_{T,\tau}$ dependent parameterisation is created for both leptonic and hadronic τ-leptons. Additionally, the five-way decay mode categorisation is utilised for τ_{had}. Leading and subleading τ-lepton distributions are combined for hadronic τ-leptons since the decay mode categorisation noticeably cuts into the statistics in some phase space regions. It was confirmed that the angular distributions agree reasonably well between the leading and subleading τ-leptons, see Figure 4.29. For lower ranges of $p_{T,\tau}$ the leading τ_{had} distribution has smaller statistics, while for higher ranges of $p_{T,\tau}$ the subleading τ_{had} distribution suffers in statistics. Thus, the compatibility check is not as reliable in these ranges. However, taking the statistical power into account a combination of the two distribution seems justified.

Ideally, one function is used to describe $\theta_{3D,i}$ for both, τ_{lep} and τ_{had}. Although some differences in the distributions are expected due to the additional neutrino in leptonic decays, they should not alter the distributions so that another function becomes necessary. The shape is strongly driven by the τ-lepton's boost which is independent of its decay. Multiple attempts to define a suitable function are documented in Appendix B.3. One example is given in Figure 4.30 for leptonic and hadronic τ-leptons with a similar boost. The function used to fit the distribution is a Landau function

$$p(x) = \frac{1}{\xi}\frac{1}{2\pi i}\int_{c-i\infty}^{c+i\infty} e^{\lambda s + s\log s} ds \tag{4.14}$$

where $\lambda = (x - x_0)/\xi$ [122, 123]. While the distributions are fairly similar due to the τ-leptons' similar boosts, the Landau function is not able to adequately describe the leptonic τ-lepton decay. The final

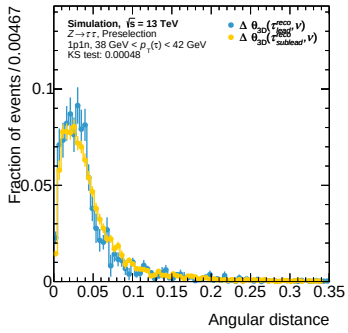

(a) Comparison of $\theta_{3D,i}$ in the range of 38 GeV $< p_{T,\tau} <$ 42 GeV.

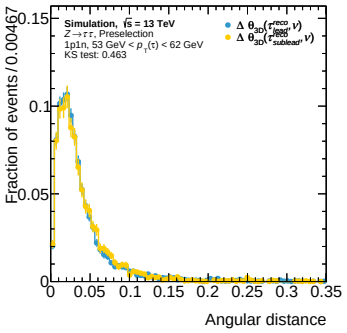

(b) Comparison of $\theta_{3D,i}$ in the range of 53 GeV $< p_{T,\tau} <$ 62 GeV.

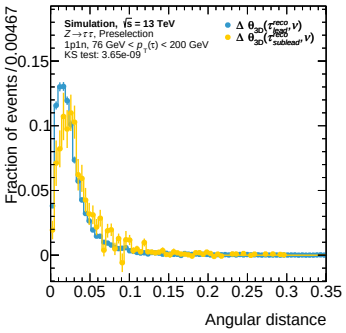

(c) Comparison of $\theta_{3D,i}$ in the range of 76 GeV $< p_{T,\tau} <$ 200 GeV.

Figure 4.29: Comparison of the $\theta_{3D,i}$ distributions between the leading and subleading τ_{had} for fully hadronic $Z \to \tau\tau$ events. A Kolmogorov test is performed to calculate the compatibility of the two histograms.

function used is a lognormal which effectively replaces the argument inside a Gaussian distribution with its logarithmic version:

$$C \cdot e^{-a\left(\log \frac{x+b}{m}\right)^2}. \tag{4.15}$$

Using this function, a more fitting description of the simulation is achieved for the same example distributions as shown before, see Figure 4.31. The remaining distributions, including the final parameterisation fits, are documented in Appendix B.4.

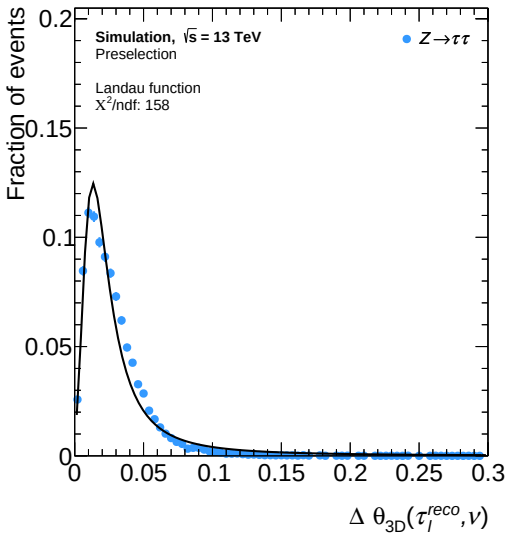

(a) Leptonic τ-lepton decays in the range of 33 GeV $<$ $p_{T,\tau} <$ 39 GeV.

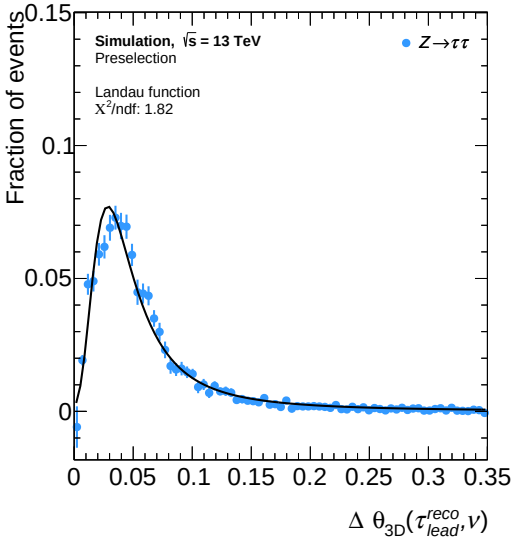

(b) Hadronic τ_{1p0n} decay in the range of 34 GeV $<$ $p_{T,\tau} <$ 38 GeV.

Figure 4.30: Angular distance p.d.f. $\theta_{3D,i}$ for leptonic τ-leptons and one example for hadronic τ-leptons. The Landau function described in Equation 4.14 is fitted and shown as the solid line.

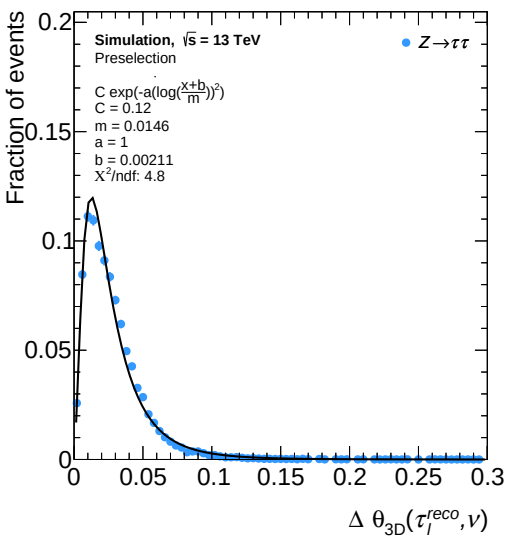

(a) Leptonic τ-lepton decays in the range of 33 GeV < $p_{\mathrm{T},\tau}$ < 39 GeV.

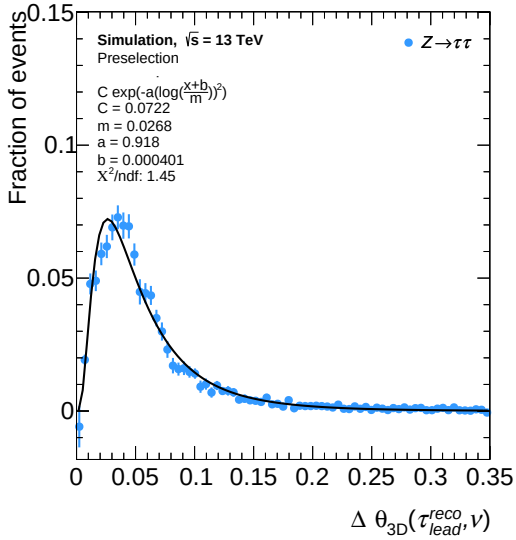

(b) Hadronic τ_{1p0n} decay in the range of 34 GeV < $p_{\mathrm{T},\tau}$ < 38 GeV.

Figure 4.31: Angular distance p.d.f. $\theta_{\mathrm{3D},i}$ for leptonic τ-leptons and one example for hadronic τ-leptons. The lognormal function described in Equation 4.15 is fitted and used for the final parameterisations.

Since the $\theta_{\mathrm{3D},i}$ distribution is sensitive to the τ-lepton boost and, thus, to $p_{\mathrm{T},\tau}$, the final parameterisation is a function of $p_{\mathrm{T},\tau}$. The procedure is as follows: for a specific decay mode, $\theta_{\mathrm{3D},i}$ is fitted in bins of $p_{\mathrm{T},\tau}$, covering 0 GeV < $p_{\mathrm{T},\tau}$ < 200 GeV. Higher transverse momenta were not accessible due to limited statistics but the covered range is well suited for the measurement described in this thesis. The parameters of the lognormal determined by the fits are themselves fitted as a function of $p_{\mathrm{T},\tau}$. In order to determine the position of a given parameter on the $p_{\mathrm{T},\tau}$ axis, the mean of the original $\theta_{\mathrm{3D},i}$ fit's $p_{\mathrm{T},\tau}$ range's distribution is used. Two of these parameters are shown for hadronic τ_{1p0n} decays in Figure 4.32. Although, the extrapolation to very low $p_{\mathrm{T},\tau}$ may not be perfect, it does not influence any ATLAS analysis since hadronic τ-leptons are only well-defined above 20 GeV as this is the minimum transverse momentum required in the determination of the τ_{had} related scale factors and uncertainties discussed in Section 3.3.4.

4.4.3 Performance of the Final MMC Version

With the newly parameterised p.d.f.s implemented, the final MMC performance has been compared to the original MMC version used in Reference [7]. This comparison, on the one hand, includes the algorithm speedup discussed in Section 4.4.1 and, on the other hand, detailed studies on the mass estimate itself that will be discussed in the following. In order to assess the impact on the measurement, the comparison is performed in the inclusive signal regions[3] defined in Section 5.2. Using the inclusive signal regions enables spotting phase space dependent effects that are important to understand because of the different sensitivities to the signal(s) in the individual regions. For this comparison the MLM mass estimate is used since it is the final estimator in the measurement, see

[3] Measurements typically define signal regions that are enriched in the targeted signal processes.

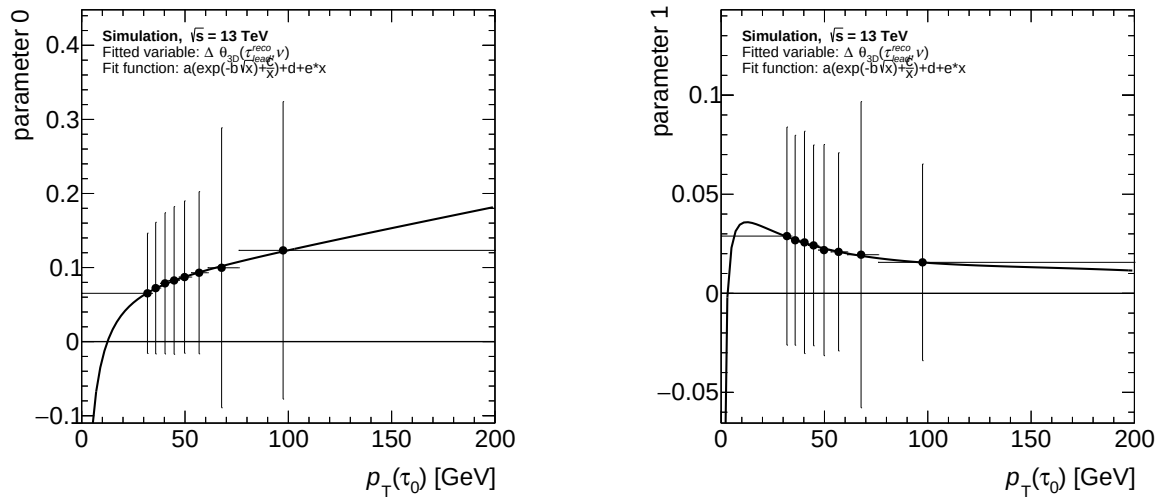

(a) Parameter C of the lognormal as a function of $p_{\mathrm{T},\tau}$.

(b) Parameter m of the lognormal as a function of $p_{\mathrm{T},\tau}$.

Figure 4.32: Transverse momentum dependent $\theta_{\mathrm{3D},i}$ parameterisations of the lognormal's parameters defined in Equation 4.15. The shown parameters are for hadronic τ_{1p0n} decays.

Section 4.2.3. Instead of its specific name MLM, the following chapters will reference this estimator by $m_{\tau\tau}^{\mathrm{MMC}}$. The MMC's parameter settings used in the measurement together with a short explanation of the parameters' meaning are given in Table B.2 in Appendix B.7.

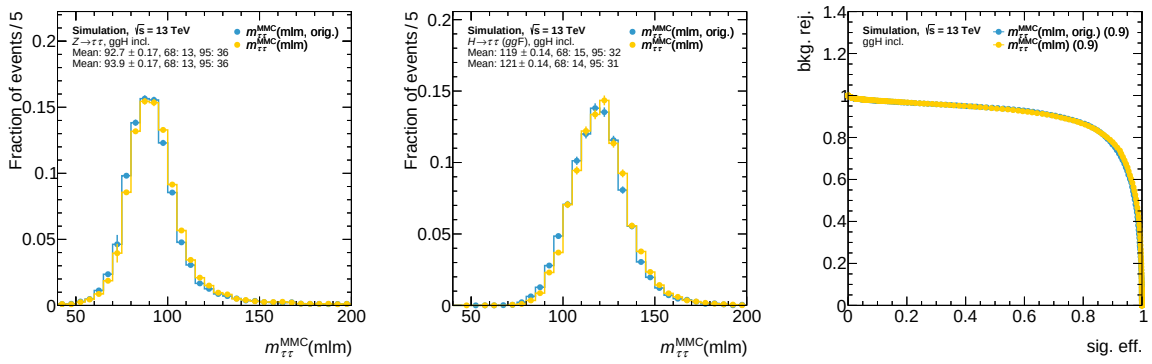

(a) $Z \to \tau\tau$ lineshapes.

(b) $H \to \tau\tau$ lineshapes.

(c) Receiver-Operating-Curve.

Figure 4.33: Performance of the final MMC version in comparison to the original MMC, showing the lineshapes of the $Z \to \tau\tau$ and $H \to \tau\tau$ processes as well as the ROC. All figures show the fully hadronic di-τ decay channel in the inclusive boosted signal region.

An example of the Receiver-Operating-Curve as well as the MMC lineshapes of the original and the final version is shown in Figure 4.33. The observed lineshapes for both $Z \to \tau\tau$ and $H \to \tau\tau$ as well as the ROC show a similar performance for both MMC versions. While this example focuses on the fully hadronic decay channel of the inclusive Boost phase space, the ROCs for all combinations of inclusive signal regions and τ-lepton decay channels are shown in Figure B.23 in Appendix B.6. The

corresponding AUCs, together with lineshape characteristics, are summarised in Table 4.5. Overall, a similar performance with respect to the original MMC could be achieved. Depending on the phase space and the di-τ final state, a small reduction of at most roughly 1 % in the area-under-the-curve is observed which mostly affects the fully leptonic decay channel. This slight decrease is most likely caused by a selection bias introduced in the calculation of the leptonic τ-lepton p.d.f.s using $Z \rightarrow \tau_{\text{lep}}\tau_{\text{had}}$. The final $\tau_{\text{lep}}\tau_{\text{lep}}$ selection is able to include τ-leptons with even lower $p_{\text{T},\tau}$ which is achieved by an involved combination of different lepton triggers. A summary of the implemented overall trigger strategy is given in Section 5.2. The effect of the selection bias on the p.d.f.s and the final performance is discussed in Appendix B.5. Comparing the lineshapes of the final MMC and the original version for $Z \rightarrow \tau\tau$ and $H \rightarrow \tau\tau$ in Appendix B.6 explains the individual ROCs. While the core mass resolution could be improved by roughly 1 % and by even more in the 95 % quantiles, depending on the phase space, the means of the $Z \rightarrow \tau\tau$ and $H \rightarrow \tau\tau$ mass distributions moved closer to each other. Since the presented measurement does not aim to measure the Higgs boson's mass but its production cross-sections these means only have to be within a physically meaningful range which is the case.

Phase Space/ Di-τ decay channel	Process	Final MMC version				Original MMC version			
		Mean	68 % quantile	95 % quantile	AUC	Mean	68 % quantile	95 % quantile	AUC
Boost									
$\tau_{\text{lep}}\tau_{\text{lep}}$	$Z \rightarrow \tau\tau$	93	15	32		97	16	36	
	$H \rightarrow \tau\tau$	114	17	35	0.83	120	17	36	0.84
$\tau_{\text{lep}}\tau_{\text{had}}$	$Z \rightarrow \tau\tau$	93	14	35		95	14	37	
	$H \rightarrow \tau\tau$	121	15	32	0.9	124	15	33	0.9
$\tau_{\text{had}}\tau_{\text{had}}$	$Z \rightarrow \tau\tau$	94	13	36		93	13	36	
	$H \rightarrow \tau\tau$	121	14	31	0.9	119	15	32	0.9
VBF									
$\tau_{\text{lep}}\tau_{\text{lep}}$	$Z \rightarrow \tau\tau$	92	16	32		95	17	33	
	$H \rightarrow \tau\tau$	114	18	36	0.82	119	18	40	0.83
$\tau_{\text{lep}}\tau_{\text{had}}$	$Z \rightarrow \tau\tau$	96	15	34		98	16	38	
	$H \rightarrow \tau\tau$	121	15	30	0.88	124	15	30	0.87
$\tau_{\text{had}}\tau_{\text{had}}$	$Z \rightarrow \tau\tau$	96	15	38		94	15	37	
	$H \rightarrow \tau\tau$	121	15	34	0.87	119	16	34	0.87
VH									
$\tau_{\text{lep}}\tau_{\text{lep}}$	$Z \rightarrow \tau\tau$	88	15	29		93	16	32	
	$H \rightarrow \tau\tau$	112	19	37	0.84	117	18	39	0.84
$\tau_{\text{lep}}\tau_{\text{had}}$	$Z \rightarrow \tau\tau$	96	15	34		98	15	35	
	$H \rightarrow \tau\tau$	121	16	33	0.86	124	16	34	0.87
$\tau_{\text{had}}\tau_{\text{had}}$	$Z \rightarrow \tau\tau$	95	14	34		93	14	36	
	$H \rightarrow \tau\tau$	121	15	31	0.89	120	15	31	0.9

Table 4.5: Overview of the final MMC performance in comparison to the original MMC version. The area-under-the-curve is only quoted for the $H \rightarrow \tau\tau$ processes since the metric needs both processes, $Z \rightarrow \tau\tau$ and $H \rightarrow \tau\tau$. Histogram metrics, i.e. the mean and quantiles, are given in GeV and rounded to integer values for easier comparison. The corresponding histograms can be found in Appendix B.6.

Finally, the new p.d.f. parameterisations should not introduce any signal-like features, i.e. peak-like structures around the Higgs mass, in the mass distributions of backgrounds originating from misidentified τ-leptons. The data-driven estimates of the misidentified τ-lepton background for the individual di-τ decay channels are described in Section 5.3.1. Instead of directly studying these data-driven estimates, the overall data distributions in inclusive control regions, enriched in misidentified τ-leptons, have been studied. These control regions provide more statistics and are

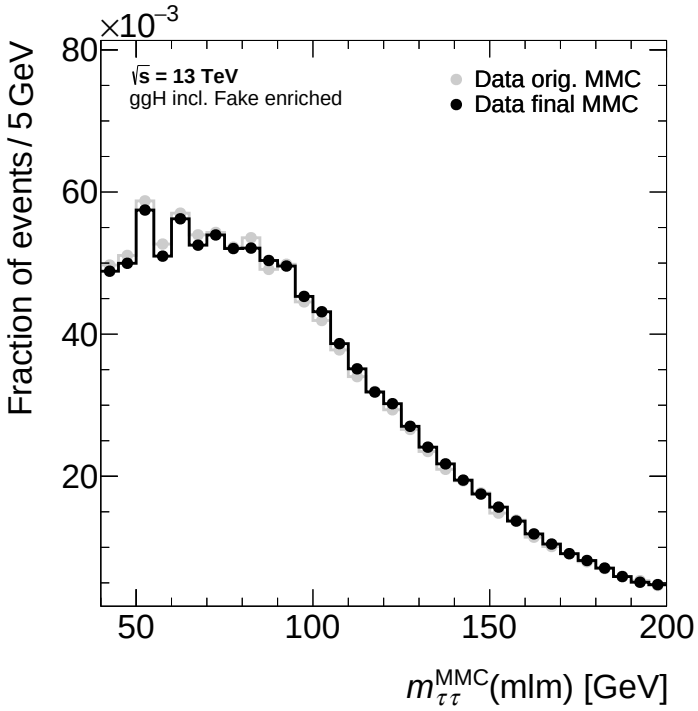

Figure 4.34: Data MMC lineshape in the fully hadronic decay channel comparing the final MMC configuration, shown in black, with the original MMC, shown in gray. The distribution is shown in the inclusive boosted region that is enriched in misidentified τ-leptons.

designed to be close to the signal region phase space with major contributions from misidentified τ-leptons. For $\tau_{\mathrm{lep}}\tau_{\mathrm{had}}$ and $\tau_{\mathrm{had}}\tau_{\mathrm{had}}$ the τ-lepton identification cuts are inverted, while for $\tau_{\mathrm{lep}}\tau_{\mathrm{lep}}$ the Top control regions are used since misidentified τ-leptons significantly contribute in those regions. As shown in Figure 4.34 for the fully hadronic di-τ decay channel in the boosted phase space, the data lineshapes are similar between the two MMC versions. Furthermore, no signal-like shape is introduced with the new parameterisations. More distributions are shown in Figure B.26 in phase space regions close to the signal regions but enriched in misidentified τ-leptons.

4.5 Outlook

A lot of effort has been put into studying different aspects of the MMC and its components, see Sections 4.3 and 4.4. However, these studies do not automatically prescribe the optimal application in the presented measurement. As shown in Figure 4.35 for the $\tau_{\mathrm{lep}}\tau_{\mathrm{had}}$ channel, the MMC's separation power depends on the τ-lepton decay mode to some degree. Utilising this observation would require the event selection to split events by the τ-lepton's decay mode and possibly adapt the data-driven background estimates. Hence, this split is not implemented in this $H \to \tau\tau$ cross-section measurement but is of possible interest for future implementations.

More ideas and aspects have been studied in various theses that were co-supervised, see References [124–127]. Since the spin of a resonance influences the momentum distributions of the

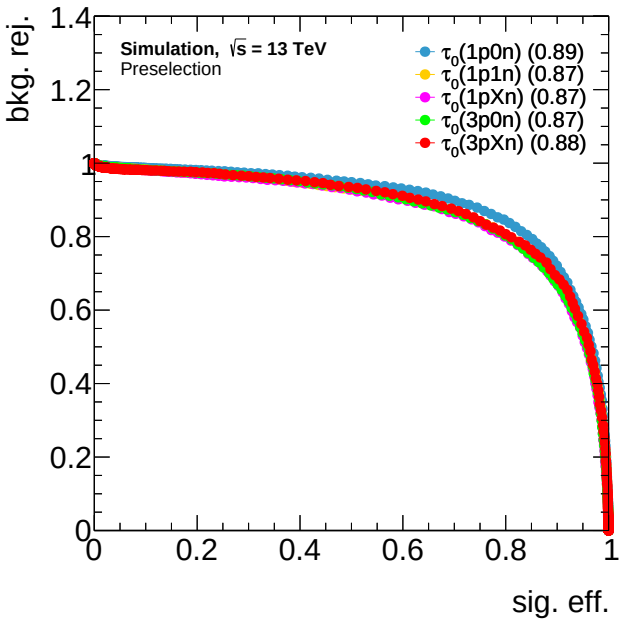

Figure 4.35: Separation power of the Missing Mass Calculator in the $\tau_{\text{lep}}\tau_{\text{had}}$ channel split into the hadronic τ-lepton decay modes.

τ-lepton's decay products as explained in Section 2.3, dedicated p.d.f.s for the MMC were studied in Reference [124]. To be more precise, helicity dependent p.d.f.s were parameterised following the same prescription discussed in Section 4.4.2. Noticeable differences between the individual sets were observed. However, the MMC's separation power did not improve. Additionally splitting the p.d.f.s by resonances, i.e. applying p.d.f.s based on $Z \to \tau\tau$ simulation only on the $Z \to \tau\tau$ simulation and $H \to \tau\tau$ based p.d.f.s only on $H \to \tau\tau$ events, improved the separation power. Even though this represents promising results, this procedure is not applicable in data as it requires knowledge of the type of event processed in the MMC. As shown in Section 4.3.2, a simple p.d.f. mixture, where the mixing is based on the visible di-τ mass, does not improve the MMC's performance.

Another study aimed at the inclusion of additional information into the MMC's likelihood, c.f. Reference [125]. Conceptually, vertex information of the τ-leptons contain yet unused information, specifically their secondary vertex. Due to the small but not negligible lifetime of τ-leptons it is possible to reconstruct their primary vertex, corresponding to their production point in the detector, and their secondary vertex, corresponding to the point of the τ-lepton decay. Reconstructing vertices is more accurate the more particles can be associated to that vertex, hence the study in Reference [125] focused on hadronic τ_{3p0n} decays. The spatial resolution of the decay particles drives the vertex resolution which is generally smaller for charged particles. With the additional vertex information, new event-based p.d.f.s were defined, utilising the additional constraints on the τ-lepton kinematics. However, several difficulties arose ranging from the treatment of the ambiguity in the neutrino equations to problems in finding actual solutions of the vertex constraints. One of the most promising introduced concepts is a likelihood classification of the possible solutions to the neutrino equations that could help alleviate the ambiguity problem. Instead of evaluating all possible combinations using the final likelihood as done in Section 4.3.1, simulated truth information were utilised to study which

solution is more likely to be the correct one. This information could finally be translated into p.d.f.s. The final conclusion of this concept study did not result in an improvement of the MMC's performance but laid important foundations to further pursue these ideas.

Approaches to replace the MMC rather than extending or improving it were studied in References [126] and [127]. These studies aimed at training a regression neural network that predicts the true invariant di-τ mass from reconstructed event information. Neural Networks provide several advantages compared to the likelihood-based approach of the MMC. The time needed to evaluate an event on a trained neural network model is only a fraction of the time needed by the MMC to process an event. Extending the likelihood used by the MMC is a challenging task as seen in Reference [125], while it is much easier to provide neural networks with additional information that can be used by the networks to extract e.g. correlations between the inputs. While still being feasibility studies focussing on the fully hadronic di-τ decay channel[4], important aspects and nuisances of training such a network architecture were uncovered. Training solely on $Z \to \tau\tau$ and $H \to \tau\tau$ samples is not suitable for the task at hand since the network would simply learn the resonance masses, minimising the loss function in the easiest possible way. This would, however, not be applicable in a measurement that includes backgrounds covering a wider mass range because such a network would also tend to predict the resonance masses for such processes. Thus, a training sample is needed with a flat mass distribution which was chosen to be an unphysical $\gamma^* \to \tau\tau$ process[5] with a mass range of $60\,\text{GeV} < m_{\tau\tau} < 220\,\text{GeV}$. The remaining structure in the mass distribution was alleviated by reweighting the events to achieve a uniform distribution. As depicted in Reference [126], training the regression network with the invariant di-τ mass as the target on this reweighted sample does not yield optimal results. Boundary effects prevent the network from predicting masses outside the range known from the training process which also affects predictions close to those boundaries. By introducing an additional term in the loss function, which reduces the penalty of predicting masses at the boundaries, the impact of this effect could be minimised. Overall, a similar performance to the MMC was achieved in the separation of the $Z \to \tau\tau$ and $H \to \tau\tau$ processes. It has to noted though, that the training with the modified loss function itself was not stable, instigating further studies.

In an attempt to circumvent the difficulty of boundary effects in the training, Reference [127] redefined the targets of the network's training to the neutrino momenta. This setup also allows to implement the τ-lepton mass constraint. The multidimensional output of this network could be used to calculate $m_{\tau\tau}$ after the network's application. However, new challenges are introduced by this setup such as an ambiguity in the neutrino direction similarly to the equations used in the MMC. Comparing these two network structures, the network trained to directly predict $m_{\tau\tau}$ outperforms the alternative setup. A study conducted in Reference [127], that applies the trained neural network using the neutrino momenta as target, on $Z \to \tau\tau$ and $H \to \tau\tau$ samples indicates that τ-lepton polarisation effects originating from the mother particle's spin are picked up in the network's training. Currently, the neural networks studied in Reference [127] are not able to reach the MMC's performance in terms of separation power.

All of these studies provide important knowledge for further development in the field of reconstructing the invariant di-τ mass. The fact that effects such as the τ-lepton polarisation are becoming of significance, points towards entering a precision regime with promising results.

[4] These first studies focus on the $\tau_{\text{had}}\tau_{\text{had}}$ channel as it entails the smallest number of neutrinos in the di-τ decay.

[5] In the physical Drell-Yan process contributions from virtual photons and Z-bosons cannot be disentangled.

CHAPTER 5

Design of the $H \rightarrow \tau\tau$ Cross-Section Measurement

Complex measurements like the measurement of the τ-lepton coupling to the Higgs boson that is discussed in this thesis are typically a collaborative effort in ATLAS. This section intends to provide a short overview of the general measurement design developed as part of this collaborative effort. More details are documented in Reference [8] on which this section is based on. The measurement is conducted in the context of the theoretical Simplified Template Cross Section (STXS) framework which will be discussed first. Afterwards, the selection applied to data and how it relates to the STXS framework will be introduced. The section concludes with a discussion of the background estimation techniques and an overview of the most important sources of uncertainties.

5.1 Simplified Template Cross Sections

Due to the multitude of possible Higgs boson couplings, various measurements targeting different production and decay modes are conducted. With increasing statistics these measurements gain in precision and become increasingly sensitive to physics beyond the Standard Model. Effects of new physics can either manifest in an overall modified cross-sections of specific processes or changes to differential cross-sections, i.e. their dependence on a given quantity. If a new physics scenario introduces new heavy particles, they contribute to loops in e.g. ggH production and, thus, increase its cross-section given that there is no destructive interference. Variations to the differential Higgs production cross-section as a function of p_{T}(H) are shown in Figure 5.1 for different scenarios of modified particle couplings to the Higgs boson. Even though the modifications to the cross-sections can become sizeable in some phase space corners, the uncertainties of the prediction and the measurement have to be considerd when interpreting the results.

Thus, achieving as precise as possible measurements is important to not only understand Standard Model scenarios precisely but also to spot possible new physics effects. In this context, the combination of measurements becomes important as individual measurements can be more or less sensitive in certain phase space regions.[1] The joint effort of experimental, i.e. ATLAS and CMS, and theory communities to define a framework which aims to minimise the dependence on theory uncertainties

[1] For example due to categorisation criteria applied to events that are needed from the experimental/analysis side.

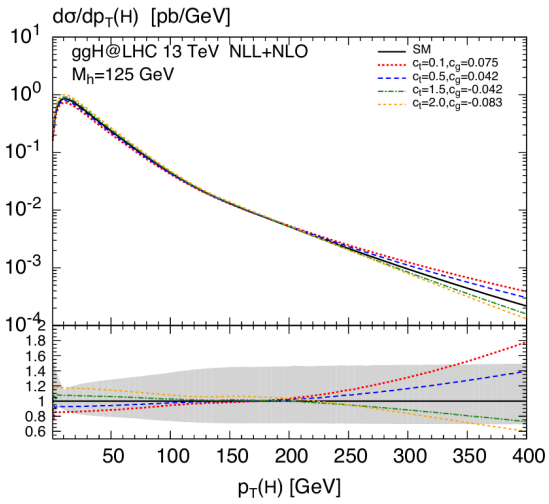

Figure 5.1: Variation of the Higgs production cross-section as a function of p_{T}(H) for different scenarios of modified particle couplings to the Higgs boson. The uncertainty of the theory prediction is shown as the shaded area in the bottom panel. Taken from Reference [128].

while allowing to easily combine multiple Higgs measurements is given with the Simplified Template Cross Sections (STXS), see Reference [45].

Typically, the combination of different Higgs decay channels is a non-trivial task that involves the unfolding of the fiducial cross-section measurement to larger phase spaces. This entails a dedicated treatment of uncertainties on the theory predictions. Within the STXS framework, the dependence of theoretical uncertainties and possibly needed extrapolations are minimised. One focus lies on reducing possible acceptance variations in the measurement. Generally, the STXS framework defines individual bins of phase space regions targeting the Higgs production modes either inclusively or split by quantities that either reduce the theory dependence or enhance new physics effects. By treating the Standard Model itself as well as the STXS bins as kinematic templates in the measurement, the theory dependence is reduced. Thus, the simulated SM signal samples are categorised according to the STXS bins based on truth quantities and therefore effectively unfolded to the STXS bins in the measurement.

To allow for the combination of measurements, the truth quantities and objects on which the STXS categorisation is based have to follow a common and if possible simple definition. The Higgs boson is considered a final state particle which consequently allows to combine measurements targeting different decay channels. Furthermore, the STXS are defined for on-shell production of the Higgs boson and a cut on the its rapidity of $\left|y_{\mathrm{H}}\right| < 2.5$[2] is applied everywhere [45]. This cut is motivated by virtually all measurements being limited to this rapidity range due to the detector designs of ATLAS and CMS. The truth jets are defined as anti-k_t jets with radius parameter 0.4 and a minimum p_{T} of 30 GeV while the τ-leptons are defined as the sum of their decay products [45]. A detailed overview of all object definitions is given in Reference [45].

The STXS bins are defined in stages that reflect the increase of available statistics in the measurements. Practically, this means that the first stage targets the inclusive Higgs production modes. With the complete Run II dataset being used for the $H \rightarrow \tau\tau$ measurement in this thesis, the more detailed

[2] The rapidity is defined as $y = \frac{1}{2} \ln \frac{E+p_z}{E-p_z}$.

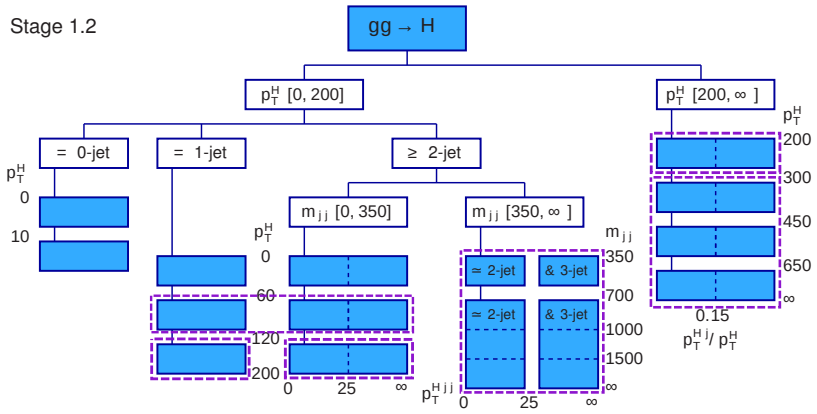

(a) Gluon-gluon fusion bins.

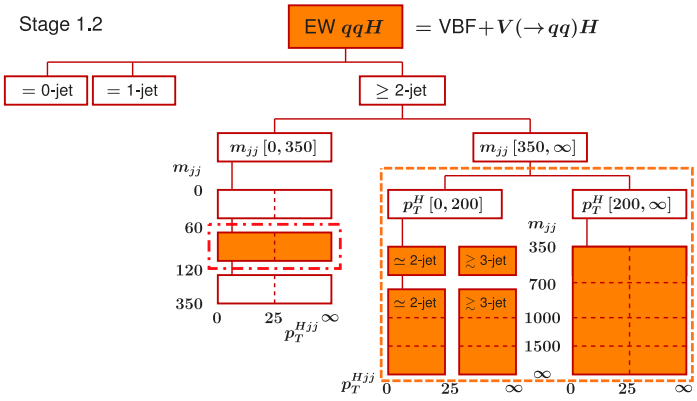

(b) Electroweak production bins. The bins grouped with the dashed line target VBFH production while the bin highlighted with the dashed and pointed line targets VH production.

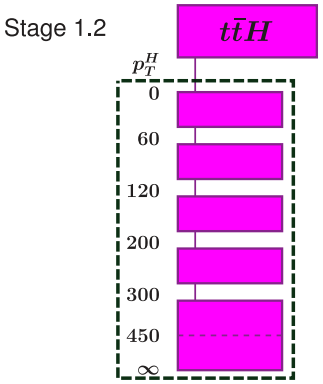

(c) $t\bar{t}H$ bins.

Figure 5.2: Overview of the STXS stage 1.2 bins. Taken from Reference [129] and modified to highlight the targeted bins in the $H \rightarrow \tau\tau$ measurement presented in this thesis.

STXS stage 1.2 is targeted. An overview of the STXS stage 1.2 bins is shown in Figure 5.2. However, due to still limited statistics some STXS bins have to be merged in the measurement and others cannot be measured at all. The limited statistics are a consequence of analysis specific selection criteria needed either for technical reasons, such as trigger requirements, or to enhance the signal to background ratio. Two STXS bins that are not included in the $H \rightarrow \tau\tau$ measurement are the 0-jet category and the low p_{T}(H) regime of the ggH production. The 0-jet category cannot be measured due to a jet requirement in the $\tau_{\mathrm{had}}\tau_{\mathrm{had}}$ channel as explained in Section 5.2. In the targeted topology of $H \rightarrow \tau\tau$ events, the low p_{T}(H) regime of 0 GeV $< p_{\mathrm{T}}$(H) $<$ 60 GeV is dominated by backgrounds and, thus, not included in the measurement. All remaining ggH STXS bins are included, albeit some bins are being merged and, therefore, correlated in the fit. Due to the limited sensitivity to the bins covering 60 GeV $< p_{\mathrm{T}}$(H) $<$ 120 GeV in the measurement, the corresponding STXS bins with one additional and more than one additional jet are merged [8]. The bin with $m_{jj} \geq 350$ GeV is used to control and measure the ggH contamination in VBFH like topologies because of the similar signatures [130].

The associated production of a Higgs boson with a vector boson is treated separately for cases

where the vector boson decays into leptons and for cases where it decays into hadrons. Hadronic decays are grouped together with VBFH production since both involve the same final state particles and interactions and can thus be interpreted as the t- and s-channel of the same process [130]. This production mode is called electroweak production and is shown in Figure 5.2(b). The STXS bin requiring $m_{jj} > 350\,\text{GeV}$ corresponds to the VBFH production while the hadronic VH production ($V(\text{had})H$) is targeted by the $60\,\text{GeV} < m_{jj} < 120\,\text{GeV}$ bin. The hadronically decaying vector boson motivates the m_{jj} cut of the VH bin. Leptonic VH production is grouped into a separate STXS category and is not discussed or targeted by this measurement as it is part of a separate analysis, see Reference [131]. This separate analysis targets decays of the vector bosons into electrons and muons in a similar setting to this measurement, i.e. the decay of the Higgs boson into two τ-leptons. Hence, VH will be used analogously to $V(\text{had})H$ in the following.

The final production mode targeted by this measurement is the $t\bar{t}H$ production that is shown in Figure 5.2(c). Due to limited statistics and, thus, sensitivity, all STXS bins are merged into a single bin for this category. The measurement only considers fully hadronic top quark decays. Other decays that include leptons are covered by a dedicated measurement, see References [132, 133]. With the presented merging scheme, overall nine individual STXS bins are measured, motivating the number of parameters of interest discussed in Section 6.2.

5.2 Event Selection

Motivated by the variety of final states of the di-τ decay channels and the Higgs production modes that are measured, a complex selection is applied to the data and simulated events. The following summary of this selection is based on Reference [8]. First, the data have to be recorded by ATLAS and, thus, suitable triggers have to be applied as explained in Section 3.2.2. The channels involving leptonically decaying τ-leptons, i.e. $\tau_e\tau_\mu$ and $\tau_{\text{lep}}\tau_{\text{had}}$, use lepton triggers because of their clean signature. It has to be noted that in the fully leptonic di-τ decay channel only events with different flavoured leptonic final states are considered. This means that one τ-lepton has to decay into an electron while the other decays into a muon. The other decays where τ-leptons decay into the same lepton flavour are not considered since the accompanying background predictions are subject to large uncertainties [8]. For the fully hadronic channel the di-τ trigger is used. An additional jet requirement [134] had to be included in the di-τ trigger in 2016 already in order to reduce the overall amount of triggered events due to the increase in instantaneous luminosity. All utilised triggers are unprescaled, i.e. all triggered events are recorded and, thus, no scaling of the recorded events is needed.[3] The unprescaled triggers with the lowest p_{T} requirements on the triggered objects for the individual data taking years of Run II are listed in References [134–137]. Detailed descriptions of the electron and muon triggers are given in References [138, 139]. In order to operate in the trigger efficiency plateau, the cuts of the fully reconstructed objects have to be set slightly harder than the cuts applied during triggering. Due to differences in the reconstruction algorithms used for the triggers and the final physics objects, the trigger efficiency is not a step function with respect to the triggered observable. This turn-on region is usually more difficult to model and associated with larger systematic uncertainties as shown for the τ-lepton trigger in Reference [78]. The final p_{T} cuts applied to the reconstructed objects are listed in Table 5.1.

[3] Prescales can be used to further reduce the rate of triggers with signatures that occur at a high frequency. Not all triggered events would be recorded and the recorded events would have to be scaled to match the number of triggered events.

Trigger signature	Data period	p_{T} threshold used in event selection
Single electron	2015	p_{T} (e) > 25 GeV
	2016-2018	p_{T} (e) > 27 GeV
Single muon	2015	p_{T} (μ) > 21 GeV
	2016-2018	p_{T} (μ) > 27.3 GeV
Electron-muon	2015-2018	p_{T} (e) > 18, p_{T} (μ) > 14.7 GeV
Ditau	2015-2018	p_{T} (leading $\tau_{\text{had-vis}}$) > 40 GeV p_{T} (sub-leading $\tau_{\text{had-vis}}$) > 30 GeV

Table 5.1: Signatures of the applied triggers with their corresponding data taking period dependent transverse momentum thresholds. Taken from Reference [8].

Further cuts are applied to the triggered events to select a phase space that is close to where the Higgs signal is located. These cuts include categorisation cuts such as the number of leptons and hadronic τ-leptons in an event that define the decay channels of the measurement. Quality criteria assure that the counted objects are likely to originate from the associated physics object. Electrons are required to pass the "Loose" identification criteria, have a transverse momentum of at least 15 GeV and lie within $|\eta| < 2.47$, excluding $1.37 < |\eta| < 1.52$ [8]. Similar cuts are applied to muons that are reconstructed as combined muons, c.f. Section 3.3.2, and have to pass the respective "Loose" identification criteria as well as having $p_{\mathrm{T}} > 10$ GeV and lie within $|\eta| < 2.47$ [8]. Lastly, τ_{had} are required to have one or three associated tracks, motivated by the most common decays discussed in Section 2.3, an overall charge of one as well as a transverse momentum of $p_{\mathrm{T}} > 20$ GeV and lie within the same η-regions as electrons [8]. Additionally, cuts on BDTs and RNNs are applied to veto muons, electrons and jets that are misreconstructed as τ_{had} [8]. The angular requirements are motivated by the detector geometry where the ECal covers $|\eta| < 2.47$ with high granularity and the excluded region $1.37 < |\eta| < 1.52$ is the transition region between the barrel and endcap calorimeters [8].

Additional cuts aim to reduce the backgrounds in the signal enriched phase space regions, or signal regions (SRs). An overview of this set of cuts is shown in Table 5.2. Some of the object quality criteria, such as the identification measures introduced in Section 3.3, are tightened while additional cuts are motivated by the physics signatures expected of the signal. The listed p_{T} requirements on the τ-leptons are given by the aforementioned trigger choices, see Table 5.1. Motivated by the neutrinos in the τ-lepton decays, a cut is applied on the missing transverse momentum $E_{\mathrm{T}}^{\mathrm{miss}} > 20$ GeV. Since the signal, the Higgs boson, is an electrically neutral particle, the τ-lepton decay products have to be oppositely charged. At least one additional jet is required due to the targeted STXS bins, see Section 5.1, where the transverse momentum cut is higher in the $\tau_{\mathrm{had}}\tau_{\mathrm{had}}$ channel because of the jet in the trigger. Kinematic cuts on invariant mass estimates, such as the visible mass $m_{e\mu}$, the collinear mass $m_{\tau\tau}^{\mathrm{coll}}$ and the transverse mass m_T, aim to reduce backgrounds originating from other processes like W + jets. Vetoing b-quark initiated jets serves two purposes: where the 85 % efficiency working point is chosen for di-τ decay channel involving leptonic decays and the 70 % working point for the

	$\tau_e\tau_\mu$	$\tau_{\text{lep}}\tau_{\text{had}}$		$\tau_{\text{had}}\tau_{\text{had}}$
		$\tau_e\tau_{\text{had}}$	$\tau_\mu\tau_{\text{had}}$	
N(e)	1	1	0	0
N(μ)	1	0	1	0
N($\tau_{\text{had-vis}}$)	0	1	1	2
e p_{T} cut [GeV]	27, 15, 18	27		
μ p_{T} cut [GeV]	10, 27.3, 14.7		27.3	
$\tau_{\text{had-vis}}$ p_{T} cut [GeV]		30		40, 30
Identification	e/μ: Medium	$e/\mu/\tau_{\text{had-vis}}$: Medium		$\tau_{\text{had-vis}}$: Medium
Isolation	e: Loose μ: Tight	e: Loose	μ: Tight	
Charge	Opposite charge	Opposite charge		Opposite charge
Kinematics	$m_{\tau\tau}^{\text{coll}} > m_Z - 25\,\text{GeV}$ $30\,\text{GeV} < m_{e\mu} < 100\,\text{GeV}$	$m_T < 70\,\text{GeV}$		
b-veto	# of b-jets = 0	# of b-jets = 0		# of b-jets = 0 (≥ 1 or 2 in ttH categories)
$E_{\text{T}}^{\text{miss}}$	$E_{\text{T}}^{\text{miss}} > 20\,\text{GeV}$	$E_{\text{T}}^{\text{miss}} > 20\,\text{GeV}$		$E_{\text{T}}^{\text{miss}} > 20\,\text{GeV}$
Leading jet	$p_{\text{T}} > 40\,\text{GeV}$	$p_{\text{T}} > 40\,\text{GeV}$		$p_{\text{T}} > 70\,\text{GeV}$, $\lvert\eta\rvert < 3.2$
Angular	$\Delta R_{e\mu} < 2.0$ $\lvert\Delta\eta_{e\mu}\rvert < 1.5$	$\Delta R_{\ell\,\tau_{\text{had-vis}}} < 2.5$ $\lvert\Delta\eta_{\ell\,\tau_{\text{had-vis}}}\rvert < 1.5$		$0.6 < \Delta R_{\tau_{\text{had-vis}}\,\tau_{\text{had-vis}}} < 2.5$ $\lvert\Delta\eta_{\tau_{\text{had-vis}}\,\tau_{\text{had-vis}}}\rvert < 1.5$
Coll. app. x_1/x_2	$0.1 < x_1 < 1.0$ $0.1 < x_2 < 1.0$	$0.1 < x_1 < 1.4$ $0.1 < x_2 < 1.2$		$0.1 < x_1 < 1.4$ $0.1 < x_2 < 1.4$

Table 5.2: Event selection for all di-τ channels in the measurement. The transverse momentum cuts are driven by the trigger signatures listed in Table 5.1 while the other cuts aim to reduce background contributions and/or improve the mass reconstruction. Descriptions of the observables are given in the text. Taken from Reference [8].

$\tau_{\text{had}}\tau_{\text{had}}$ channel. For one, this cut helps to reduce the Top background[4] since top quark decays almost always involve b-quarks, see Reference [25], and it ensures orthogonality with respect to the $t\bar{t}H$ signal regions that do contain top quark decays. Angular cuts on $|\Delta\eta|$ and ΔR are implemented to reject backgrounds. Due to the τ-lepton's boost from the Higgs boson decay, they are less likely to be emitted back-to-back. A lower bound on ΔR in the $\tau_{\text{had}}\tau_{\text{had}}$ channel ensures that the triggered objects do not overlap. Finally, cuts on the visible momentum fractions x_1 and x_2, that have been introduced in Equation 4.4 in Section 4.1.2, are applied to improve the mass reconstruction.

Based on this selection, ensuring the quality of the objects and rejecting backgrounds, a further categorisation targeting the individual Higgs production modes, and, ultimately, the STXS bins discussed earlier, is introduced. Since the fully hadronic $t\bar{t}H$ production involves multiple jets and the decay of top quarks, this signature is utilised in the selection. It has to be noted that, in contrast to the other production modes, the $t\bar{t}H$ production is only measured in the fully hadronic di-τ decay channel. The number of required jets for this production mode helps to reduce backgrounds. Thus, the $b\bar{b}H$ production is not explicitly targeted by this measurement as the smaller number of jets results in larger background contributions. Characteristic for the VBFH production are two jets with a large rapidity gap, and, thus, high invariant mass, that originate from the hard scattered quarks. The $V(\text{had})H$ topology is characterised by the hadronically decaying vector boson. For all of these categories multivariate techniques, to be more precise boosted decision trees, are implemented to either enhance the signal over background ratio or the purity of the targeted Higgs production mode. An overview of the used variables is shown in Table C.1 in Appendix C.1. The ttH tagger treats $t\bar{t}H$ production as signal[5] and $Z \to \tau\tau$ and $t\bar{t}$ as background in two separate taggers. The VBF tagger treats VBFH production as signal and ggH production and $Z \to \tau\tau$ as backgrounds. Similarly, the VH tagger treats VH production as signal and all other Higgs production modes as backgrounds [8]. All taggers are used to split events into categories of higher purity (with suffix _1) while the other events are kept in categories of lower purity (with suffix _0) which enhances the overall sensitivity in the measurement. The lower purity regions are typically populated with more events and help to constrain background related uncertainties in phase regions close to the higher purity signal regions.

$N_{\text{jets}}(p_T > 30\,\text{GeV})$	p_T(H) bins in GeV			
	[100, 120]	[120, 200]	[200, 300]	[300, ∞[
Exactly 1	boost_0_1J	boost_1_1J	boost_2	boost_3
At least 2	boost_0_ge2J	boost_1_ge2J		

Table 5.3: Definition of the boosted categories following the definition of the targeted STXS bins. Taken from Reference [8].

Events that fail to be classified into one of these categories are collected in the boost category if $p_T(\text{H}) > 100\,\text{GeV}$ is fulfilled.[6] This category targets ggH production and is further split according to the targeted STXS bins. The individual boosted categories are listed in Table 5.3. The lowest

[4] The Top background comprises single top quark and $t\bar{t}$ production.

[5] Other production modes show minor contributions as is due to the jet requirements of the category.

[6] The transverse momentum of the reconstructed Higgs boson $p_T(\text{H})$ is defined by the vectorial sum of the visible τ-leptons and E_T^{miss}.

p_{T}(H) bins have a lower boundary of 100 GeV instead of 60 GeV as they do in the STXS definition. This is motivated by the boost requirement of the category to suppress background. Overall, this categorisation results in 32 signal regions: two signal regions targeting $t\bar{t}H$ production, six signal regions targeting VBFH production, six signal regions targeting VH production and 18 signal regions targeting ggH production.

The final categories in combination with with the categorisation cuts are shown in Figure 5.3. It also highlights which reconstructed event category or region corresponds to which STXS bin. No dedicated analysis region for the high m_{jj} ggH STXS bin is defined as its main purpose is to control the ggH contamination in the VBFH bins. The expected signal yields per category and the purity of the targeted STXS signal processes per category are shown in Figure 5.4. Especially for the VBFH and V(had)H categories, the effect of the taggers is clearly noticeable in the high purity regions.

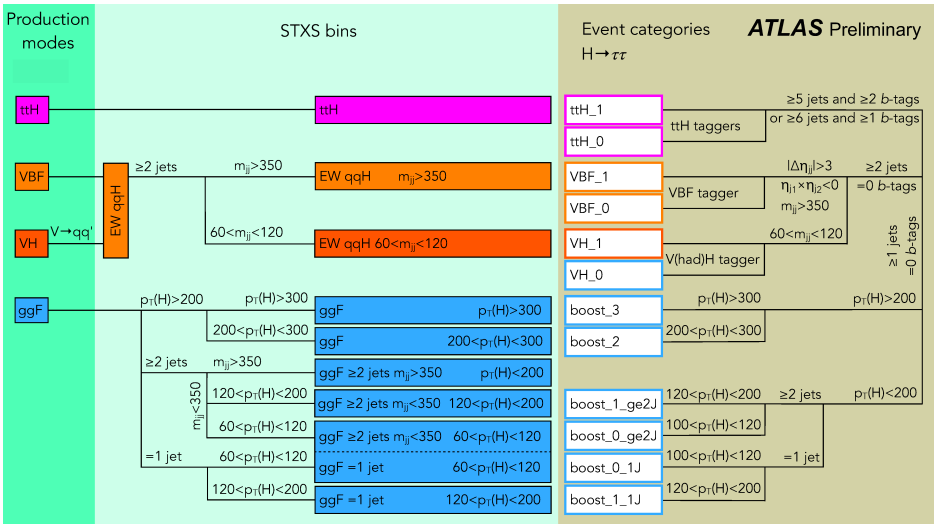

Figure 5.3: Matching of truth level STXS bins to reconstructed analysis regions. Taken from Reference [8] and modified to only show the relevant information.

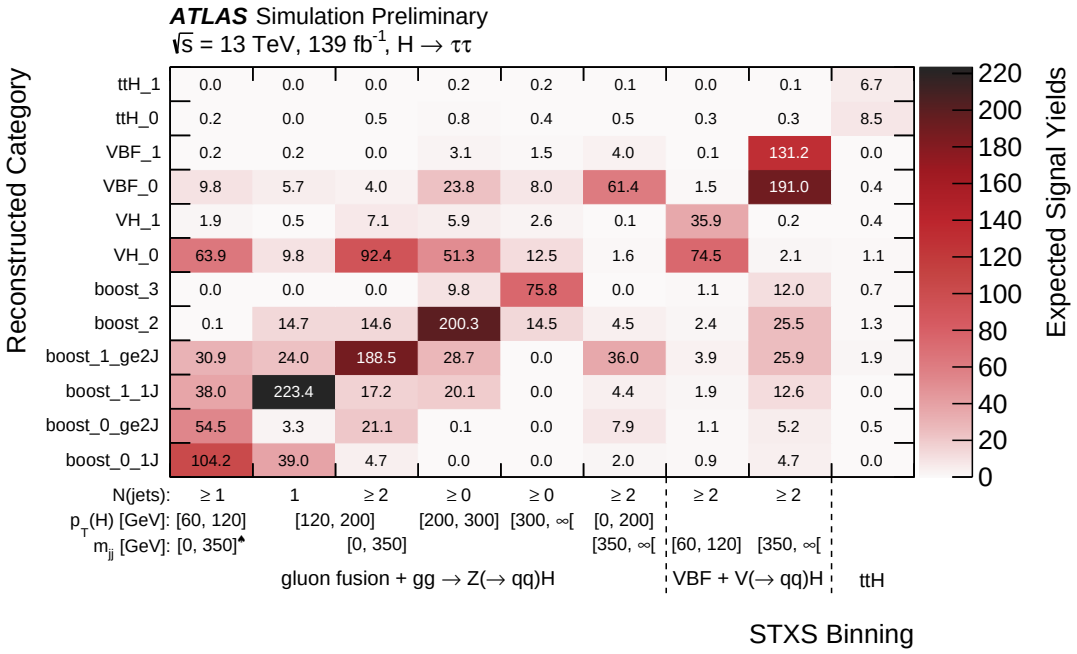

(a)

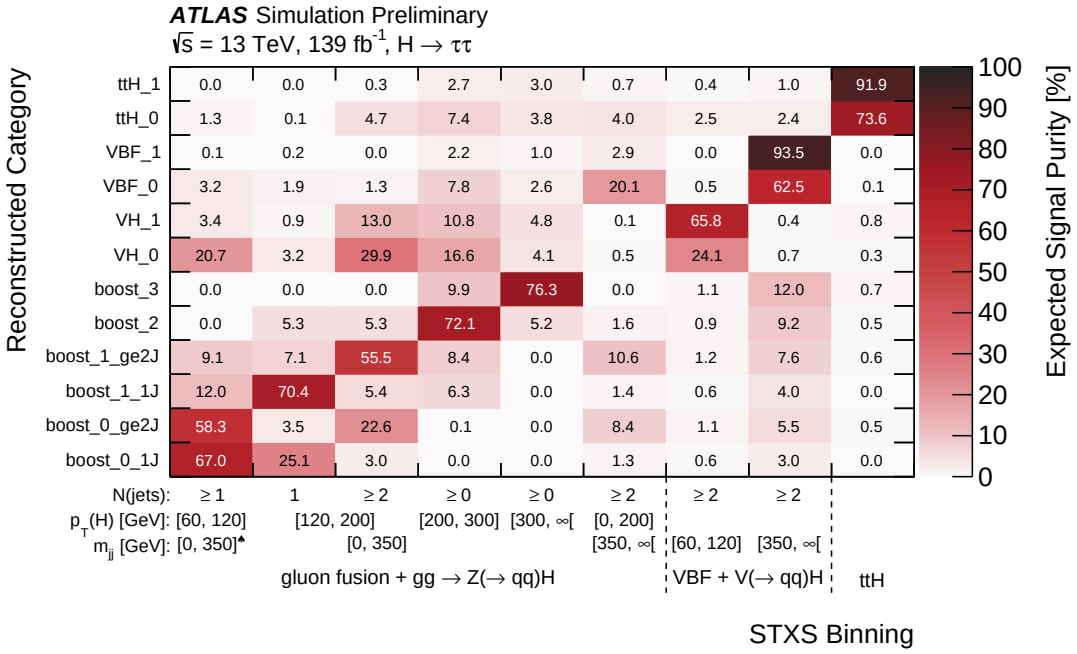

(b)

Figure 5.4: Overall yield (a) and relative contribution (b) of the Higgs signal in the STXS bins to the reconstructed signal regions. The spades symbol ♠ specifies that the m_{jj} cut in the STXS classification is only applied to events with more than one jet. Taken from Reference [8].

5.3 Background Processes

Depending on the di-τ decay channel and the phase space region, different backgrounds are important for the measurement. The relative event composition in all signal regions is shown in Figure 5.5.

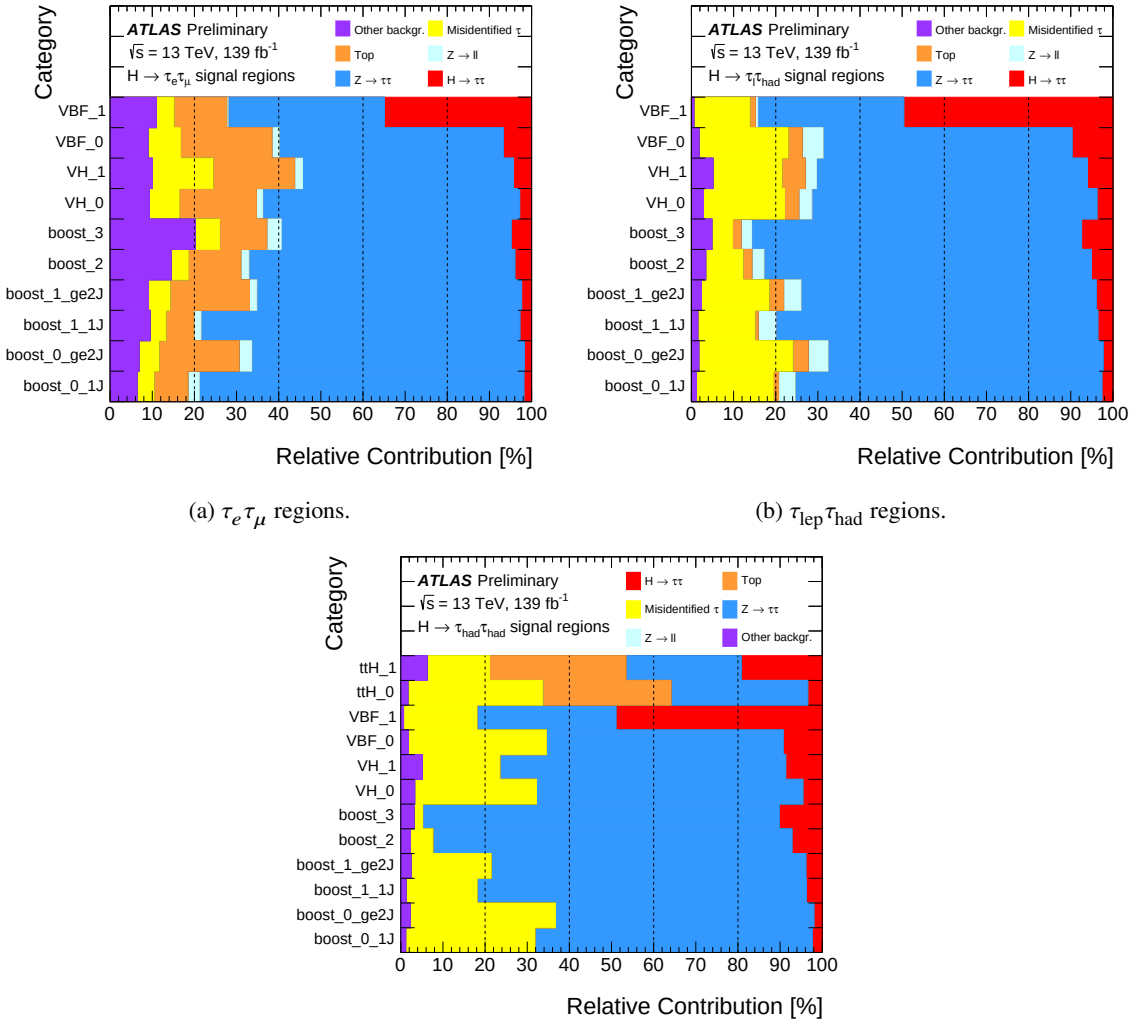

(a) $\tau_e\tau_\mu$ regions.

(b) $\tau_{\text{lep}}\tau_{\text{had}}$ regions.

(c) $\tau_{\text{had}}\tau_{\text{had}}$ regions.

Figure 5.5: Event composition in all signal regions. A mass cut of 100 GeV $< m_{\tau\tau}^{\text{MMC}} <$ 150 GeV is applied. Taken from Reference [8].

The most abundant und thus overall most important background is $Z \to \tau\tau$, or, more precisely, $Z(\to \tau\tau)$ + jets, events. Kinematically, $Z \to \tau\tau$ events are very similar to $H \to \tau\tau$ events since both involve two real τ-leptons. Signatures like the two characteristic jets in VBFH production, but also other signal-like signatures, can likewise occur for $Z \to \tau\tau$ processes. In the signal regions these events are estimated using simulated samples, see Table 3.1, that are validated and cross normalised to control regions. The concepts behind these specific control regions will be discussed in Section 5.3.2.

The next background in order of abundance are misidentified τ-leptons, or Fakes, which include misidentified τ_{lep} and τ_{had}. Different processes with at least one jet that is misidentified as an electron, muon or τ_{had}, dependng on the τ-lepton final state, are collected in this category. All di-τ channels implement data driven techniques to estimate this type of background. More details will be given in Section 5.3.1.

The contribution of other backgrounds strongly depends on the di-τ channel and the phase space of the signal region. Taking the Top background as an example, it shows major contributions to the $\tau_e\tau_\mu$ channel and the signal regions targeting $t\bar{t}H$ production. The b-jet veto applied to all regions, except for the ttH signal regions, are efficient in suppressing the Top background, especially in the channels involving hadronic τ-leptons. Control regions are defined for the $\tau_e\tau_\mu$ and $\tau_{\text{lep}}\tau_{\text{had}}$ channel requiring at least one b-jet. These regions are included in the fit to control the normalisation of the Top background.

Other smaller backgrounds are di-boson processes, $t\bar{t}+V$ and $H \rightarrow WW^*$ which are grouped together in "Other backgrounds". All of them are estimated using MC and fixed to their SM prediction. Similarly, the $Z \rightarrow \ell\ell$ process is estimated from MC and fixed to its SM prediction. While the normalisation of these processes is in principal fixed, it can still be varied via systematic uncertainties. Mismeasurements of $E_{\text{T}}^{\text{miss}}$ are required in $Z(\rightarrow \ell\ell)$ + jets events to pass the event selection due to the lack of neutrinos. Its contribution to the $\tau_{\text{lep}}\tau_{\text{had}}$ channel is sizeable due to the misidentification of an electron as a hadronic τ-lepton in $Z(\rightarrow ee)$ + jets events.

5.3.1 Misidentified τ-leptons

Misidentified τ-leptons are estimated via two different data driven techniques depending on the di-τ decay channel. In case of the $\tau_e\tau_\mu$ channel the matrix method [140] is applied. It estimates the number of misidentified leptons passing the signal region selection from the total number of loose leptons, tight leptons and efficiencies of real and misidentified (fake) leptons: [140]

$$N_{\text{f}}^{\text{t}} = \frac{\epsilon_{\text{f}}}{\epsilon_{\text{r}} - \epsilon_{\text{f}}}(\epsilon_{\text{r}} N^{\text{l}} - N^{\text{t}}) \,.$$

The selection for tight leptons is the one defined in Table 5.2 and the loose selection removes the lepton isolation criteria and for electrons it additionally loosens the identification working point [8]. For two leptons this equations becomes a matrix and the total number of misidentified τ-leptons is given by the sum of events with two misidentified leptons and events where either lepton is faked. Dedicated control regions are used to calculate the efficiencies for electrons and muons separately. Furthermore, the efficiencies are parameterised as a function of the lepton p_{T} and η [8]. Monte Carlo simulation is used to calculate the real efficiencies and data with subtracted simulated contributions from real leptons are used for the fake efficiencies.

The other two di-τ decay channels utilise the fake factors [141] approach. For the $\tau_{\text{lep}}\tau_{\text{had}}$ and $\tau_{\text{had}}\tau_{\text{had}}$ channels the major contribution to the misidentified τ-lepton background stems from jets that are misidentified as hadronic τ-lepton decays. Similarly to the matrix method, data events enriched in misidentified τ-leptons are selected by inverting the hadronic τ-lepton identification criteria, and weighted to construct the misidentified τ-lepton templates in the signal regions. The distinct feature of this method is the acknowledgement of possible differences in these templates depending on whether they originate from gluons or quarks being misidentified as τ-leptons. Thus, the weights, or fake factors, are extracted from two sets of control regions, one enriched in gluon initiated jets that is a

multijet (QCD) region, and one enriched in quark initiated jets that is a W + jets region. A weighting is applied to the fake factors to account for the different quark and gluon composition in the signal regions.

In the fully hadronic di-τ decay channel the method is modified to account for the fact that up to two jets can be mistaken as τ-leptons. The fake factors are calculated in a W + jets control region, similar to the one in the $\tau_{\text{lep}}\tau_{\text{had}}$ channel. This control region is split further into a region where the $\tau_{\text{had-vis}}$ identification is inverted and another one with inverted identification and a lower identification boundary. The combination of these fake factors yields the final misidentified τ-lepton estimate accounting for events where both τ_{had} are faked by jets and events where either τ_{had} is faked. Alternative fake factors, extracted from regions with different quark-gluon fractions, are used to estimate a composition uncertainty.

Dedicated control regions are used to validate the modelling of the individual methods, see Figure 5.6. The observed modelling of the data in these control regions is reasonably well, considering the statistical limitations of the overall yields.

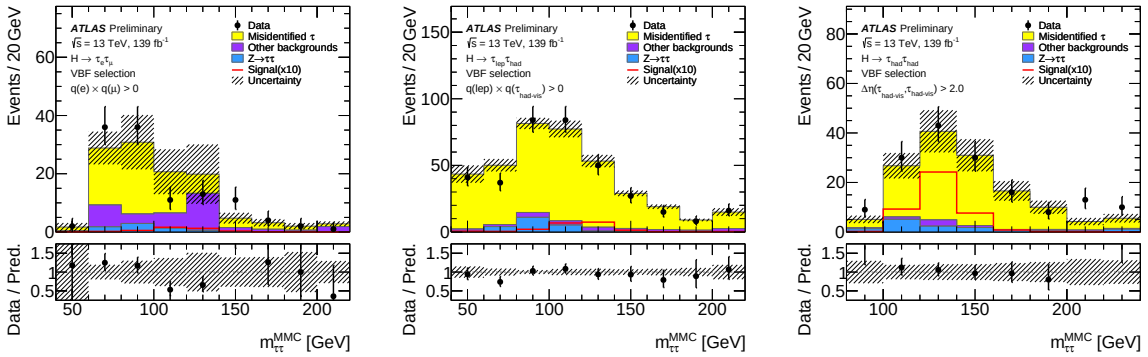

(a) Misidentified τ-lepton enriched $\tau_e\tau_\mu$ region.

(b) Misidentified τ-lepton enriched $\tau_{\text{lep}}\tau_{\text{had}}$ region.

(c) Misidentified τ-lepton enriched $\tau_{\text{had}}\tau_{\text{had}}$ region.

Figure 5.6: Misidentified τ-lepton enriched regions for all di-τ channels showing the modelling of the respective data driven misidentified τ-lepton estimation technique. Taken from Reference [8].

5.3.2 Validating $Z \to \tau\tau$ through $Z \to \ell\ell$ Events

Being the background with the highest contribution to the signal regions, a very good understanding of the $Z(\to \tau\tau)$ + jets process is necessary for a precise $H \to \tau\tau$ measurement. The $Z \to \tau\tau$ background in the SRs is modelled using Monte Carlo samples. It can be validated, however, with a simplified embedding [8]. This method should not be confused with the embedding procedures implemented in References [142–144]. The original embedding replaces detector signatures of leptons in $Z \to \ell\ell$ events selected in data with simulated τ_{had} signatures and re-runs all reconstruction algorithms. In the simplified embedding approach $Z \to \ell\ell$ events are selected and the lepton p_{T} is rescaled to match the spectrum of τ-leptons decays with a subsequent recalculation of all event quantities. Weights accounting for the kinematic differences between the prompt leptons and τ-leptons as well as normalisation differences due to e.g. triggers are derived from simulation. These weights are parameterised in terms of the p_{T} and η of the τ-lepton before its decay [8]. Since the leptons

originating from leptonic τ-lepton decays are non-prompt, weights have to be calculated for them as well. The reweighted p_{T} distribution is shown in Figure 5.7 exemplatory for hadronic τ-leptons. It also shows the recalculated $E_{\mathrm{T}}^{\mathrm{miss}}$ distribution after the reweighting. For both observables a good agreement between $Z \to \tau\tau$ and reweighted $Z \to \ell\ell$ events is observed.

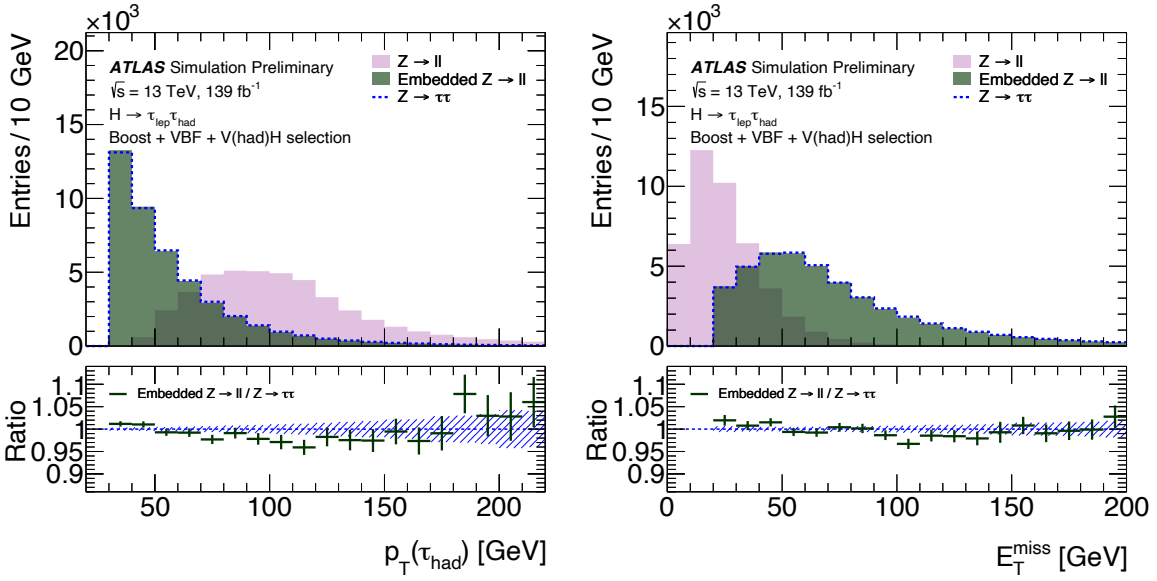

(a) (b)

Figure 5.7: Original lepton p_{T} (a) and $E_{\mathrm{T}}^{\mathrm{miss}}$ (b) spectrum in $Z \to \ell\ell$ events as well as after reweighting to match the spectra of $Z \to \tau\tau$ events. The ratio after reweighting with respect to $Z \to \tau\tau$ is shown. Taken from Reference [8].

This method allows to mimic $Z \to \tau\tau$ kinematics using $Z \to \ell\ell$ events. Thus, high statistics $Z \to \ell\ell$ control regions are defined that are used to validate the modelling of the $Z \to \tau\tau$ background and additionally control the $Z \to \tau\tau$ normalisation in the fit as control regions with one bin, see Section 6.2. In the control regions, the method is applied to data and all contributing simulated processes which, apart from $Z \to \ell\ell$, are mainly smaller contributions from Top and di-boson processes. The modelling of some key variables after the simplified embedding procedure is shown in Figure 5.8. The shown variables are either used to classify events in the event selection or as input to at least one of the taggers, see Table C.1. Since the $\tau_{\mathrm{lep}}\tau_{\mathrm{had}}$ channel includes one leptonically and one hadronically decaying τ-lepton and, thus, both embedding weight parameterisations are important for the corresponding embedded regions, the examples have been chosen to show these regions. While the overall modelling is satisfactory, the slope observed for m_{jj} is consistent with results from dedicated Z + jets measurements, see References [145, 146].

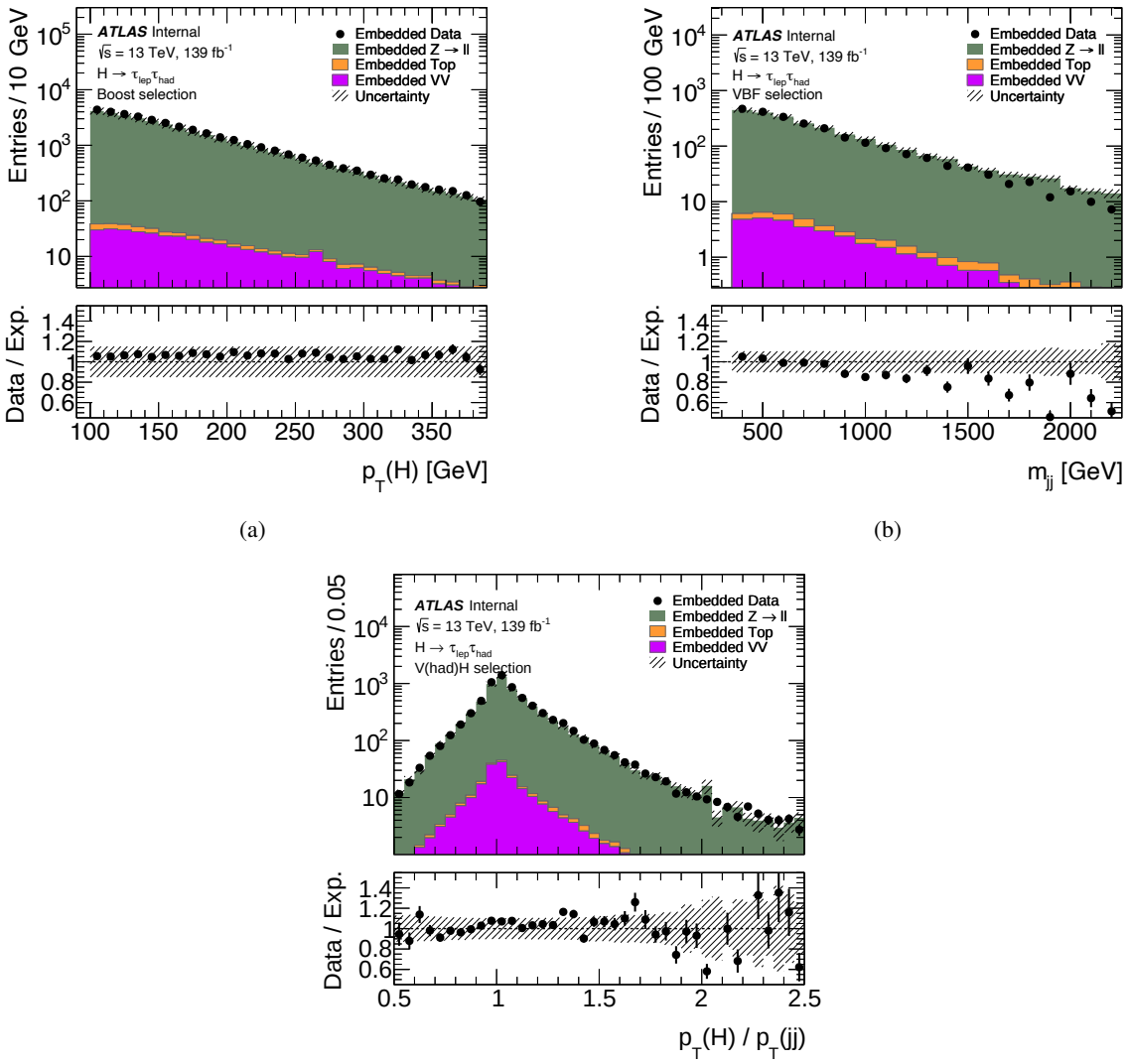

(a) (b)

(c)

Figure 5.8: Modelling of key event variables with the simplified embedding technique. Taken from Reference [8].

5.4 Systematic Uncertainties

Apart from statistical uncertainties on the collected data, systematic uncertainties play a major role in every measurement. They represent the level to which different aspects of the predictions and reconstruction methods are known. Most of the uncertainties vary the normalisation of a process through variations of the considered quantity, e.g. the $\tau_{\text{had-vis}}$ energy corrections, but also the shape is subject to variations. These shape variations on the observable $m_{\tau\tau}^{\text{MMC}}$ can arise from the normalisation variations being binned in e.g. $p_{\text{T},\tau}$. Usually, these two effects are treated as fully correlated. The magnitude of the normalisation variations for the most important experimental uncertainties is shown in Table 5.4 for the individual di-τ decay channels. Other uncertainties include identification, trigger and energy scale variations of electrons and muons. Short descriptions of how these uncertainties are determined can be found in Section 3.3 and its cited references. In the final fit model some uncertainties are split into multiple components with respect to the table. The luminosity uncertainty only applies to processes that are normalised by theory, i.e. to their cross-sections, and not to processes whose normalisation is determined in the fit as described in Section 6.2.

Source of uncertainty	Relative size		
	$\tau_e\tau_\mu$	$\tau_{\text{lep}}\tau_{\text{had}}$	$\tau_{\text{had}}\tau_{\text{had}}$
Luminosity	1.7%		
$E_{\text{T}}^{\text{miss}}$ scale	10 – 20% [80]		
$E_{\text{T}}^{\text{miss}}$ resolution	5 – 20% [80]		
Jets			
Jet energy scale	1 – 5%		
Jet energy resolution	0.5 – 1.5%		
b-tagging	1 – 8% [73]		
$\tau_{\text{had-vis}}$			
identification		2 – 6% per τ_{had}	
trigger			1 – 1.5%
electron rejection		1 – 2%	
reconstruction efficiency		1.5% per τ_{had}	
energy scale		1 – 4%	
Fake transfer factors			
Stat. unc.	10%	15%	15%
Flavour composition		10%	15%
Jet and b-tag dependencies	35%		
Used process dependencies	15%		5%
Prompt lepton/τ_{had} contamination	15%	10%	

Table 5.4: Overview of the most important experimental uncertainties for all di-τ decay channels. The process dependency uncertainty for misidentified τ-leptons in the $\tau_{\text{had}}\tau_{\text{had}}$ channel arise from a comparison to an alternative set of fake factors extracted from same sign control regions. Numbers are taken from Reference [8] if not stated otherwise.

Theoretical uncertainties on the predictions are considered for both background processes and signal processes, with the details summarised in Reference [8]. These uncertainties are mostly relevant for $t\bar{t}$ and Z + jets as the other processes estimated from MC only show minor contributions. Aspects of the simulations that are related to the description of QCD and Monte Carlo generators, discussed in Sections 2.1.3 and 3.4 respectively, are covered. Generally, this also includes the statistical power of the simulated samples, i.e. the amount of simulated raw events.

For $t\bar{t}$ the uncertainties target the matrix element and parton shower generators. Other aspects covered include the proton PDFs as well as the initial state and final state radiation models [8].

A larger impact on the sensitivity is expected from the variations of the Z + jets process due to its larger contribution. The following uncertainties are included for this process with variations strongly depending on the di-τ final state and the phase space. It should be noted that the numbers are estimated from the inputs that are used in the fit. They cover variations of the renormalisation and factorisation scales (roughly 1 – 19%), variations of the resummation scale (roughly 5 – 15%), variations of α_s (roughly 0.1 – 1.2%), variations of the jet-to-parton matching scheme (roughly 1.2 – 6%) and variations of the proton PDFs (roughly 0.2 – 3.5%).

Uncertainties on the signal predictions follow a similar scheme of variations of the renormalisation and factorisation scales, proton PDFs and α_s. The resulting cross-section variations are summarised in Reference [45]. Additionally, variations arising from the STXS classification, e.g. migrations between STXS bins, are considered. Details on these uncertainties are given in References [8, 45, 147–149].

Finally, the experimental uncertainties are propagated through the simplified embedding technique to assess residual variations between data and simulation in the corresponding control regions. Studies regarding residuals that arise from weight variations are documented in Appendix C.2, showing that no sizeable variations except for one uncertainty source remain. This also emphasises the closure of the method. All other uncertainties that modify whole events like jet variations are propagated through the simplified embedding procedure to the fit. Additionally, the theory uncertainties on Z + jets are also considered in these control regions. Uncertainties of 1% are assigned to the embedded $Z \to \ell\ell$ process in the control regions to account for migration effects originating from mismodelling between $Z \to \ell\ell$ and $Z \to \tau\tau$ [8].

CHAPTER 6

Statistical Analysis

The $H \rightarrow \tau\tau$ couplings measurement presented in this thesis is able to target multiple STXS bins by utilising the full Run II dataset recorded by ATLAS. However, measuring multiple STXS bins entails the categorisation of the events into multiple signal regions as described in Chapter 5. This, in turn, quickly leads to very complex setups to extract the desired information from the data. Typically, these types of measurements are conducted as blind analyses, i.e. the setup should be validated and understood before actual data is being studied, thus avoiding possible (unintended) biases towards certain results.

This chapter will first introduce the basic concepts of the type of fit used to match the theoretical predictions encoded in the simulations to the recorded data. In the process the sought after quantities, i.e. the cross-sections of the targeted STXS bins, are determined. Next, the specific fit model used for the $H \rightarrow \tau\tau$ couplings measurement is introduced. Finally, a few concepts used to validate the fit model and their observations will be discussed.

6.1 Profile Likelihood Fits

The concepts of data analysis in high energy physics are highlighted in a multitude of literature. Some of them are References [150–153] on which this introduction is based on. Generally, the idea is to minimise a measure[1] that quantifies the agreement of simulated events to measured data. This process of minimisation is usually referred to as fitting.

A fit in its simplest form would only be able to vary the normalisation of the signal, thus extracting this information from the data. This example demonstrates that the result of a fit, or, to be more precise, the deduced information, always depends on the presumed fit model. It presumes a perfectly correct prediction of all backgrounds resulting in no degree of freedom in the fit being able to vary the background normalisation nor the shape. If the background prediction would be off by a hypothetical 10%, this difference would be absorbed into the signal normalisation, being the only degree of freedom in the minimisation. This not only shows the importance of the chosen model but also of well-motivated estimates for uncertainties related to different aspects of the measurement. The uncertainties of this measurement introduced in Section 5.4 cover theory predictions, reconstruction

[1] Or maximise a measure depending on its definition. The minimisation will be representative for both cases in the following.

and other object calibration/identification techniques as well as methodological uncertainties such as uncertainties related to the estimation of misidentified τ-leptons.

6.1.1 Likelihood

The measure maximised in the $H \to \tau\tau$ measurement is the likelihood. It assigns probability values to an observed event x based on a model encoded in a probability distribution function (p.d.f.) f:

$$\mathscr{L}(x) = f(x)\,,$$

where the event is considered a random variable. In a more general approach the p.d.f. usually incorporates systematic uncertainties as parameters $\vec{\theta}$, also referred to as nuisance parameters (NPs). Thus, the likelihood becomes dependent on the actual parameter values $\vec{\theta}$. Typically, multiple events N are included in a measurement such that the total likelihood is defined as the product of the individual likelihoods, ultimately leading to the extended likelihood: [153]

$$\mathscr{L}\left(x;\vec{\theta}\right) = \frac{e^{-\mu(\vec{\theta})}\mu(\vec{\theta})^N}{N!}\prod_i^N f(x_i;\vec{\theta})\,.$$

The term in front of the product over the individual events represents a Poisson distribution with mean μ. By including this Poisson distribution in the likelihood the absolute normalisation of the events is taken into account. The fitting procedure of the maximum likelihood estimator tries to find the set of parameter values $\vec{\theta}$ that maximises the likelihood value. Often not the likelihood itself but rather the negative of its logarithm is used for this: [153]

$$-\log\mathscr{L}\left(x;\vec{\theta}\right) = -\log\left(\frac{e^{-\mu(\vec{\theta})}\mu(\vec{\theta})^N}{N!}\right)\sum_i^N \log f(x_i;\vec{\theta})\,. \tag{6.1}$$

The logarithm transforms the product in the likelihood into a sum which is easier to compute numerically. For similar reasons the negative of the likelihood is used, turning the maximisation of the parameter estimation into a minimisation.

In this measurement, events are grouped into bins of histograms instead of using individual events as described in Equation 6.1. Although in principle it would be possible to conduct the measurement on the individual events, this would entail a number of disadvantages. Those range from technical arguments, such as no direct way of visualising the result or estimating the goodness of the fit, to more analysis specific reasons. With the full Run II dataset available for the measurement it becomes more accurate[2] but at the same time a per-event evaluation of the likelihood becomes increasingly computing intense. Additionally, the underlying model has to be encoded in a smooth p.d.f. for a per-event evaluation. This smooth p.d.f. does not only have to be known, analytically or estimated from Monte Carlo, for the "nominal" prediction but also for every systematic variation in the measurement. Both of these arguments make a per-event evaluation for the $H \to \tau\tau$ measurement unfeasible which

[2] At the least the statistical uncertainty is reduced.

is why the data and, thus, the likelihood are binned:

$$-\log \mathscr{L}\left(n_i; \vec{\theta}\right) = -\sum_{i}^{N} \log \frac{e^{-\mu(\vec{\theta})} \mu(\vec{\theta})^{n_i}}{n_i!} \,. \tag{6.2}$$

The binned likelihood replaces the p.d.f. function by a Poisson model of the events and sums over all bins of the histogram n_i. Thus, this representation does not depend on a specific p.d.f. choice any more while also addressing other disadvantages of the per-event evaluation previously discussed. However, the binning choice becomes integral for the sensitivity of the measurement. For a single bin the likelihood is reduced to a counting experiment and, thus, all information in the shapes of the distributions that could possibly distinguish backgrounds and signal are lost. Hence, ideally a binning is chosen that retains features in the distributions, i.e. the bin size should be smaller than the feature size, if the statistical power permits.

6.1.2 Profile Likelihood Ratio

While the estimate of the best fit point, i.e. the point in the parameter space that maximises the likelihood, is based on Equation 6.2 the uncertainty definition of the parameters usually goes a step further. The statistics used to define these uncertainties is the likelihood ratio: [150]

$$\lambda(\mu) = \frac{\mathscr{L}\left(\mu, \hat{\hat{\vec{\theta}}}\right)}{\mathscr{L}\left(\hat{\mu}, \hat{\vec{\theta}}\right)} \,, \tag{6.3}$$

with the parameter of interest in the fit being denoted as μ while the nuisance parameters are $\vec{\theta}$. The result of the unconditional maximum likelihood estimation (MLE), i.e. the fit, is given in the denominator where $\hat{\mu}$ and $\hat{\vec{\theta}}$ are the results of the MLE. The enumerator represents a conditional MLE where μ is fixed and $\hat{\hat{\vec{\theta}}}$ are the parameter values maxisimising the likelihood under this fixed condition. Specific test statistics can be defined based on the statistics $\lambda(\mu)$ that are typically used in measurements searching for new physics signals and if no signal is found to set exclusion limits on e.g. the coupling of the new physics process. Details on these test statistics are given in Reference [150]. Since the signal in this measurement is already well-established there is no need to set exclusion limits. However, the properties of the statistics $\lambda(\mu)$ play an important role in the definition and estimation of the parameter uncertainties.

Based on the asymptotic properties of the statistics $\lambda(\mu)$ two separate approaches of parameter uncertainties are possible. The first approach defines the uncertainty utilising the covariance matrix of all parameters which can be estimated via the second derivative of the likelihood at the best fit point [150]. This, however, assumes a parabolic shape of the likelihood in the parameter space close to its best fit point and by construction yields symmetric uncertainties. Another approach defines the parameter uncertainties via a variation of the negative likelihood by 0.5 around its minimum, see Reference [152] for more details. Although this method is computationally more expensive, it is less dependent on the exact shape of the likelihood and also able to capture asymmetric uncertainties. Thus, the second method, also often referred to as likelihood scan, is used to estimate the uncertainties on the parameters of interest in this measurement.

6.1.3 Nuisance Parameters

So far, systematic uncertainties, or nuisance parameters (NPs), have only been included in a general way in Equation 6.2. Typically, auxiliary measurements are conducted to provide estimates of these uncertainties which are propagated to the fit as priors. This prior in principle can take any functional form but is most often a Gaussian distribution where the width is defined by the auxiliary measurement and the mean is zero for the "nominal" prediction. When validating and studying fit models, a unified representation of possibly different sized NPs is used. In this representation, the "pull" is defined as the difference between the pre-fit and post-fit means of the NP in terms of its pre-fit width.[3] The "constraint" represents the ratio of the pre-fit and post-fit width of the NP.

A special case of NPs are so-called gammas. These parameters account for the statistical uncertainties on simulated samples[4]. Due to the statistical nature of the simulation process, the uncertainty on the number of simulated events is typically modelled with a Poisson distribution. Their name, gammas, originates from the posterior distribution resembling a gamma function due to the choice of a flat prior, see Reference [151].

The parameters of interest (POIs) in a measurement can effectively be interpreted as NPs without a prior. With respect to their definition in the likelihood function they do not stand out in any way in comparison to other prior-less NPs such as normalisation factors (NFs).

The actual implementation of the model uses HistFactory [154] which is based on RooStats [155]. This implementation does not allow to define correlations between individual NPs a priori but rather determines all correlations during the fit. More details on the individual terms in the likelihood are given in Reference [154].

6.2 Fit Model

As the $H \to \tau\tau$ measurement discussed in this thesis is based on the binned likelihood introduced in Equation 6.2, the fit model is not represented by a specific p.d.f. choice but rather by the binned distributions in the regions included in the fit. The regions are motivated by the selection discussed in Section 5.2 with $m_{\tau\tau}^{\text{MMC}}$, introduced in detail in Section 4, being the binned observable in those regions. While the systematic uncertainties have been discussed in Section 5.4, their final implementation in the fit model is often only decided when validating the fit as discussed in the following sections. Finally, it is possible to give the fit degrees of freedom that vary the normalisation of processes without constraint terms as it would be the case for NPs. These degrees of freedom are referred to as normalisation factors (NFs) and are intended to provide the ability to measure a process' normalisation in data. This can become important in corners of phase space where the theory prediction is known to deviate from observations to some extent which may be difficult to capture in the corresponding NPs. Examples of this effect are the deviations observed in the Z + jets process for $p_{\text{T}}^{\ell\ell}$, see Reference [156], and m_{jj}, see Reference [157].

The complete fit model regarding the regions and NF setup is summarised in Figure 6.1 where the signal regions correspond to the event categories that have been shown in Figure 5.3. According to the selection discussed earlier, the $t\bar{t}H$ regions are solely implemented in the $\tau_{\text{had}}\tau_{\text{had}}$ channel while the Top control regions are only implemented in the $\tau_e\tau_\mu$ and $\tau_{\text{lep}}\tau_{\text{had}}$ channels. Generally, the idea of the

[3] The wording mean and width are chosen to illustrate the meaning of the values for a Gaussian prior.

[4] The raw number of simulated events is decisive for this uncertainty, not the normalised prediction.

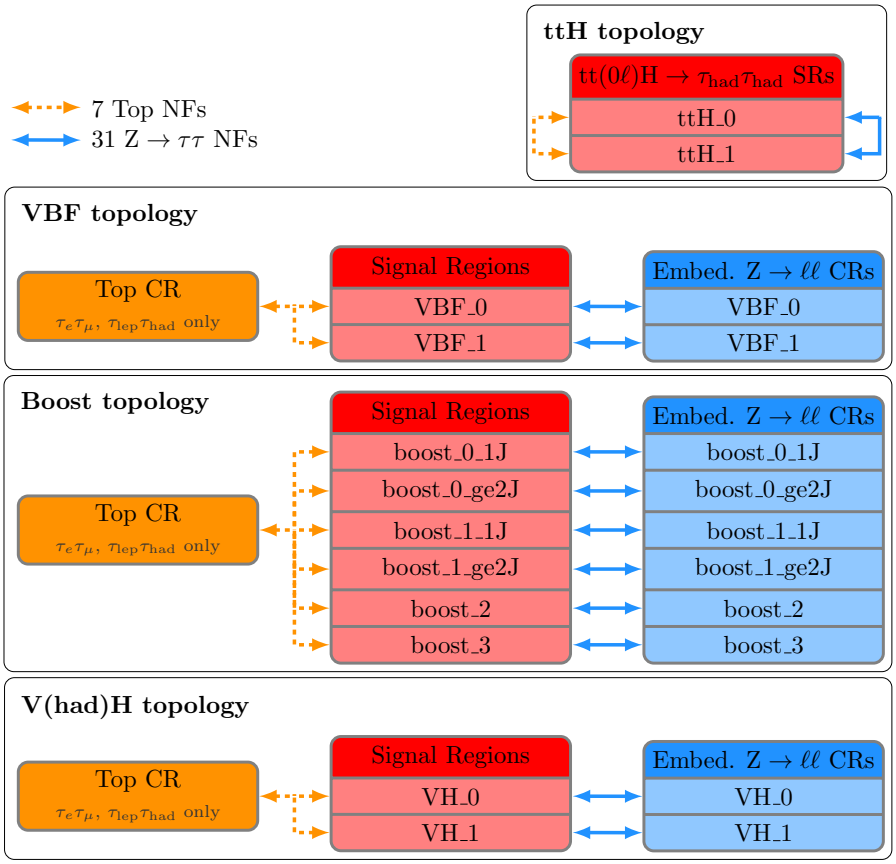

Figure 6.1: Sketch of the fit model depicting the regions in the fit and how they are cross normalised. If not stated otherwise, the region is implemented for the $\tau_e\tau_\mu$, the $\tau_{\text{lep}}\tau_{\text{had}}$ and the $\tau_{\text{had}}\tau_{\text{had}}$ channel. Taken from Reference [8].

model is to measure the normalisation of the dominating backgrounds in dedicated control regions and, thus, in data.

For the Top background this is achieved in topology-inclusive control regions[5]. Since the Top background is negligible in the $\tau_{\text{had}}\tau_{\text{had}}$ channel, except for the $t\bar{t}H$ regions, no dedicated Top control region is defined. Due to its unique signature and, thus, selection, no dedicated control regions for the $t\bar{t}H$ regions are defined but rather the lower purity region ttH_0 with its larger statistics acts as a combination of control region and signal region. With two NFs, one for the $\tau_e\tau_\mu$ channel and one for the $\tau_{\text{lep}}\tau_{\text{had}}$ channel, per inclusive VBFH and VH signal region and one for the $t\bar{t}H$ signal region this setup results in a total of seven NFs for the Top backgrounds.

Thanks to the Z+jets control regions utilising the simplified embedding which yields high statistics regions close to the signal phase space, it is possible to pair each signal region with a corresponding Z+jets control region. This allows to measure the normalisation of the dominant $Z \to \tau\tau$ background per phase space region in data. For the $t\bar{t}H$ regions the $Z \to \tau\tau$ background is again cross normalised between the high purity and low purity region. Overall, this setup leads to 31 NFs for the $Z \to \tau\tau$

[5] This means that the control region is inclusive in e.g. the VBFH phase space and is not split into the final signal categories.

backgrounds, one for each non-$t\bar{t}H$ signal region, see Section 5.2, resulting in a total of 30 NFs and one additional shared NF for both $t\bar{t}H$ signal regions.

Three separate measurements are conducted, differing in their definition of the parameters of interest. For all POI setups the signal templates correspond to the finest granularity STXS templates, i.e. the non-merged bins shown in Figure 5.2. The merging of STXS bins described in Section 5.1 corresponds to the simultaneous measurement of nine POIs. These POIs correlate the STXS templates accordingly and, thus, merge the STXS bins in the measurement. All other bins that are not explicitly part of the measured POIs are fixed to their Standard Model predictions. Another measurement targets the four major inclusive $H \to \tau\tau$ production modes discussed in Section 2.2.3 by further correlating the STXS templates. The final measurement measures the inclusive $H \to \tau\tau$ production cross-section by correlating all STXS templates. It has to be noted that in the more inclusive measurements only the relative sizes of the STXS templates are fixed to the Standard Model prediction. With the current quoted mass of the Higgs boson being $m_H = 125.10 \pm 0.14\,\text{GeV}$ [25] the presented measurement does not provide sensitivity to the mass parameter, given the resolution of the di-τ mass reconstruction, and is thus fixed. The only sensitivity would originate in variations of the predicted production rates and branching ratios which do not vary significantly enough in the quoted uncertainty range to be measureable in this analysis.

6.2.1 Smoothing, Pruning & Symmetrisation

Due to the fit model relying on MC predictions instead of p.d.f.s and those predictions being subject to statistical fluctuations it is important to be aware of this limitation and implement proper treatments. This is achieved by applying dedicated algorithms in multiple individual steps whose details are documented in Reference [158] on which this description is based on. It is important to note that those algorithms should never affect the "nominal" MC predictions but rather solely the systematic variations.

First, a smoothing is applied. Its purpose is to identify fluctuations within the systematic variations that are most likely caused by limited statistics instead of real physical effects. Once those fluctuations are identified, they are alleviated by e.g. weighting according to the systematic variations in the neighbouring bins. Small systematic uncertainties with a total variation of less than 1% are neglected in the fit as they may still be caused by statistical fluctuations and do not represent important degrees of freedom. This threshold applies to normalisation variations, with respect to the total yield, and to shape variations, where it is sufficient if the relative variation in a single bin exceeds the threshold. Finally, some systematic variations are only defined in one direction, e.g. variations arising from the comparison of two Monte Carlo generators. However, within the HistFactory framework, systematic uncertainties have to be provided in the form of two histograms at $\pm 1\sigma$. Thus, these systematic variations are symmetrised when passed to HistFactory to build the final likelihood. The impact of these steps on the final result was verified to be small.

6.2.2 Binning

With the fit model being based on the MC predictions, the binning choice of the histograms used in the fit is essential for a stable and precise measurement. If the bin size chosen is larger than the size of physical features, like the structure of the $Z \to \tau\tau$ peak, vital information that could help increasing the sensitivity to the POIs would be lost. On the other hand, if the bin size is too small,

and, thus, dominated by statistical fluctuations of the MC predictions, the measurement's result would become unstable. Another aspect to consider are variable bin sizes of histograms. Solutions to find estimates of equidistant bin sizes have been given with e.g. Sturge's rule, see Reference [159]. However, it may be beneficial to consider a coarse binning in observable ranges with little physical feature information and a finer binning in ranges with more feature information, e.g. the $Z \to \tau\tau$ peak. Even though HistFactory only supports equidistantly binned histograms, this technical limitation can be circumvented by a transformation from variable bin sizes to an equidistant binning beforehand.[6]

This motivated the implementation of an algorithm designed for this measurement which automatically calculates the binning of all 32 signal regions based on only a few parameters. Its main idea is to merge bins until a certain relative uncertainty per bin is reached and include the systematic variations in this calculation. Since the algorithm is based on histograms, a finely binned input with equidistant 5 GeV bins in $m_{\tau\tau}^{\text{MMC}}$ is used as a starting point. The merging of bins starts on the high edge of the histograms with large $m_{\tau\tau}^{\text{MMC}}$ values and moves to the low edge of the histograms with small $m_{\tau\tau}^{\text{MMC}}$ values. By default bins are merged unless the relative uncertainty of a bin is smaller than a predefined threshold α_{unc}. This threshold is modified based on the previously discussed goals of an appropriate binning. Thus, if the ratio of signal to backgrounds in terms of bin yields becomes larger than a certain additional threshold $\alpha_{\text{S/B}}$, the original threshold α_{unc} is multiplied by a factor f_{mult}. This ensures that physical features of the signal are retained by the binning procedure. Lastly, if the statistical uncertainty of a bin becomes smaller than a threshold α_{stat}, the threshold α_{unc} is multiplied by the same factor f_{mult}. Motivated by the goal to resolve the $Z \to \tau\tau$ peak structure, this condition ensures preservation of the features in bins with high statistics. The procedure is summarised as pseudocode in Algorithm 1.

Algorithm 1 : Pseudocode describing the binning algorithm implemented for the $H \to \tau\tau$ measurement.

```
Data : Histograms of all simulations and systematic variations
Result : Binning for m_ττ^MMC
calculate combined systematic variation;
set α_unc, α_S/B, α_stat and f_mult;
while bin; starting from upper histogram edge do
    if S/B > α_S/B or stat. unc. < α_stat then
        α_unc *= f_mult;
    if rel. tot. unc. < α_unc then
        continue;
    else
        merge;
```

Variations of this algorithm were studied yielding either the same final binning or the loss of all shape information of the $Z \to \tau\tau$ peak in certain phase space regions. One of these variations replaced the ratio of signal to backgrounds by the significance estimate $\frac{S}{\sqrt{S+B}}$. Due to the high overall statistics in most regions this did not result in a different binning output. Another variation specificly targeted the misidentified τ-lepton background and demanded all final bins to contain statistically significant

[6] The actual bin width is irrelevant in the likelihood.

yields of that background, i.e. $\frac{\text{yield}_{\text{Fake}}}{\sqrt{\text{yield}_{\text{Fake}}}} \geq 1$, to reduce the impact of statistical fluctuations on the data driven templates. This condition resulted in an artificial split of bins with statistically significant misidentified τ-lepton contributions next to bins with zero yield. Thus, an additional veto ensuring that all bins in all signal regions contain a non-zero yield of that background was implemented. However, since especially the high p_{T}(H) signal regions contain very few misidentified τ-lepton events, these conditions resulted in the loss of practically all shape information. Similar observations were made when requiring a fraction of 5% of misidentified τ-lepton events in all bins. The impact of bins with zero yields of specific backgrounds was studied in detail, see Appendix D.1.1, and found to be negligible.

With only four parameters, in contrast to arbitrary binning choices in all 32 signal regions, it is possible to scan this four dimensional space for the best parameter combination. The performances of individual parameter combinations are evaluated with Asimov data fits[7] with the goal of increasing the sensitivity to the measurement's POIs. Acknowledging the fact that different Higgs production modes will be measured, the optimisation is based on the setup with four POIs, one for each production mode. The most detailed POI setup measuring the nine STXS bins is not used to simplify the analysis of the results. Since the parameter scan is computationally expensive, the study was conducted with a preliminary fit model and could not be repeated with the final fit model. Main differences of the preliminary model comprise an incomplete nuisance parameter model, with the most most sizeable NPs being included, and a preliminary version of the misidentified τ-lepton estimation. The final parameter set is deduced from the occurance of individual parameter values yielding the highest sensitivities. To calculate the occurance of these values, the combinations resulting in sensitivities within 1% of all POIs' individual best combinations are considered. In principle, different parameter combinations can yield the best sensitivity with respect to each POI. It was verified that the parameter combination obtained by this method at most degrades the sensitivity by 8 permille compared to the best sensitivity per POI. These variations are considered to be of statistical nature in the likelihood minimisation. The parameter combination as well as the impact on the measurement's sensitivity are summarised in Table 6.1. A reference binning inspired by the $H \rightarrow \tau\tau$ measurement conducted in Reference [7] is used to quantity the sensitivity improvements. The $m_{\tau\tau}^{\text{MMC}}$ distribution of one exemplary signal region is shown in Figure 6.2 for the reference binning and the final binning. As intended by the binning algorithm's design, the $Z \rightarrow \tau\tau$ peak and the mass region close to the Higgs signal peak are finely binned as long as the relative uncertainty permits.

Additionally, the robustness of the algorithm was studied via the dependence of the measurement's sensitivity as a function of the individual parameters. This dependence is shown for α_{unc} and the two POIs targeting the ggH and VBFH production modes in Figure 6.3. It shows the uncertainty on the given POI as a function of α_{unc} for the nine best parameter combinations in terms of sensitivity. Generally, the shown parameter combinations tend to evolve towards a common minimum. Other POIs and algorithm parameters are shown in Appendix D.1.2 and confirm this observation with some variations due to statistical fluctuations in the likelihood minimisation.

Finally, bins with large gamma posteriors were merged until the posterior was of the order of 20% in Asimov fits. This precautionary measure was implemented as the interpretation of a bin's yield gets more difficult with larger gammas. In extreme scenarios, very large gammas would be able to absorb localised systematic variations. The effect of this measure was verified to be small. All $m_{\tau\tau}^{\text{MMC}}$ distributions in all signal regions with their final binning are shown in Appendix E.1.

[7] Asimov data are pseudodata exactly matching the MC predictions.

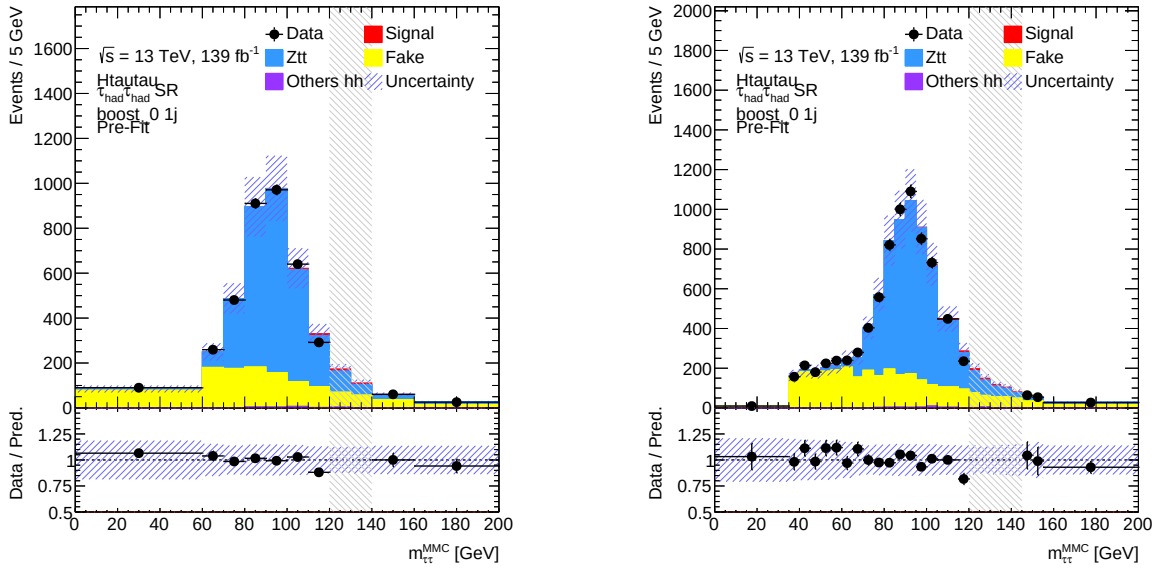

(a) Reference binning.

(b) Final binning.

Figure 6.2: Distribution of $m_{\tau\tau}^{\mathrm{MMC}}$ in the low p_{T}(H) signal region targeting ggH production with no additional jets. The reference binning inspired by the $H \to \tau\tau$ measurement conducted in Reference [7] as well as the final binning used in this measurement are shown. Bins fulfilling the criteria described in Section 6.3.1 are blinded.

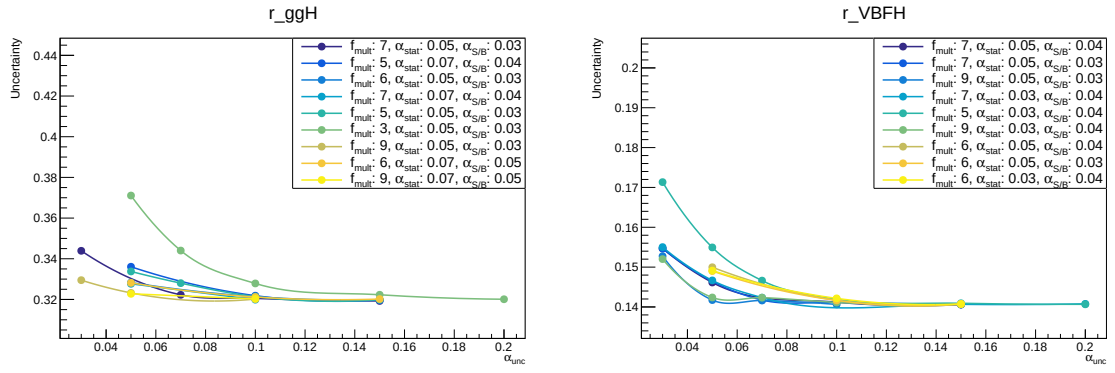

(a) POI targeting the ggH production inclusively.

(b) POI targeting the VBFH production inclusively.

Figure 6.3: Uncertainty on two POIs of the measurement as a function of the binning algorithm's α_{unc}. Smaller uncertainties correspond to a higher sensitivity of the measurement. The nine best parameter combinations for the respective POI are shown.

Parameter of interest	Sensitivity improvement		
	Overall	Statistical uncertainty	Systematic uncertainty
$H \to \tau\tau$ production	3%	1%	4%
ggH production	6%	2%	7%
VBFH production	2%	1%	6%
VH production	9%	6%	18%
$t\bar{t}H$ production	7%	6%	18%
STXS bins			
$t\bar{t}H$	7%	6%	17%
EW qqH			
$m_{jj} > 350\,\text{GeV}$	2%	1%	2%
$60\,\text{GeV} < m_{jj} < 120\,\text{GeV}$	10%	6%	22%
ggF			
$p_\text{T}(\text{H}) > 300\,\text{GeV}$	2%	2%	2%
$200\,\text{GeV} < p_\text{T}(\text{H}) < 300\,\text{GeV}$	6%	2%	17%
ggF ≥ 1 jet			
$60\,\text{GeV} < p_\text{T}(\text{H}) < 120\,\text{GeV}$	1%	−2%	3%
ggF =1 jet			
$120\,\text{GeV} < p_\text{T}(\text{H}) < 200\,\text{GeV}$	11%	3%	21%
ggF ≥ 2 jet $m_{jj} < 350\,\text{GeV}$			
$120\,\text{GeV} < p_\text{T}(\text{H}) < 200\,\text{GeV}$	4%	1%	7%
ggF ≥ 2 jet $m_{jj} > 350\,\text{GeV}$			
$p_\text{T}(\text{H}) < 200\,\text{GeV}$	6%	2%	10%

Table 6.1: Sensitivity/Uncertainty improvements using the binning resulting from the binning algorithm with respect to a reference binning inspired by Reference [7] for all fit setups.

6.3 Validation & Partially Unblinded Fits

A very important part of measurement strategies in ATLAS is that they are conducted blind. This means that the measurement is constructed without knowledge of the recorded data until a mature likelihood model is built. Once the likelihood model is constructed, it is validated and studied using the already introduced Asimov datasets as well as further setups including real data. An overview of the conducted studies in the context of this thesis, their general goal and the utilised (pseudo-)data is given in Table 6.2. More details and the motivation for the individual setups will be discussed in the referred sections.

Goal	Data	Section
Fit convergence	Asimov pseudodata	6.3
Linearity	Asimov pseudodata	6.3
Numerical stability	Asimov pseudodata	6.3
$Z \to \tau\tau$ NF model	Asimov pseudodata	D.2.1
Pulls & constraints of individual NPs; NP model	Sideband data	6.3.1
Pulls & constraints of individual NPs; NP model	Data (random signal scaling)	6.3.2
Importance of signal enriched bins	Data (sideband and random signal scaling)	6.3.3
Predict NP behaviour	Toys	7
Overall model consistency	Toys	7

Table 6.2: Overview of the conducted studies in the context of this thesis on the likelihood model. Studies targeting individual NPs are not explicitly listed. The utilised data as well as the section in which the study is discussed are listed.

Studies based on Asimov pseudodata can already reveal a lot of information about the likelihood model. First and foremost are questions related to the stability of the model, and, thus, the MLE, and uncertainty estimation as well as the general viability of the model. Executing all of these steps with respect to the Asimov pseudodata provides information whether it is possible to find a minimum for the given likelihood model. Even if the fit is successful, there might be problems in the model which the pulls and constraints of the individual NPs and NFs can hint at. The pulls and constraints for the final model of this measurement are shown in Appendix D.2.2 for the fit to Asimov pseudodata. Since the Asimov dataset by construction perfectly matches the prediction, no NP nor NF should get pulled with respect to their nominal values in a well-behaving model, i.e. NF pulls should be at one and NP pulls at zero. Nuisance parameter constraints larger than unity indicate issues in the fit convergence. On the other hand, smaller constraints can help identify NPs which the measurement might be able to constraint in a fit to real data. This effect will be discussed in more detail in Chapter 7. However, if constraints become unphysically small, the causes have to be studied and understood. The linearity of the fit model has been validated by scaling the signal process(es) in the Asimov dataset and confirming that the fit yields the scaling as the result(s) of the POI(s).

The numerical stability of the model is studied by varying the initial parameter values before the minimisation. This variation has been implemented by sampling a random number from a uniform

distribution between ±0.2 around the NP's nominal value. Since the minimisation is a numerical process slight deviations, due to e.g. machine precision, are to be expected. All parameters with a difference in their pull that is greater than 0.0001 when comparing an Asimov fit with randomised initial values to an Asimov fit with nominal initial values are shown in Figure 6.4. No statistically significant differences are observed, meaning that the randomised initial values do not significantly influence the fit result.

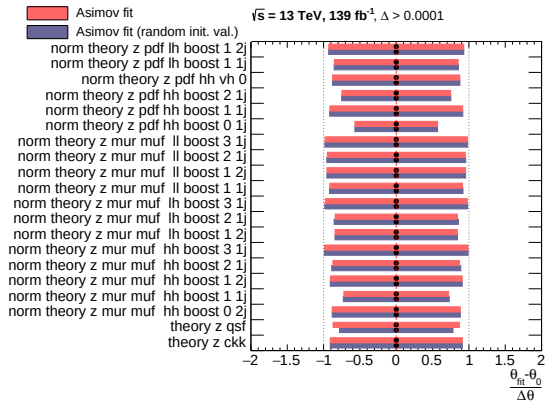

(a) Nuisance parameters related to Z + jets theory predictions.

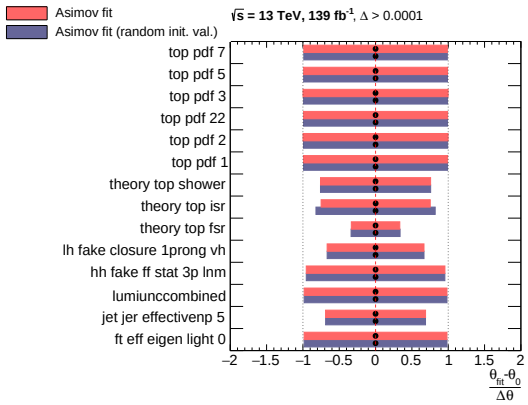

(b) All other nuisance parameters.

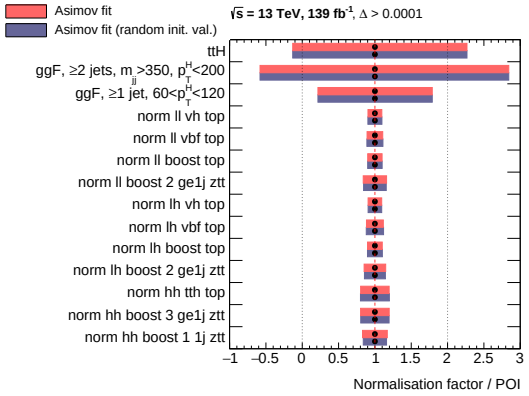

(c) Normalisation factors and parameters of interest.

Figure 6.4: Nuisance parameters, normalisation factors and parameters of interest for the Asimov fit (light red) and the Asimov fit with randomised initial values (dark blue). Only parameters with a difference greater than 0.0001 in their pulls after the fit are shown. The units (GeV) in the naming of the POIs have been omitted.

Generally, Asimov fits can be used to compare multiple fit models without biasing the measurement's result. Different possible $Z \to \tau\tau$ normalisation factor models are an example for such studies and are documented in Appendix D.2.1.

To further scrutinise the model it has to be tested on recorded data. However, these studies are supposed to be conducted as blind as possible, therefore they are referred to as partially unblinded fits. In the following, two approaches to incorporate recorded data without completely unblinding the measurement are introduced.

6.3.1 Sideband Fit

The first of the two approaches that will be discussed is the more rigorous one when it comes to ensuring that no information about the signal is extracted.[8] This is achieved by completely removing the signal enriched bins from the fit. All other bins, including all control regions, will be fitted to the recorded data. In order to define signal enriched bins two criteria, either of which has to be fulfilled, are implemented that may differ for other measurements:

1. All bins between 110 GeV and 150 GeV of $m_{\tau\tau}^{\text{MMC}}$.
2. All bins with an expected yield ratio of signals to backgrounds greater than 5%.

The first criterion is motivated by the expected $m_{\tau\tau}^{\text{MMC}}$ distribution for the signal shown in e.g. Figure B.25. In very pure regions, in terms of signal contribution, this first criterion might not be sufficient to exclude all possible signal information from the fit. Furthermore, possible phase space dependent shifts or resolutions of the MMC could lead to the signal leaking into neighbouring bins. These scenarios are handled by the second criterion. The importance of this second criterion becomes clear in the $\tau_e\tau_\mu$ vbf_1 signal region which consequently is completely removed from the sideband fit. Due to the remaining bins in the fit being outside of the expected signal mass range, this setup is called sideband fit. With this method, no dedicated precautions have to be taken when examining results. The removed bins correspond to the blinded bins in the $m_{\tau\tau}^{\text{MMC}}$ distributions shown in Appendix E.1.

To ensure comparability to the other fit setups, the removal of bins only happens after the histogram manipulations described in Section 6.2.1. The smoothing procedure especially depends on neighbouring bins, and would thus yield different results if the bins were removed beforehand. Since bins with zero yield are problematic in the likelihood evaluation, the neighbouring bins to the removed bins are moved so that they will become direct neighbours.

Studies on a preliminary fit model revealed large pulls of nuisance parameters related to the τ_{had} identification ("taus eff rnnid syst") and efficiency ("taus eff reco total"), see Figure 6.5. Since these NPs act on hadronically decaying τ-leptons it is expected that the process mainly responsible for these pulls is the Z + jets process as it comprises the largest source of real τ_{had} in the measurement. Thus, the impact of the cross-normalisation scheme with the Z + jets control regions was studied by removing those control regions from the fit. By removing the CRs, as shown in Figure 6.5(a), the pulls of the two τ_{had} NPs could be alleviated. Correlations between the τ_{had} NPs and the Z + jets theory NPs result in changes of the Z + jets theory NPs. This is to be expected since both NP categories vary the normalisation of the Z + jets process. Comparisons of the $Z \to \tau\tau$ normalisation factors with and without the control regions in Figure 6.5(b)-(d) show that the NFs in di-τ decay channels involving leptonic τ-leptons are less affected than the $\tau_{\text{had}}\tau_{\text{had}}$ channel. This confirms an interplay between the Z + jets normalisation and the two τ_{had} related NPs.

It was found that the pull of the identification NP is a technical artifact due to both NPs acting on the τ_{had} normalisation in a similar way. By inflating the prior of the reconstruction efficiency NP by a factor of four, effectively alleviating the NP's prior, the pull of the identification NP could be reduced as shown in Figure 6.6. The motivation for this approach originates from the identification efficiency being measured in a well-defined analysis using data and the reconstruction efficiency uncertainty being estimated from simulation, see Reference [76]. While a scale factor could be measured for the identification efficiency, this was not possible for the reconstruction efficiency. The

[8] Here, even unintended collection of information from e.g. log files do not contain any viable information on the signal.

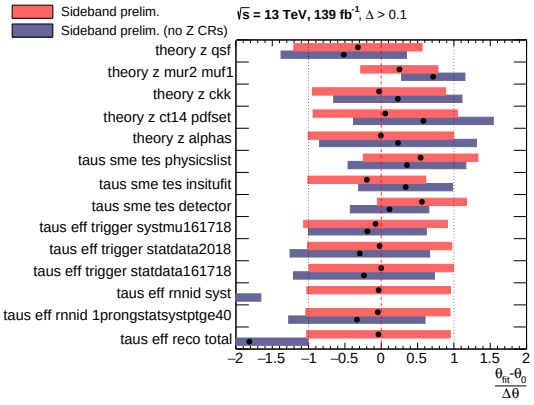

(a) Nuisance parameter related to Z + jets theory predictions and τ_{had}.

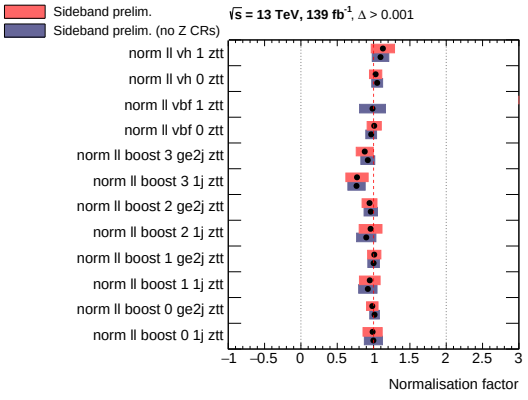

(b) $Z \to \tau\tau$ normalisation factors in the $\tau_e\tau_\mu$ channel.

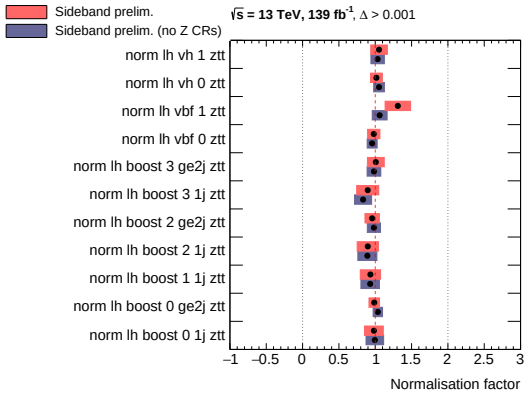

(c) $Z \to \tau\tau$ normalisation factors in the $\tau_{\text{lep}}\tau_{\text{had}}$ channel.

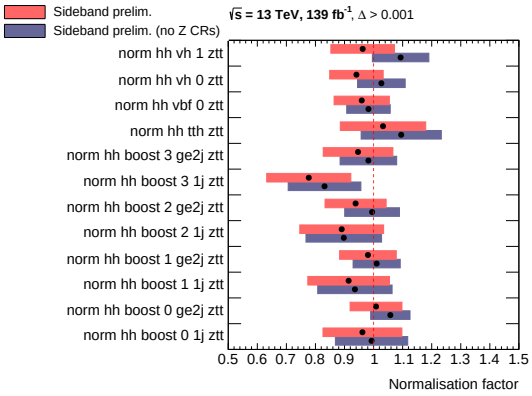

(d) $Z \to \tau\tau$ normalisation factors in the $\tau_{\text{had}}\tau_{\text{had}}$ channel.

Figure 6.5: Pulls and constraints of nuisance parameters and normalisation factors for a preliminary fit model in the sideband fit setup. A setup with (light red) and without the Z + jets control regions (dark blue) in the fit are compared. Only parameters with a difference greater than 0.001 for NFs and 0.1 for NPs in their mean value after the fit are shown.

fit model used in this measurement allows to measure this efficiency for the first time in ATLAS by cross-normalising the Z + jets process between the signal regions and control regions. Thus, the final fit model simultaneously measures the reconstruction efficiency in-situ by inflating its prior. Continuing studies regarding this uncertainty are documented in Appendix D.3.2.

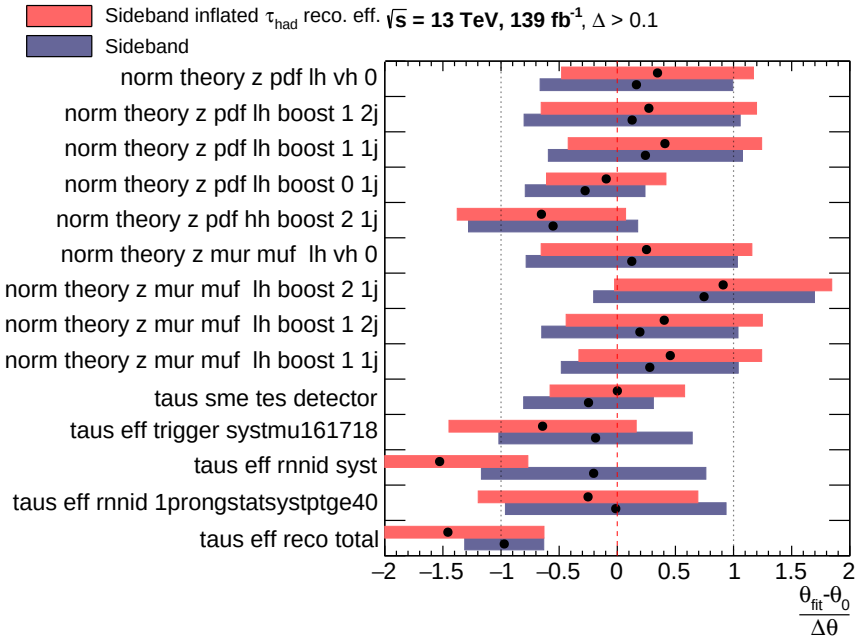

Figure 6.6: Effect of inflating the τ_{had} reconstruction efficiency NP by a factor of four (light red) compared to the default NP prior (dark blue) in the sideband fit using the final fit model. Only NPs whose pull changes by more than 0.1 are shown.

This example shows the power of the sideband fit setup, even though it is completely agnostic of parts of the $m_{\tau\tau}^{\text{MMC}}$ distributions. The pulls and constraints of all nuisance parameters and normalisation factors, without the POI(s), are documented in Appendix D.3.1.

6.3.2 Random Signal Strength Fit

With the sideband fit just introduced, a lot of information on the fit model can be extracted. However, the caveat of removing the signal enriched bins might skew some of the observations. This can happen, for example, if a nuisance parameter shows a change of sign in its envelope in one of the removed bins. Random signal strength fits implement a way of including those bins again without revealing any information on the signal. The following studies performed in the context of this thesis are based on the conceptual implementation of these fits as part of the collaborative effort in Reference [160]. The idea is to not remove any signal sensitive bins but rather hide the signal sensitivity by simultaneously scaling all signals with a random unknown factor μ, hence the name random μ or random signal strength fit. Thus, even unintentionally checking the measurement's result would not yield the real result due to the unknown scaling. As additional measures to not get biased towards certain results, the following cautionary steps have been implemented:

1. No or only very limited examination of the log files so as to not extract any information on the signal unintentionally.

2. No scrutinisation of signal theory uncertainties.

The random scaling factor μ is drawn from a Gaussian distribution $G(1.5, 0.3)$. Its parameters with a mean of 1.5 and width of 0.3 are motivated by the intention to avoid fit stability issues arising from very large, very small or even negative scalings.

Some studies are prone to be conducted with the random signal strength fit setup as they rely on the full observable spectrum for some backgrounds. Thus, the Z + jets theory nuisance parameter scheme was studied with this setup. Pulls and constraints observed in the sideband fit have been confirmed in the random signal strength fit for the PDF and $\mu_R\mu_F$ Z + jets theory uncertainties, see Appendix D.3.1. Due to the fact that these uncertainties are purely based on theoretical variations and the measurement targets a variety of phase spaces, the scheme of correlating these NPs over all regions was deemed not appropriate. The alternative scheme discussed in the following attempts to mitigate effects of pulls and/or constraints from one kinematic region to another. Additionally, the shape variations and normalisation variations were decorrelated since the inducing theoretical variations do not warrant a physical motivation for them to be correlated. Thus, all kinematic regions as well as the shape and normalisation variations are decorrelated in the final model while the pairings of signal regions and control regions are kept correlated. Details of this study such as the impact of the correlation scheme on the parameters of interest are documented in Appendix D.3.3. As part of the validation of the decorrelated NP scheme the effect on the $Z \to \tau\tau$ yields in all signal regions has been studied, see Figure 6.7. This effect is separated into yield changes around the Z + jets peak and yield changes in the vicinity of the signal, all of which have been found to be of the expected small magnitude. Studying these changes in the signal mass range is only possible in the random signal strength fit setup as these bins would have been removed in the sideband fit setup.

Since both the Z + jets theory uncertainties as well as the τ_{had} reconstruction efficiency discussed in Section 6.3.1 act on the Z + jets normalisation, the interplay of these two NP categories has been studied. The effect of the inflated τ_{had} reconstruction efficiency prior and finally its pull on the Z + jets theory uncertainties was estimated by replacing the τ_{had} prior with its postfit values. In the representation of the prior as a Gaussian distribution this effectively means that the mean of zero and width of one are replaced by the postfit pull and constraint, respectively. This effect is best studied in random signal strength fits to reflect all possible deviations in the Z + jets spectrum. All nuisance parameters with changes in their pull greater than 0.05 in a fit with the modified prior are shown in Figure 6.8. No normalisation factor shows deviations that would fulfill this criterion. The only NPs that fulfill the criterion are the two τ_{had} NPs that are correlated due to their similar impact on the Z + jets process as discussed in Section 6.3.1. As the modified prior allows the fit to pull the τ_{had} reconstruction efficiency even further without a larger penalty on the likelihood, this compensates parts of the identification efficiency pull.

6.3.3 Importance of Signal Enriched Bins

By comparing the pulls and constraints of the individual nuisance parameters and normalisation factors between the sideband fit setup and the random signal strength fit setup, the importance of the signal enriched bins in the measurement can be studied. This comparison is shown in Figure 6.9 for NPs and NFs with deviations that are considered significant in that sense that they probably do not

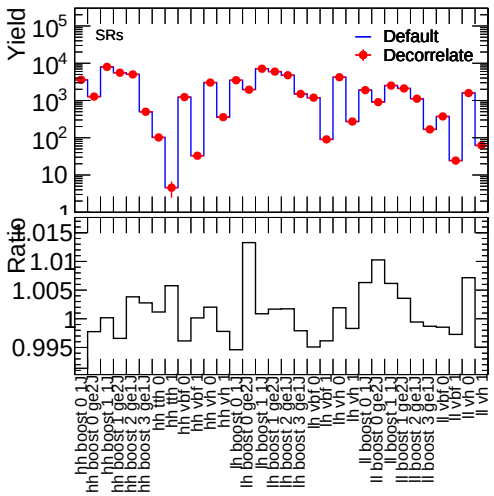

(a) $Z \rightarrow \tau\tau$ yield changes in the range of $75\,\text{GeV} < m_{\tau\tau}^{\text{MMC}} < 100\,\text{GeV}$.

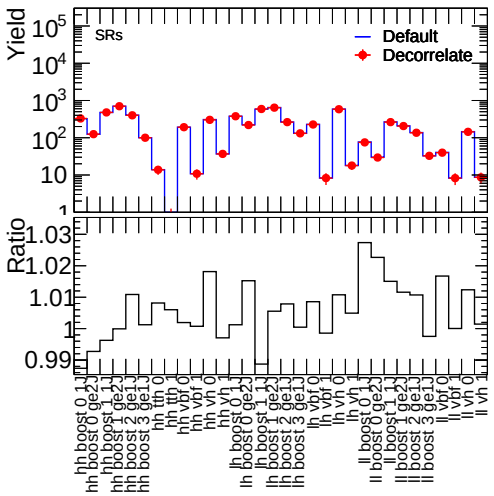

(b) $Z \rightarrow \tau\tau$ yield changes in the range of $110\,\text{GeV} < m_{\tau\tau}^{\text{MMC}} < 150\,\text{GeV}$.

Figure 6.7: Effect of decorrelating the PDF and $\mu_R\mu_F$ Z + jets theory uncertainties across all kinematic regions as well as shape and normalisation components on the $Z \rightarrow \tau\tau$ yield. The results of the random signal strength fit are used to calculate the yields with the POI(s) set to one. The decorrelated scheme (red dots) is compared to the default fully correlated scheme (blue line) and the ratio Default/Decorrelate is shown.

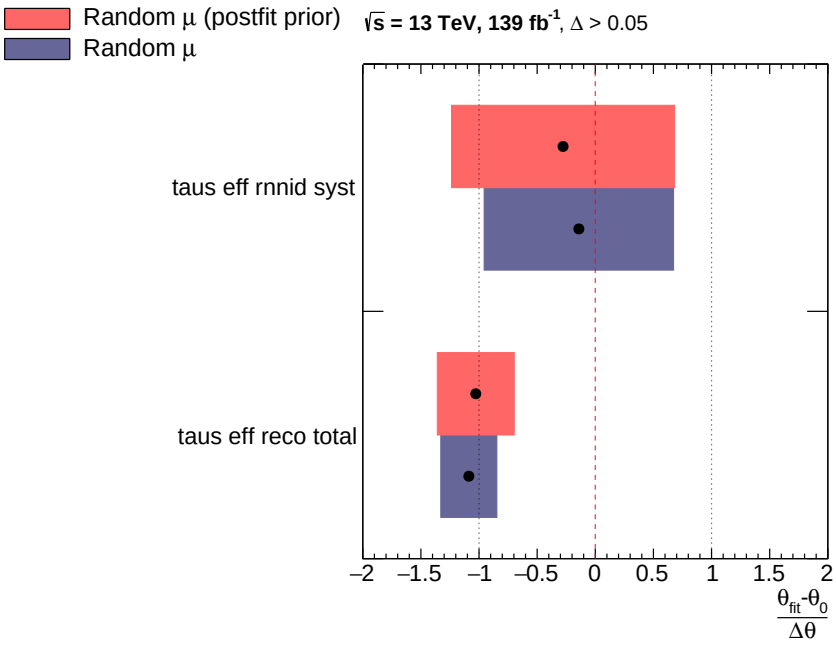

Figure 6.8: Nuisance parameters with pull changes greater than 0.05 in the random signal strength fit when replacing the inflated τ_{had} reconstruction efficiency prior (dark blue) with a prior according to its postfit values (light red).

originate from fit stability differences. Most normalisation factors do not fulfill this criterion, meaning they are rather stable with respect to the inclusion of signal enriched bins. The only exceptions are the $Z \to \tau\tau$ NFs in the $\tau_e\tau_\mu$ vbf_1 region and the Top NF in the $t\bar{t}H$ regions, for which either the complete signal region or a considerable amount of bins are removed in the sideband fit. Jet related nuisance parameters are sensitive to the whole $m_{\tau\tau}^{\text{MMC}}$ spectrum of the Z + jets process which results in the differences shown in Figure 6.9(b). Even though the sideband fit is able to retain most of the Z + jets spectrum, some differences are to be expected, as shown in Figure 6.9(d), due to the removal of large parts of the spectrum's falling edge. A similar reasoning is responsible for the changes in the misidentified τ-lepton related nuisance parameters, see Figure 6.9(c), even if the background does not show a peaking structure like Z + jets. Overall, the agreement of both setups is remarkable considering all signal enriched bins are removed in the sideband fit.

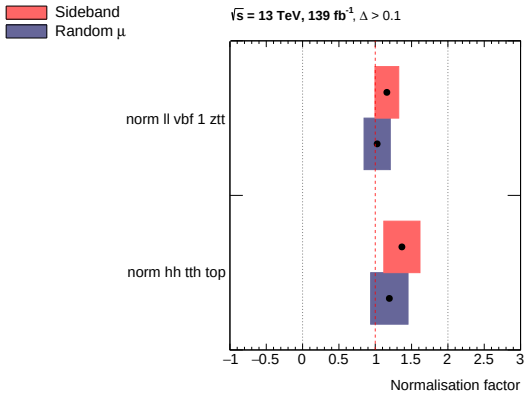

(a) Normalisation factors.

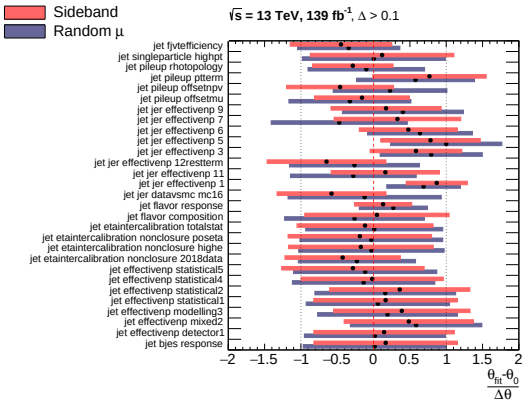

(b) Nuisance parameters related to jets.

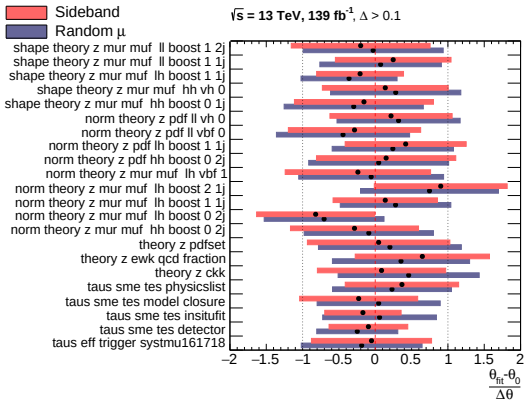

(c) Nuisance parameters related to Z + jets theory uncertainties and τ_{had}.

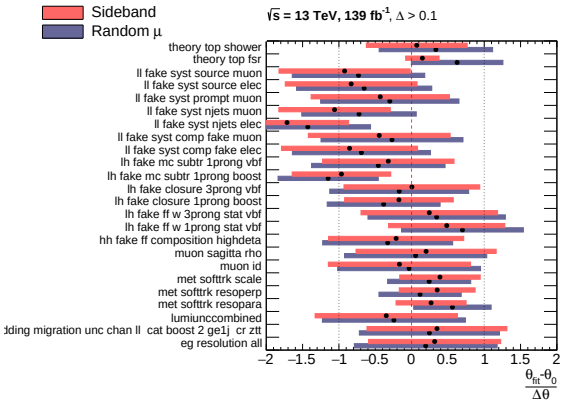

(d) All other nuisance parameters.

Figure 6.9: Pulls and constraints of nuisance parameters and normalisation factors of the final fit model in the sideband fit setup (light red) and the random signal strength fit setup (dark blue). Only parameters with a difference greater than 0.1 in their mean value after the fits are shown.

CHAPTER 7

Intermezzo: A New Approach to Validating Fit Models

With increasing available data statistics the fit models in ATLAS measurements tend to get more evolved and increase in complexity. Established ways to understand and validate these models have been introduced in Section 6.3. They rely on either Asimov pseudodata or partially unblinded fits including real recorded data. While these fits reveal a lot of information and are especially useful to study individual effects as it was demonstrated in Section 6.3, they are not capable of assessing the overall consistency of the fit model or even predict certain behaviours *before* including real data.

This chapter introduces a new way of studying complex fit models, providing additional information. By generating "toy" datasets, it is possible to predict which nuisance parameters in the model could get pulled or constrained in a fit to recorded data based on the measurement's sensitivity to them. Additionally, the method provides a stable estimate of the overall consistency of the fit model with respect to the data once the measurement is (partially) unblinded. A description of what toy datasets are and how they are generated is given in Section 7.1 with the subsequent sections detailing the aforementioned advantages of the approach.

It has to be noted, however, that none of the additional information provided by this new method can and also never will replace thorough scrutiny of the fit model using Asimov fits and partially unblinded fits. Effects like the pull of the τ_{had} reconstruction efficiency NP described in Section 6.3.1 can only be studied using those established approaches.

7.1 Generating Toys

Toy datasets are a class of pseudodata that do not neccessarily exactly reflect the simulation like Asimov pseudodata do. The idea is to let the toy pseudodata, or toys, reflect the statistical fluctuations of real data as well as the nuisance parameters in the model in a controlled way. Thus, studies based on toys typically repeat the fit a large number of times with each fit having its own unique toy dataset. A single fit using randomised toy data does not yield additional information in comparison to the already introduced validation methods as it resembles the random nature of real data to the best knowledge. However, the ensemble of toy fits does provide new information. Computational limitations often restrict the number of times this procedure can be repeated. This holds especially true for complex fit models as the required resources for the MLE and uncertainty estimates scale accordingly.

Methods to generate individual toy datasets are provided by the RooStats [155] framework. An important concept to note in this context are RooStats' GlobalObservables that have to be randomised in addition to the Poissonian variation of the expected data yield. These observables encode the meaning of the NP's nominal value, which is typically determined in auxiliary measurements, in the likelihood. In a Frequentist approach they have to be randomised as the auxiliary measurements underly statistical variations themselves and, thus, only the coverage of the prior can be known but not the true nominal value. As the likelihood implementation in ATLAS follows this Frequentist approach, the results of toy based studies could become biased otherwise. By randomising the GlobalObservables, each individual NP is effectively randomised for every single set of toys.

This randomisation of the GlobalObservables has to be taken into account when evaluating the pulls of individual fit results. In the following representation of pulls, using the definition

$$\frac{\theta_{\text{fit}} - \theta_0}{\Delta\theta}$$

as already introduced and shown in Section 6.1.3, the new observable values correspond to a variation of θ_0. The resulting effect is shown in Figure 7.1 based on a pseudo-measurement that is constructed not to be sensitive to the shown nuisance parameter ("alpha_background_sys2"). As already mentioned,

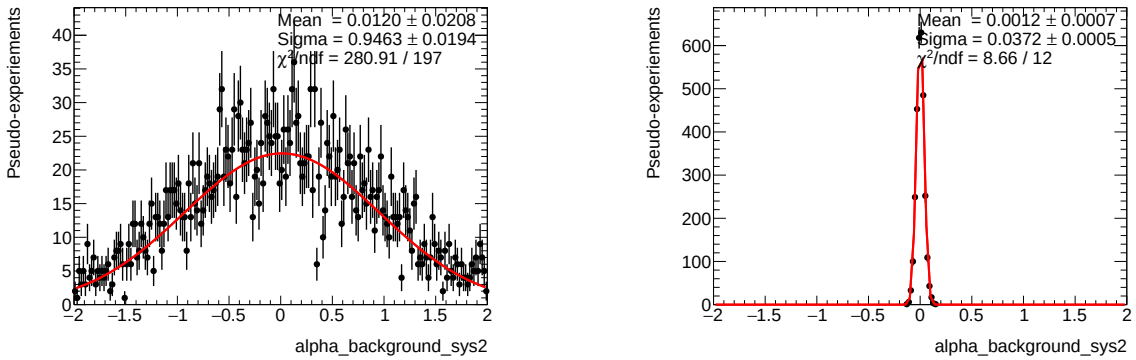

(a) Pull distribution not considering the randomised GlobalObservables values.

(b) Pull distribution subtracting the randomised GlobalObservables values.

Figure 7.1: Pull distribution of a nuisance parameter in a pseudo-measurement. The measurement is constructed not to be sensitive to the NP, i.e. the pulls are expected to scatter closely around zero. 3000 toys have been generated. The pull distributions are fitted to Gaussian functions (solid lines).

the ensemble of fits yield additional information, thus the figure shows the distribution of observed pulls in the 3000 generated toy fits. Since the individual pulls are the result of randomised measurements, their distribution is expected to follow a Gaussian distribution in the limit of large numbers, c.f. central limit theorem [161]. If the randomised GlobalObservables values are not taken into account, the pull distribution follows the randomly sampled observable values that have been drawn according to the Gaussian prior with a mean of zero and a width of one, see Figure 7.1(a). However, if the measurement is not sensitive to the given NP, a narrow Gaussian distribution with a small width is expected since the fit should not be able to pull the NP. Once the random observable values are taken into account, i.e. subtracted from the "raw" pull, the expected distribution is restored, see Figure 7.1(b). Thus, the GlobalObservables will be randomised in the following while taking the randomised

value into account when evaluating the pulls. More details on the expected distributions for nuisance parameters to which the fit is or is not sensitive are given in Section 7.2.

7.1.1 Validation

The toy generation can be validated through the ensemble of pull distributions for all nuisance parameters and normalisation factors. To do so, information about the individual pull distributions as introduced in Figure 7.1 are extracted via Gaussian fits to the same. For each individual NP and NF the difference between its nominal value and the mean of the fitted Gaussian distribution, normalised to the uncertainty of the fitted Gaussian distribution's mean, can be calculated. The uncertainty of the fitted mean is multiplied by $\sqrt{2}$ since the uncertainty itself is a random variable for each NP and NF in each toy fit. Thus, error propagation results in the additional factor that has to be taken into account. In the following, this quantity will be referred to as the distribution of pull deviations. The resulting distribution is shown in Figure 7.2 using the final fit model of the $H \rightarrow \tau\tau$ measurement. A total of 500 toys has been sampled where all NPs are randomised for every individual toy as explained before. The distribution's number of entries corresponds to the number of nuisance parameters and normalisation factors in the fit model. As the entries are effectively the result of drawing random numbers, the distribution of pull deviations is expected to follow a Gaussian with a mean of zero and a width of one in the limit of large numbers, c.f. central limit theorem.

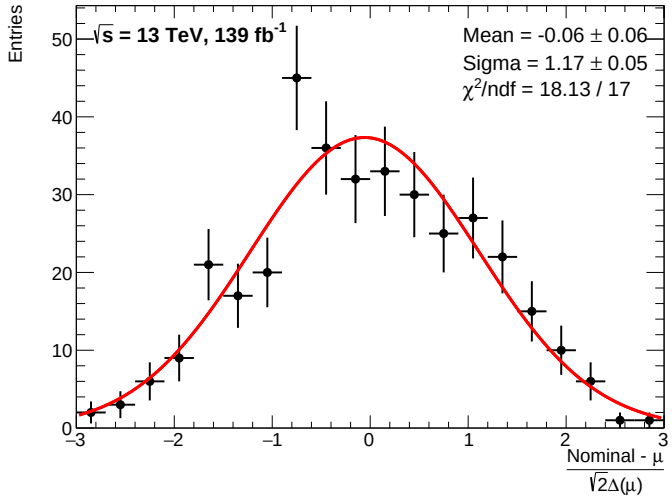

Figure 7.2: Distribution of pull deviations observed in 500 toy fits for all NPs and NFs of the final fit model where the number of entries corresponds to the total number of NPs and NFs in the fit model. The pull deviation is defined as the difference between the NP's/NF's nominal value and the mean of the Gaussian fit to its individual pull distribution. This difference is normalised to $\sqrt{2}$ times the mean's uncertainty of the Gaussian fit. The nominal values for NFs is taken to be one and for NPs to be zero in the chosen representation. A Gaussian function (solid line) is fitted to the distribution of pull deviations.

To quantify the agreement of the pull deviations with its expectation, a Gaussian fit to the distribution is performed. The fit's mean is a measure of possible overall biases in the toy generation. For the toys generated with the final fit model the mean is compatible with zero and, thus, no statistically

significant bias is observed for the toy sampling. The fit's width quantifies the agreement of the presumed underlying model of the individual NP pull distributions with the generated toy pseudodata. By fitting the pull distributions to Gaussian functions, deviations from this Gaussian model can result in a modified width of the pull deviations. Since the width shows a statistically significant deviation from its expectation, a width consistent with one, with an observed value of 1.17 ± 0.05, possible causes have to be understood.

Three distinct hypotheses for deviations from the Gaussian model of the pull distributions have been identified. The first reason is related to the numerical stability of the MLE. Nuisance parameters to which the fit is not sensitive to are typically not pulled but the numerical stability in the likelihood minimisation can lead to small variations of the pull close to zero as shown in Figure 7.3(b). This effect is of no physical importance as the variations are tiny. However, the variations do not follow the Gaussian model of the pull distributions since the underlying cause is of technical nature.

Another reason is the occurence of physical boundaries of possible parameter values within the fit model. As the likelihood is limited by e.g. the restriction that no bin should return a negative yield as a result of the fit, some parameters may experience such boundaries. This effect is shown in Figure 7.3(a) for the Top NF in the $\tau_e\tau_\mu$ VBFH phase space with a lower boundary of roughly 0.8.

Finally, it is possible that some parameters might be highly correlated to bins with low statistics, resulting in a similar effect as the previous presumed cause. In contrast to the parameter directly acting on low statistics bins as before, the parameter experiences the boundary only indirectly through correlations in this hypothesis. These parameters are hard to identify as their pull distributions are only skewed indirectly through correlations.

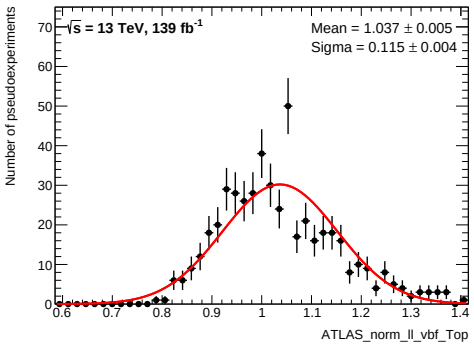

(a) Pull distribution of the Top NF in the $\tau_e\tau_\mu$ VBFH phase space.

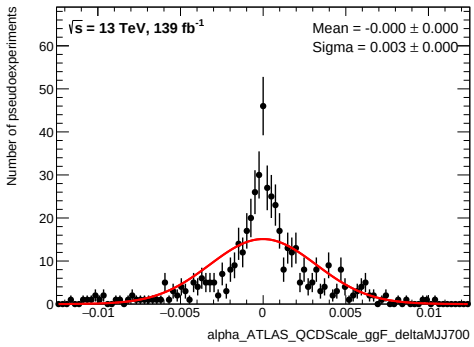

(b) Pull distribution of a signal theory uncertainty.

Figure 7.3: Pull distributions of nuisance parameters showing deviations from the presumed Gaussian model. 500 toys have been generated for the final fit model. The pull distributions are fitted to Gaussian functions (solid lines).

With the identified examples of deviations from the presumed pull distribution's Gaussian model, the observed width of the pull deviations is considered understood. In order to quantify exact regions that could indicate problematic behaviour, more detailed studies have to be conducted. These studies have to be based on pseudo-measurements in which full control over all yields, nuisance parameters etc. is given.

7.2 A Priori Extraction of Information

With the toy fits introduced in the previous section, it is possible to assess which NPs the measurement is sensitive to for the given model, and, thus, predict possible pulls and constraints in a fit to real data. Since the toys reflect the statistical nature of data, the ensemble of pulls and constraints for a given NP provide the necessary information.

Nuisance parameters, to which the fit model is not sensitive, are typically those with a prior determined from auxiliary measurements for which the fit cannot extract additional information. The additional information to further constrain a nuisance parameter can, for example, originate from shape variations of observables in high statistics phase spaces not accesible in the auxiliary measurements. A similar reasoning can be applied for possible pulls. Thus, nuisance parameters can be sorted into categories based on whether they are expected to possibly be pulled or constrained.

It is important to note that the classification can only quantify if a pull/constraint is *possible*. No statement can be made about whether a pull/constraint actually does occur in a fit to real data based on these categories. However, if a nuisance parameter is expected to not be pulled or constrained by this procedure but a pull/constraint is observed in data, this can hint towards possible inconsistencies in the fit model. Further detailed investigations should be conducted in such a scenario.

7.2.1 Categories

In the following, the categories predicting possible NP behaviours in a fit to real data are introduced. First, the NPs can be classified into two categories concerning their constraints: whether or not to expect a possible constraint.

In principle, the distribution of constraints for a single NP is a random distribution and should follow a Gaussian distribution in the limit of large numbers. However, in the implemented representation of NPs in HistFactory [154] and RooStats [155] an unconstrained nuisance parameter corresponds to a constraint of one. For well-behaved fit models this number never becomes greater than one as this would indicate issues in the implementation of this NP's model. In this case, the measurement would prefer to relax the corresponding prior, although it is determined by an auxiliary measurement. Thus, constraints greater than one should not occur in likelihood based measurements. This effectively imposes a bound on the constraint distributions of the nuisance parameters which often leads to distributions deviating from the Gaussian model as shown in Figure 7.4(a). In order to classify all NPs into categories the constraint distributions are fitted to Gaussian functions, nevertheless. For nuisance parameters whose mean constraint's distance to the boundary is sufficiently large the Gaussian function is able to model the distribution as shown in Figure 7.4(b). Parameters whose means are close to the boundary cannot be modelled by a Gaussian distribution, see Figure 7.4(a).

Based on the observed distributions, the following criteria were implemented to distinguish NPs that are and are not expected to be constrained in a fit to data:

$$\begin{aligned} \text{Possible constraint:} \quad & \sigma > 0.05 \text{ or} \\ & |1-\mu| > \sigma \text{ and } |1-\mu| > 0.05 \\ \text{No constraint:} \quad & \text{else}\,. \end{aligned}$$

Due to the Gaussian fits sometimes not being able to model the constraint distributions, a case distinction is applied for the classification. If the Gaussian fit results in a mean greater than one the

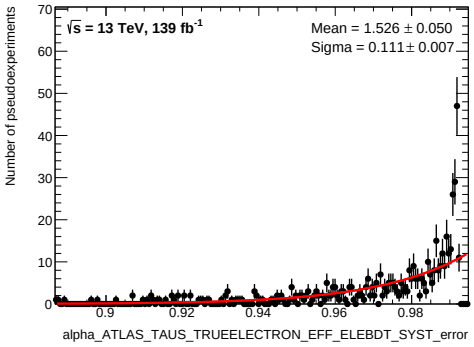

(a) Pull distribution of an NP with no expected constraint.

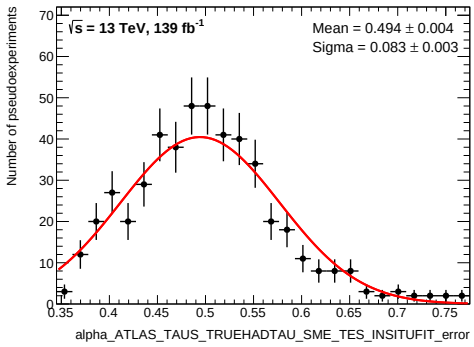

(b) Pull distribution of an NP with an expected possible constraint.

Figure 7.4: Examples of pull distributions for nuisance parameters that are not expected to be constrained and expected to possibly be constrained in a fit to data. 500 toys have been generated for the final fit model. The pull distributions are fitted to Gaussian functions (solid lines).

distribution is typically not modelled adequately. In these cases the mean μ and width σ are not taken from the Gaussian fits but rather directly as the mean of the distribution and its uncertainty.

Similarly, it is possible to classify nuisance parameters according to whether a pull can be expected or not. As the pull distributions are typically less affected by boundaries most of them can be described by a Gaussian function. The definition of the categories does not rely on the actual mean of the distribution since it is expected to scatter around values close to their nominal value. If a statistically significant deviation in the mean with respect to the nominal value for a single NP would be observed, it would hint towards a possible bias for the given fit model. Instead, the categorisation utilises the width of the pull distribution in combination with the mean of the constraint distribution which in this context will be called mean of the errors. The categories are defined as follows:

$$\begin{aligned} \text{Possible pull:} \quad & \frac{\sigma}{\text{mean(errors)}} \geq 0.05 \\ \text{No pull:} \quad & \frac{\sigma}{\text{mean(errors)}} < 0.05\,. \end{aligned}$$

Taking into account the observations for the constraint distributions, the mean of the errors is taken from a Gaussian fit or the distribution itself following the same case distinction as before. The classification is motivated by the pull distributions being narrow, compared to the average observed constraint for NPs to which the measurement is not sensitive as shown in Figure 7.5(a) and 7.4(a). If the measurement is sensitive to a specific nuisance parameter, the pull distribution's width increases, see Figure 7.5(b).

The exact cuts quoted for the classification in this section are motivated by observations in the $H \to \tau\tau$ measurement. Similarly to the validation introduced in Section 7.1.1, these cuts should be optimised using pseudo-measurements giving full control over the model and providing a more stable estimate for suitable cut values.

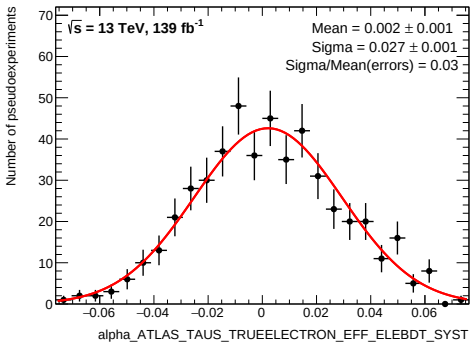

(a) Pull distribution of an NP with no expected pull.

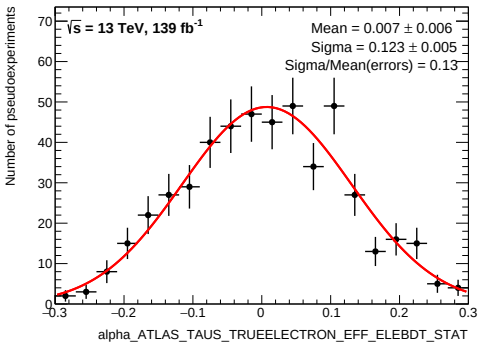

(b) Pull distribution of an NP with an expected possible pull.

Figure 7.5: Examples of pull distributions for nuisance parameters that are not expected to be pulled and expected to possibly be pulled in a fit to data. 500 toys have been generated for the final fit model. The pull distributions are fitted to Gaussian functions (solid lines).

7.2.2 Application

The predicted classification described in Section 7.2.1 is tested by comparing those predictions to the observed pulls and constraints of the unblinded $H \to \tau\tau$ measurement. Based on the categorisation, different background colours are introduced to visualise the expected NP behaviour:

Gray A possible pull is expected.

Red No pull is expected.

Yellow A possible constraint is expected.

The absence of the "possible constraint" background indicates that no constraint is expected. As shown in Figure 7.6, all observed pulls and constraints for nuisance parameters related to the τ_{had} objects have been predicted by the classification. At the same time, no unexpected pulls or constraints are observed, confirming a well-behaved model and fit. The same holds true for the other nuisance parameters which are documented in Appendix D.4.

7.3 A Posteriori Extraction of Information

Once the measurement is (partially) unblinded, the toy fits can be used to assess the overall agreement of the fit model with respect to the recorded data. It has to be noted that the toys can only reflect the chosen fit model. Thus, conclusions can only be drawn in the context of that model.

In addition to the global agreement of the model with the data, the significance of individual pulls can be quantified. Reference [162] introduces a measure of the pull significance in terms of standard deviations defined as

$$Z_t = \frac{\hat{t}}{\sqrt{1-\sigma_t}}\,, \tag{7.1}$$

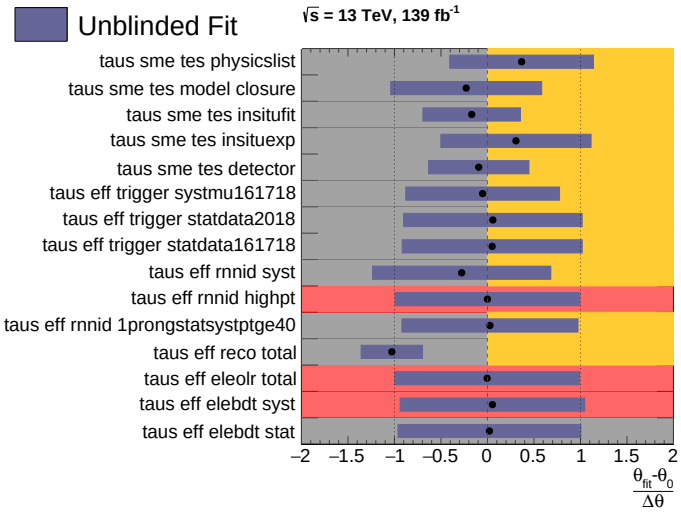

Figure 7.6: Pulls and constraints observed in the unblinded fit for the τ_{had} related nuisance parameters. The background colour highlights the expected NP categories discussed in Section 7.2.1.

with $\hat{t}$ being the observed pull and σ_t being the observed constraint. This measure relies on the assumption of the nuisance parameters being modelled by Gaussian distributions. While this assumption is valid for most NPs, it is possible that it is not applicable for some NPs, e.g. when (physical) boundaries become important as discussed in Section 7.1.1. Additionally, if a nuisance parameter's constraint is close to one, the denominator of Equation 7.1 increases up to a point where the estimate of the pull significance becomes unreasonably large. Keeping these caveats in mind, the estimate yields reliable results in all other situations.

A more robust estimate alleviating the aforementioned caveats is given based on the toy fits. Instead of quantifying the significance of a pull in terms of standard deviations the likeliness of the pull is quantified using a p-value. The p-value is defined in the range between zero and one and indicates possible deviations from the model for values close to these boundaries. Using the Iverson bracket notation, see Reference [163], it can be written as:

$$p = \left(\sum_{i=0}^{N_{\text{toys}}} [\hat{t}_{\text{toy},i} < \hat{t}_{\text{fit}}] \right) / N_{\text{toys}} \,. \tag{7.2}$$

Observed pulls are denoted as $\hat{t}$ while the Iverson bracket yields one if the statement is true and zero otherwise. This definition of the p-value does not presume any specific model of the pull distribution and is also valid in the extreme parameter regions. The two examples shown in Figure 7.7 underline the robustness of the measure. Even nuisance parameters experiencing pulls of more than 1σ, see Figure 7.7(b), are quantified as compatible with the fit model if the model permits a pull at this order of magnitude. Additionally, the measure yields a stable estimate for nuisance parameters with no significant constraint, see Figure 7.7(a) where the observed constraint of the NP in the unblinded fit is roughly 0.99.

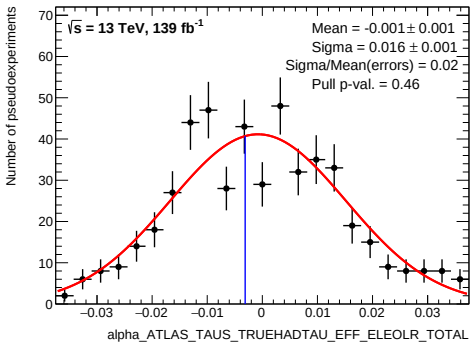

(a) Pull distribution of the electron overlap removel for τ_{had}.

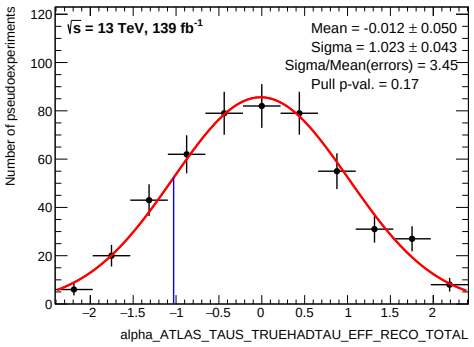

(b) Pull distribution of the τ_{had} reconstruction efficiency.

Figure 7.7: Examples of pull distributions for two example nuisance parameters. The pull's p-value is indicated in the figures with the pull being visualised with a blue line. 500 toys have been generated for the final fit model. The pull distributions are fitted to Gaussian functions (solid lines).

7.3.1 Global Consistency of Fit Models

With the toy based estimate of a pull's significance, the approach can be generalised further to be applicable to the complete fit model. Instead of focussing on single nuisance parameters, the method can be used to assess the overall consistency of the data with the implemented fit model. Since the measurement is subject to statistical variations it is possible that individual NPs are pulled by e.g. more than 0.5σ. The global consistency assessment sets these cases into context with the pulls of all other NPs and, thus, incorporates the look-elsewhere-effect [164]. Although the global approach cannot identify individual problematic nuisance parameters, it is capable of identifying global issues in the definition of the likelihood that would manifest with NPs clustering at certain p-values.

By calculating the p-values for all individual toy fits the global procedure is verified. To be more precise, the p-values are calculated for all individual NPs in all toy fits, yielding an overall number of entries equal to 500 times the number of NPs in the fit model. As expected, a flat p-value distribution is observed for the ensemble of all toys as shown in Figure 7.8. The consistency of data with the fit model is assessed via the agreement of the p-value distributions for toys and data. Since only the shape of this figure of merit is of relevance, both distributions are normalised to unity for an easier assessment of their compatibility. While some statistical fluctuations are expected, a remarkable overall consistency is observed.

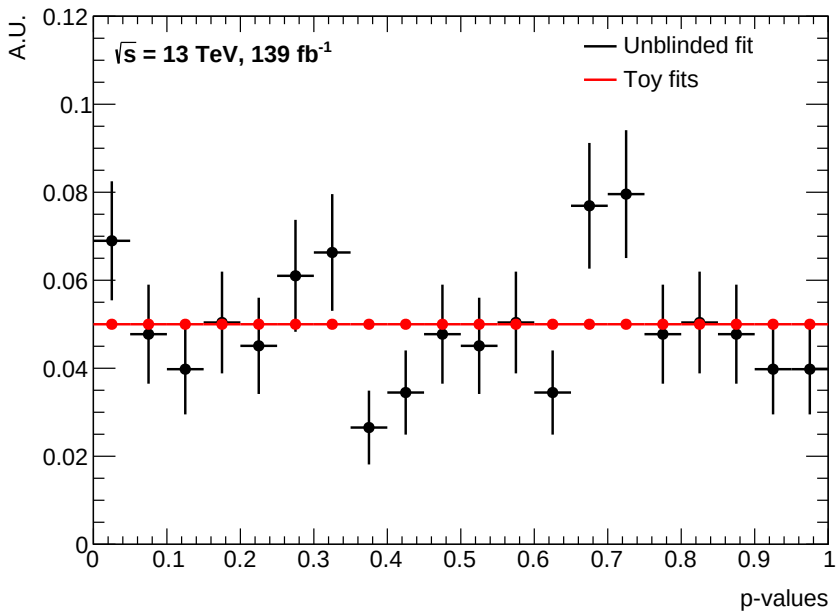

Figure 7.8: Distribution of p-values for the NPs in the unblinded fit and all toy fits. The number of entries corresponds to the overall number of NPs in the fit model times the amount of performed fits. The unblinded fit is performed once while 500 toy fits have been conducted. Both distributions are normalised to unity for an easier assessment of their compatibility.

CHAPTER 8

Results

With the fit model having been thoroughly validated using the techniques discussed in Chapters 6 and 7 the final results can be extracted by fitting to the recorded dataset with an integrated luminosity of 139 fb^{-1}. The validity of the studies performed on the fit model has been confirmed in a collaborative effort. By only scaling the signal(s), the random signal strength fit is presumed to resemble the unblinded fit result most accurately. Thus, the differences between these two fits in the nuisance parameter and normalisation factor pulls can be studied. This study was originally conducted as part of the collaborative work, see Reference [160], and has been repeated for this thesis to stress the likeness of the two fits. A single nuisance parameter shows a pull difference greater than 1×10^{-4} while no normalisation factor fulfills this criterion, see Figure 8.1.

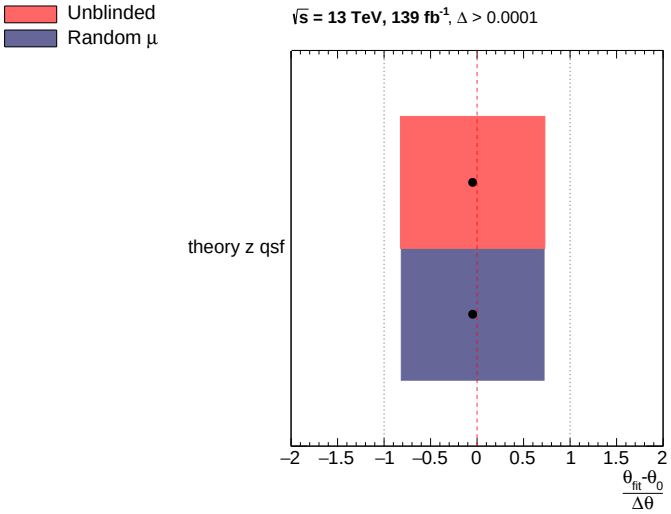

Figure 8.1: Nuisance parameters of the final fit model with a difference in their pull greater than 0.0001 between the random signal strength (dark blue) and the unblinded fit (light red). The differences in the normalisation factors do not fulfil this criterion.

Additionally, the validity of the conducted fits can be verified via the $m_{\tau\tau}^{\text{MMC}}$ distributions after the individual fits. The fits should generally improve the agreement between the data and the simulations. As shown in Figure 8.2(a) and (b) for the vbf_1 signal region of the $\tau_{\text{lep}}\tau_{\text{had}}$ channel, the sideband fit

and the unblinded fit lead to a good agreement between data and simulations. Some small deviations in the modelling between the sideband fit and the unblinded fit are observed that originate from the exclusion of all signal enriched bins from the fit, see also Section 6.3.3. It is not possible to visualise the result of the random signal strength fit without being able to extract information about the signal from the $m_{\tau\tau}^{\text{MMC}}$ distribution. Thus, no mass distributions for these fits are shown. The chosen signal

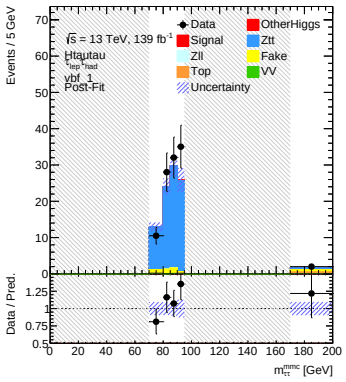

(a) Mass distribution after the sideband fit. The ratio between data and the prediction is shown in the lower panel.

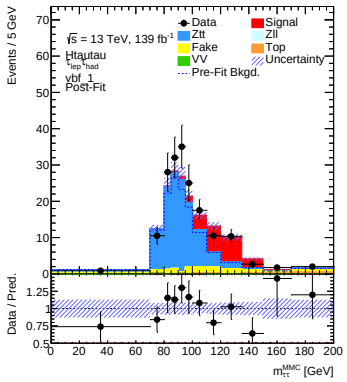

(b) Mass distribution after the unblinded fit. The ratio between data and the prediction is shown in the lower panel.

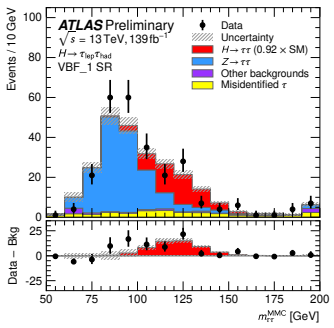

(c) Mass distribution after the unblinded fit in an alternative binning. The difference between data and the background prediction is shown in the lower panel.

Figure 8.2: Mass distributions after the sideband fit and the unblinded fit in the vbf_1 signal region of the $\tau_{\text{lep}}\tau_{\text{had}}$ channel. Figure (c) shows the result in an alternative binning that was not used in the fit and solely serves for illustrative purposes.

region shown in Figure 8.2 is one of the highest purity regions in terms of relative signal contribution, see Figure 5.5 in Section 5.3. In order to visualise the overall Higgs signal summed over all signal regions, the mass distributions have to be transformed into a common binning. This common binning is not used in the fit but solely serves illustrative purposes. Even though the histogram manipulations, such as the smoothing discussed in Section 6.2.1, can strongly depend on the chosen binning, it was verified that the final yields of individual processes only differ in the percent range between the binning used in the fit and the common binning. To account for these small differences process-dependent scale factors are introduced for the visualisation of the mass distributions in the common binning. The final result in the common binning is shown for the vbf_1 signal region of the $\tau_{\text{lep}}\tau_{\text{had}}$ channel in Figure 8.2(c). A similar level of agreement between data and simulations is observed, thus verifying the procedure of using the common binning. Finally, it is possible to combine multiple signal regions using the common binning. The combination of all signal regions of the fit is shown in Figure 8.3. Overall, the $m_{\tau\tau}^{\text{MMC}}$ distribution is well-described by the simulation and a clear Higgs boson peak close to 125 GeV is visible.

After confirming that the fit model studies based on random signal strength fits are most likely also valid for the unblinded fit and that the $m_{\tau\tau}^{\text{MMC}}$ distribution is well-described by the simulations after the unblinded fit, the results of the different cross-section measurements can be examined in detail. Differences between the sideband fit and random signal strength fit have been discussed in Section 6.3.3, showing that qualitative trends are similar for both setups and, thus, also for the

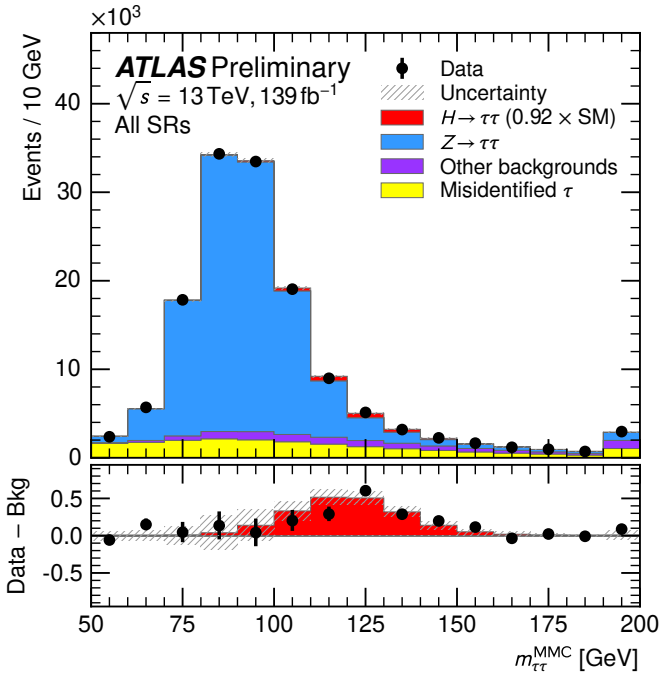

Figure 8.3: Mass distribution after the unblinded fit for the combination of all signal regions in the common binning. The procedure for this combination is explained in the text. Taken from Reference [8].

unblinded fit. Following the discussion of the measurement's results, a brief contextualisation with respect to other similar $H \to \tau\tau$ measurements will be given.

8.1 Cross-Section Measurement

In this section the measured $H \to \tau\tau$ cross-sections for the three setups introduced in Section 6.2 will be discussed. All results are measured in the rapidity range $|y_{\mathrm{H}}| < 2.5$ as discussed in Section 5.1. The measured inclusive $H \to \tau\tau$ production cross-section is

$$2.90 \pm 0.21\ (\mathrm{stat})^{+0.37}_{-0.32}\ (\mathrm{syst})\ \mathrm{pb}$$

which agrees with the Standard Model prediction of 3.15 ± 0.09 pb. A breakdown of the inclusive measurement into the individual di-τ channels is shown in Figure 8.4 with the results being normalised to the SM prediction. These results per di-τ decay channel were obtained by including only the specific reconstructed regions in the fit that correspond to the given channel. While the $\tau_{\mathrm{lep}}\tau_{\mathrm{had}}$ and $\tau_{\mathrm{had}}\tau_{\mathrm{had}}$ channel agree with the SM values, a downward deviation of the cross-section in the $\tau_e\tau_\mu$ channel of more than 1σ is observed. However, the $\tau_e\tau_\mu$ channel provides the lowest sensitivity to the measurement as highlighted by the relative uncertainties on the measured cross-sections in Figure 8.4. Since only di-τ decays with leptons of different flavour are included in the $\tau_e\tau_\mu$ channel, the overall accessible statistics of $H \to \tau\tau$ decays is further limited compared to channels including hadronic decays with overall larger branching fractions, see Section 2.3.

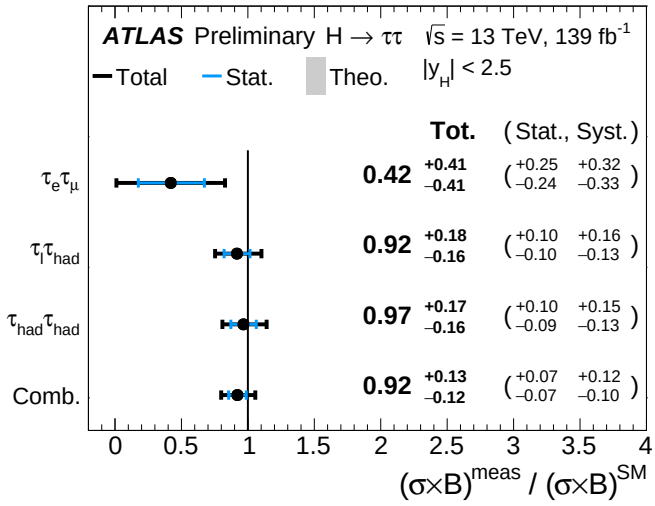

Figure 8.4: Measured inclusive $H \rightarrow \tau\tau$ production cross-section normalised to the Standard Model prediction for which the theoretical uncertainty is given. The results of di-τ channel exclusive measurements are shown also. Taken from Reference [8].

The next measurement setup in order of increasing detail targets the four major Higgs production modes discussed in Section 2.2.3 using four POIs. All four measured cross-sections, shown in Figure 8.5(a) and summarised in Table 8.1, are in agreement with the SM prediction. Although the regions in the VBFH phase space do not provide the largest data statistics, their purity allows for the most precise cross-section measurement out of the four modes. The VBFH production mode has been observed with an observed (expected) significance of $5.3(6.2)\sigma$ [8]. Additionally, evidence for the ggH production mode has been observed with an observed (expected) significance of $3.9(4.6)\sigma$ [8]. Similarly to the inclusive measurement split by di-τ decay channel, the inclusive measurement can be split by topological regions that target specific production modes as shown in Figure 8.5(b). Overall, these results agree with the four POI setup within their uncertainties. Some differences are to be expected, though, as the two setups differ in the included regions in the fit, and, thus, their correlations across regions, as well as which signal(s) are scaled by the different POIs. Taking the VBFH measurement as an example, in the region exclusive setup the POI scales all signal(s) of the inclusive measurement while only the VBFH STXS templates are scaled by the corresponding POI in the four POI setup. The difference observed for $t\bar{t}H$ between both setups will be addressed in the peer-reviewed publication with an updated flavour tagging nuisance parameter model.

Finally, the most detailed cross-section measurement is conducted within the STXS framework. The results are shown in Figure 8.6 and in Table 8.2, overall yielding cross-sections compatible with the Standard Model. As described in Section 5.1 the VBFH, VH and $t\bar{t}H$ production modes are measured inclusively. In the STXS framework the VBFH and VH production correspond to two separate electroweak bins. Possible new physics effects would become apparent, for example, in the ggH bins with $p_{\mathrm{T}}(\mathrm{H}) > 200\,\mathrm{GeV}$ [130]. No statistically significant deviations from the Standard Model predictions are observed in these bins.

The correlations between the individual POIs of the production mode dependent $H \rightarrow \tau\tau$ cross-section measurement are shown in Figure 8.7(a) and for the STXS measurement in Figure 8.7(b). Both

Production Mode	SM prediction	Result	Stat. unc.	Syst. unc. [pb]		
	[pb]	[pb]	[pb]	Th. sig.	Th. bkg.	Exp.
$t\bar{t}H$	0.031 ± 0.003	0.048 ± 0.045	±0.027	±0.011	±0.027	±0.018
VH	0.118 ± 0.003	0.11 ± 0.04	±0.02	±0.02	±0.01	±0.02
ggF	2.8 ± 0.1	2.7 ± 0.9	±0.4	±0.6	±0.1	±0.5
VBF	0.22 ± 0.01	0.196 ± 0.040	±0.026	±0.024	±0.005	±0.016
$pp \rightarrow H$	3.15 ± 0.09	2.90 ± 0.40	±0.22	±0.26	±0.06	±0.22

Table 8.1: Measured production mode dependent $H \rightarrow \tau\tau$ cross-sections. The systematic uncertainty is split into components related to the theory signal and background predictions as well as experimental uncertainties. Taken from Reference [8].

STXS bin				SM prediction	Result	Stat. unc.	Syst. unc. [pb]		
Process	m_{jj} [GeV]	p_T(H) [GeV]	N_{jets}	[pb]	[pb]	[pb]	Th. sig.	Th. bkg.	Exp.
ggF + $gg \rightarrow Z(\rightarrow qq)H$	[0, 350]$^\spadesuit$	[60, 120]	≥ 1	0.39 ± 0.06	0.17 ± 0.39	±0.22	±0.06	±0.15	±0.29
		[120, 200]	= 1	0.047 ± 0.011	0.018 ± 0.030	±0.018	±0.004	±0.004	±0.019
	[0, 350]	[120, 200]	≥ 2	0.059 ± 0.020	0.036 ± 0.039	±0.027	±0.009	±0.009	±0.025
		[200, 300]	≥ 0	0.030 ± 0.009	0.031 ± 0.011	±0.009	±0.003	±0.001	±0.006
		[300, ∞[	≥ 0	0.008 ± 0.003	0.009 ± 0.004	±0.003	±0.001	±0.000	±0.001
	[350, ∞[	[0, 200]	≥ 2	0.055 ± 0.013	0.14 ± 0.11	±0.05	±0.06	±0.01	±0.07
EWK	[60, 120]		≥ 2	0.033 ± 0.001	0.031 ± 0.020	±0.017	±0.003	±0.001	±0.010
	[350, ∞[		≥ 2	0.090 ± 0.002	0.071 ± 0.017	±0.014	±0.010	±0.002	±0.006
$t\bar{t}H$				0.031 ± 0.003	0.047 ± 0.046	±0.032	±0.011	±0.027	±0.018

Table 8.2: Measured $H \rightarrow \tau\tau$ production cross-sections within the STXS framework. As the m_{jj} cuts are only well-defined for at least two jets, they are only applied on those events which is indicated by the ♠ symbol. The systematic uncertainty is split into components related to the theory signal and background predictions as well as experimental uncertainties. Taken from Reference [8].

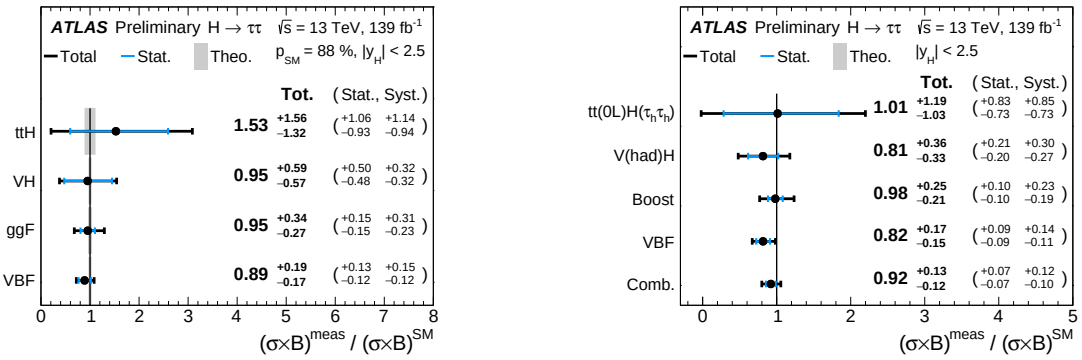

(a) Measured $H \to \tau\tau$ production cross-sections of the four major production modes.

(b) Measured $H \to \tau\tau$ production cross-sections in region exclusive fits.

Figure 8.5: Production mode dependent $H \to \tau\tau$ cross-sections. As a comparison, the cross-sections measured with the inclusive setup but using only exclusive regions are shown. Taken from Reference [8].

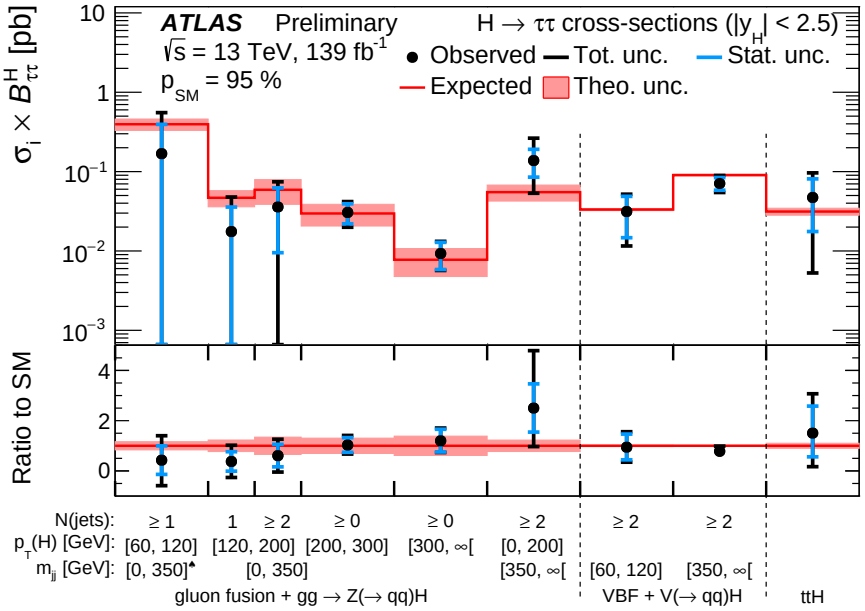

Figure 8.6: Measured $H \to \tau\tau$ production cross-sections within the STXS framework. Their absolute values as well as their ratio normalised to the Standard Model predictions are shown. Taken from Reference [8].

measurements exhibit similar structures in the observed correlations. They are likely to be caused by the signal purities shown in Figure 5.4(b) in Section 5.2. Due to the VBFH-like signature of the ggH production with at least two jets and $m_{jj} > 350\,\text{GeV}$, it contributes significantly to the lesser purity VBFH regions, thus being the probable explanation for the observed correlation between VBFH and ggH production. Since the $t\bar{t}H$ regions are defined by a characteristic and unique signature, the other production modes' contributions to these regions are negligible. This results in the observed small correlations between $t\bar{t}H$ and the other production modes. Ultimately, the correlations across the different POIs could possibly be further reduced by constructing signal regions with even higher purity. However, as multivariate analysis techniques are already implemented for the VBFH, VH and $t\bar{t}H$ regions, this endeavour could prove challenging.

8.1.1 Impact of Uncertainties

In principle, the impact of individual uncertainty (groups) on the measured POI(s) can be assessed for all measurement setups. However, to simplify the discussion of these impacts the focus will lie on the inclusive $H \to \tau\tau$ measurement. Apart from production mode specific theory uncertainties and phase space dependent experimental uncertainties, the observations in the inclusive measurement reflect the general behaviour. Theory uncertainties that, for example, solely apply to VH production mode by construction have a larger impact on the corresponding POI compared to the inclusive POI.

Individual nuisance parameters can be ranked according to their impact on the measurement's POI(s). This ranking is computed by calculating the difference in the best-fit POI value between the nominal fit and conditional fits fixing the investigated NP to its post-fit pull varied by the constraint in both directions. The ten highest ranked NPs are shown in Figure 8.8. While most of them are related to theory prediction uncertainties on the signal(s), one jet related NP is highly ranked as well as the luminosity uncertainty. It has to be noted that the luminosity uncertainty is only applied to small backgrounds that are fixed to their Standard Model predictions unlike the Top, misidentified τ-lepton and $Z \to \tau\tau$ backgrounds whose normalisation is determined in the fit. Thus, this degree of freedom provides a lever to the fit allowing for normalisation variations of those backgrounds without varying the other backgrounds.

The result of a more inclusive measure of the impact of nuisance parameter groups is summarised in Table 8.3. By removing nuisance parameter categories from the fit the final uncertainty on a given POI generally decreases. Error propagation of the difference of this new uncertainty with respect to the original uncertainty that includes all NPs provides the impact's estimate. The observed NP category impacts align with the observations of individual NP impacts in Figure 8.8. The signal theory uncertainties have the largest impact on the result, followed by Jet and $E_{\text{T}}^{\text{miss}}$ related uncertainties. As the Jet and $E_{\text{T}}^{\text{miss}}$ related uncertainties directly modify the shape and normalisation of $m_{\tau\tau}^{\text{MMC}}$, this category is to be expected to have a significant impact. Due to correlations between the NP categories, the summed impacts using error propagation do not reflect the total uncertainty. Overall, the measurement is limited by systematic uncertainties rather than statistical uncertainties related to the dataset size.

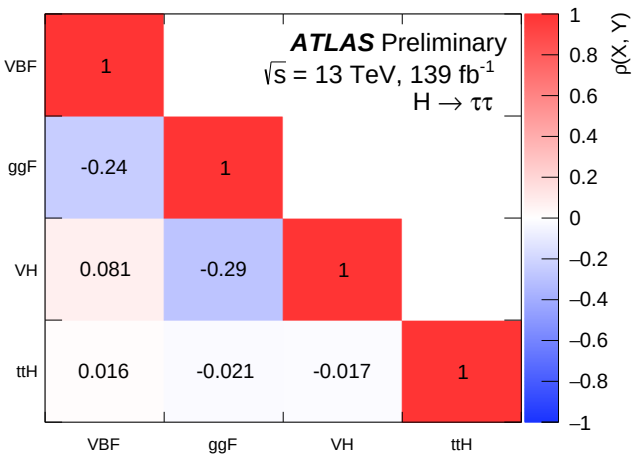

(a) Observed correlations in the four POI setup.

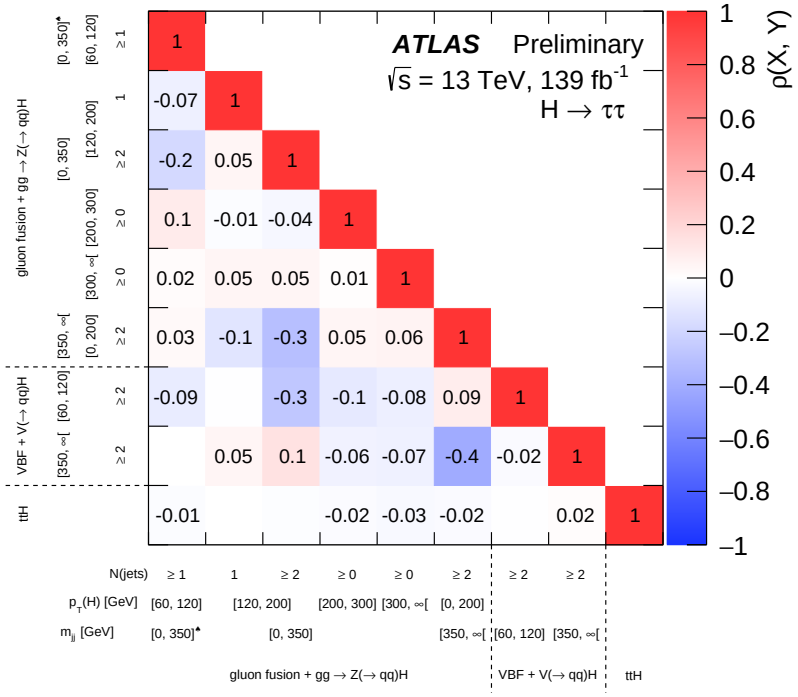

(b) Observed correlations in the STXS setup.

Figure 8.7: Correlations between the POIs used to measure the production mode dependent cross-sections and the STXS cross-sections. Taken from Reference [8].

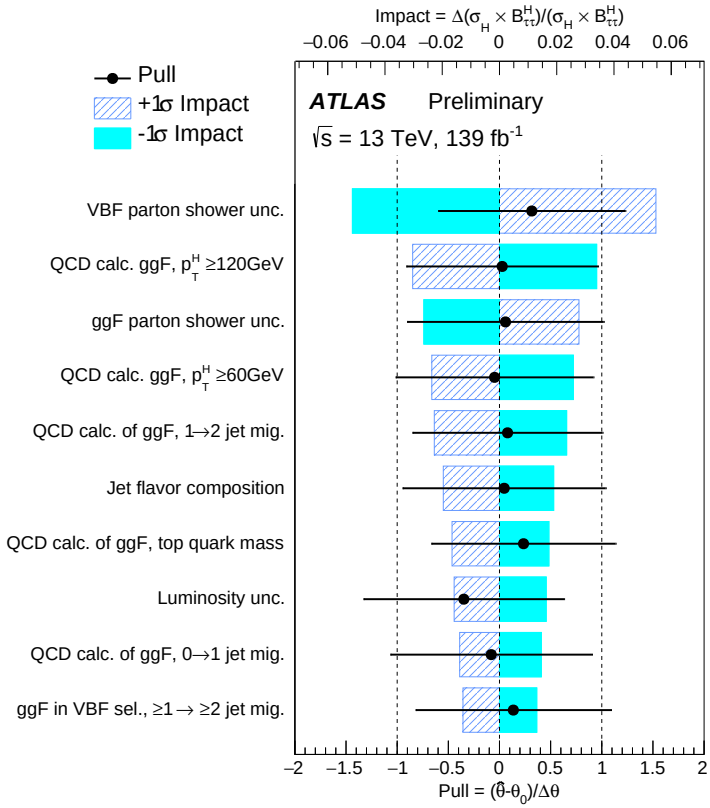

Figure 8.8: Highest ranked nuisance parameters with respect to their impact on the inclusive $H \to \tau\tau$ production cross-section. Taken from Reference [8].

Source of uncertainty	Impact on $\Delta\sigma/\sigma(pp \to H \to \tau\tau)$ [%]	
	Observed	Expected
Theoretical uncertainty in signal	8.1	8.6
Jet and $E_{\mathrm{T}}^{\mathrm{miss}}$	4.2	4.1
Background sample size	3.7	3.4
Hadronic τ decays	2.0	2.1
Misidentified τ	1.9	1.8
Luminosity	1.7	1.8
Theoretical uncertainty in Top processes	1.4	1.2
Theoretical uncertainty in Z+jets processes	1.1	1.1
Flavour tagging	0.5	0.5
Electrons and muons	0.4	0.3
Total systematic uncertainty	11.1	11.0
Data sample size	6.6	6.3
Total	12.8	12.5

Table 8.3: Expected and observed impact of uncertainty categories on the POI in the inclusive $H \to \tau\tau$ cross-section measurement. Taken from Reference [8].

8.2 Results in the Context of Other $H \to \tau\tau$ Measurements

Single measurements are subject to statistical data fluctuations. Thus, they can confirm agreement with a certain theoretical model or observation of a new effect with a certain confidence but they have to be interpreted within the context of additional and if possible similar measurements. Consistent results strengthen the drawn conclusions. In the following, the measurement presented in this thesis will briefly be compared to two other $H \to \tau\tau$ coupling measurements conducted by the ATLAS and CMS collaborations.

8.2.1 ATLAS Measurement with 36 fb^{-1}

The first measurement to which the results discussed in Section 8.1 will be compared to has been conducted by the ATLAS collaboration with a smaller dataset of 36 fb^{-1}, published in Reference [7]. The 36 fb^{-1} dataset has also been recorded during Run II and covers the years 2015 and 2016. It has to be noted that the reconstruction algorithms and measurements of uncertainties and scale factors discussed in Section 3.3 have been updated for the full dataset, including the years 2015 and 2016, in the presented analysis. This measurement can be considered the predecessor of the measurement presented in this thesis. While the overall analysis design is similar to the presented measurement, some aspects do differ, making a direct one-to-one comparison of e.g. individual nuisance parameters difficult. The most striking changes with respect to the predecessor analysis comprise updated misidentified τ-lepton estimates, the restriction of the $\tau_e\tau_\mu$ channel to differently flavoured leptons and the usage of the simplified embedding technique introduced in Section 5.3.2 for the Z + jets control regions. Other differences are partly motivated by the increased dataset, giving access to more production modes such as VH and $t\bar{t}H$ and a finer binned STXS measurement.

Nevertheless, especially the inclusive $H \to \tau\tau$ measurements of both analyses are suitable for a comparison. Due to the outlined differences in the analysis setup no detailed in-depth analysis will be given. With an observed $H \to \tau\tau$ production cross-section of $3.77^{+1.06}_{-0.95}$ pb the predecessing result agrees with the presented measurement within the uncertainties [7]. As outlined in Reference [7], theory uncertainties on the signals also proved to be the largest source of uncertainty in this analysis. The highest ranked nuisance parameters for both measurements are signal theory uncertainties and jet related uncertainties.

The increase in luminosity with respect to the predecessor measurement and, thus, data statistics naively can result in an improvement of some uncertainty components by a factor of:

$$\sqrt{\frac{139\,\text{fb}^{-1}}{36\,\text{fb}^{-1}}} \approx 2\,. \tag{8.1}$$

However, this scaling does not automatically apply to all sources of uncertainty such as uncertainties on theoretical predictions which are decoupled from the data statistics as they rely on prescriptions from the theory communites. The observed impacts of the individual uncertainty categories are compared to the predecessor measurement in Table 8.4, highlighting their ratios. Thanks to the efforts of the theory communites a ratio of 1.37 is achieved for the theoretical uncertainties on the signal prediction. The theoretical uncertainties related to the background predictions could be improved by a factor of 2.28. As these uncertainties do not directly impact the signal, the improvement is likely the result of multiple advancements, on the one hand, the theory community's prescriptions

Source of uncertainty	Observed impact on $\Delta\sigma / \sigma(pp \to H \to \tau\tau)$ [%]		Ratio
	$139\,\text{fb}^{-1}$ [8]	$36\,\text{fb}^{-1}$ [7]	$\frac{36\,\text{fb}^{-1}}{139\,\text{fb}^{-1}}$
Theoretical uncertainty in signal	8.1	11.1	1.37
Jet and $E_{\text{T}}^{\text{miss}}$	4.2	10.2	2.43
Background sample size	3.7	10.4	2.81
Hadronic τ decays	2.0	3.7	1.85
Misidentified τ	1.9	4.4	2.32
Luminosity	1.7	2.9	1.71
Theoretical uncertainty in backgrounds	1.8	4.1	2.28
Flavour tagging	0.5	3.4	6.80
Electrons and muons	0.4	1.1	2.75
Total systematic uncertainty	11.1	21.5	1.94
Data sample size	6.6	16	2.42
Total	12.8	26.5	2.07

Table 8.4: Observed impact of uncertainty categories on the POI in the inclusive $H \to \tau\tau$ cross-section measurement presented in this thesis as well as Reference [7]. Their respective dataset's luminosity is used as a short-hand notation to refer to these measurements. The arithmetic mean is shown for Reference [7]. For a better comparison the theoretical uncertainties in Top and Z + jets have been grouped into backgrounds to match Reference [7]. Numbers are taken from the provided references in the table.

of these uncertainties and on the other hand, the measurement design itself. By introducing Z + jets control regions, that are paired with the individual signal regions and utilise the simplified embedding technique, the final impact on the signal was reduced. Although the simulated background sample size is not directly dependent on the luminosity, the number of simulated events typically scales similarly to provide sufficient statistics for the modelling of observales. An additional extension of the number of simulated $Z \to \tau\tau$ events, see Reference [8], results in the observed ratio of 2.81. Finally, the experimental uncertainties are usually the results of measurements themselves, see Section 3.3. Thus, the final uncertainties are composed of statistical components as well as systematic components which means that the scaling introduced in Equation 8.1 only represents an upper bound if an uncertainty measurement is dominated by its statistical component. Nevertheless, in most uncertainty categories corresponding to the experimental uncertainties, a scaling close to this upper bound is observed and, in some cases, even improvements beyond. Especially striking is the improvement of the flavour tagging uncertainty's impact by a factor of 6.8. This improvement cannot solely be explained by the improvement of the uncertainty determination described in Reference [73] with respect to Reference [165]. The measurement design as well as the corresponding uncertainty prescriptions are possible other explanations for the observed improvement. By including signal regions targeting the $t\bar{t}H$ production mode, shape information of distributions containing b-quark initiated jets are included for the first time in the $H \to \tau\tau$ measurement. Also, it has to be noted that the flavour tagging category is one of the categories with the smallest impact on the measured $H \to \tau\tau$ cross-section.

Overall, an improvement of the measured cross-section's uncertainty by a factor of 2.07 is observed which is the result of enhancements beyond a pure increase in data statistics. The measured cross-sections and observations of which uncertainties impact the analyses the most are consistent between the measurement presented in this thesis and the predecessing measurement.

8.2.2 CMS Measurement with 137 fb^{-1}

The second measurement drawn in for comparison has been conducted by the CMS collaboration based on a similar sized dataset with an integrated luminosity of 137 fb^{-1} collected during Run II, see Reference [166]. While the general analysis strategy is similar for both measurements, some key aspects do differ. Similar background estimation techniques have been implemented in both measurements in terms of the usage of data driven techniques for misidentified τ-lepton backgrounds and Monte Carlo simulations for smaller backgrounds. The major background of Z + jets is estimated via an embedding procedure in the CMS analysis that resembles the procedure described in References [143, 144] rather than the simplified embedding implemented in the measurement presented in this thesis.

Instead of solely relying on the invariant di-τ mass as the observable and defining signal regions through other variables and multivariate techniques, the CMS measurement implements a two-dimensional approach. Effectively, the invariant di-τ mass, $m_{\tau\tau}$, is split into bins of a second observable. This second observable is chosen depending on the signal region and either helps separating signal from background or gives access to the targeted STXS bins. In case of the boosted categories it is chosen to be p_{T}(H) since the STXS bins are split accordingly.

Although both measurements aim to measure the $H \rightarrow \tau\tau$ cross-sections within the STXS framework, the final merging scheme of STXS bins differs. While the CMS measurement does not target $t\bar{t}H$ production, it does implement a more resolved measurement of the VBFH like production. The individual merging schemes for the electroweak STXS production bins are shown in Figure 8.9 and the merging schemes for the gluon-gluon fusion STXS production bins in Figure 8.10. Apart from the more resolved VBFH like production in the CMS measurement, it does not specifically target the VH like production bin. This production mode is part of the more inclusive non-VBF topology. No dedicated reconstructed category has been implemented for this production mode and, thus, these events are mostly sorted into the boosted categories. The main differences regarding the gluon-gluon

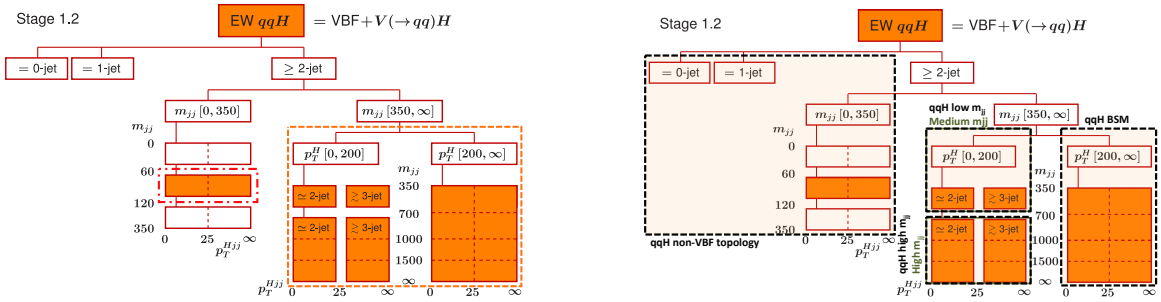

(a) ATLAS scheme. Taken from Reference [129] and modified.

(b) CMS scheme. Taken from Reference [166].

Figure 8.9: STXS merging schemes implemented in the ATLAS [8] and the CMS [166] measurement, respectively. The electroweak production bins are shown.

fusion production bins concern the granularity of bins with more than one jet and bins with exactly one jet. On the one hand, bins with more than one jet show a finer granularity in the ATLAS scheme and on the other hand, the CMS scheme additionally targets the low p_{T}(H) bin with exactly one jet. Due to the trigger requirements discussed in Section 5.2, the ATLAS scheme is not able to include the bins with no additional jets, which the CMS scheme is able to do. These differences in the merging schemes render a direct comparison of measured STXS cross-sections difficult. Thus, the main focus

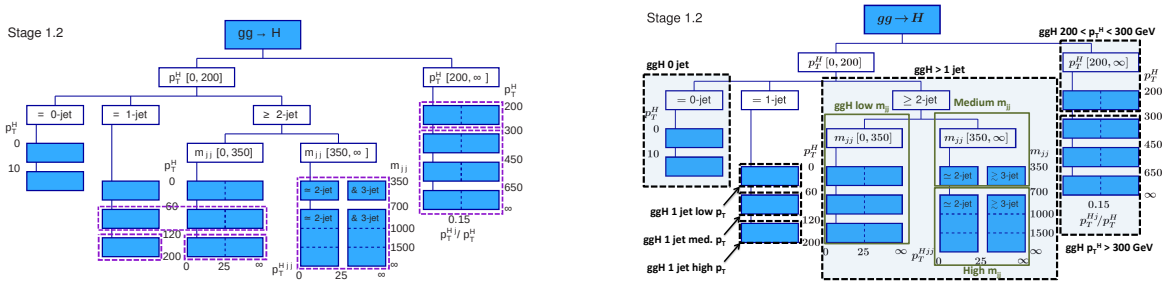

(a) ATLAS scheme. Taken from Reference [129] and modified.

(b) CMS scheme. Taken from Reference [166].

Figure 8.10: STXS merging schemes implemented in the ATLAS [8] and the CMS [166] measurement, respectively. The gluon-gluon fusion production bins are shown.

will lie on the measured inclusive $H \rightarrow \tau\tau$ production cross-sections.

The inclusive $H \rightarrow \tau\tau$ production cross-section normalised to the Standard Model prediction has been measured to be $0.85^{+0.12}_{-0.11}$ by the CMS collaboration [166]. This result agrees with the measured cross-section discussed in Section 8.1 within their uncertainties. Both measurements achieve a similar relative precision of roughly 14 %. A detailed comparison of how uncertainties impact the measured cross-section cannot be performed as the needed information are not given in Reference [166]. While the magnitudes of the uncertainties are listed, no information about their impact on the measured cross-sections are provided. Overall, the discussed results statistically agree with the Standard Model predictions and show consistent behaviour.

CHAPTER 9

Conclusion

Possible new physics effects originating from theories beyond the Standard Model (SM) can either be directly observed in searches for new particles or through deviations from the theoretical expectation of Standard Model processes. Since its discovery in 2012 [1, 2] a Standard Model-like Higgs boson has been experimentally established. With the increasing amount of data collected at the LHC, the Higgs measurements of ATLAS and CMS have become more and more precise. Due to the mass of the τ-lepton it is expected to exhibit the strongest coupling to the Higgs boson out of all leptons. In contrast to measurements targeting the coupling to other third generation fermions like bottom quarks, the expected backgrounds are smaller since processes producing multiple jets play a less significant role in the di-τ channel. Hence, the Higgs boson coupling in τ-lepton decays can be measured with higher precision than other fermionic decays. The presented work measures the inclusive $H \rightarrow \tau\tau$ production cross-section as well as more detailed cross-sections split by production mode or split into bins of the theoretical Simplified Template Cross Sections (STXS) framework in which cross-sections are measured as a function of other observables such as the transverse momentum of the Higgs boson.

While the general measurement design is the result of collaborative efforts, detailed contributions to the mass reconstruction as well as the validation and understanding of the fit model are documented in this thesis. All di-τ decay combinations are included in the measurement, except for di-leptonic decays of the same lepton flavour, due to the limited sensitivity it provides and the large uncertainties of its accompanying backgrounds. With the dataset of 139 fb^{-1} recorded during Run II, reconstructed categories targeting the four major Higgs production modes, gluon-gluon fusion (ggH), vector boson fusion (VBFH), associated production with a vector boson (VH) and associated production with a pair of top quarks ($t\bar{t}H$), are defined. By utilising multivariate analysis techniques, the inclusive VBFH, VH and $t\bar{t}H$ categories are further split into regions of higher (signal) purity and lower purity. The major backgrounds are either estimated using data driven techniques (misidentified τ-leptons) or from simulations that are simultaneously constrained in control regions in the fit ($Z \rightarrow \tau\tau$ and Top). A novel simplified embedding procedure has been implemented to provide high statistics Z + jets control regions for this purpose. Other smaller backgrounds are normalised to their Standard Model expectations and are varied within uncertainties.

The invariant di-τ mass, estimated by the Missing Mass Calculator (MMC), is the final discriminating observable used in the measurement. Thorough studies on the algorithm as well as the included probability density functions (p.d.f.s) have been performed. Overall, a similar performance with respect to its implementation used in Reference [7] in terms of Z + jets versus Higgs boson separation

has been achieved while speeding up the algorithm by a factor of roughly two to four, depending on the di-τ channel. At the same time, the MMC's code has been refactored, making it more accessible and adaptable for users. Together with the presented studies this thesis provides a full documentation of every step and p.d.f. choice of the algorithm.

The final fit model has been thoroughly validated using Asimov pseudodata and partially unblinded fits. In this context, some aspects of the model and implementations of nuisance parameters have been studied in detail. As a result of these studies, the τ_{had} reconstruction efficiency uncertainty has been determined for the first time in an in-situ measurement in an ATLAS analysis. Additionally, a new toy-based approach to validate complex fit models has been introduced. With this approach, predictions on which nuisance parameters might get pulled or constrained in the fit to real data are made possible for the first time. Furthermore, the overall consistency of the chosen model with respect to (partially) unblinded fits can be assessed in a stable way.

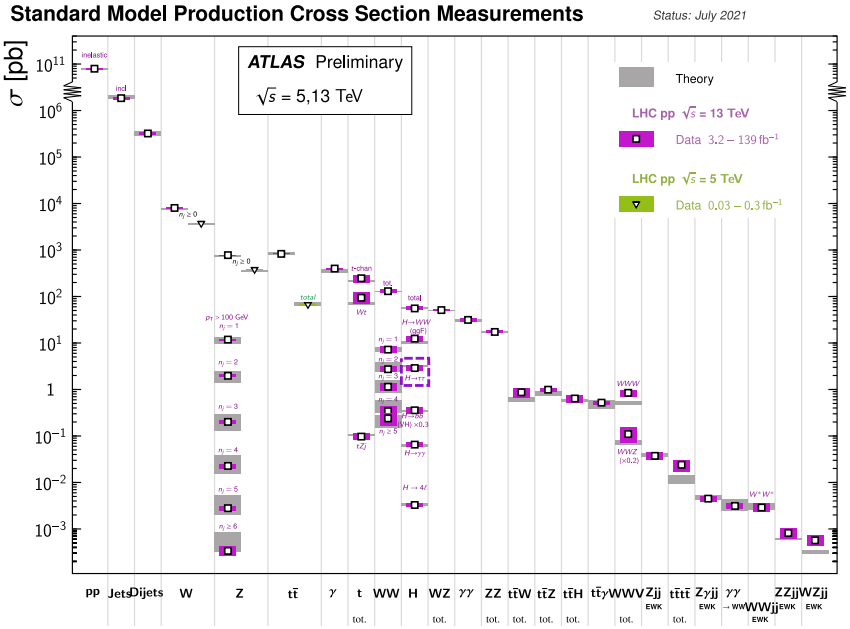

Figure 9.1: Measured SM production cross-sections at ATLAS using datasets at 5 TeV and 13 TeV. Taken from Reference [167] and modified to highlight the $H \rightarrow \tau\tau$ cross-section contributed by this measurement.

All measured $H \rightarrow \tau\tau$ cross-sections agree with the SM predictions within their uncertainties, achieving the highest precision and level of detail of an ATLAS $H \rightarrow \tau\tau$ measurement to date. The inclusive cross-section is measured to be $2.90 \pm 0.21\,(\text{stat})\,^{+0.37}_{-0.32}\,(\text{syst})$ pb which is in agreement with the SM prediction of 3.15 ± 0.09 pb [8]. A first time ATLAS standalone observation of VBFH production in the di-τ channel has been confirmed with a significance of 5.3σ [8]. Evidence for ggH production in the di-τ channel has been observed with a significance of 3.9σ [8]. The agreement of the measured cross-section with the SM prediction is highlighted in Figure 9.1, showing the measured SM production cross-sections at ATLAS. With respect to other Higgs boson analyses measuring fermionic couplings, the presented measurement achieves the highest precision, see e.g. References [168, 169] for analyses with the Higgs boson decaying into two bottom quarks.

One of the advantages of the STXS framework is the capability to combine multiple measurements even with different final states. The latest iteration of such a combination for ATLAS analyses can be found in Reference [170]. It includes the results presented in this thesis as well as other updated anayses. Although, no detailed breakdown of individual analyses' contribution to the STXS combination is given, the provided production mode inclusive comparison gives an idea of this measurement's contribution. Typically, the STXS bins measured with the smallest uncertainties, especially the VBFH production mode, provide sensitivity. Furthermore, continuing measurements utilising the $H \rightarrow \tau\tau$ process can be conducted such as the measurement of the Higgs boson's combined charge conjugation and parity (CP) properties. A first result, based on the theoretical idea for such a measurement given in References [38, 39], has been published by the CMS collaboration which is in agreement with a Standard Model-like Higgs boson [43].

Towards Run III and the HL-LHC Datasets with larger statistics will be gathered at the LHC during its upcoming Run III and its extension to higher luminosities, the High-Luminosity LHC (HL-LHC) [171]. As the measurement is overall limited by systematic uncertainties, further increasing data statistics do not automatically translate into increased sensitivities in all phase spaces. However, certain production modes do benefit from increased statistics such as the cross-section measurements of the VH and $t\bar{t}H$ production modes. Additionally, more detailed STXS schemes become accessible with increasing statistics. In this context, the application of neural networks to define regions of high signal purity could be studied.

Further studies regarding the mass reconstruction based on the presented work, or following a new approach using neural networks, could improve the measurement's overall sensitivity, given that they result in an improved resolution and, thus, separation power of $Z \rightarrow \tau\tau$ and $H \rightarrow \tau\tau$. A small excerpt of such studies that already have been conducted is given in Section 4.5. Instead of improving the mass reconstruction itself, reducing the impact of Jet and $E_{\mathrm{T}}^{\mathrm{miss}}$ related uncertainties on the same could possibly increase the sensitivity as this uncertainty category is the second leading source of systematic uncertainties in the measurement.

Another approach to possibly improve the measurement's sensitivity could be the explicit utilisation of the available hadronic τ-lepton decay mode classification. The MMC's separation power depends on the τ-lepton decay mode. Since the τ-lepton energy resolution and angular resolution depend on its decay mode this behaviour is to be expected. Decay modes with little to no neutral hadronic activity and dominated by charged pions can utilise the tracker information to its full potential. Furthermore, the decay mode could be used to define individual τ_{had} identification working points, depending on the contribution of misidentified τ-leptons to specific decay modes. This could either help to further reduce the misidentified τ-lepton background in di-τ channels that include hadronic τ-leptons or to increase the available statistics in these channels. By lowering the identification requirement and imposing decay mode requirements at the same time, the overall statistics can possibly be increased while keeping a similar level of misidentified τ-lepton background in decay modes with small misidentified τ-lepton contributions.

Altogether, future measurements of the $H \rightarrow \tau\tau$ process promise a wealth of interesting results, either through improvements of the presented measurement or through measurements of other Higgs boson properties in this decay. More detailed studies of the introduced validation techniques for complex fit models can help in the understanding of future likelihood models. With increasing statistics and advancements of measurement techniques these models will likely increase in their complexity.

Bibliography

[1] ATLAS Collaboration, *Observation of a new particle in the search for the Standard Model Higgs boson with the ATLAS detector at the LHC*, Phys. Lett. B **716** (2012) 1, arXiv: 1207.7214 [hep-ex] (cit. on pp. 1, 12, 127).

[2] CMS Collaboration, *Observation of a New Boson at a Mass of 125 GeV with the CMS Experiment at the LHC*, Phys. Lett. B **716** (2012) 30, arXiv: 1207.7235 [hep-ex] (cit. on pp. 1, 12, 127).

[3] O. S. Brüning et al., *LHC Design Report*, CERN Yellow Reports: Monographs, CERN, 2004, URL: https://cds.cern.ch/record/782076 (cit. on pp. 1, 17).

[4] L. Evans and P. Bryant, *LHC Machine*, Journal of Instrumentation **3** (2008) S08001, URL: https://doi.org/10.1088/1748-0221/3/08/s08001 (cit. on pp. 1, 17).

[5] M. Chalmers, *The Large Hadron Collider: 10 years and counting*, CERN, URL: https://home.cern/news/news/accelerators/large-hadron-collider-10-years-and-counting (visited on 19/09/2021) (cit. on p. 1).

[6] ATLAS Collaboration, *ATLAS data quality operations and performance for 2015–2018 data-taking*, JINST **15** (2020) P04003, arXiv: 1911.04632 [physics.ins-det] (cit. on pp. 1, 19).

[7] ATLAS Collaboration, *Cross-section measurements of the Higgs boson decaying into a pair of τ-leptons in proton-proton collisions at $\sqrt{s} = 13$ TeV with the ATLAS detector*, Phys. Rev. D **99** (7 2019) 072001, URL: https://link.aps.org/doi/10.1103/PhysRevD.99.072001 (cit. on pp. 2, 39, 43, 49, 52, 57, 58, 62, 92–94, 122, 123, 127, 171, 172, 189).

[8] ATLAS Collaboration, *Measurements of Higgs boson production cross-sections in the $H \to \tau^+\tau^-$ decay channel in pp collisions at $\sqrt{s} = 13$ TeV with the ATLAS detector*, ATLAS-CONF-2021-044, CERN, 2021, URL: https://cds.cern.ch/record/2779179 (cit. on pp. 2, 18, 19, 23–26, 69, 71–84, 89, 115–118, 120, 121, 123–125, 128, 179).

[9] C. N. Yang and R. L. Mills, *Conservation of Isotopic Spin and Isotopic Gauge Invariance*, Phys. Rev. **96** (1 1954) 191, URL: https://link.aps.org/doi/10.1103/PhysRev.96.191 (cit. on pp. 3, 6).

[10] G. Münster, *Von der Quantenfeldtheorie zum Standardmodell*, De Gruyter, 2019, ISBN: 9783110638547, URL: https://doi.org/10.1515/9783110638547 (cit. on pp. 3, 5, 7).

[11] M. Diehl and W. Hollik, "The Standard Model: Our Picture of the Microcosm", *Physics at the Terascale*, John Wiley & Sons, Ltd, chap. 2 23, ISBN: 9783527634965, eprint: https://onlinelibrary.wiley.com/doi/pdf/10.1002/9783527634965.ch2, URL: https://onlinelibrary.wiley.com/doi/abs/10.1002/9783527634965.ch2 (cit. on pp. 3–10).

[12] R. Wolf, "The Higgs Boson in the Standard Model of Particle Physics", *The Higgs Boson Discovery at the Large Hadron Collider*, Springer International Publishing, 2015 15, ISBN: 978-3-319-18512-5, URL: https://doi.org/10.1007/978-3-319-18512-5_2 (cit. on pp. 3, 7, 10).

[13] A. Angelis and M. Pimenta, *Introduction to particle and astroparticle physics: Questions to the universe*, 2015 1, ISBN: 978-88-470-2687-2 (cit. on pp. 3, 7).

[14] Muon g-2 Collaboration, *Measurement of the Positive Muon Anomalous Magnetic Moment to 0.46 ppm*, Phys. Rev. Lett. **126** (14 2021) 141801, URL: https://link.aps.org/doi/10.1103/PhysRevLett.126.141801 (cit. on p. 4).

[15] Muon g-2 Collaboration, *Measurement of the anomalous precession frequency of the muon in the Fermilab Muon g − 2 Experiment*, Phys. Rev. D **103** (7 2021) 072002, URL: https://link.aps.org/doi/10.1103/PhysRevD.103.072002 (cit. on p. 4).

[16] N. e. a. MissMJ, *Standard Model of Elementary Particles modified version*, 2014, URL: https://commons.wikimedia.org/wiki/File:Standard_Model_of_Elementary_Particles_modified_version.svg (visited on 12/06/2021) (cit. on p. 4).

[17] R. Wolf, "Higgs Boson Searches Before the Advent of the Large Hadron Collider", *The Higgs Boson Discovery at the Large Hadron Collider*, Springer International Publishing, 2015 53, ISBN: 978-3-319-18512-5, URL: https://doi.org/10.1007/978-3-319-18512-5_3 (cit. on p. 5).

[18] S. L. Glashow, *Partial Symmetries of Weak Interactions*, Nucl. Phys. **22** (1961) 579 (cit. on p. 5).

[19] S. Weinberg, *A Model of Leptons*, Phys. Rev. Lett. **19** (1967) 1264 (cit. on p. 5).

[20] A. Salam, *Weak and Electromagnetic Interactions*, Conf. Proc. C **680519** (1968) 367 (cit. on p. 5).

[21] UA1 Collaboration, *Experimental Observation of Isolated Large Transverse Energy Electrons with Associated Missing Energy at* $\sqrt{s}$ = 540 *GeV*, Phys. Lett. B **122** (1983) 103 (cit. on pp. 6, 30).

[22] UA2 Collaboration, *Observation of Single Isolated Electrons of High Transverse Momentum in Events with Missing Transverse Energy at the CERN anti-p p Collider*, Phys. Lett. B **122** (1983) 476 (cit. on p. 6).

[23] UA1 Collaboration, *Experimental Observation of Lepton Pairs of Invariant Mass Around 95 GeV/*c^2 *at the CERN SPS Collider*, Phys. Lett. B **126** (1983) 398 (cit. on p. 6).

[24] UA2 Collaboration, *Evidence for $Z^0 \to e^+e^-$ at the CERN $\bar{p}p$ Collider*, Phys. Lett. B **129** (1983) 130 (cit. on p. 6).

[25] Particle Data Group, *Review of Particle Physics*, PTEP **2020** (2020) 083C01 (cit. on pp. 6, 13, 14, 27, 29–32, 45, 46, 75, 90).

[26] S.-O. Moch and K. Rabbertz, "Hard QCD: Still Going Strong", *Physics at the Terascale*, John Wiley & Sons, Ltd, chap. 4 73, ISBN: 9783527634965, eprint: https://onlinelibrary.wiley.com/doi/pdf/10.1002/9783527634965.ch4, URL: https://onlinelibrary.wiley.com/doi/abs/10.1002/9783527634965.ch4 (cit. on pp. 7, 25).

[27] P. W. Higgs, *Broken Symmetries and the Masses of Gauge Bosons*, Phys. Rev. Lett. **13** (16 1964) 508, URL: https://link.aps.org/doi/10.1103/PhysRevLett.13.508 (cit. on p. 7).

[28] F. Englert and R. Brout, *Broken Symmetry and the Mass of Gauge Vector Mesons*, Phys. Rev. Lett. **13** (9 1964) 321, URL: https://link.aps.org/doi/10.1103/PhysRevLett.13.321 (cit. on p. 7).

[29] G. S. Guralnik, C. R. Hagen and T. W. B. Kibble, *Global Conservation Laws and Massless Particles*, Phys. Rev. Lett. **13** (20 1964) 585, URL: https://link.aps.org/doi/10.1103/PhysRevLett.13.585 (cit. on p. 7).

[30] J. Ellis, *Higgs Physics*, (2013) 117, 52 pages, 45 figures, Lectures presented at the ESHEP 2013 School of High-Energy Physics, to appear as part of the proceedings in a CERN Yellow Report, arXiv: 1312.5672, URL: https://cds.cern.ch/record/1638469 (cit. on p. 8).

[31] H. Yukawa, *On the Interaction of Elementary Particles I*, Proc. Phys. Math. Soc. Jap. **17** (1935) 48 (cit. on p. 9).

[32] N. Cabibbo, *Unitary Symmetry and Leptonic Decays*, Phys. Rev. Lett. **10** (12 1963) 531, URL: https://link.aps.org/doi/10.1103/PhysRevLett.10.531 (cit. on p. 10).

[33] M. Kobayashi and T. Maskawa, *CP-Violation in the Renormalizable Theory of Weak Interaction*, Progress of Theoretical Physics **49** (1973) 652, ISSN: 0033-068X, eprint: https://academic.oup.com/ptp/article-pdf/49/2/652/5257692/49-2-652.pdf, URL: https://doi.org/10.1143/PTP.49.652 (cit. on p. 10).

[34] G. Hiller and U. Uwer, "Quark Flavour Physics", *Physics at the Terascale*, John Wiley & Sons, Ltd, chap. 8 163, ISBN: 9783527634965, eprint: https://onlinelibrary.wiley.com/doi/pdf/10.1002/9783527634965.ch8, URL: https://onlinelibrary.wiley.com/doi/abs/10.1002/9783527634965.ch8 (cit. on p. 10).

[35] BaBar Collaboration, *Observation of CP violation in the B^0 meson system*, Phys. Rev. Lett. **87** (2001) 091801, arXiv: hep-ex/0107013 (cit. on p. 10).

[36] Belle Collaboration, *Observation of large CP violation in the neutral B meson system*, Phys. Rev. Lett. **87** (2001) 091802, arXiv: hep-ex/0107061 (cit. on p. 10).

[37] Belle-II Collaboration, *The Belle II Physics Book*, PTEP **2019** (2019) 123C01, ed. by E. Kou and P. Urquijo, [Erratum: PTEP 2020, 029201 (2020)], arXiv: 1808.10567 [hep-ex] (cit. on p. 10).

[38] S. Berge, W. Bernreuther and S. Kirchner, *Determination of the Higgs CP-mixing angle in the tau decay channels at the LHC including the Drell–Yan background*, Eur. Phys. J. C **74** (2014) 3164, arXiv: 1408.0798 [hep-ph] (cit. on pp. 10, 129).

[39] S. Berge, W. Bernreuther and S. Kirchner, *Prospects of constraining the Higgs boson's CP nature in the tau decay channel at the LHC*, Phys. Rev. D **92** (2015) 096012, arXiv: 1510.03850 [hep-ph] (cit. on pp. 10, 129).

[40] M. Hübner, *Effects of tau decay product reconstruction in a Higgs CP analysis with the ATLAS experiment*, MA thesis: Universität Bonn, 2016, URL: https://web.physik.uni-bonn.de/group/view.php?&group=1&lang=de&c=t&id=81 (visited on 26/07/2021) (cit. on pp. 10, 36, 43, 45).

[41] A. Manthei, *Studies towards constraining the CP properties of the Higgs boson in its decays to tau leptons*, MA thesis: Universität Bonn, 2019, URL: https://web.physik.uni-bonn.de/group/view.php?&group=1&lang=de&c=t&id=122 (visited on 02/10/2021) (cit. on p. 10).

[42] Maike Christina Hansen, *Studies into measuring the Higgs CP-state in $H \to \tau\tau$ decays at ATLAS*, PhD thesis: Rheinische Friedrich-Wilhelms-Universität Bonn, 2020, URL: https://hdl.handle.net/20.500.11811/8456 (cit. on p. 10).

[43] CMS Collaboration, *Analysis of the CP structure of the Yukawa coupling between the Higgs boson and τ leptons in proton-proton collisions at $\sqrt{s} = 13$ TeV*, (2021), arXiv: 2110.04836 [hep-ex] (cit. on pp. 10, 129).

[44] A. D. Sakharov, *Violation ofCPin variance,Casymmetry, and baryon asymmetry of the universe*, Soviet Physics Uspekhi **34** (1991) 392, URL: https://doi.org/10.1070/pu1991v034n05abeh002497 (cit. on p. 10).

[45] LHC Higgs Cross Section Working Group, *Handbook of LHC Higgs Cross Sections: 4. Deciphering the Nature of the Higgs Sector*, **2/2017** (2016), arXiv: 1610.07922 [hep-ph] (cit. on pp. 12, 13, 70, 84).

[46] ATLAS Collaboration, *LHC Higgs Working Group, Higgs Production Cross Sections*, 2021, URL: https://twiki.cern.ch/twiki/bin/view/LHCPhysics/CERNYellowReportPageAt13TeV (visited on 02/08/2021) (cit. on p. 12).

[47] ATLAS Collaboration, *Determination of spin and parity of the Higgs boson in the $WW^* \to e\nu\mu\nu$ decay channel with the ATLAS detector*, Eur. Phys. J. C **75** (2015) 231, arXiv: 1503.03643 [hep-ex] (cit. on p. 12).

[48] ATLAS Collaboration,
Test of CP invariance in vector-boson fusion production of the Higgs boson in the $H \to \tau\tau$ channel in proton−proton collisions at $\sqrt{s} = 13$ TeV with the ATLAS detector,
Phys. Lett. B **805** (2020) 135426, arXiv: 2002.05315 [hep-ex] (cit. on p. 12).

[49] ATLAS Collaboration, *CP Properties of Higgs Boson Interactions with Top Quarks in the $t\bar{t}H$ and tH Processes Using $H \to \gamma\gamma$ with the ATLAS Detector*,
Phys. Rev. Lett. **125** (2020) 061802, arXiv: 2004.04545 [hep-ex] (cit. on p. 12).

[50] A. Pich, *Precision tau physics*, Progress in Particle and Nuclear Physics **75** (2014) 41,
ISSN: 0146-6410, URL:
https://www.sciencedirect.com/science/article/pii/S0146641013001087
(cit. on p. 13).

[51] A. La Rosa, *The ATLAS Insertable B-Layer: from construction to operation*,
JINST **11** (2016) C12036, ed. by C. Gemme and L. Rossi,
arXiv: 1610.01994 [physics.ins-det] (cit. on p. 15).

[52] J. Haffner, *The CERN accelerator complex. Complexe des accélérateurs du CERN*,
(2013), General Photo, URL: https://cds.cern.ch/record/1621894 (cit. on p. 18).

[53] M. Schaumann et al., "First Xenon-Xenon Collisions in the LHC",
9th International Particle Accelerator Conference, 2018 (cit. on p. 17).

[54] ATLAS Collaboration,
Luminosity Determination using $Z \to \ell\ell$ events at $\sqrt{s} = 13$ TeV with the ATLAS detector,
ATL-DAPR-PUB-2021-001, CERN, 2021,
URL: https://cds.cern.ch/record/2752951 (cit. on p. 19).

[55] ATLAS Collaboration, *The ATLAS Detector*, 2021,
URL: https://atlas.cern/discover/detector (visited on 25/09/2021) (cit. on p. 18).

[56] CMS Collaboration, *Detector*, 2021,
URL: https://cms.cern/detector (visited on 28/09/2021) (cit. on p. 18).

[57] ATLAS Collaboration, *The ATLAS Experiment at the CERN Large Hadron Collider*,
JINST **3** (2008) S08003 (cit. on p. 18).

[58] LHCb Collaboration, *The LHCb Detector at the LHC*, JINST **3** (2008) S08005 (cit. on p. 18).

[59] ATLAS Collaboration,
Luminosity determination in pp collisions at $\sqrt{s} = 8$ TeV using the ATLAS detector at the LHC,
Eur. Phys. J. C **76** (2016) 653, arXiv: 1608.03953 [hep-ex] (cit. on p. 19).

[60] G. Avoni et al.,
The new LUCID-2 detector for luminosity measurement and monitoring in ATLAS,
Journal of Instrumentation **13** (2018) P07017,
URL: https://doi.org/10.1088/1748-0221/13/07/p07017 (cit. on p. 19).

[61] J. Pequenao, *Computer generated image of the whole ATLAS detector*, 2008,
URL: https://cds.cern.ch/record/1095924 (cit. on p. 20).

[62] Steffen Schaepe,
Search for Supersymmetry in Tau Lepton Final States with the ATLAS Detector,
PhD thesis: Rheinische Friedrich-Wilhelms-Universität Bonn, 2016,
URL: https://hdl.handle.net/20.500.11811/6695 (cit. on p. 20).

[63] ATLAS Collaboration, *ATLAS Insertable B-Layer: Technical Design Report*,
ATLAS-TDR-19; CERN-LHCC-2010-013, 2010,
URL: https://cds.cern.ch/record/1291633 (cit. on p. 20),
Addendum: ATLAS-TDR-19-ADD-1; CERN-LHCC-2012-009, 2012, URL:
https://cds.cern.ch/record/1451888.

[64] ATLAS Collaboration, *Performance of the ATLAS Trigger System in 2015*,
Eur. Phys. J. C **77** (2017) 317, arXiv: 1611.09661 [hep-ex] (cit. on p. 21).

[65] M. Shochet et al., *Fast TracKer (FTK) Technical Design Report*, tech. rep.,
ATLAS Fast Tracker Technical Design Report, 2013,
URL: https://cds.cern.ch/record/1552953 (cit. on p. 21).

[66] ATLAS Collaboration, *Electron and photon performance measurements with the ATLAS detector using the 2015–2017 LHC proton-proton collision data*, JINST **14** (2019) P12006,
arXiv: 1908.00005 [hep-ex] (cit. on p. 22).

[67] ATLAS Collaboration,
Topological cell clustering in the ATLAS calorimeters and its performance in LHC Run 1,
Eur. Phys. J. C **77** (2017) 490, arXiv: 1603.02934 [hep-ex] (cit. on p. 22).

[68] ATLAS Collaboration, *Muon reconstruction and identification efficiency in ATLAS using the full Run 2 pp collision data set at* $\sqrt{s}$ = 13 *TeV*, Eur. Phys. J. C **81** (2021) 578,
arXiv: 2012.00578 [hep-ex] (cit. on p. 22).

[69] ATLAS Collaboration, *Muon reconstruction performance of the ATLAS detector in proton–proton collision data at* $\sqrt{s}$ =*13 TeV*, Eur. Phys. J. C **76** (2016) 292,
arXiv: 1603.05598 [hep-ex] (cit. on p. 23).

[70] ATLAS Collaboration,
Validation of the muon momentum corrections for the ATLAS simulation using the $\Upsilon \to \mu\mu$ *channel based on 36.5* fb^{-1} *of pp collision data collected in 2015 and 2016*,
ATL-PHYS-PUB-2019-018, CERN, 2019,
URL: https://cds.cern.ch/record/2674152 (cit. on p. 23).

[71] ATLAS Collaboration,
Jet reconstruction and performance using particle flow with the ATLAS Detector,
Eur. Phys. J. C **77** (2017) 466, arXiv: 1703.10485 [hep-ex] (cit. on p. 23).

[72] M. Cacciari, G. P. Salam and G. Soyez, *The anti-*k_t *jet clustering algorithm*,
JHEP **04** (2008) 063, arXiv: 0802.1189 [hep-ph] (cit. on p. 23).

[73] ATLAS Collaboration, *ATLAS b-jet identification performance and efficiency measurement with* $t\bar{t}$ *events in pp collisions at* $\sqrt{s}$ = 13 *TeV*, Eur. Phys. J. C **79** (2019) 970,
arXiv: 1907.05120 [hep-ex] (cit. on pp. 23, 83, 123).

[74] ATLAS Collaboration, *Optimisation and performance studies of the ATLAS b-tagging algorithms for the 2017-18 LHC run*, ATL-PHYS-PUB-2017-013, CERN, 2017, URL: https://cds.cern.ch/record/2273281 (cit. on p. 23).

[75] ATLAS Collaboration, *Jet energy scale and resolution measured in proton-proton collisions at $\sqrt{s}$ = 13 TeV with the ATLAS detector*, (2020), arXiv: 2007.02645 [hep-ex] (cit. on p. 23).

[76] ATLAS Collaboration, *Reconstruction, Energy Calibration, and Identification of Hadronically Decaying Tau Leptons in the ATLAS Experiment for Run-2 of the LHC*, ATL-PHYS-PUB-2015-045, CERN, 2015, URL: https://cds.cern.ch/record/2064383 (cit. on pp. 23, 97).

[77] ATLAS Collaboration, *Reconstruction of hadronic decay products of tau leptons with the ATLAS experiment*, Eur. Phys. J. C **76** (2016) 295, arXiv: 1512.05955 [hep-ex] (cit. on pp. 23, 24).

[78] ATLAS Collaboration, *Measurement of the tau lepton reconstruction and identification performance in the ATLAS experiment using pp collisions at $\sqrt{s}$ = 13 TeV*, ATLAS-CONF-2017-029, CERN, 2017, URL: https://cds.cern.ch/record/2261772 (cit. on pp. 23, 24, 72, 145).

[79] ATLAS Collaboration, *Identification of hadronic tau lepton decays using neural networks in the ATLAS experiment*, ATL-PHYS-PUB-2019-033, CERN, 2019, URL: https://cds.cern.ch/record/2688062 (cit. on p. 24).

[80] ATLAS Collaboration, *Performance of missing transverse momentum reconstruction with the ATLAS detector using proton-proton collisions at $\sqrt{s}$ = 13 TeV*, Eur. Phys. J. C **78** (2018) 903, arXiv: 1802.08168 [hep-ex] (cit. on pp. 24, 83).

[81] ATLAS Collaboration, *Reconstruction of primary vertices at the ATLAS experiment in Run 1 proton–proton collisions at the LHC*, Eur. Phys. J. C **77** (2017) 332, arXiv: 1611.10235 [physics.ins-det] (cit. on p. 24).

[82] S. Gieseke and Z. Nagy, "Monte Carlo Generators and Fixed-order Calculations: Predicting the (Un)Expected", *Physics at the Terascale*, John Wiley & Sons, Ltd, chap. 5 97, ISBN: 9783527634965, eprint: https://onlinelibrary.wiley.com/doi/pdf/10.1002/9783527634965.ch5, URL: https://onlinelibrary.wiley.com/doi/abs/10.1002/9783527634965.ch5 (cit. on p. 25).

[83] J. Butterworth et al., *PDF4LHC recommendations for LHC Run II*, J. Phys. G **43** (2016) 023001, arXiv: 1510.03865 [hep-ph] (cit. on p. 26).

[84] J. Pumplin et al., *New Generation of Parton Distributions with Uncertainties from Global QCD Analysis*, JHEP **07** (2002) 012, arXiv: hep-ph/0201195 (cit. on p. 26).

[85] ATLAS Collaboration, *Measurement of the Z/γ^* boson transverse momentum distribution in pp collisions at $\sqrt{s}$ = 7 TeV with the ATLAS detector*, JHEP **09** (2014) 145, arXiv: 1406.3660 [hep-ex] (cit. on p. 26).

[86] R. D. Ball et al., *Parton distributions for the LHC run II*, JHEP **04** (2015) 040, arXiv: 1410.8849 [hep-ph] (cit. on p. 26).

[87] R. D. Ball et al., *Parton distributions with LHC data*, Nucl. Phys. B **867** (2013) 244, arXiv: 1207.1303 [hep-ph] (cit. on p. 26).

[88] ATLAS Collaboration, *ATLAS Pythia 8 tunes to* 7 *TeV data*, ATL-PHYS-PUB-2014-021, 2014, URL: https://cds.cern.ch/record/1966419 (cit. on p. 26).

[89] H.-L. Lai et al., *New parton distributions for collider physics*, Phys. Rev. D **82** (2010) 074024, arXiv: 1007.2241 [hep-ph] (cit. on p. 26).

[90] J. Alwall et al., *The automated computation of tree-level and next-to-leading order differential cross sections, and their matching to parton shower simulations*, JHEP **07** (2014) 079, arXiv: 1405.0301 [hep-ph] (cit. on p. 26).

[91] E. Bothmann et al., *Event Generation with Sherpa 2.2*, SciPost Phys. **7** (2019) 034, arXiv: 1905.09127 [hep-ph] (cit. on p. 25).

[92] S. Frixione, P. Nason and G. Ridolfi, *A Positive-weight next-to-leading-order Monte Carlo for heavy flavour hadroproduction*, JHEP **09** (2007) 126, arXiv: 0707.3088 [hep-ph] (cit. on pp. 25, 39).

[93] P. Nason, *A New method for combining NLO QCD with shower Monte Carlo algorithms*, JHEP **11** (2004) 040, arXiv: hep-ph/0409146 (cit. on pp. 25, 39).

[94] S. Frixione, P. Nason and C. Oleari, *Matching NLO QCD computations with Parton Shower simulations: the POWHEG method*, JHEP **11** (2007) 070, arXiv: 0709.2092 [hep-ph] (cit. on pp. 25, 39).

[95] S. Alioli et al., *A general framework for implementing NLO calculations in shower Monte Carlo programs: the POWHEG BOX*, JHEP **06** (2010) 043, arXiv: 1002.2581 [hep-ph] (cit. on pp. 25, 39).

[96] H. B. Hartanto et al., *Higgs boson production in association with top quarks in the POWHEG BOX*, Phys. Rev. D **91** (2015) 094003, arXiv: 1501.04498 [hep-ph] (cit. on p. 25).

[97] T. Sjöstrand et al., *An introduction to PYTHIA 8.2*, Comput. Phys. Commun. **191** (2015) 159, arXiv: 1410.3012 [hep-ph] (cit. on p. 25).

[98] P. Ilten, *Tau Decays in Pythia 8*, Nuclear Physics B - Proceedings Supplements **253-255** (2014) 77, The Twelfth International Workshop on Tau-Lepton Physics (TAU2012), ISSN: 0920-5632, URL: https://www.sciencedirect.com/science/article/pii/S0920563214001509 (cit. on p. 25).

[99] P. Golonka et al., *The tauola-photos-F environment for the TAUOLA and PHOTOS packages, release II*, Computer Physics Communications **174** (2006) 818, ISSN: 0010-4655, URL: https://www.sciencedirect.com/science/article/pii/S0010465506000403 (cit. on p. 25).

[100] ATLAS Collaboration, *The ATLAS Simulation Infrastructure*, Eur. Phys. J. C **70** (2010) 823, arXiv: 1005.4568 [physics.ins-det] (cit. on p. 25).

[101] S. Agostinelli et al., *Geant4—a simulation toolkit*,
Nuclear Instruments and Methods in Physics Research Section A: Accelerators, Spectrometers, Detectors and Associated Equipment **506** (2003) 250, ISSN: 0168-9002, URL: https://www.sciencedirect.com/science/article/pii/S0168900203013688 (cit. on p. 25).

[102] ATLAS Collaboration, *Luminosity Public Results Run 2*, 2021,
URL: https://twiki.cern.ch/twiki/bin/view/AtlasPublic/LuminosityPublicResultsRun2#Pileup_Interactions_and_Data_Tak (visited on 11/08/2021) (cit. on p. 26).

[103] R. Ellis et al., *Higgs decay to τ+τ- A possible signature of intermediate mass Higgs bosons at high energy hadron colliders*, Nuclear Physics B **297** (1988) 221, ISSN: 0550-3213,
URL: https://www.sciencedirect.com/science/article/pii/0550321388900193 (cit. on p. 29).

[104] A. Elagin et al., *A New Mass Reconstruction Technique for Resonances Decaying to di-tau*, Nuclear Instruments & Methods in Physics Research Section A-accelerators Spectrometers Detectors and Associated Equipment - NUCL INSTRUM METH PHYS RES A **654** (2011) 481 (cit. on pp. 29, 31, 33, 35, 36).

[105] C. Lester and D. Summers,
Measuring masses of semi-invisibly decaying particle pairs produced at hadron colliders, Physics Letters B **463** (1999) 99, ISSN: 0370-2693, URL: https://www.sciencedirect.com/science/article/pii/S0370269399009454 (cit. on p. 31).

[106] ATLAS Collaboration, *Search for the Standard Model Higgs boson in the H to $\tau^+\tau^-$ decay mode in $\sqrt{s}$ = 7 TeV pp collisions with ATLAS*, JHEP **09** (2012) 070,
arXiv: 1206.5971 [hep-ex] (cit. on p. 31).

[107] ATLAS Collaboration, *DiTauMassTools Package*, 2021,
URL: https://gitlab.cern.ch/atlas/athena/-/tree/21.2/PhysicsAnalysis/TauID/DiTauMassTools (visited on 27/07/2021) (cit. on p. 32).

[108] F. Dekking et al.,
A modern introduction to probability and statistics. Understanding why and how,
Springer-Verlag London, 2005, ISBN: 978-1-85233-896-1 (cit. on p. 33).

[109] W. J. Stewart, *Probability, Markov Chains, Queues, and Simulation*,
Princeton University Press, 2009, URL: https://doi.org/10.1515/9781400832811 (cit. on p. 33).

[110] A. Joseph,
"Markov Chain Monte Carlo Methods in Quantum Field Theories: A Modern Primer", SpringerBriefs in Physics, Springer, 2019, arXiv: 1912.10997 [hep-th] (cit. on p. 33).

[111] A. Barbu and S. Zhu, *Monte Carlo Methods*, Springer, 2020, ISBN: 978-981-13-2970-8 (cit. on p. 34).

[112] N. Metropolis et al., *Equation of State Calculations by Fast Computing Machines*, The Journal of Chemical Physics **21** (1953) 1087, eprint: https://doi.org/10.1063/1.1699114, URL: https://doi.org/10.1063/1.1699114 (cit. on p. 34).

[113] W. K. Hastings, *Monte Carlo Sampling Methods Using Markov Chains and Their Applications*, Biometrika **57** (1970) 97 (cit. on p. 34).

[114] S. Alioli et al., *NLO vector-boson production matched with shower in POWHEG*, JHEP **07** (2008) 060, arXiv: 0805.4802 [hep-ph] (cit. on p. 39).

[115] S. Alioli et al., *Vector boson plus one jet production in POWHEG*, JHEP **01** (2011) 095, arXiv: 1009.5594 [hep-ph] (cit. on p. 39).

[116] E. Re, *NLO corrections merged with parton showers for Z+2 jets production using the POWHEG method*, JHEP **10** (2012) 031, arXiv: 1204.5433 [hep-ph] (cit. on p. 39).

[117] B. Jager, S. Schneider and G. Zanderighi, *Next-to-leading order QCD corrections to electroweak Zjj production in the POWHEG BOX*, JHEP **09** (2012) 083, arXiv: 1207.2626 [hep-ph] (cit. on p. 39).

[118] F. Schissler and D. Zeppenfeld, *Parton Shower Effects on W and Z Production via Vector Boson Fusion at NLO QCD*, JHEP **04** (2013) 057, arXiv: 1302.2884 [hep-ph] (cit. on p. 39).

[119] J. M. Campbell et al., *W and Z Bosons in Association with Two Jets Using the POWHEG Method*, JHEP **08** (2013) 005, arXiv: 1303.5447 [hep-ph] (cit. on p. 39).

[120] ATLAS Collaboration, *Object-based missing transverse momentum significance in the ATLAS Detector*, ATLAS-CONF-2018-038, 2018, URL: https://cds.cern.ch/record/2630948 (cit. on p. 43).

[121] Christian Limbach, *Development of a new reconstruction and classification method for Tau leptons and its application in the ATLAS detector at the LHC*, PhD thesis: Rheinische Friedrich-Wilhelms-Universität Bonn, 2015, URL: https://hdl.handle.net/20.500.11811/6466 (cit. on pp. 45, 46).

[122] K. Kölbig and B. Schorr, *A program package for the Landau distribution*, Computer Physics Communications **31** (1984) 97, ISSN: 0010-4655, URL: https://www.sciencedirect.com/science/article/pii/0010465584900857 (cit. on p. 60).

[123] K. Kölbig and B. Schorr, *Erratum to: "A program package for the Landau distribution" [Comput. Phys. Commun. 31 (1984) 97–111]*, Computer Physics Communications **178** (2008) 972, ISSN: 0010-4655, URL: https://www.sciencedirect.com/science/article/pii/S0010465508001136 (cit. on p. 60).

[124] R. Hmaid, *Verwendung der τ-Helizität zur Erstellung einer neuen Parametrisierung für den Missing Mass Calculator*, Bachelor's thesis: Universität Bonn, 2020, URL: https://web.physik.uni-bonn.de/group/view.php?&group=1&lang=de&c=t&id=126 (visited on 08/10/2021) (cit. on pp. 65, 66).

[125] K. Bass, *Impact of τ decay vertices on the kinematic reconstruction of τ leptons and the determination of the higgs boson mass in $H\longrightarrow \tau\tau$ decays in ATLAS*, Master's thesis: Universität Bonn, 2021, URL: https://web.physik.uni-bonn.de/group/view.php?&group=1&lang=de&c=t&id=124 (visited on 26/07/2021) (cit. on pp. 65–67).

[126] M. Werres, *Estimating the Mass of Di-Tau Systems in the ATLAS Experiment Using Neural Network Regression*, Master's thesis: Universität Bonn, 2019, URL: https://web.physik.uni-bonn.de/group/view.php?&group=1&lang=de&c=t&id=102 (visited on 26/07/2021) (cit. on pp. 65, 67).

[127] L. Herrmann, *Optimization of a Regression-Based Deep Neural Network for Di-Tau Mass Reconstruction in ATLAS*, Master's thesis: Universität Bonn, 2020, URL: https://web.physik.uni-bonn.de/group/view.php?&group=1&lang=de&c=t&id=121 (visited on 26/07/2021) (cit. on pp. 65, 67).

[128] M. Grazzini et al., *Modeling BSM effects on the Higgs transverse-momentum spectrum in an EFT approach*, JHEP **03** (2017) 115, arXiv: 1612.00283 [hep-ph] (cit. on p. 70).

[129] LHC Higgs Cross Section Working Group, *LHC XS working group STXS Stage 1.2*, 2020, URL: https://twiki.cern.ch/twiki/bin/view/LHCPhysics/LHCHXSWGFiducialAndSTXS (visited on 16/08/2021) (cit. on pp. 71, 124, 125).

[130] N. Berger et al., *Simplified Template Cross Sections - Stage 1.1*, (2019), arXiv: 1906.02754 [hep-ph] (cit. on pp. 71, 72, 116).

[131] ATLAS Collaboration, *Search for the Standard Model Higgs boson produced in association with a vector boson and decaying into a tau pair in pp collisions at $\sqrt{s} = 8$ TeV with the ATLAS detector*, Phys. Rev. D **93** (2016) 092005, arXiv: 1511.08352 [hep-ex] (cit. on p. 72).

[132] ATLAS Collaboration, *Search for the associated production of the Higgs boson with a top quark pair in multilepton final states with the ATLAS detector*, Phys. Lett. B **749** (2015) 519, arXiv: 1506.05988 [hep-ex] (cit. on p. 72).

[133] ATLAS Collaboration, *Evidence for the associated production of the Higgs boson and a top quark pair with the ATLAS detector*, Phys. Rev. D **97** (2018) 072003, arXiv: 1712.08891 [hep-ex] (cit. on p. 72).

[134] ATLAS Collaboration, *Trigger Menu in 2016*, ATL-DAQ-PUB-2017-001, 2017, URL: https://cds.cern.ch/record/2242069 (cit. on p. 72).

[135] ATLAS Collaboration, *2015 start-up trigger menu and initial performance assessment of the ATLAS trigger using Run-2 data*, ATL-DAQ-PUB-2016-001, 2016, URL: https://cds.cern.ch/record/2136007 (cit. on p. 72).

[136] ATLAS Collaboration, *Trigger Menu in 2017*, ATL-DAQ-PUB-2018-002, 2018, URL: https://cds.cern.ch/record/2625986 (cit. on p. 72).

[137] ATLAS Collaboration, *Trigger Menu in 2018*, ATL-DAQ-PUB-2019-001, 2019, URL: https://cds.cern.ch/record/2693402 (cit. on p. 72).

[138] ATLAS Collaboration, *Performance of electron and photon triggers in ATLAS during LHC Run 2*, Eur. Phys. J. C **80** (2020) 47, arXiv: 1909.00761 [hep-ex] (cit. on p. 72).

[139] ATLAS Collaboration, *Performance of the ATLAS muon triggers in Run 2*, JINST **15** (2020) P09015, arXiv: 2004.13447 [hep-ex] (cit. on p. 72).

[140] ATLAS Collaboration, *Estimation of non-prompt and fake lepton backgrounds in final states with top quarks produced in proton-proton collisions at $\sqrt{s}$ = 8 TeV with the ATLAS detector*, ATLAS-CONF-2014-058, CERN, 2014, URL: https://cds.cern.ch/record/1951336 (cit. on p. 79).

[141] ATLAS Collaboration, *Measurements of Higgs boson production and couplings in the four-lepton channel in pp collisions at center-of-mass energies of 7 and 8 TeV with the ATLAS detector*, Phys. Rev. D **91** (2015) 012006, arXiv: 1408.5191 [hep-ex] (cit. on p. 79).

[142] ATLAS Collaboration, *Evidence for the Higgs-boson Yukawa coupling to tau leptons with the ATLAS detector*, JHEP **04** (2015) 117, arXiv: 1501.04943 [hep-ex] (cit. on p. 80).

[143] ATLAS Collaboration, *Modelling $Z \to \tau\tau$ processes in ATLAS with τ-embedded $Z \to \mu\mu$ data*, JINST **10** (2015) P09018, arXiv: 1506.05623 [hep-ex] (cit. on pp. 80, 124).

[144] CMS Collaboration, *An embedding technique to determine $\tau\tau$ backgrounds in proton-proton collision data*, JINST **14** (2019) P06032, arXiv: 1903.01216 [hep-ex] (cit. on pp. 80, 124).

[145] ATLAS Collaboration, *Measurements of the production cross section of a Z boson in association with jets in pp collisions at $\sqrt{s}$ = 13 TeV with the ATLAS detector*, Eur. Phys. J. C **77** (2017) 361, arXiv: 1702.05725 [hep-ex] (cit. on p. 81).

[146] ATLAS Collaboration, *Measurement of the cross-section for electroweak production of dijets in association with a Z boson in pp collisions at $\sqrt{s}$ = 13 TeV with the ATLAS detector*, Phys. Lett. B **775** (2017) 206, arXiv: 1709.10264 [hep-ex] (cit. on p. 81).

[147] *Les Houches 2017: Physics at TeV Colliders Standard Model Working Group Report*, 2018, arXiv: 1803.07977 [hep-ph] (cit. on p. 84).

[148] I. W. Stewart and F. J. Tackmann, *Theory Uncertainties for Higgs and Other Searches Using Jet Bins*, Phys. Rev. D **85** (2012) 034011, arXiv: 1107.2117 [hep-ph] (cit. on p. 84).

[149] S. Gangal and F. J. Tackmann,
Next-to-leading-order uncertainties in Higgs+2 jets from gluon fusion,
Phys. Rev. D **87** (2013) 093008, arXiv: 1302.5437 [hep-ph] (cit. on p. 84).

[150] G. Cowan et al., *Asymptotic formulae for likelihood-based tests of new physics*,
Eur. Phys. J. C **71** (2011) 1554, [Erratum: Eur.Phys.J.C 73, 2501 (2013)],
arXiv: 1007.1727 [physics.data-an] (cit. on pp. 85, 87).

[151] K. Cranmer, "Practical Statistics for the LHC",
2011 European School of High-Energy Physics, 2014 267,
arXiv: 1503.07622 [physics.data-an] (cit. on pp. 85, 88).

[152] S. Brandt, *Data Analysis*, 2014, ISBN: 978-3-319-03761-5 (cit. on pp. 85, 87).

[153] L. Lista, *Statistical Methods for Data Analysis in Particle Physics*, 2017,
ISBN: 978-3-319-62839-4 (cit. on pp. 85, 86).

[154] K. Cranmer et al.,
HistFactory: A tool for creating statistical models for use with RooFit and RooStats, tech. rep.,
New York U., 2012, URL: https://cds.cern.ch/record/1456844
(cit. on pp. 88, 107, 204).

[155] L. Moneta et al., *The RooStats Project*, 2011, arXiv: 1009.1003 [physics.data-an]
(cit. on pp. 88, 104, 107).

[156] ATLAS Collaboration, *Measurement of the transverse momentum distribution of Drell–Yan lepton pairs in proton–proton collisions at $\sqrt{s}$ = 13 TeV with the ATLAS detector*,
Eur. Phys. J. C **80** (2020) 616, arXiv: 1912.02844 [hep-ex] (cit. on p. 88).

[157] ATLAS Collaboration, *Differential cross-section measurements for the electroweak production of dijets in association with a Z boson in proton–proton collisions at ATLAS*,
Eur. Phys. J. C **81** (2021) 163, arXiv: 2006.15458 [hep-ex] (cit. on p. 88).

[158] ATLAS Collaboration, *Measurement of the Higgs boson coupling properties in the $H\rightarrow \tau\tau$ decay channel at $\sqrt{s}$ = 13 TeV with the ATLAS detector*,
internal report ATL-COM-PHYS-2020-721, CERN, 2020,
URL: https://cds.cern.ch/record/2741326 (cit. on p. 90).

[159] H. A. Sturges, *The Choice of a Class Interval*,
Journal of the American Statistical Association **21** (1926) 65, ISSN: 01621459,
URL: http://www.jstor.org/stable/2965501 (cit. on p. 91).

[160] F. Sauerburger, *Prelim. title: Measurement of $H\rightarrow \tau\tau$ decays using machine learning techniques in proton-proton collisions at $\sqrt{s}$=13 TeV with the ATLAS detector at the LHC*,
PhD thesis: Universität Freiburg, 2021, unpublished thesis (cit. on pp. 99, 113).

[161] G. Upton and I. Cook, *A Dictionary of Statistics (2 rev. ed.)* Oxford University Press, 2014,
ISBN: 9780199541454 (cit. on p. 104).

[162] N. Morange, *Beautiful Higgs Boson*,
Habilitation à diriger des recherches: Université Paris-Saclay, 2021,
URL: http://hal.in2p3.fr/tel-03341303 (cit. on p. 109).

[163] D. E. Knuth, *Two Notes on Notation*, The American Mathematical Monthly **99** (1992) 403, ISSN: 00029890, 19300972, URL: http://www.jstor.org/stable/2325085 (cit. on p. 110).

[164] A. E. Bayer and U. Seljak, *The look-elsewhere effect from a unified Bayesian and frequentist perspective*, JCAP **10** (2020) 009, arXiv: 2007.13821 [physics.data-an] (cit. on p. 111).

[165] ATLAS Collaboration, *Performance of b-Jet Identification in the ATLAS Experiment*, JINST **11** (2016) P04008, arXiv: 1512.01094 [hep-ex] (cit. on p. 123).

[166] CMS Collaboration, *Measurement of Higgs boson production in the decay channel with a pair of τ leptons*, CMS-PAS-HIG-19-010, CERN, 2020, URL: https://cds.cern.ch/record/2725590 (cit. on pp. 124, 125).

[167] ATLAS Collaboration, *Standard Model Summary Plots June 2021*, ATL-PHYS-PUB-2021-032, CERN, 2021, URL: https://cds.cern.ch/record/2777014 (cit. on p. 128).

[168] ATLAS Collaboration, *Measurements of Higgs bosons decaying to bottom quarks from vector boson fusion production with the ATLAS experiment at $\sqrt{s}$ = 13 TeV*, Eur. Phys. J. C **81** (2021) 537, arXiv: 2011.08280 [hep-ex] (cit. on p. 128).

[169] ATLAS Collaboration, *Measurements of WH and ZH production in the $H \to b\bar{b}$ decay channel in pp collisions at 13 TeV with the ATLAS detector*, Eur. Phys. J. C **81** (2021) 178, arXiv: 2007.02873 [hep-ex] (cit. on p. 128).

[170] ATLAS Collaboration, *Combined measurements of Higgs boson production and decay using up to 139 fb^{-1} of proton-proton collision data at $\sqrt{s}$ = 13 TeV collected with the ATLAS experiment*, ATLAS-CONF-2021-053, CERN, 2021, URL: https://cds.cern.ch/record/2789544 (cit. on p. 129).

[171] I. Zurbano Fernandez et al., *High-Luminosity Large Hadron Collider (HL-LHC): Technical design report*, **10/2020** (2020), ed. by I. Béjar Alonso et al., URL: https://cds.cern.ch/record/2749422 (cit. on p. 129).

[172] ATLAS Collaboration, *Measurement of τ polarisation in $Z/\gamma^* \to \tau\tau$ decays in proton–proton collisions at $\sqrt{s}$ = 8 TeV with the ATLAS detector*, Eur. Phys. J. C **78** (2018) 163, arXiv: 1709.03490 [hep-ex] (cit. on p. 147).

APPENDIX A

Improved Determination of the Tau Energy Scale

The measurement of the tau energy scale (TES) and the corresponding uncertainties described in Reference [78] is a tag-and-probe measurement. Its basic idea is to perform the measurement, which targets the residuals between the MC based energy scale calibration and what is observed in data, for a well-known process in a well-known phase space. In the case of τ-lepton performance measurements, e.g. the TES measurement, this is typically done using $Z \rightarrow \tau\tau$ events with one τ-lepton decaying into a muon and the other hadronically. The muon is used to trigger the event and called the tag while the τ_{had} is the lepton being probed. By varying the τ-lepton's energy and minimising the χ^2 of the $m_{\tau\tau}^{\text{vis}}$ distribution TES is measured in data. The variation of the τ-lepton energy directly translates to a modified $m_{\tau\tau}^{\text{vis}}$ distribution as explained in Section 4.1.1. Uncertainties in this measurement are treated uncorrelated and measured individually by also minimising the χ^2 of the systematically varied mass distribution. The final uncertainty is the quadratic sum of the individual uncertainties considered.

For the new approach, which is supposed to provide a more precise measurement of TES and its uncertainty[1], multiple changes are implemented. This section aims to describe the current status of the ideas behind this new approach, the actual measurement is not finalised at this point in time. The idea of a tag-and-probe measurement is kept and the same process of $Z \rightarrow \tau\tau$ is targeted. However, instead of minimising the χ^2 a maximum likelihood fit is implemented which is able to spot correlations of different sources of uncertainties during its minimisation. This possibly helps to reduce the final uncertainty on TES depending on these correlations.

The main difference with respect to the original measurement is the idea of separating different components of the tau energy scale. With the particle flow approach described in Section 3.3.4 multiple subdetectors play an important role in the τ-lepton reconstruction and possibly introduce their own energy scales. First, these different components have to be identified in the resolution of $p_{\text{T},\tau}$. This is done in bins of the electromagnetic energy fraction of the τ-lepton:

$$\varepsilon_{\text{EM}} = p_{\text{T},\tau_{\text{neutral}}}^{\text{vis, truth}} / p_{\text{T},\tau}^{\text{vis, truth}} \,,$$

which is sensitive to the amount of energy deposited in the tracker compared to the energy measured in the ECal. If ε_{EM} is close to zero, most of the τ-lepton energy is measured in the tracker and, thus, likely to have decayed solely into charged pions. Similarly, for values of ε_{EM} approaching one most of the τ-lepton energy is measured in the calorimeters. The reconstruction motivates the different

[1] And also a first-time measurement of the tau energy resolution (TER) in data.

resolution terms identified in the overall τ-lepton resolution where all resolutions are assumed to follow Gaussian distributions:

Core The core resolution is given by the tracker resolution and, thus, should have the smallest σ and be close to zero, i.e. the bias should be negligible.

EM The electromagnetic component of the resolution corresponds to the ECal resolution and is typically a bit larger than for the tracker. Depending on the phase space some bias is possible for this component.

Tail The tail resolution originates from so-called "confusion" in the particle flow reconstruction. It is typically associated with wrongly classified energy deposits in the calorimeter when subtracting the energy deposits of charged pions measured in the tracker from the ECal.

In order to achieve stable fits over the whole ε_{EM} range a few physically motivated constraints are implemented. The goal of these fits is to parameterise the normalisation of the individual components as a function of ε_{EM}. The following studies are based on a POWHEG $Z \rightarrow \tau\tau$ sample corresponding to the data taking of the years 2015 and 2016.

First, the widths of the Gaussian distributions for the Core and EM component are measured in phase space regions enriched in the respective τ-lepton energy compositions, i.e. at $\varepsilon_{\text{EM}} = 0$ for the Core component and $\varepsilon_{\text{EM}} > 0.95$ for the EM component. The results of these fits fixate σ_{Core} and σ_{EM} for the next steps since they are not expected to vary as a function of ε_{EM}. Additionally, the normalisations of all three components have to add up to one with the chosen normalisation for the overall τ-lepton resolution distribution.

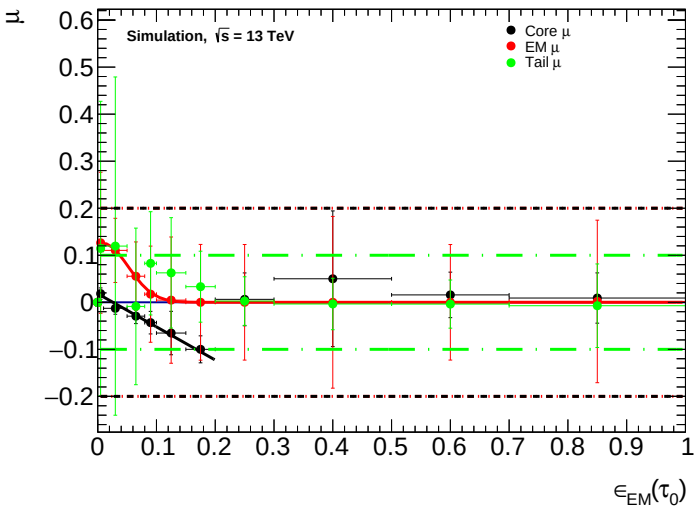

Figure A.1: Means of the Gaussian fits for every τ-lepton resolution component as a function of ε_{EM}. The dashed lines indicate the constraints on the means. The means of the core component and of the EM component are fitted to the tails of Gaussian distributions, respectively.

Next, a first iteration of fits in bins of ε_{EM} is performed. In addition to the constraints already described, the means of the Gaussian distributions are only allowed to float within ±0.2 around

zero. This prevents unphysical behaviour of components with very small normalisations in certain phase spaces. Furthermore, it is required that the mean of the EM component is positive. This constraint is motivated by the observation that otherwise the meanings of the EM component and the Core component can swap due to their similar Gaussian widths. The fits of this first iteration are used to parameterise the means of the Gaussian distributions as a function of ε_{EM} in order to reduce the uncertainty of the normalisation determination in the next step. It was observed, as shown in Figure A.1, that the means of the Core component show more variation than naively expected which can be explained by the energy calibration using boosted regression trees. This calibration shifts the Core component and the EM component so that the overall $p_{\text{T},\tau}$ is well calibrated. With the parameterisation of the Gaussian means another iteration of fits to the τ-lepton resolution in bins of ε_{EM} is performed. Two examples for these fits are shown in Figure A.2, highlighting all resolution components and the combined resolution function. Finally, the parameterisation of the

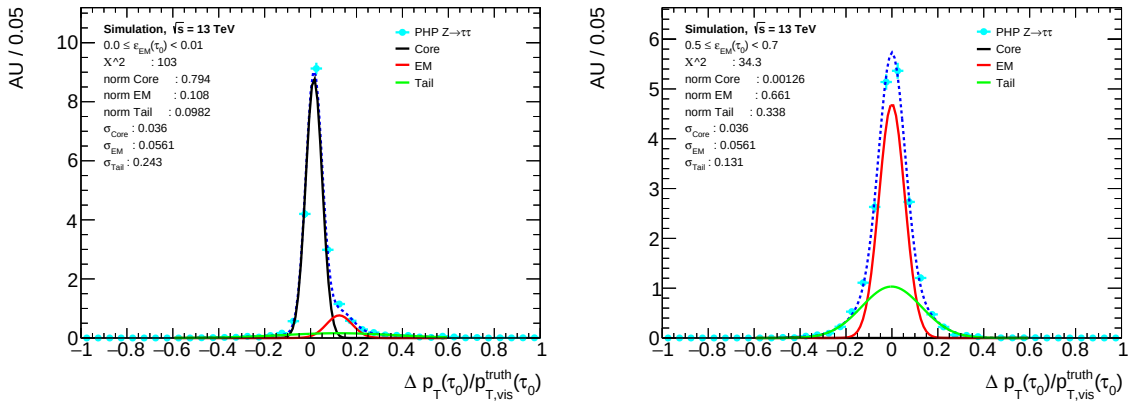

(a) Fit to the $p_{\text{T},\tau}$ resoution for small ε_{EM}.

(b) Fit to the $p_{\text{T},\tau}$ resoution for intermediate ε_{EM}.

Figure A.2: Fits of the $p_{\text{T},\tau}$ resolution in two bins of ε_{EM}. The individual Gaussian fits corresponding to the resolution components are shown as well as the combined Gaussian distribution depicted by the dashed line.

components' normalisation as a function of ε_{EM} is shown in Figure A.3. The functions used for the parameterisations are based on the Fermi-Dirac distribution:

$$f(x) = \frac{a}{e^{(x+b)/c} + 1}$$

with an additional first order polynomial for the EM component. The uncertainty of this parameterisation is indicated by the dashed lines in Figure A.3 and implemented as an uncertainty in the fit model. Since the measurement is designed to measure the individual τ-lepton resolution components an observable more sensitive to these components than $m_{\tau\tau}^{\text{vis}}$ is chosen. Inspired by the Run I τ-lepton polarisation measurement in ATLAS, the utilised observable is Υ which is defined as: [172]

$$\Upsilon = \frac{E_{\pi^\pm} - E_{\pi^0}}{E_{\pi^\pm} + E_{\pi^0}} \approx 2 \cdot \frac{p_{\text{T,all tracks}}}{p_{\text{T},\tau}} - 1\,.$$

Consequently, the observable is sensitive to the τ-lepton polarisation and similar effects to the ones observed in Reference [172]. Thus, similar sources of uncertainties have to be considered.

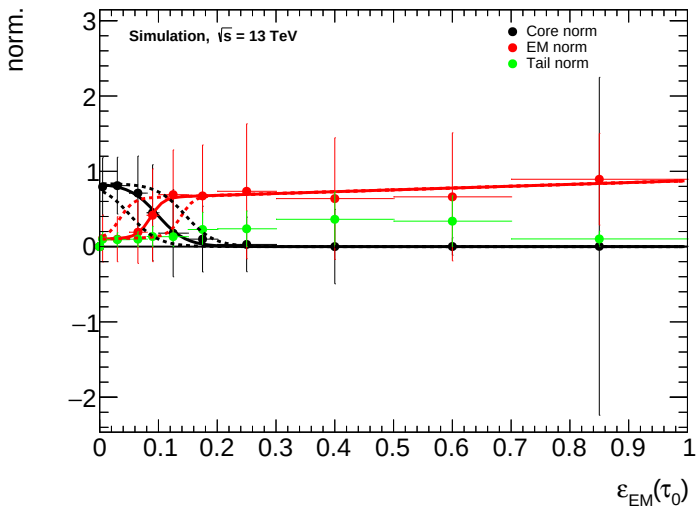

Figure A.3: Parameterisation of the resolution components' normalisation as a function of $\varepsilon_{\mathrm{EM}}$. The uncertainties are shown as dashed lines.

Since the observable is sensitive to the components of TES it is also sensitive to the τ-lepton decay mode. Hence, the final measurement is ideally performed simultaneously with the measurement of the efficiency scale factors of the decay mode classification.

APPENDIX B

Additional Studies with the MMC

B.1 Cut Selection for p.d.f. Parameterisations

	$\tau_{\text{lep}}\,\tau_{\text{had}}$	$\tau_{\text{had}}\,\tau_{\text{had}}$
Object counting	# of $e/\mu > 1$	# of $e/\mu = 0$, # of $\tau_{\text{had-vis}} = 2$
p_{T} cut	e/μ : $p_{\text{T}} > 25\,\text{GeV}$ $\tau_{\text{had-vis}}$: $p_{\text{T}} > 35\,\text{GeV}$	$\tau_{\text{had-vis}}$ leading: $p_{\text{T}} > 35\,\text{GeV}$ $\tau_{\text{had-vis}}$ subleading: $p_{\text{T}} > 25\,\text{GeV}$
ID		both BDT medium, at least one BDT tight
Charge product	Opposite charge	Opposite charge
Angular	$\Delta R_{\ell\,\tau_{\text{had-vis}}} < 2.5$ $\lvert\Delta\eta_{\ell\,\tau_{\text{had-vis}}}\rvert < 1.5$	$0.6 < \Delta R_{\tau_{\text{had-vis}}\,\tau_{\text{had-vis}}} < 2.5$ $\lvert\Delta\eta_{\tau_{\text{had-vis}}\,\tau_{\text{had-vis}}}\rvert < 1.5$
$E_{\text{T}}^{\text{miss}}$	$E_{\text{T}}^{\text{miss}} > 20\,\text{GeV}$ $\min\left(\Delta\phi\left(\tau_{\text{had}}, E_{\text{T}}^{\text{miss}}\right)\right) < \frac{\pi}{4}$	$E_{\text{T}}^{\text{miss}} > 20\,\text{GeV}$ $\min\left(\Delta\phi\left(\tau_{\text{had}}, E_{\text{T}}^{\text{miss}}\right)\right) < \frac{\pi}{4}$

Table B.1: Summary of the event selection applied to create the p.d.f. parameterisations for the MMC.

B.2 Parameterisation of Momentum Ratio p.d.f.s

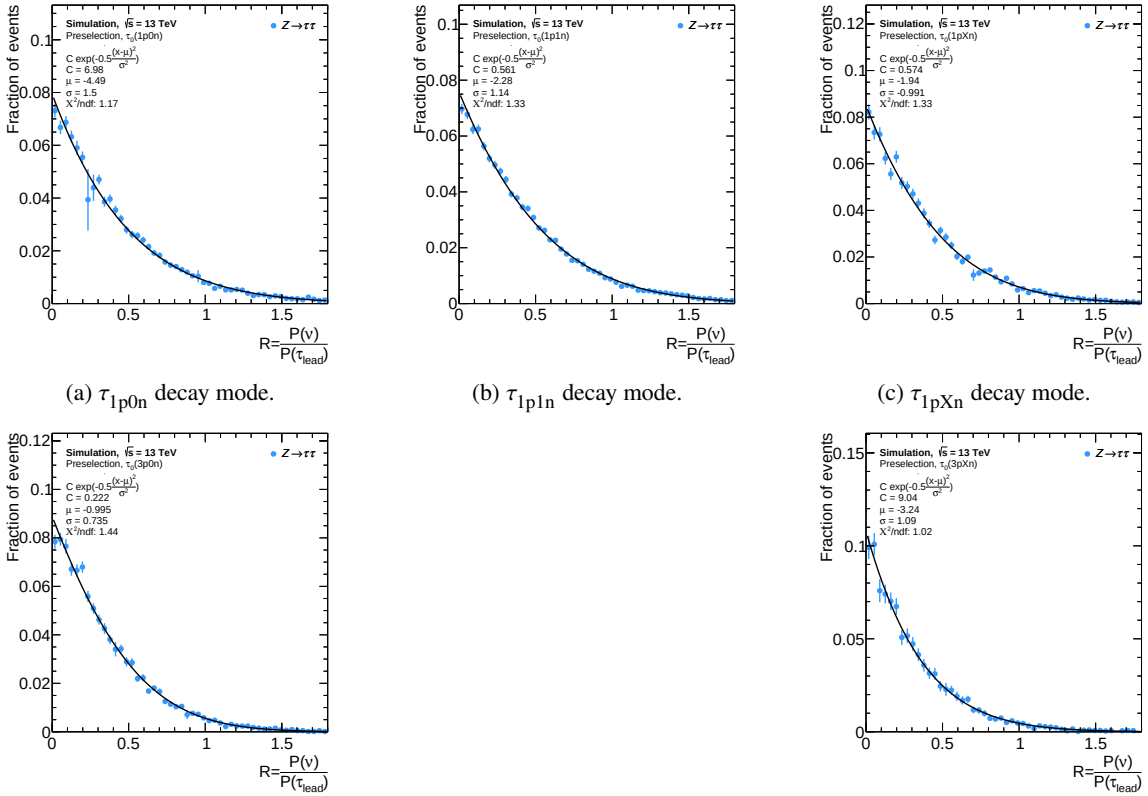

(a) τ_{1p0n} decay mode. (b) τ_{1p1n} decay mode. (c) τ_{1pXn} decay mode.

(d) τ_{3p0n} decay mode. (e) τ_{3pXn} decay mode.

Figure B.1: Parameterisations of the ratio of the neutrino momentum and the reconstructed visible τ-lepton momentum based on the SHERPA $Z \rightarrow \tau\tau$ sample. The parameterisations (solid lines) are shown for the leading τ-lepton of the fully hadronic decay channel.

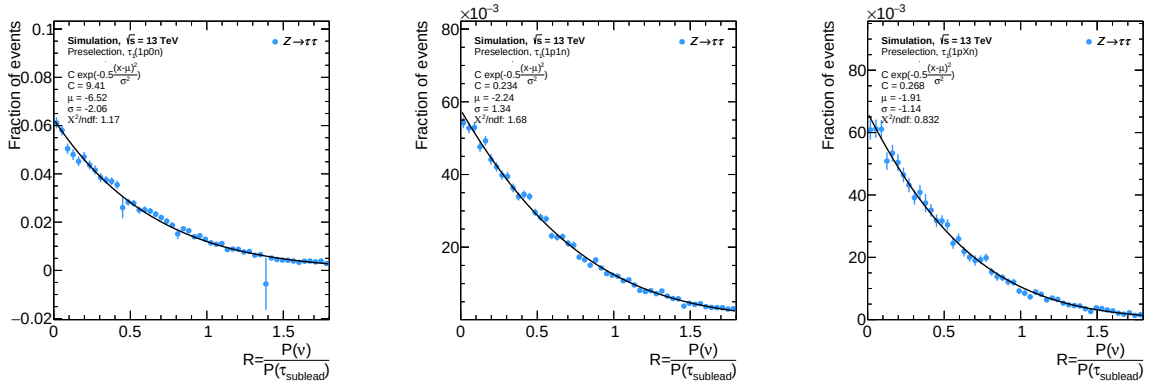

(a) τ_{1p0n} decay mode. (b) τ_{1p1n} decay mode. (c) τ_{1pXn} decay mode.

(d) τ_{3p0n} decay mode. (e) τ_{3pXn} decay mode.

Figure B.2: Parameterisations of the ratio of the neutrino momentum and the reconstructed visible τ-lepton momentum based on the SHERPA $Z \rightarrow \tau\tau$ sample. The parameterisations (solid lines) are shown for the subleading τ-lepton of the fully hadronic decay channel.

B.3 Alternative Fit Functions for Angular p.d.f.

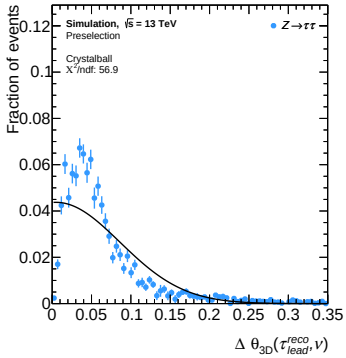

(a) τ_{1p0n} in the range 0 GeV $<$ $p_{\text{T},\tau} \leq$ 34 GeV. A crystalball function is used.

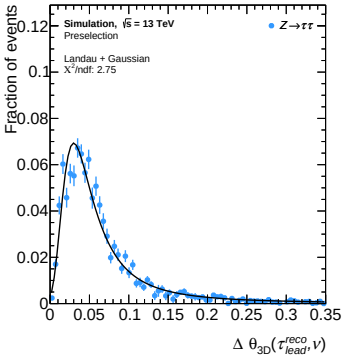

(b) τ_{1p0n} in the range 0 GeV $<$ $p_{\text{T},\tau} \leq$ 34 GeV. A combination of a landau function and a Gaussian is used. The error matrix of the fit is not valid.

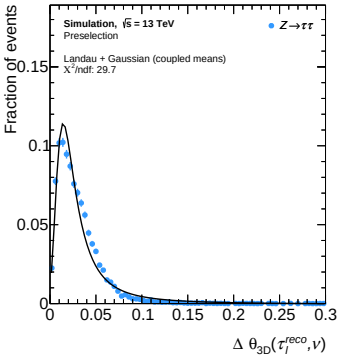

(c) τ_{lep} in the range 29 GeV $<$ $p_{\text{T},\tau} \leq$ 33 GeV. A combination of a Landau function and a Gaussian is used where their means are coupled.

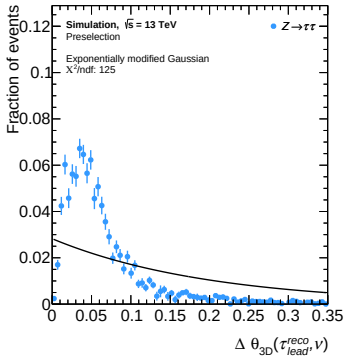

(d) τ_{1p0n} in the range 0 GeV $<$ $p_{\text{T},\tau} \leq$ 34 GeV. An exponentially modified Gaussian is used.

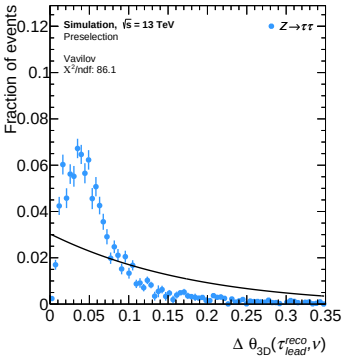

(e) τ_{1p0n} in the range 0 GeV $<$ $p_{\text{T},\tau} \leq$ 34 GeV. A Vavilov function is used.

Figure B.3: Parameterisations of the angular distance between the neutrino and the reconstructed visible τ-lepton based on the SHERPA $Z \rightarrow \tau\tau$ sample. Alternative fit functions (solid lines) are shown for τ_{lep} and τ_{had}.

B.4 Parameterisation of Angular p.d.f.s

Parameterisation of Angular p.d.f.s for 1p0n Decays

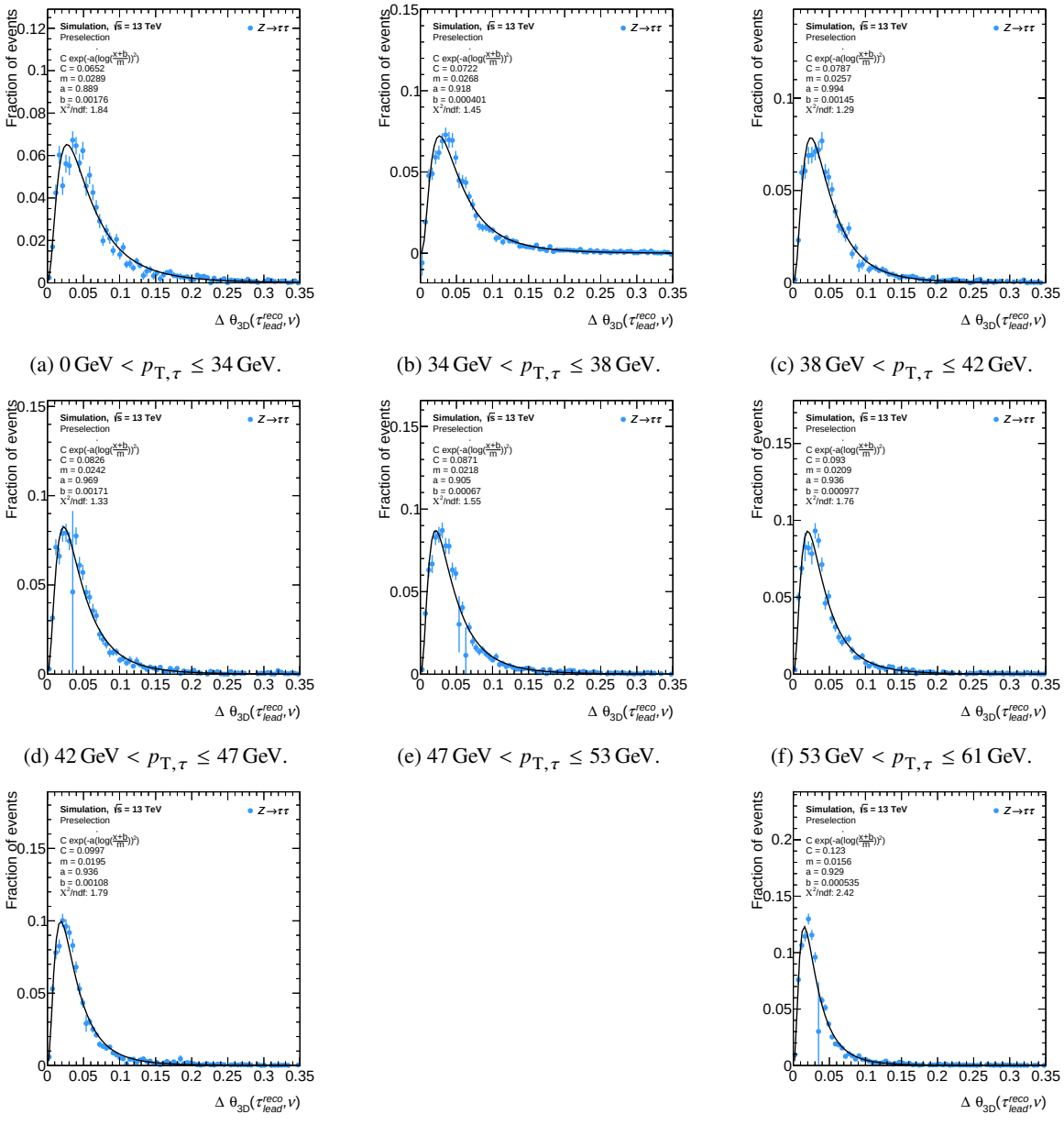

(a) 0 GeV $< p_{\mathrm{T},\tau} \leq$ 34 GeV.

(b) 34 GeV $< p_{\mathrm{T},\tau} \leq$ 38 GeV.

(c) 38 GeV $< p_{\mathrm{T},\tau} \leq$ 42 GeV.

(d) 42 GeV $< p_{\mathrm{T},\tau} \leq$ 47 GeV.

(e) 47 GeV $< p_{\mathrm{T},\tau} \leq$ 53 GeV.

(f) 53 GeV $< p_{\mathrm{T},\tau} \leq$ 61 GeV.

(g) 61 GeV $< p_{\mathrm{T},\tau} \leq$ 76 GeV.

(h) 76 GeV $< p_{\mathrm{T},\tau} \leq$ 200 GeV.

Figure B.4: Parameterisations of the angular distance between the neutrino and the reconstructed visible τ-lepton based on the SHERPA $Z \rightarrow \tau\tau$ sample. The parameterisations (solid lines) are shown for the τ_{1p0n} decay mode.

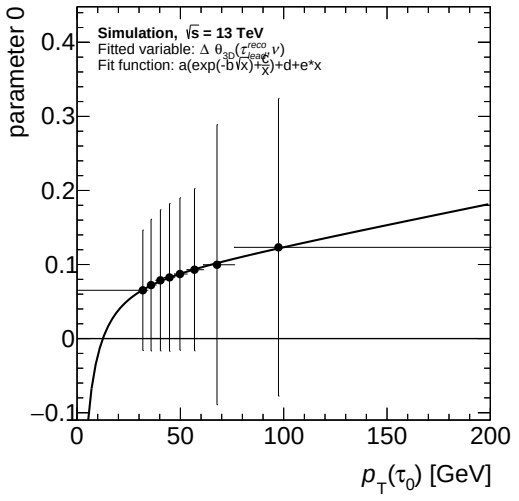

(a) Parameter C.

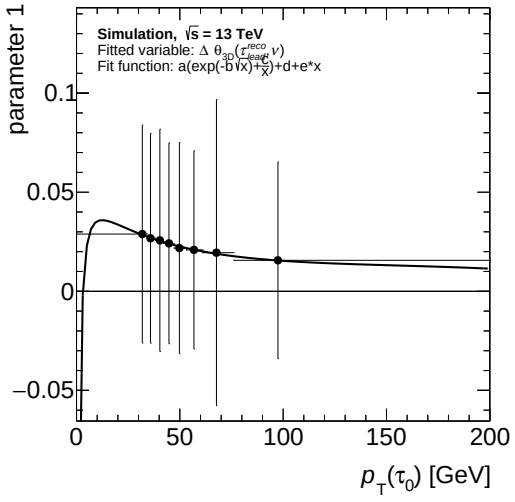

(b) Parameter m.

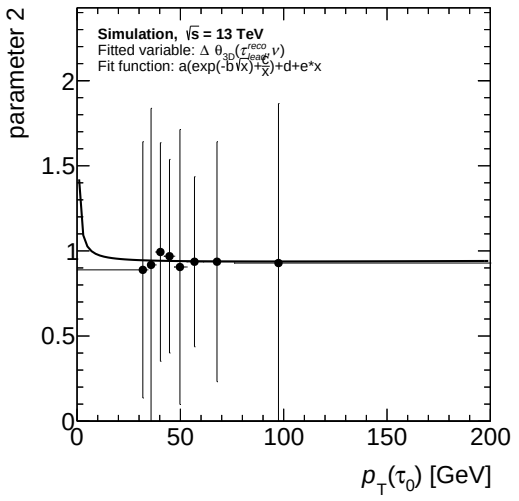

(c) Parameter a.

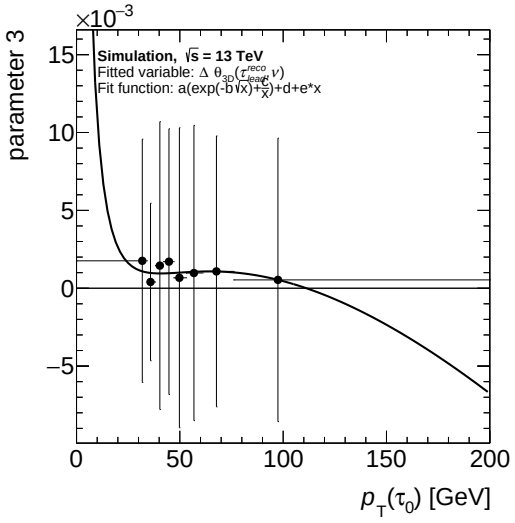

(d) Parameter b.

Figure B.5: $p_{\mathrm{T},\tau}$ dependent parameterisations of the angular distance between the neutrino and the reconstructed visible τ-lepton based on the SHERPA $Z \rightarrow \tau\tau$ sample. The parameterisations are shown for the τ_{1p0n} decay mode and the parameter values are extracted from the fits shown in Figure B.4.

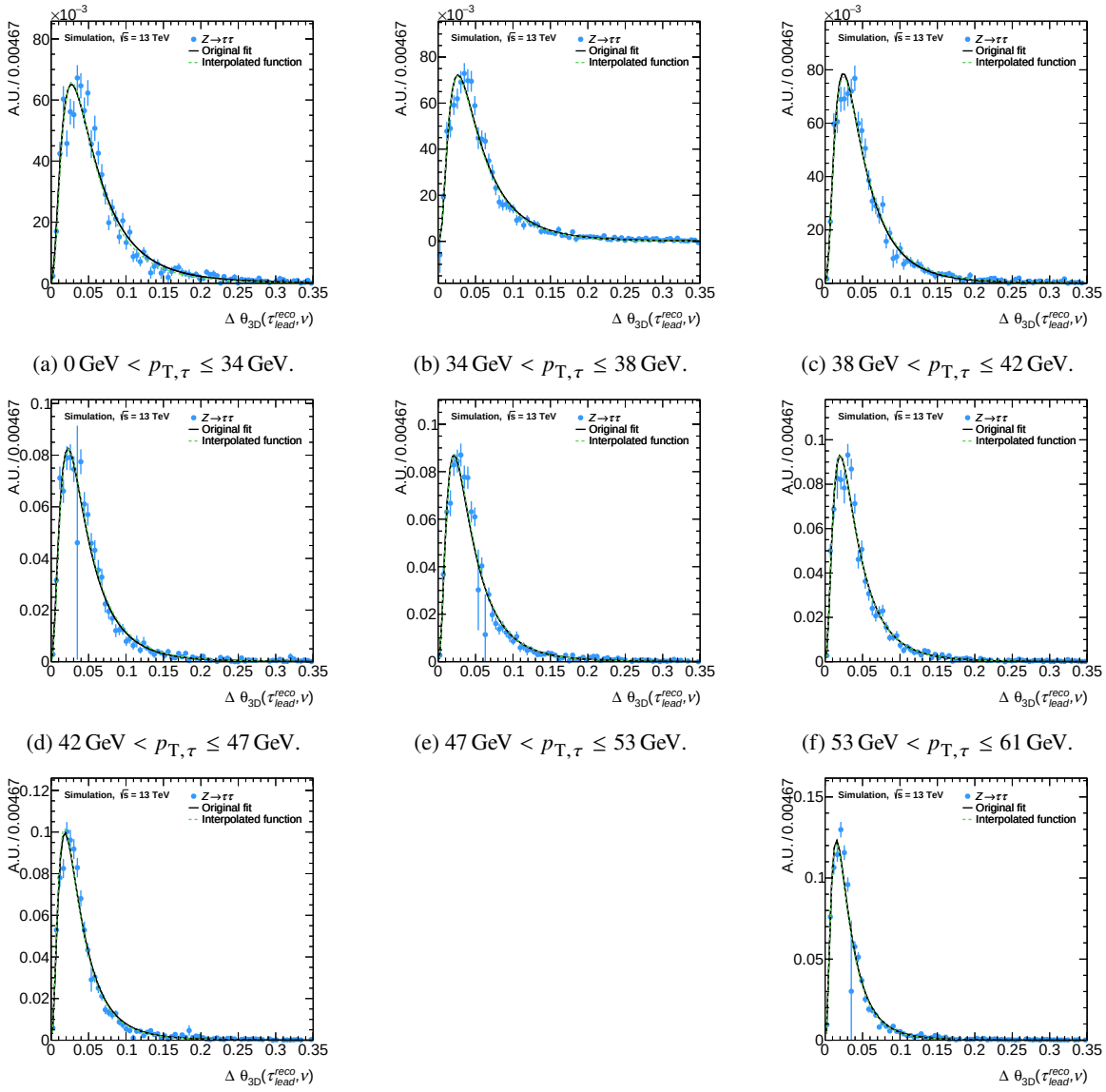

(a) 0 GeV $< p_{\mathrm{T},\tau} \leq$ 34 GeV. (b) 34 GeV $< p_{\mathrm{T},\tau} \leq$ 38 GeV. (c) 38 GeV $< p_{\mathrm{T},\tau} \leq$ 42 GeV.

(d) 42 GeV $< p_{\mathrm{T},\tau} \leq$ 47 GeV. (e) 47 GeV $< p_{\mathrm{T},\tau} \leq$ 53 GeV. (f) 53 GeV $< p_{\mathrm{T},\tau} \leq$ 61 GeV.

(g) 61 GeV $< p_{\mathrm{T},\tau} \leq$ 76 GeV. (h) 76 GeV $< p_{\mathrm{T},\tau} \leq$ 200 GeV.

Figure B.6: Parameterisations of the angular distance between the neutrino and the reconstructed visible τ-lepton based on the SHERPA $Z \to \tau\tau$ sample. The parameterisations are shown for the $\tau_{1\mathrm{p0n}}$ decay mode. Additionally, the resulting function of the $p_{\mathrm{T},\tau}$ interpolation derived in Figure B.5 is shown.

Parameterisation of Angular p.d.f.s for 1p1n Decays

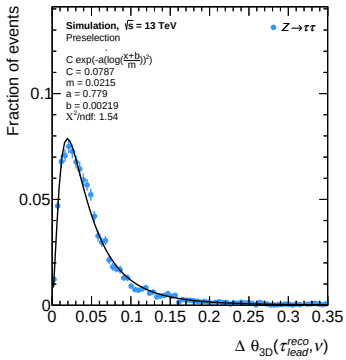

(a) 0 GeV $< p_{\mathrm{T},\tau} \leq$ 34 GeV.

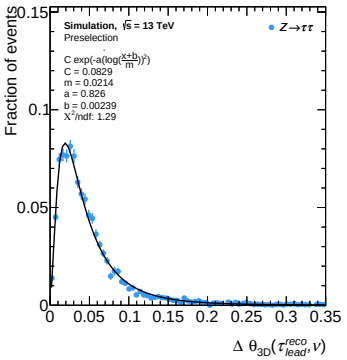

(b) 34 GeV $< p_{\mathrm{T},\tau} \leq$ 38 GeV.

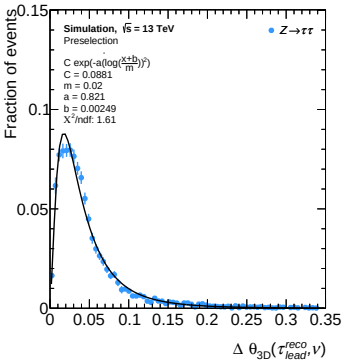

(c) 38 GeV $< p_{\mathrm{T},\tau} \leq$ 42 GeV.

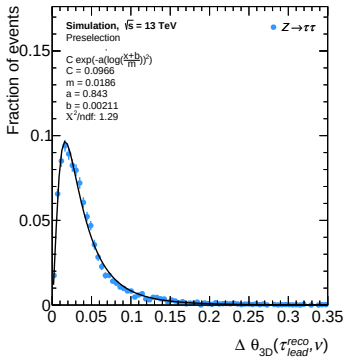

(d) 42 GeV $< p_{\mathrm{T},\tau} \leq$ 47 GeV.

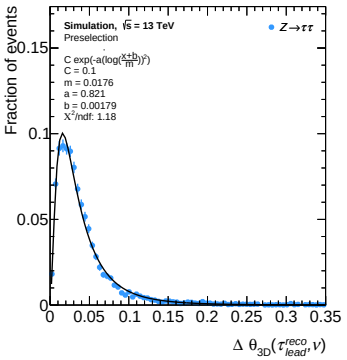

(e) 47 GeV $< p_{\mathrm{T},\tau} \leq$ 53 GeV.

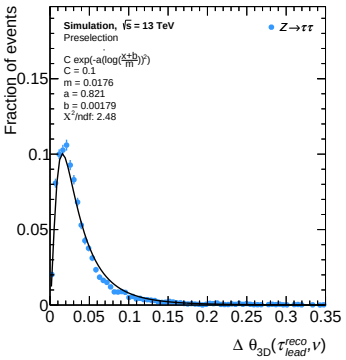

(f) 53 GeV $< p_{\mathrm{T},\tau} \leq$ 62 GeV.

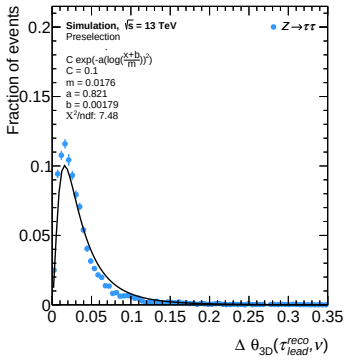

(g) 62 GeV $< p_{\mathrm{T},\tau} \leq$ 76 GeV.

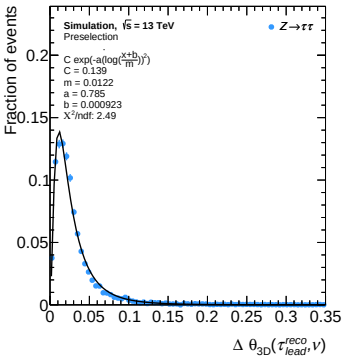

(h) 76 GeV $< p_{\mathrm{T},\tau} \leq$ 200 GeV.

Figure B.7: Parameterisations of the angular distance between the neutrino and the reconstructed visible τ-lepton based on the SHERPA $Z \rightarrow \tau\tau$ sample. The parameterisations (solid lines) are shown for the $\tau_{1\mathrm{p1n}}$ decay mode.

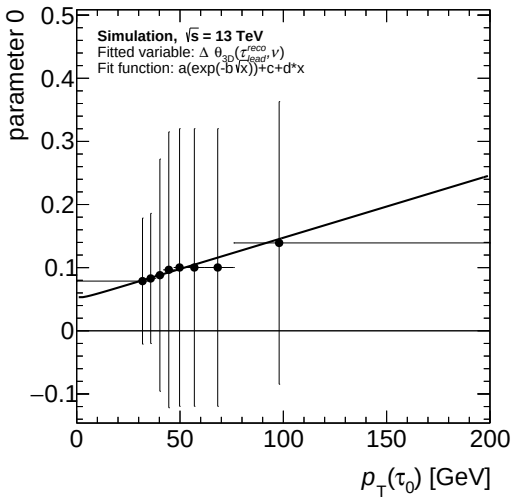

(a) Parameter C.

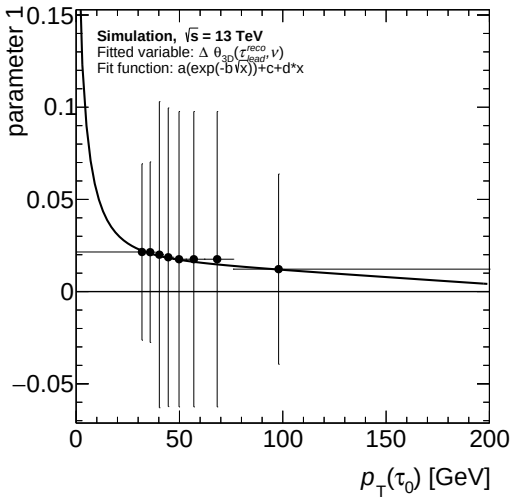

(b) Parameter m.

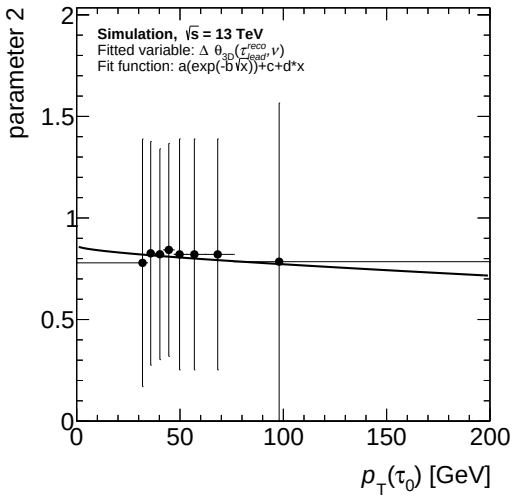

(c) Parameter a.

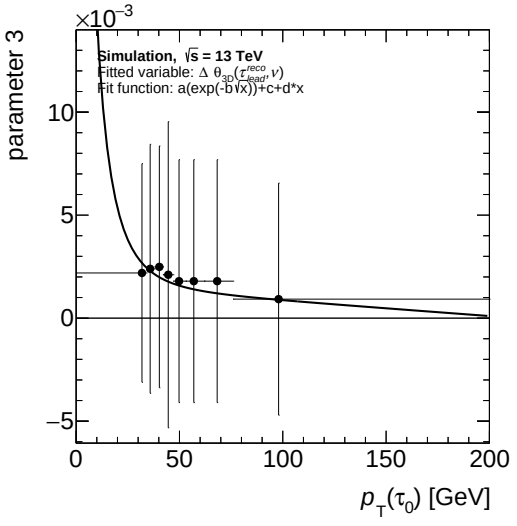

(d) Parameter b.

Figure B.8: $p_{\mathrm{T},\tau}$ dependent parameterisations of the angular distance between the neutrino and the reconstructed visible τ-lepton based on the SHERPA $Z \to \tau\tau$ sample. The parameterisations are shown for the $\tau_{1\mathrm{p}1\mathrm{n}}$ decay mode and the parameter values are extracted from the fits shown in Figure B.7.

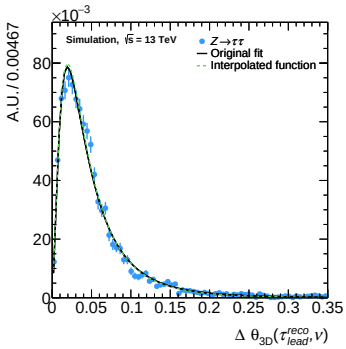

(a) 0 GeV $< p_{\mathrm{T},\tau} \leq$ 34 GeV.

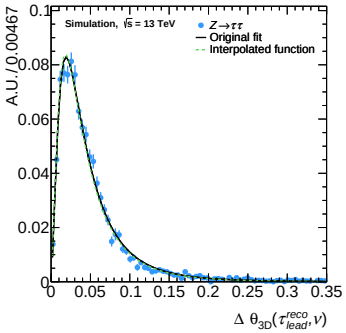

(b) 34 GeV $< p_{\mathrm{T},\tau} \leq$ 38 GeV.

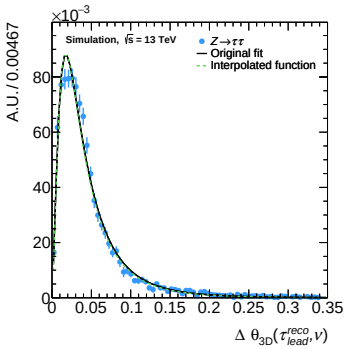

(c) 38 GeV $< p_{\mathrm{T},\tau} \leq$ 42 GeV.

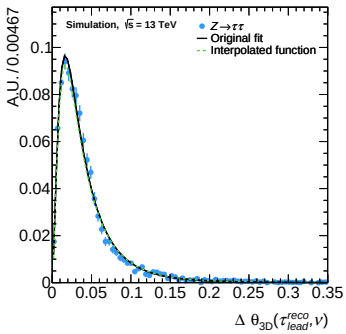

(d) 42 GeV $< p_{\mathrm{T},\tau} \leq$ 47 GeV.

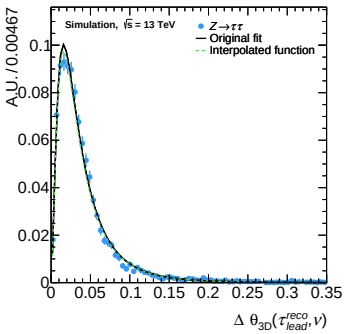

(e) 47 GeV $< p_{\mathrm{T},\tau} \leq$ 53 GeV.

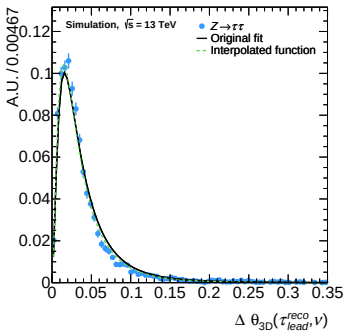

(f) 53 GeV $< p_{\mathrm{T},\tau} \leq$ 62 GeV.

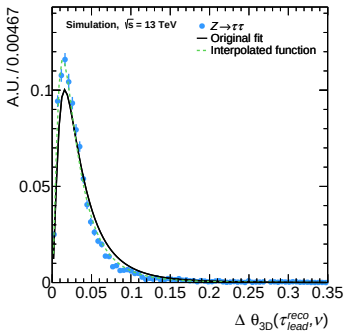

(g) 62 GeV $< p_{\mathrm{T},\tau} \leq$ 76 GeV.

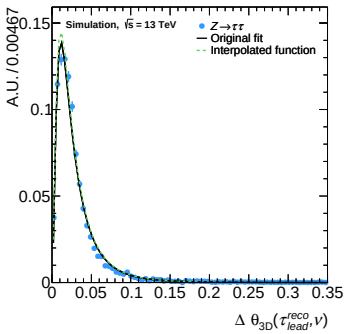

(h) 76 GeV $< p_{\mathrm{T},\tau} \leq$ 200 GeV.

Figure B.9: Parameterisations of the angular distance between the neutrino and the reconstructed visible τ-lepton based on the SHERPA $Z \rightarrow \tau\tau$ sample. The parameterisations are shown for the $\tau_{1\mathrm{p1n}}$ decay mode. Additionally, the resulting function of the $p_{\mathrm{T},\tau}$ interpolation derived in Figure B.8 is shown.

Parameterisation of Angular p.d.f.s for 1pXn Decays

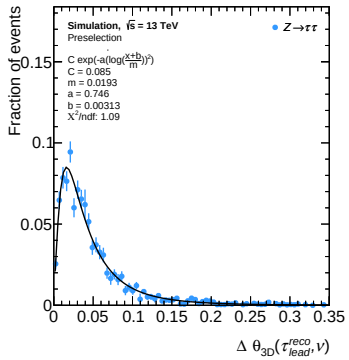

(a) 0 GeV $< p_{\mathrm{T},\tau} \leq$ 35 GeV.

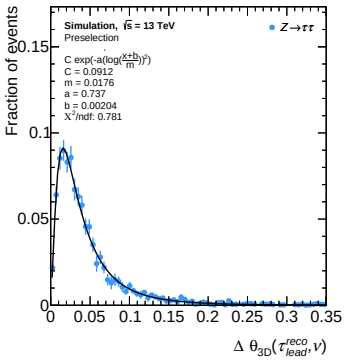

(b) 35 GeV $< p_{\mathrm{T},\tau} \leq$ 40 GeV.

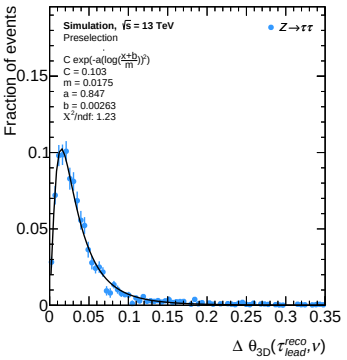

(c) 40 GeV $< p_{\mathrm{T},\tau} \leq$ 45 GeV.

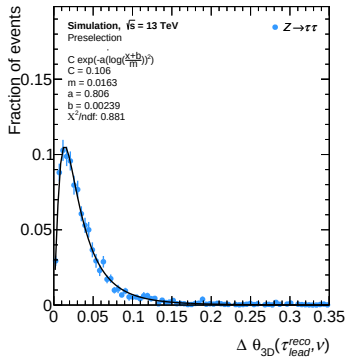

(d) 45 GeV $< p_{\mathrm{T},\tau} \leq$ 49 GeV.

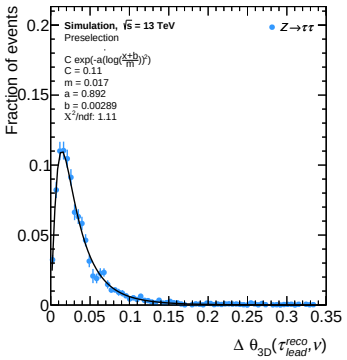

(e) 49 GeV $< p_{\mathrm{T},\tau} \leq$ 56 GeV.

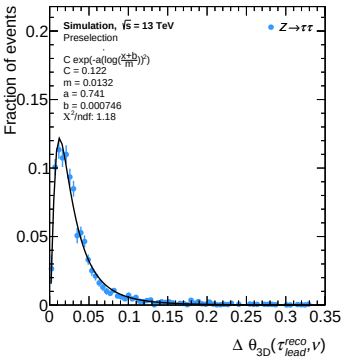

(f) 56 GeV $< p_{\mathrm{T},\tau} \leq$ 64 GeV.

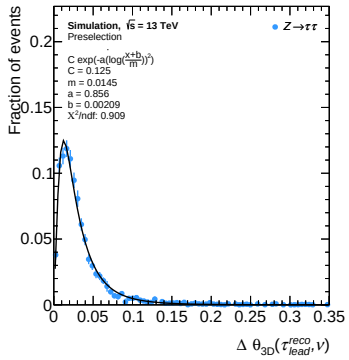

(g) 64 GeV $< p_{\mathrm{T},\tau} \leq$ 79 GeV.

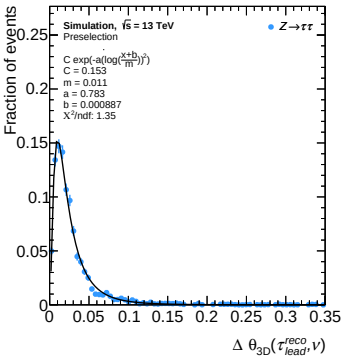

(h) 79 GeV $< p_{\mathrm{T},\tau} \leq$ 200 GeV.

Figure B.10: Parameterisations of the angular distance between the neutrino and the reconstructed visible τ-lepton based on the SHERPA $Z \rightarrow \tau\tau$ sample. The parameterisations (solid lines) are shown for the τ_{1pXn} decay mode.

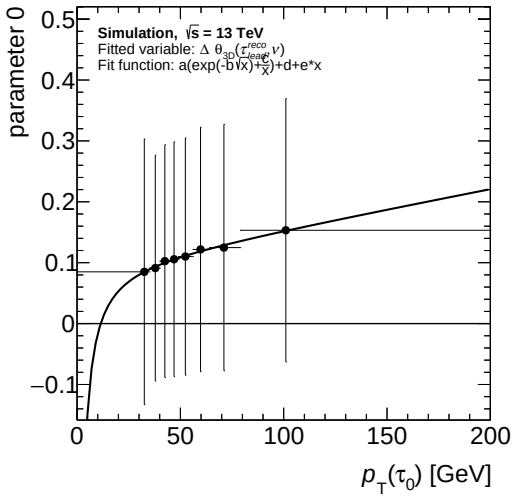

(a) Parameter C.

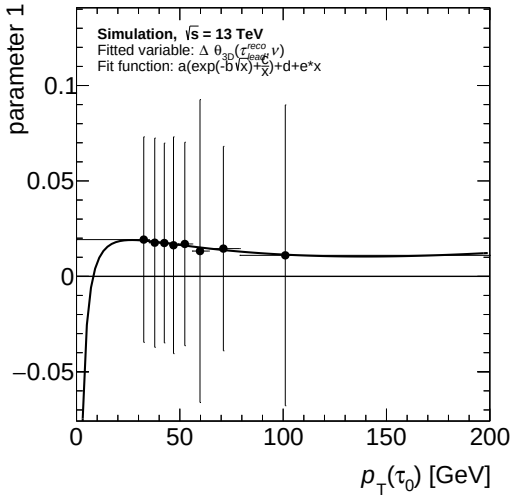

(b) Parameter m.

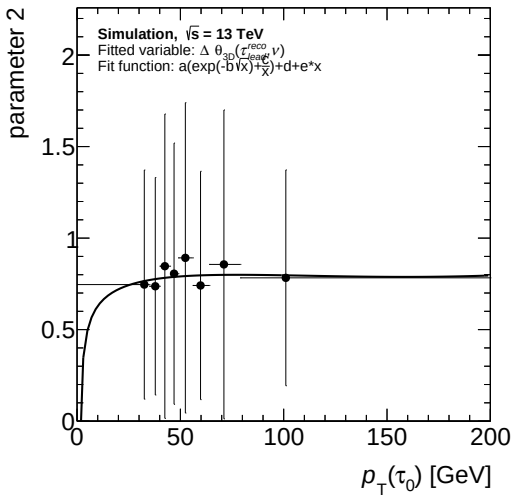

(c) Parameter a.

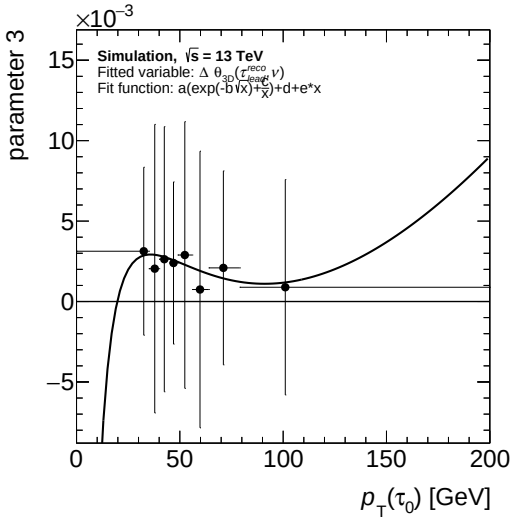

(d) Parameter b.

Figure B.11: $p_{\mathrm{T},\tau}$ dependent parameterisations of the angular distance between the neutrino and the reconstructed visible τ-lepton based on the SHERPA $Z \rightarrow \tau\tau$ sample. The parameterisations are shown for the τ_{1pXn} decay mode and the parameter values are extracted from the fits shown in Figure B.10.

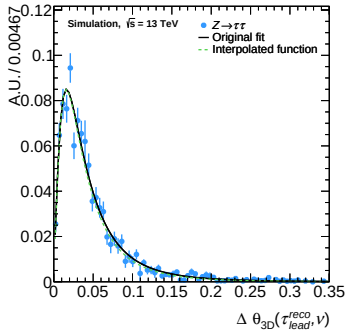

(a) 0 GeV $< p_{\mathrm{T},\tau} \leq$ 35 GeV.

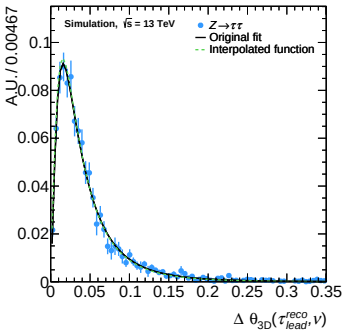

(b) 35 GeV $< p_{\mathrm{T},\tau} \leq$ 40 GeV.

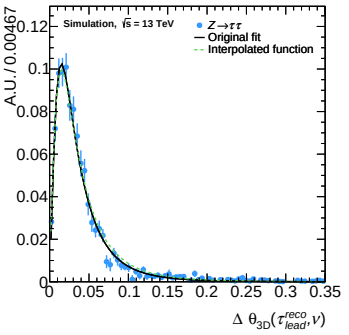

(c) 40 GeV $< p_{\mathrm{T},\tau} \leq$ 45 GeV.

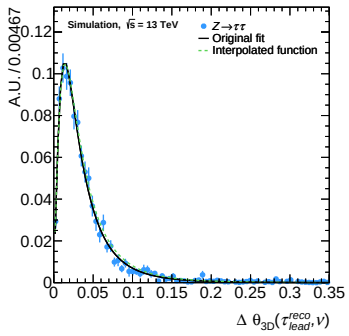

(d) 45 GeV $< p_{\mathrm{T},\tau} \leq$ 49 GeV.

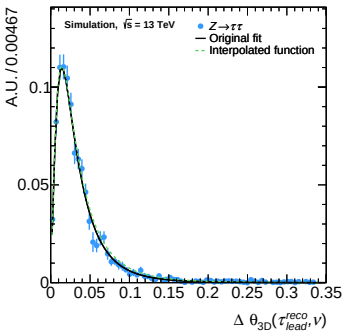

(e) 49 GeV $< p_{\mathrm{T},\tau} \leq$ 56 GeV.

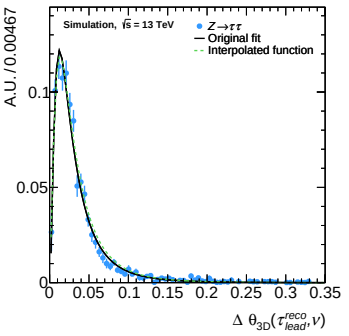

(f) 56 GeV $< p_{\mathrm{T},\tau} \leq$ 64 GeV.

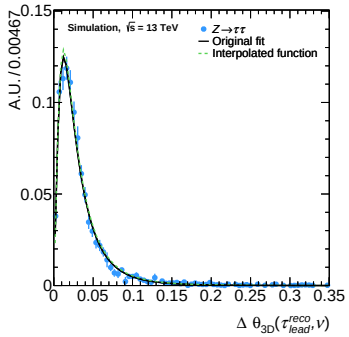

(g) 64 GeV $< p_{\mathrm{T},\tau} \leq$ 79 GeV.

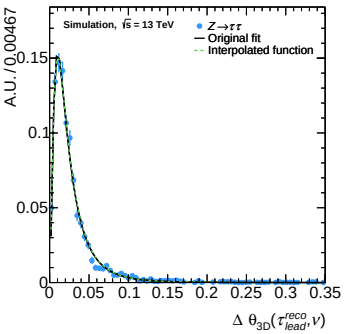

(h) 79 GeV $< p_{\mathrm{T},\tau} \leq$ 200 GeV.

Figure B.12: Parameterisations of the angular distance between the neutrino and the reconstructed visible τ-lepton based on the SHERPA $Z \to \tau\tau$ sample. The parameterisations are shown for the $\tau_{1\mathrm{pXn}}$ decay mode. Additionally, the resulting function of the $p_{\mathrm{T},\tau}$ interpolation derived in Figure B.11 is shown.

Parameterisation of Angular p.d.f.s for 3p0n Decays

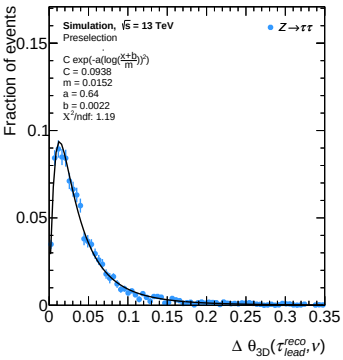

(a) 0 GeV $< p_{\mathrm{T},\tau} \leq$ 40 GeV.

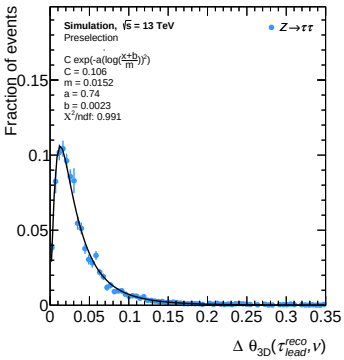

(b) 40 GeV $< p_{\mathrm{T},\tau} \leq$ 48 GeV.

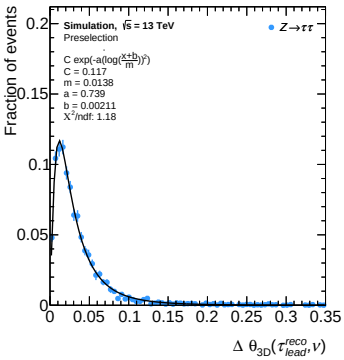

(c) 48 GeV $< p_{\mathrm{T},\tau} \leq$ 57 GeV.

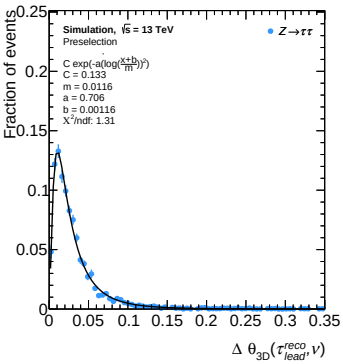

(d) 57 GeV $< p_{\mathrm{T},\tau} \leq$ 71 GeV.

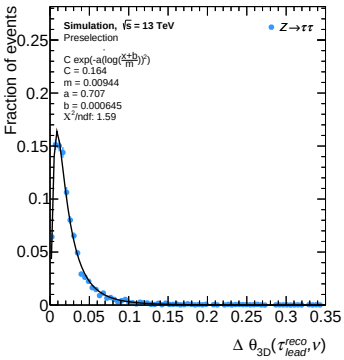

(e) 71 GeV $< p_{\mathrm{T},\tau} \leq$ 200 GeV.

Figure B.13: Parameterisations of the angular distance between the neutrino and the reconstructed visible τ-lepton based on the SHERPA $Z \rightarrow \tau\tau$ sample. The parameterisations (solid lines) are shown for the τ_{3p0n} decay mode.

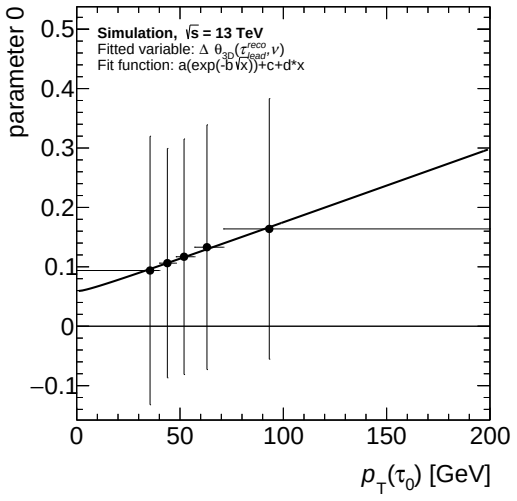

(a) Parameter C.

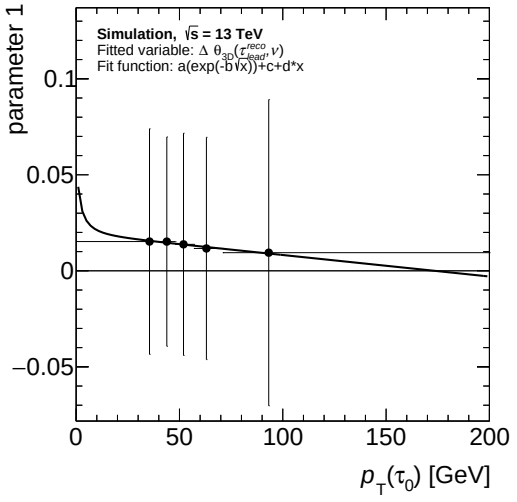

(b) Parameter m.

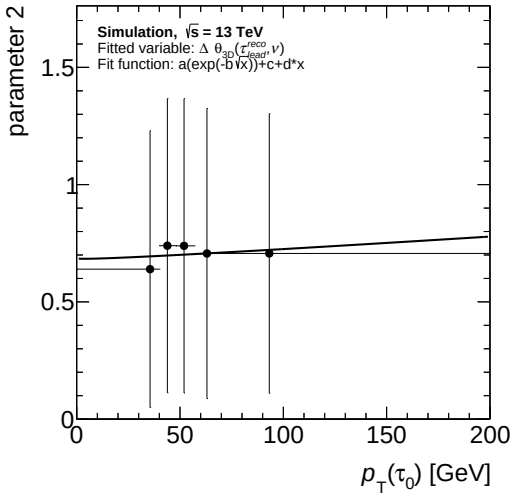

(c) Parameter a.

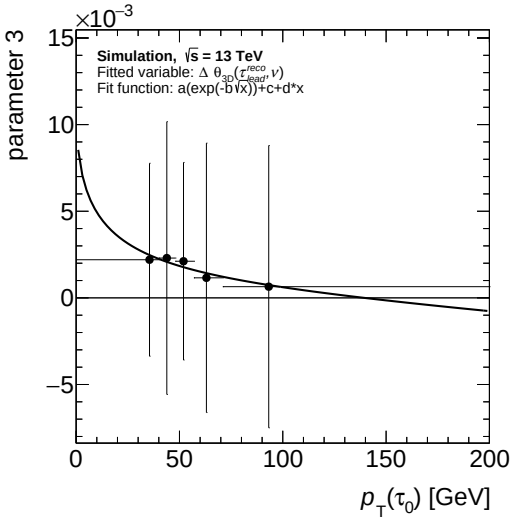

(d) Parameter b.

Figure B.14: $p_{\mathrm{T},\tau}$ dependent parameterisations of the angular distance between the neutrino and the reconstructed visible τ-lepton based on the SHERPA $Z \rightarrow \tau\tau$ sample. The parameterisations are shown for the τ_{3p0n} decay mode and the parameter values are extracted from the fits shown in Figure B.13.

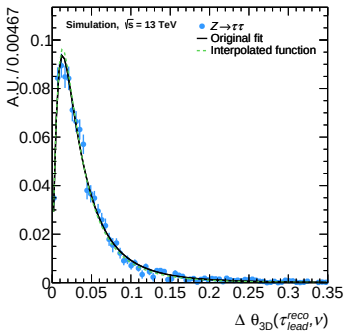

(a) 0 GeV $< p_{\mathrm{T},\tau} \leq$ 40 GeV.

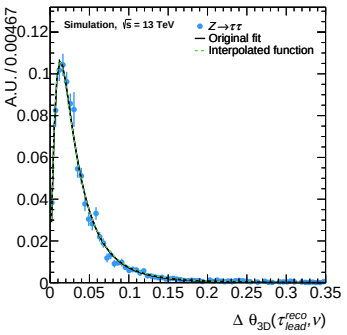

(b) 40 GeV $< p_{\mathrm{T},\tau} \leq$ 48 GeV.

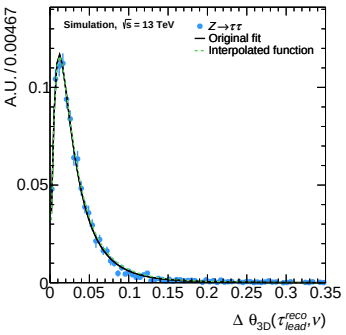

(c) 48 GeV $< p_{\mathrm{T},\tau} \leq$ 57 GeV.

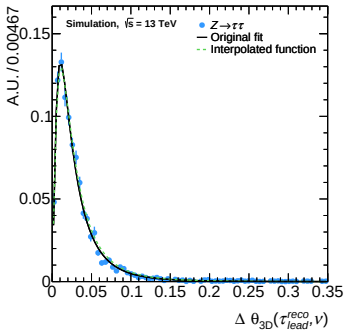

(d) 57 GeV $< p_{\mathrm{T},\tau} \leq$ 71 GeV.

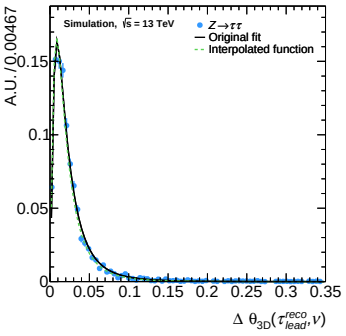

(e) 71 GeV $< p_{\mathrm{T},\tau} \leq$ 200 GeV.

Figure B.15: Parameterisations of the angular distance between the neutrino and the reconstructed visible τ-lepton based on the SHERPA $Z \rightarrow \tau\tau$ sample. The parameterisations are shown for the $\tau_{3\mathrm{p0n}}$ decay mode. Additionally, the resulting function of the $p_{\mathrm{T},\tau}$ interpolation derived in Figure B.14 is shown.

Parameterisation of Angular p.d.f.s for 3pXn Decays

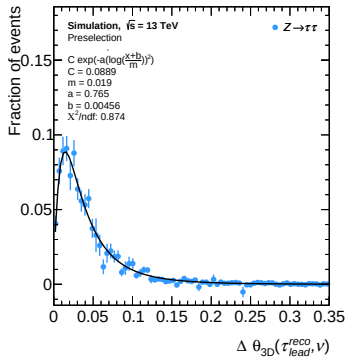

(a) 0 GeV $< p_{\mathrm{T},\tau} \leq$ 40 GeV.

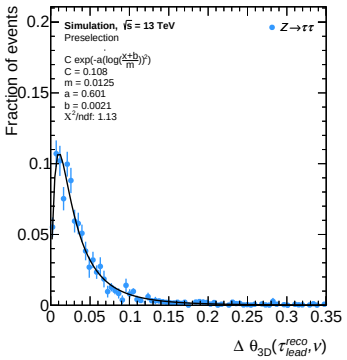

(b) 40 GeV $< p_{\mathrm{T},\tau} \leq$ 47 GeV.

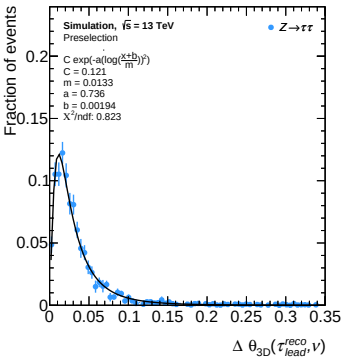

(c) 47 GeV $< p_{\mathrm{T},\tau} \leq$ 56 GeV.

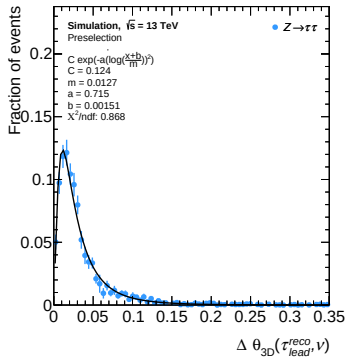

(d) 56 GeV $< p_{\mathrm{T},\tau} \leq$ 70 GeV.

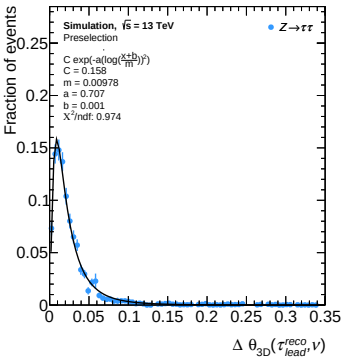

(e) 70 GeV $< p_{\mathrm{T},\tau} \leq$ 200 GeV.

Figure B.16: Parameterisations of the angular distance between the neutrino and the reconstructed visible τ-lepton based on the SHERPA $Z \to \tau\tau$ sample. The parameterisations (solid lines) are shown for the $\tau_{3\mathrm{pXn}}$ decay mode.

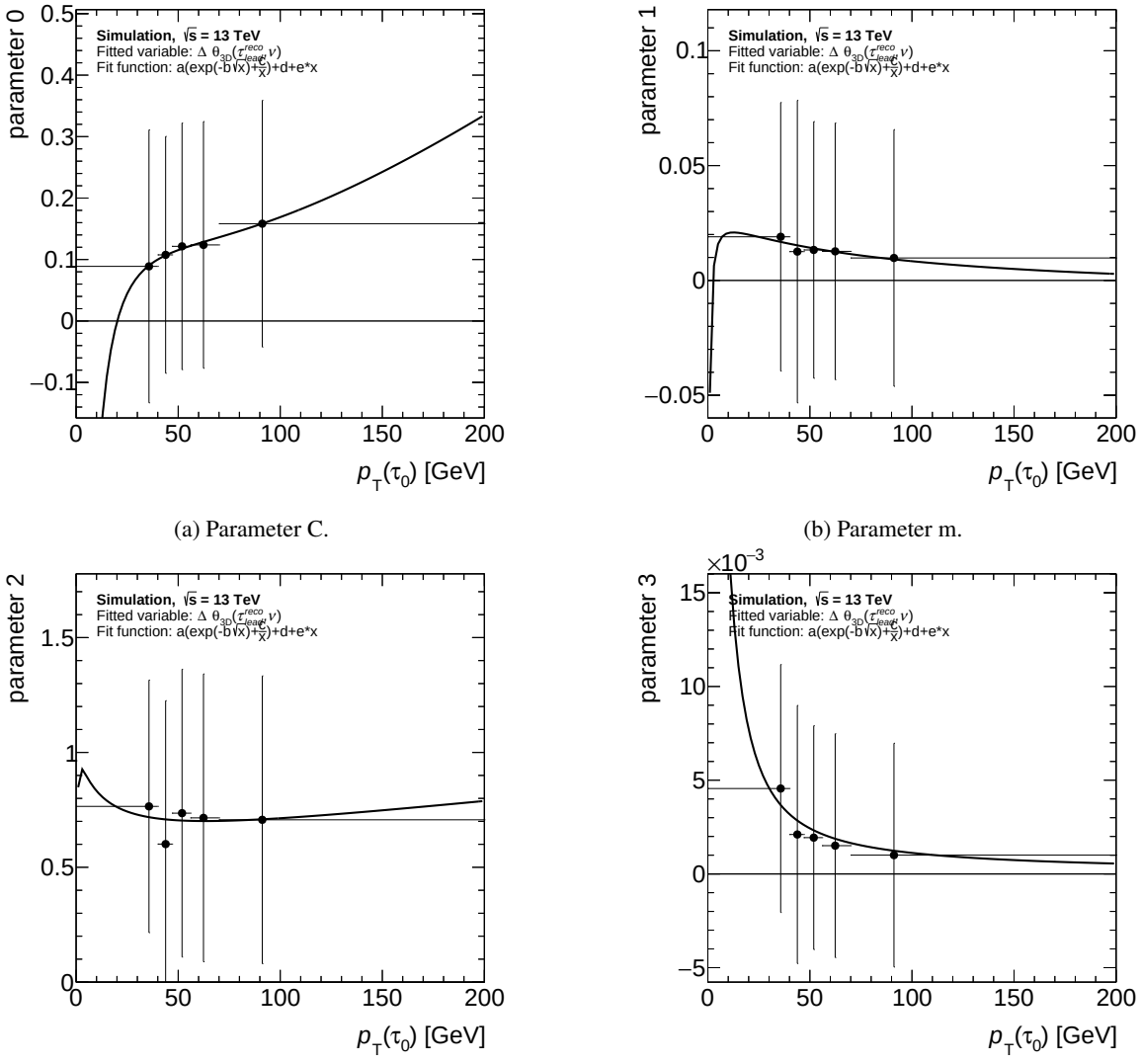

(a) Parameter C.

(b) Parameter m.

(c) Parameter a.

(d) Parameter b.

Figure B.17: $p_{\mathrm{T},\tau}$ dependent parameterisations of the angular distance between the neutrino and the reconstructed visible τ-lepton based on the SHERPA $Z \rightarrow \tau\tau$ sample. The parameterisations are shown for the τ_{3pXn} decay mode and the parameter values are extracted from the fits shown in Figure B.16.

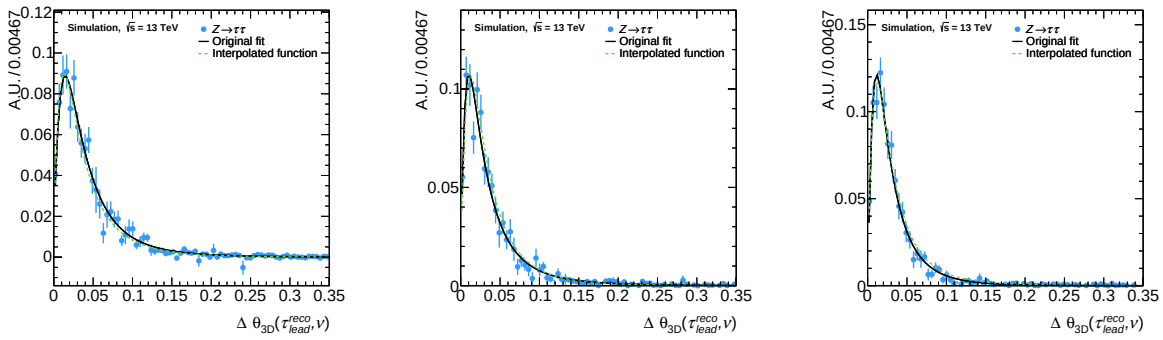

(a) 0 GeV $< p_{\mathrm{T},\tau} \leq$ 40 GeV. (b) 40 GeV $< p_{\mathrm{T},\tau} \leq$ 47 GeV. (c) 47 GeV $< p_{\mathrm{T},\tau} \leq$ 56 GeV.

(d) 56 GeV $< p_{\mathrm{T},\tau} \leq$ 70 GeV. (e) 70 GeV $< p_{\mathrm{T},\tau} \leq$ 200 GeV.

Figure B.18: Parameterisations of the angular distance between the neutrino and the reconstructed visible τ-lepton based on the SHERPA $Z \to \tau\tau$ sample. The parameterisations are shown for the $\tau_{3\mathrm{pXn}}$ decay mode. Additionally, the resulting function of the $p_{\mathrm{T},\tau}$ interpolation derived in Figure B.17 is shown.

Parameterisation of Angular p.d.f.s for Leptonic Decays

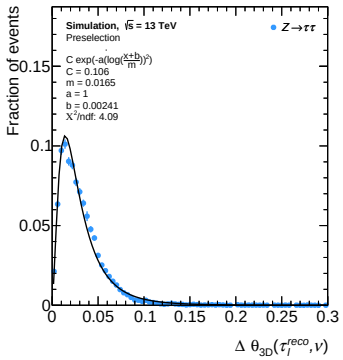

(a) 0 GeV $< p_{\mathrm{T},\tau} \leq$ 29 GeV.

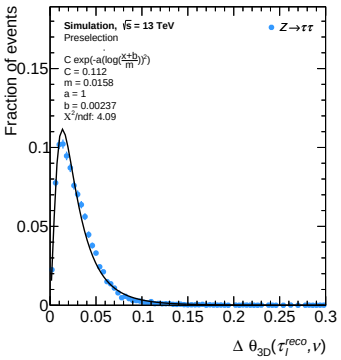

(b) 29 GeV $< p_{\mathrm{T},\tau} \leq$ 33 GeV.

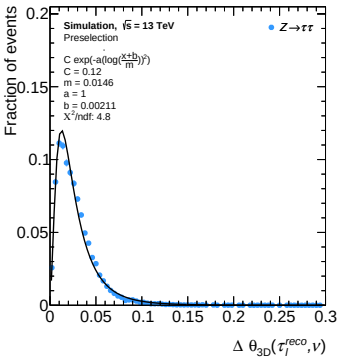

(c) 33 GeV $< p_{\mathrm{T},\tau} \leq$ 39 GeV.

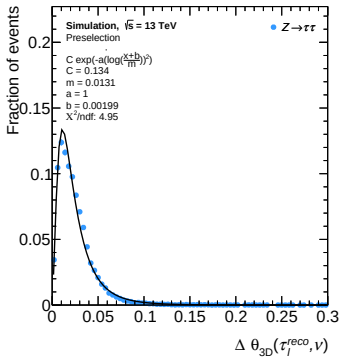

(d) 39 GeV $< p_{\mathrm{T},\tau} \leq$ 50 GeV.

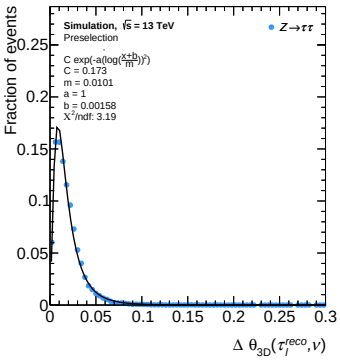

(e) 50 GeV $< p_{\mathrm{T},\tau} \leq$ 200 GeV.

Figure B.19: Parameterisations of the angular distance between the neutrino and the reconstructed visible τ-lepton based on the SHERPA $Z \rightarrow \tau\tau$ sample. The parameterisations (solid lines) are shown for the τ_{lep} decay mode.

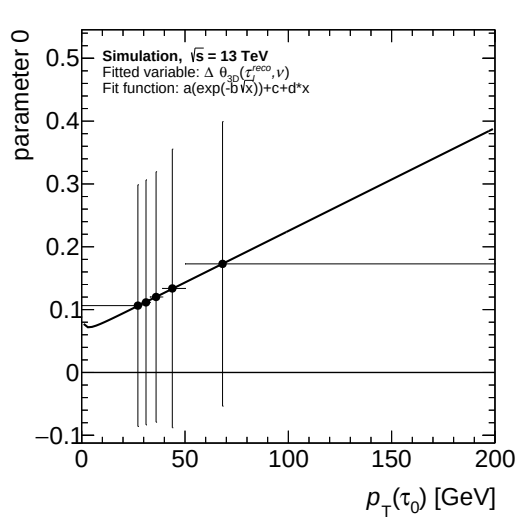

(a) Parameter C.

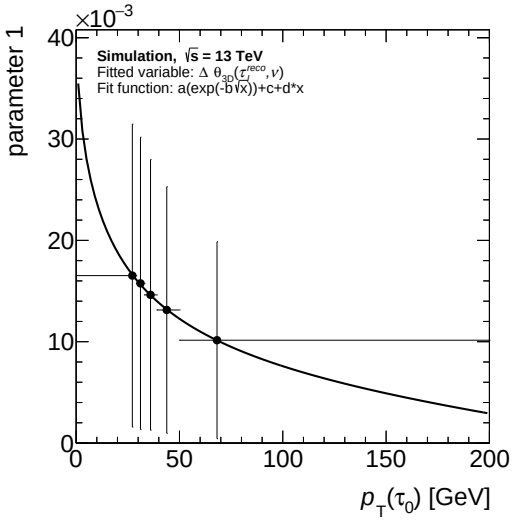

(b) Parameter m.

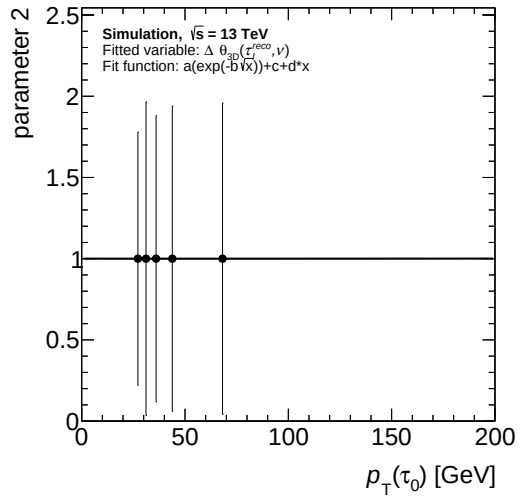

(c) Parameter a.

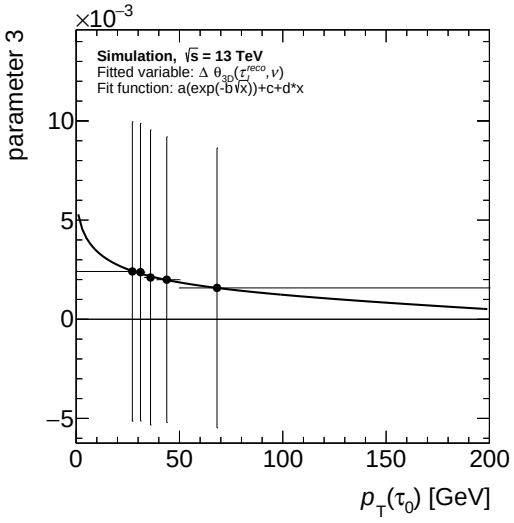

(d) Parameter b.

Figure B.20: $p_{\mathrm{T},\tau}$ dependent parameterisations of the angular distance between the neutrino and the reconstructed visible τ-lepton based on the SHERPA $Z \rightarrow \tau\tau$ sample. The parameterisations are shown for the τ_{lep} decay mode and the parameter values are extracted from the fits shown in Figure B.19.

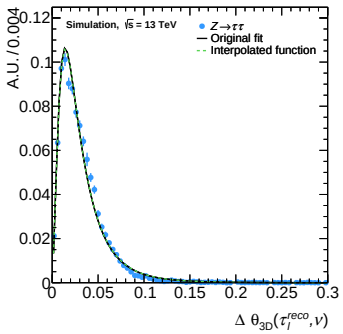

(a) 0 GeV $< p_{\mathrm{T},\tau} \leq$ 29 GeV.

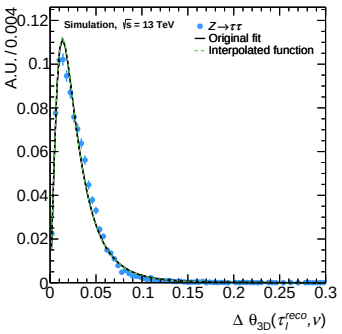

(b) 29 GeV $< p_{\mathrm{T},\tau} \leq$ 33 GeV.

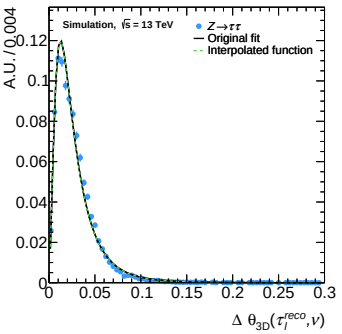

(c) 33 GeV $< p_{\mathrm{T},\tau} \leq$ 39 GeV.

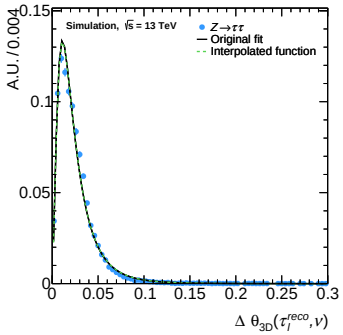

(d) 39 GeV $< p_{\mathrm{T},\tau} \leq$ 50 GeV.

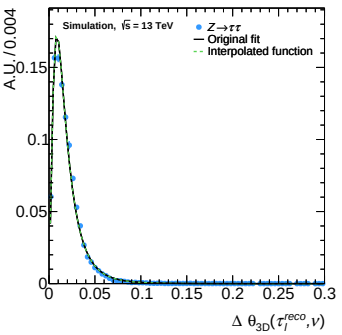

(e) 50 GeV $< p_{\mathrm{T},\tau} \leq$ 200 GeV.

Figure B.21: Parameterisations of the angular distance between the neutrino and the reconstructed visible τ-lepton based on the SHERPA $Z \rightarrow \tau\tau$ sample. The parameterisations are shown for the τ_{lep} decay mode. Additionally, the resulting function of the $p_{\mathrm{T},\tau}$ interpolation derived in Figure B.20 is shown.

B.5 Leptonic τ-lepton p.d.f. Bias

The p.d.f. parameterisations for leptonic τ-lepton decays are based on $Z \rightarrow \tau\tau$ simulations in the $\tau_{\text{lep}}\tau_{\text{had}}$ channel. This choice is motivated by the available statistics of the specific sample compared to the available statistics of the fully leptonic $Z \rightarrow \tau\tau$ sample at that point. As the final event selection of the $\tau_e\tau_\mu$ channel is able to include τ-leptons with lower transverse momentum than the minimum requirement used for the parameterisation, see Table B.1, they become important in the $\tau_e\tau_\mu$ channel. Generally, the τ-lepton p.d.f.s of leptonic decays should not differ in similar momentum ranges between the $\tau_e\tau_\mu$ and the $\tau_{\text{lep}}\tau_{\text{had}}$ channel. However, due to the $\tau_{\text{lep}}\tau_{\text{had}}$ channel not being able to directly include very low momentum τ-leptons, the parameterisation extrapolation to low momenta becomes more relevant. The impact on the separation power of low momentum τ-leptons on the MMC's separation power is studied by imposing a common lower threshold on $p_{\text{T},\tau}$ for both τ-leptons in the $\tau_e\tau_\mu$ channel. For this study, the original MMC version used in Reference [7] serves as a reference point. While the separation power is decreased by roughly 1 % for the nominal $\tau_e\tau_\mu$ selection, the two MMC versions become more similar with increasing lower $p_{\text{T},\tau}$ thresholds. Already at a lower of threshold of 20 GeV, the two versions are mostly compatible, even though this value is still below the selection criteria used for the parameterisation. This emphasises that the extrapolation does work up to a certain point. Additionally, it has to be noted that the overall separation power depends on the lower $p_{\text{T},\tau}$ bounds for both versions and increases with increasing thresholds.

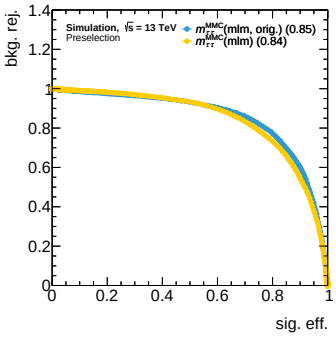

(a) ROC of the $\tau_{\text{lep}}\tau_{\text{lep}}$ channel with the nominal selection.

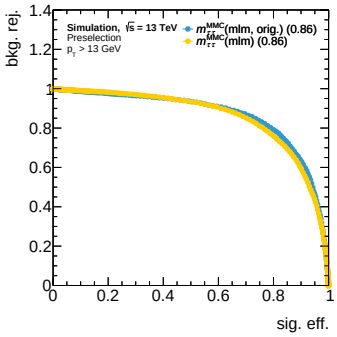

(b) ROC of the $\tau_{\text{lep}}\tau_{\text{lep}}$ channel with a $p_{\text{T},\tau}$ cut of $p_{\text{T}} > 13\,\text{GeV}$.

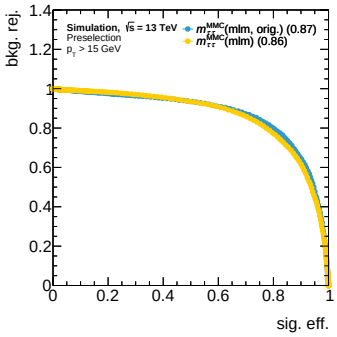

(c) ROC of the $\tau_{\text{lep}}\tau_{\text{lep}}$ channel with a $p_{\text{T},\tau}$ cut of $p_{\text{T}} > 15\,\text{GeV}$.

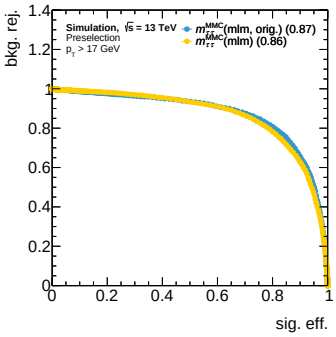

(d) ROC of the $\tau_{\text{lep}}\tau_{\text{lep}}$ channel with a $p_{\text{T},\tau}$ cut of $p_{\text{T}} > 17\,\text{GeV}$.

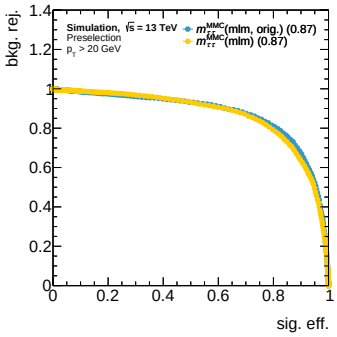

(e) ROC of the $\tau_{\text{lep}}\tau_{\text{lep}}$ channel with a $p_{\text{T},\tau}$ cut of $p_{\text{T}} > 20\,\text{GeV}$.

Figure B.22: Receiver-Operating-Curves of the MMC in the $\tau_{\text{lep}}\tau_{\text{lep}}$ final state. Different minimal $p_{\text{T},\tau}$ thresholds are applied to illustrate the effect of low p_{T} τ_{lep} on the performance in comparison to the MMC version used in Reference [7] (mlm, orig.).

B.6 Final MMC Performance

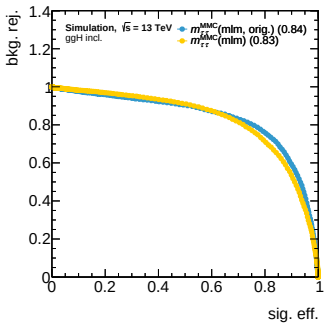

(a) Inclusive boosted signal regions in the $\tau_{\text{lep}}\tau_{\text{lep}}$ channel.

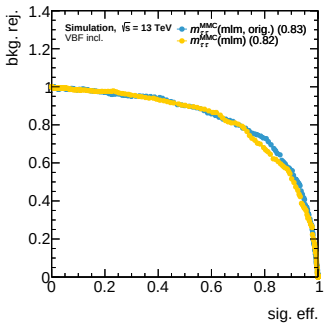

(b) Inclusive VBF-like signal regions in the $\tau_{\text{lep}}\tau_{\text{lep}}$ channel.

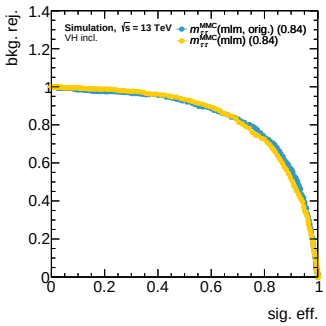

(c) Inclusive VH-like signal regions in the $\tau_{\text{lep}}\tau_{\text{lep}}$ channel.

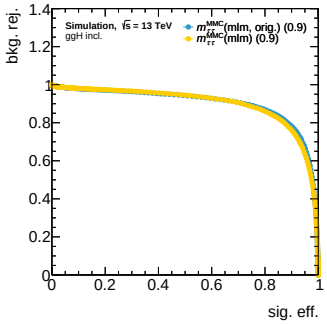

(d) Inclusive boosted signal regions in the $\tau_{\text{lep}}\tau_{\text{had}}$ channel.

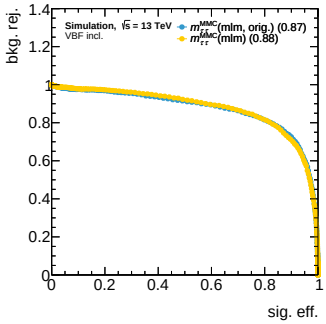

(e) Inclusive VBF-like signal regions in the $\tau_{\text{lep}}\tau_{\text{had}}$ channel.

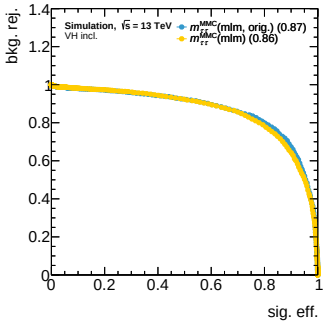

(f) Inclusive VH-like signal regions in the $\tau_{\text{lep}}\tau_{\text{had}}$ channel.

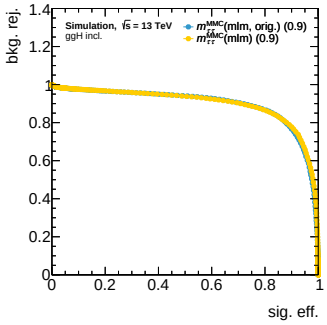

(g) Inclusive boosted signal regions in the $\tau_{\text{had}}\tau_{\text{had}}$ channel.

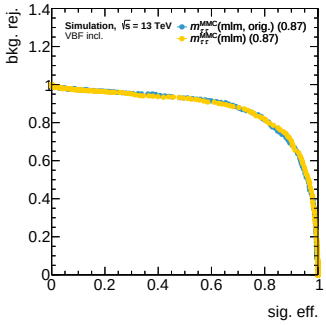

(h) Inclusive VBF-like signal regions in the $\tau_{\text{had}}\tau_{\text{had}}$ channel.

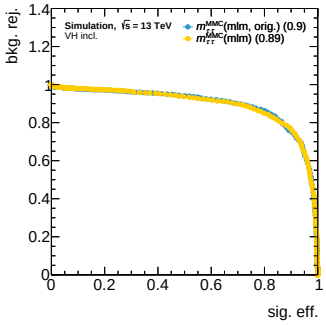

(i) Inclusive VH-like signal regions in the $\tau_{\text{had}}\tau_{\text{had}}$ channel.

Figure B.23: Receiver-Operating-Curves of the MMC in the inclusive signal regions for all individual di-τ decay channels comparing the final MMC configuration, shown in yellow, with the original MMC, shown in blue.

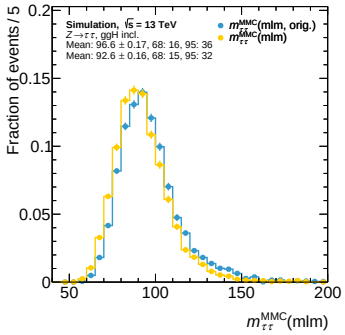

(a) Inclusive boosted signal regions in the $\tau_{\mathrm{lep}}\tau_{\mathrm{lep}}$ channel.

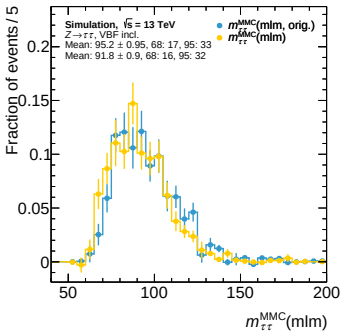

(b) Inclusive VBF-like signal regions in the $\tau_{\mathrm{lep}}\tau_{\mathrm{lep}}$ channel.

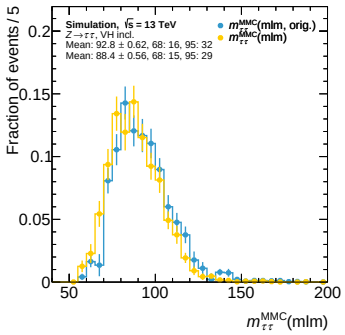

(c) Inclusive VH-like signal regions in the $\tau_{\mathrm{lep}}\tau_{\mathrm{lep}}$ channel.

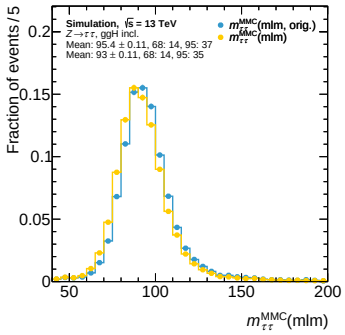

(d) Inclusive boosted signal regions in the $\tau_{\mathrm{lep}}\tau_{\mathrm{had}}$ channel.

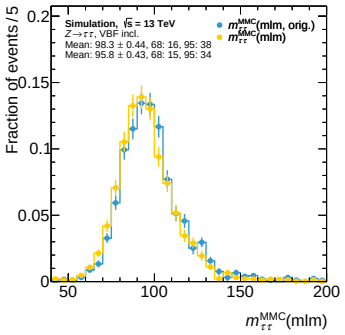

(e) Inclusive VBF-like signal regions in the $\tau_{\mathrm{lep}}\tau_{\mathrm{had}}$ channel.

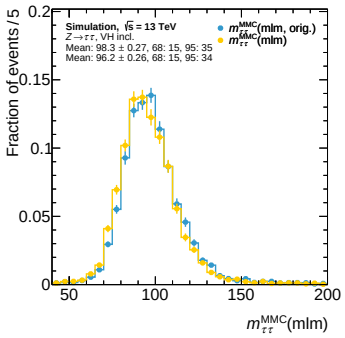

(f) Inclusive VH-like signal regions in the $\tau_{\mathrm{lep}}\tau_{\mathrm{had}}$ channel.

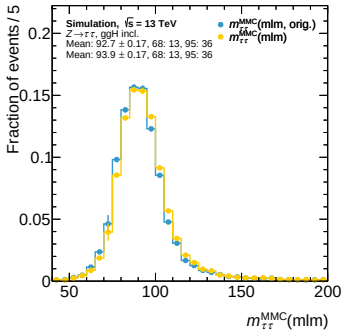

(g) Inclusive boosted signal regions in the $\tau_{\mathrm{had}}\tau_{\mathrm{had}}$ channel.

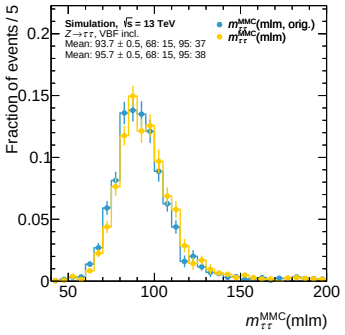

(h) Inclusive VBF-like signal regions in the $\tau_{\mathrm{had}}\tau_{\mathrm{had}}$ channel.

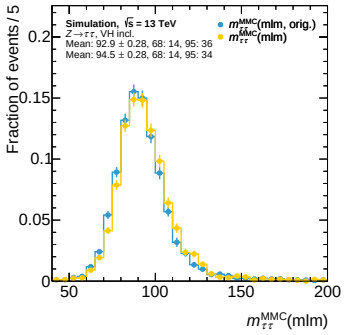

(i) Inclusive VH-like signal regions in the $\tau_{\mathrm{had}}\tau_{\mathrm{had}}$ channel.

Figure B.24: MMC lineshape of the $Z \to \tau\tau$ process in the inclusive signal regions for all individual di-τ decay channels comparing the final MMC configuration, shown in yellow, with the original MMC, shown in blue.

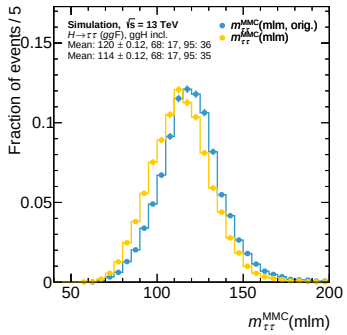

(a) Inclusive boosted signal regions in the $\tau_{\text{lep}}\tau_{\text{lep}}$ channel.

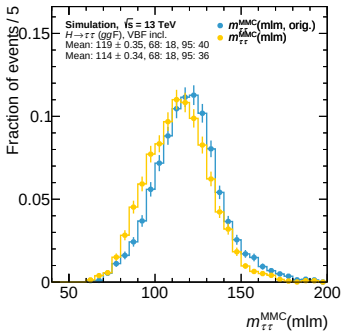

(b) Inclusive VBF-like signal regions in the $\tau_{\text{lep}}\tau_{\text{lep}}$ channel.

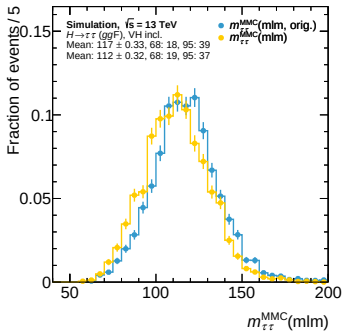

(c) Inclusive VH-like signal regions in the $\tau_{\text{lep}}\tau_{\text{lep}}$ channel.

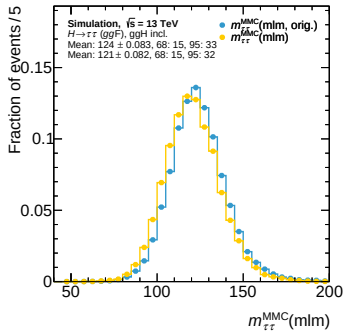

(d) Inclusive boosted signal regions in the $\tau_{\text{lep}}\tau_{\text{had}}$ channel.

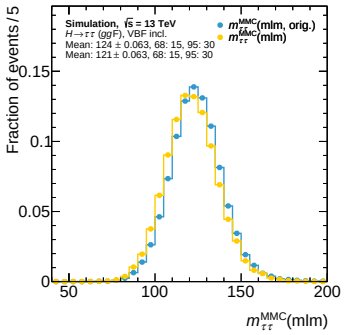

(e) Inclusive VBF-like signal regions in the $\tau_{\text{lep}}\tau_{\text{had}}$ channel.

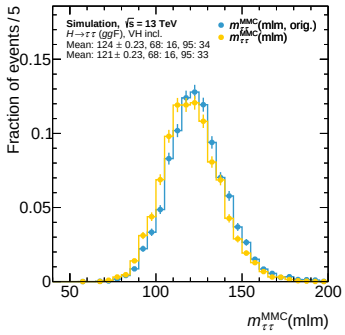

(f) Inclusive VH-like signal regions in the $\tau_{\text{lep}}\tau_{\text{had}}$ channel.

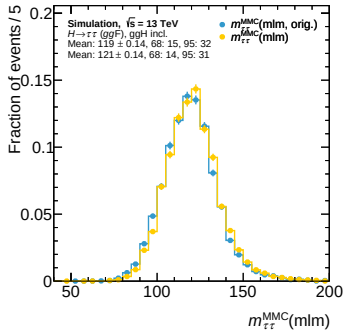

(g) Inclusive boosted signal regions in the $\tau_{\text{had}}\tau_{\text{had}}$ channel.

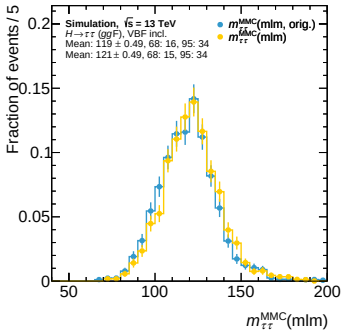

(h) Inclusive VBF-like signal regions in the $\tau_{\text{had}}\tau_{\text{had}}$ channel.

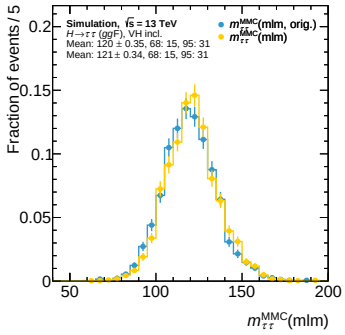

(i) Inclusive VH-like signal regions in the $\tau_{\text{had}}\tau_{\text{had}}$ channel.

Figure B.25: MMC lineshape of the $H \to \tau\tau$ process in the inclusive signal regions for all individual di-τ decay channels comparing the final MMC configuration, shown in yellow, with the original MMC, shown in blue.

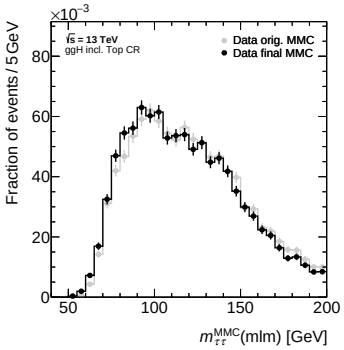

(a) Inclusive boosted regions in the $\tau_{\mathrm{lep}}\tau_{\mathrm{lep}}$ channel.

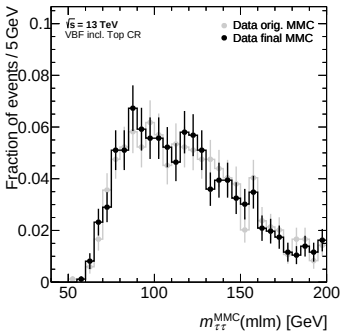

(b) Inclusive VBF-like regions in the $\tau_{\mathrm{lep}}\tau_{\mathrm{lep}}$ channel.

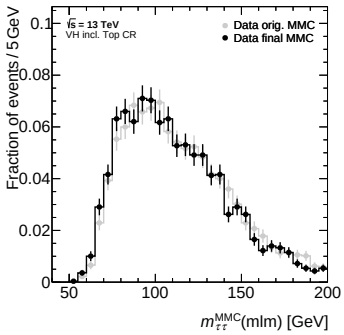

(c) Inclusive VH-like regions in the $\tau_{\mathrm{lep}}\tau_{\mathrm{lep}}$ channel.

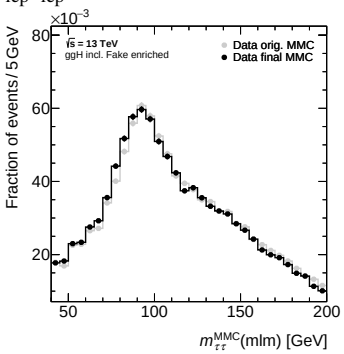

(d) Inclusive boosted regions in the $\tau_{\mathrm{lep}}\tau_{\mathrm{had}}$ channel.

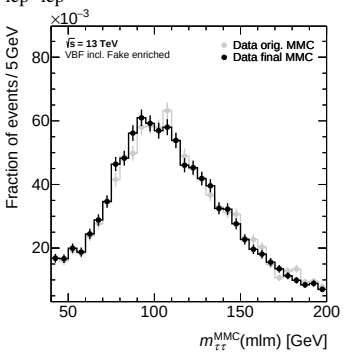

(e) Inclusive VBF-like regions in the $\tau_{\mathrm{lep}}\tau_{\mathrm{had}}$ channel.

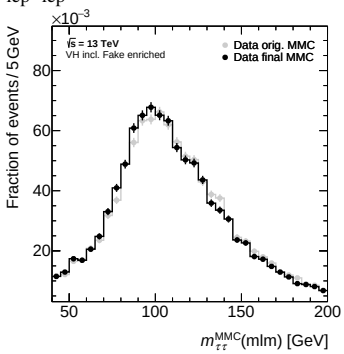

(f) Inclusive VH-like regions in the $\tau_{\mathrm{lep}}\tau_{\mathrm{had}}$ channel.

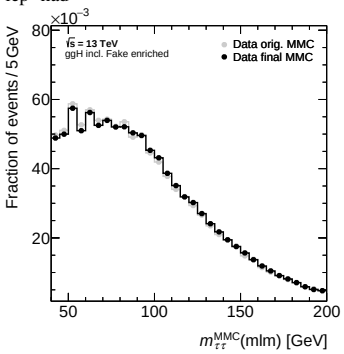

(g) Inclusive boosted regions in the $\tau_{\mathrm{had}}\tau_{\mathrm{had}}$ channel.

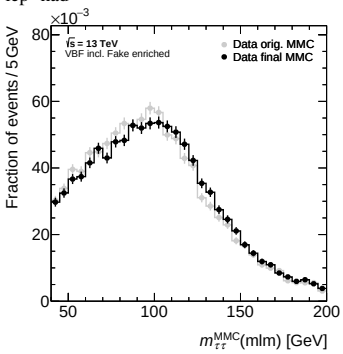

(h) Inclusive VBF-like regions in the $\tau_{\mathrm{had}}\tau_{\mathrm{had}}$ channel.

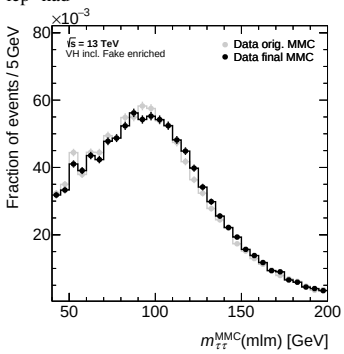

(i) Inclusive VH-like regions in the $\tau_{\mathrm{had}}\tau_{\mathrm{had}}$ channel.

Figure B.26: MMC lineshape of data normalised to unity in misidentified τ-lepton enriched regions for all individual di-τ decay channels comparing the final MMC configuration, shown in black, with the original MMC, shown in gray. A different colour scheme has been chosen to highlight that these figures show data.

B.7 Algorithm Parameter Settings Used in the Measurement

Option	$\tau_{\text{lep}}\tau_{\text{lep}}$	$\tau_{\text{lep}}\tau_{\text{had}}$	$\tau_{\text{had}}\tau_{\text{had}}$	Comments
Decorate	False	False	False	default, use accessor methods
FloatStoppingCrit	True	True	True	default, see Section 4.4.1
CalibSet	2019	2019	2019	default, new parameterisations, see Section 4.4.2
NsigmaMET	4	-1	-1	default for $\tau_{\text{lep}}\tau_{\text{had}}$ and $\tau_{\text{had}}\tau_{\text{had}}$
UseTailCleanup	0	-1	-1	default, disabled
UseVerbose	0	-1	-1	default, disabled
NiterFit2	30	-1	-1	default, disabled
NiterFit3	10	-1	-1	default, disabled
UseTauProbability	1	1	1	relevant for previous p.d.f. sets, adds momentum ratio p.d.f.
UseMnuProbability	-1	-1	-1	new option, includes neutrino mass p.d.f., see Section 4.4.2
UseDefaults	-1	-1	-1	default, disabled
UseEfficiencyRecovery	-1	-1	-1	default, disabled
UseMETDphiLL	1	-1	-1	not implemented for $\tau_{\text{lep}}\tau_{\text{had}}$ and $\tau_{\text{had}}\tau_{\text{had}}$, turns off $\Delta\phi_{\tau\tau}$ correction in $E_{\text{T}}^{\text{miss}}$ resolution if set to false for $\tau_{\text{lep}}\tau_{\text{lep}}$
ParamFilePath	MMC_params_v1_fixed.root			default, holds parameterised p.d.f.s
$p_{\text{T}}^{\text{jet}}$ required for jets entering the number of jet counting	30	30	30	

Table B.2: Parameter settings of the MMC for all di-τ decay channels. "NsigmaMET" defines the width of $E_{\text{T}}^{\text{miss}}$ probability density function in the Markov Chain in terms of $\sigma(E_{\text{T}}^{\text{miss}})$. The default setting lets the MMC decide the number of $\sigma(E_{\text{T}}^{\text{miss}})$ used in the Markov Chain. If "UseTailCleanup" is enabled, proposed states with a reconstructed mass exceeding the visible mass by roughly a factor of two or very high neutrino momenta are re-sampled in the fully leptonic di-τ channel. The number of maximum iterations can be controlled via "NiterFit2" and "NiterFit3" when the MMC is run in the mode dedicated for lepton flavour violating measurements. This mode is not enabled for this analysis as it presumes a direct Higgs boson decay into a light lepton and a leptonic τ-lepton decay, reducing the overall number of neutrinos compared to $\tau_{\text{lep}}\tau_{\text{lep}}$ decays. Events with a failed mass reconstruction can be re-run if "UseEfficiencyRecovery" is enabled.

APPENDIX C

Additional Studies of the Measurement Design

C.1 Tagger Variables

	Variable	VBF	V(had)H	ttH vs $t\bar{t}$	ttH vs $Z \to \tau\tau$
Jet properties	Invariant mass of 2 leading jets	•	•		
	$p_{\mathrm{T}}(jj)$	•	•		
	Product of η of 2 leading jets	•			
	Sub-leading jet p_{T}	•			
	Leading jet η				•
	Sub-leading jet η				•
	Scalar sum of all jets p_{T}			•	•
	Scalar sum of all b-tagged jets p_{T}				•
	Best W-candidate dijet invariant mass			•	•
	Best t-quark-candidate three-jet invariant mass			•	•
Angular distances	$\Delta\phi$(jet 0, jet 1)	•			
	$\lvert\Delta\eta$(jet 0, jet 1)$\rvert$	•	•		
	ΔR(jet 0, jet 1)		•		
	$\Delta R(\tau\tau, jj)$		•		
	$\Delta R(\tau, \tau)$		•	•	
	Smallest ΔR (any 2 jets)			•	
	$\lvert\Delta\eta(\tau, \tau)\rvert$			•	•
τ prop.	$p_{\mathrm{T}}(\tau\tau)$			•	
	Sub-leading τ p_{T}				•
	Sub-leading τ η				•
H cand.	$p_{\mathrm{T}}(Hjj)$	•	•		
	$p_{\mathrm{T}}(H)/p_{\mathrm{T}}(jj)$		•		
$\vec{E}_{\mathrm{T}}^{\mathrm{miss}}$	Missing transverse energy $E_{\mathrm{T}}^{\mathrm{miss}}$		•	•	•
	Smallest $\Delta\phi$ $(\tau, \vec{E}_{\mathrm{T}}^{\mathrm{miss}})$				•

Table C.1: Overview of the variables used in the taggers discussed in Section 5.2. Variables that are used in a specific tagger are marked with a bullet •. Similarly to the calculation of the Higgs boson's transverse momentum in the event categorisation, the H candidate is defined as the vectorial sum of the two τ-leptons and $\vec{E}_{\mathrm{T}}^{\mathrm{miss}}$. The best W-candidate is defined as the pair of jets with an invariant mass closest to the invariant mass of the W-boson. Both jets are required not to be identified as b-quark initiated jets. The best t-quark-candidate is defined via the best W-candidate and an additional jet resulting in an invariant mass closest to the top quark's invariant mass. The additional jet is required to be identified as a b-quark initiated jet due to the decay signature of the top quark. Taken from Reference [8].

C.2 Residual Uncertainties in Z + Jets Control Regions

The Z + jets control regions used in the fit utilise the simplified embedding procedure introduced in Section 5.3.2. After the procedure the $Z \to \ell\ell$ events in the control regions resemble $Z \to \tau\tau$ events and are cross normalised with the signal regions. Thus, all systematic uncertainties applied to $Z \to \tau\tau$ in the signal regions, see Section 5.4, have to be applied to $Z \to \ell\ell$ in the control regions. In contrast to the signal regions, all variations in the Z + jets control regions solely affect the normalisations since the control regions themselves have no shape information in the fit[1].

Event wide kinematic variations are simply propagated through the method for all simulated samples. Variations arising from weights are propagated through the simplified embedding procedure as well. However, this has to be done for both, data and simulations, in the control regions. Since it is not possible to implement systematic variations on data, the residual differences between the data and MC variations are finally applied to the simulations. In a perfect scenario the variations on the embedded data and MC would be exactly the same and, thus, cancel each other out. For some uncertainties this cancellation shows almost perfect closure as shown for one component of the uncertainty related to the di-τ trigger in Figure C.1.

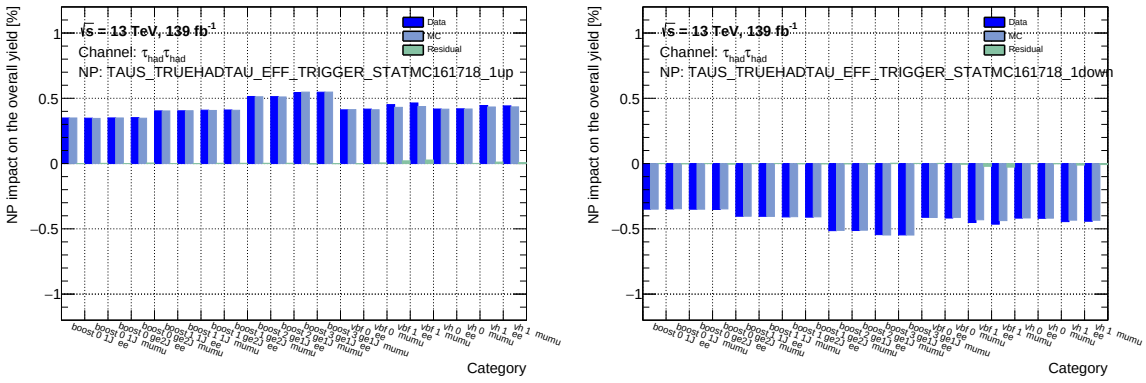

(a) Up variation.

(b) Down variation.

Figure C.1: Residual variations of one systematic uncertainty related to the di-τ trigger. The variations per control region for the $\tau_{\text{had}}\tau_{\text{had}}$ channel are shown.

However, it is possible that the cancellation does not result in a vanishing final variation. Two effects are mainly responsible for this. The first effect is given by the statistical uncertainties on the data and simulations in the control regions. Since the uncertainties are typically binned in e.g. p_{T} of an object this can lead to different variations being applied to data and MC. This effect is shown in Figure C.2 for one uncertainty component of the τ-lepton energy scale. It shows that in regions with small statistics, e.g. vbf_1 and vh_1, the final variation does not vanish. Ultimately, these variations driven by statistical variations are not propagated to the fit as they lack physical motivation. The shown uncertainty is applied to τ_{had} decays and, thus, should have a larger impact on events with more hadronic τ-leptons which is exactly what can be observed.

The other effect is a result of the simplified embedding procedure itself. If the events before the

[1] They have no shape information as they are only one-bin regions.

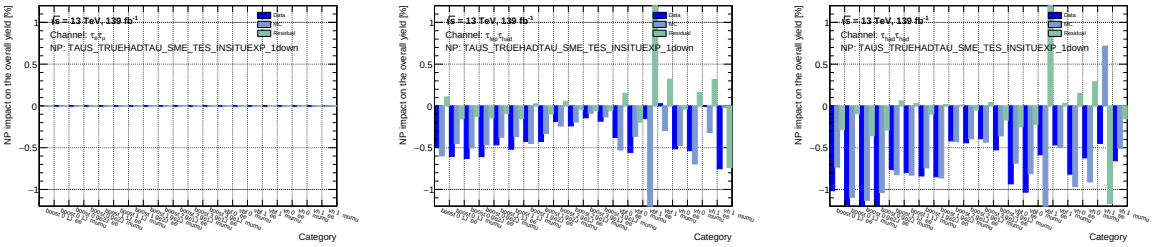

(a) $\tau_e\tau_\mu$ channel. (b) $\tau_{\text{lep}}\tau_{\text{had}}$ channel. (c) $\tau_{\text{had}}\tau_{\text{had}}$ channel.

Figure C.2: Residual variations of one systematic uncertainty related to the τ_{had} energy scale. The down variations per control region for all di-τ channels are shown.

embedding and after the embedding contain the same objects, e.g. $Z \to ee$ becoming $Z \to \tau\tau \to \mu e$, the same sources of uncertainties have to be applied twice on simulations but only once for data. This effect is shown in Figure C.3 for an uncertainty related to the electron identification. With an increasing number of electrons in the final di-τ channel the magnitude of the MC variation increases. The effect is not as pronounced for the data variations since the first effect becomes important in certain regions as well. The uncertainty shown in Figure C.3 is also the only one showing non-negligible variations that are not solely caused by statistical fluctuations and, thus, the only one propagated to the fit. In the final fit model a more detailed uncertainty scheme for the electron identification uncertainty was implemented.

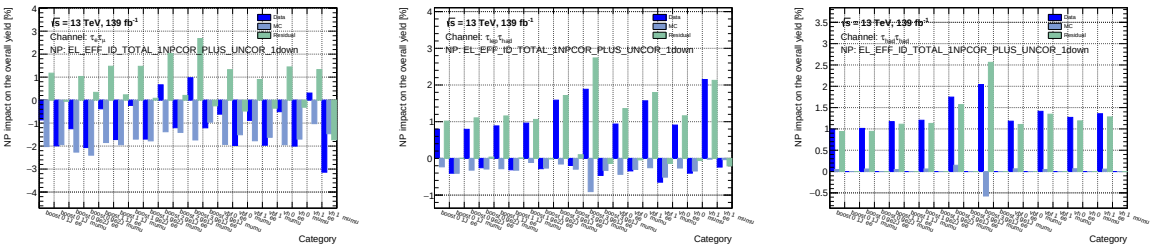

(a) $\tau_e\tau_\mu$ channel. (b) $\tau_{\text{lep}}\tau_{\text{had}}$ channel. (c) $\tau_{\text{had}}\tau_{\text{had}}$ channel.

Figure C.3: Residual variations of one systematic uncertainty related to the electron identification. The down variations per control region for all di-τ channels are shown.

APPENDIX D

Additional Studies Related to the Fit Model

D.1 Binning Algorithm Studies

This appendix intends to document additional studies on the binning algorithm introduced in Section 6.2.2. These generally show the stability of the algorithm in Appendix D.1.2 and the impact of a general drawback of binned distributions in Appendix D.1.1.

D.1.1 Impact of Empty Bins

As explained in Section 6.2.2, the binned distributions in the likelihood fit should resolve physical features as long as the available statistics permits. Since the signal regions contain multiple processes with different relative contributions the question of available statistics becomes non-trivial. For backgrounds contributing the major amount of events, such as $Z \rightarrow \tau\tau$ events, the statistics may be sufficient for a certain binning but could result in empty bins for other minor backgrounds. If a bin remains empty for certain processes, it is not possible to estimate the uncertainty of these processes in this bin. Thus, the final uncertainty of this bin could be underestimated in the final likelihood.

This effect was studied for a preliminary binning obtained by a preliminary version of the binning algorithm. First, an estimate of the uncertainty that is missing in the likelihood due to empty bins has to be constructed. By considering the statistical uncertainty of neighbouring bins of the same process a rough estimate is obtained. Three individual scenarios have to be distinguished based on the number of non-empty neighbouring bins:

0 non-empty bins Divide total integral of all bins by the number of bins and assume a 100% statistical and an additional 100% systematic uncertainty.

1 non-empty bin Assign the statistical uncertainty of the neighbouring bin as an estimate.

2 non-empty bins Assign the average of the statistical uncertainties of both neighbouring bins as an estimate.

The resulting changes to the total uncertainty per $m_{\tau\tau}^{\text{MMC}}$ bin is shown in Figure D.1 for the $\tau_e\tau_\mu$ vbf_1 signal regions where the largest impact was observed. In the majority of the other regions and bins the relative changes of the total uncertainties were observed to be well below 1%.

chan ll cat vbf 1 sr

	0.0 - 65.0	65.0 - 75.0	75.0 - 80.0	80.0 - 85.0	85.0 - 90.0	90.0 - 95.0	95.0 - 100.0	100.0 - 105.0	105.0 - 110.0	110.0 - 115.0	115.0 - 120.0	120.0 - 125.0	125.0 - 130.0	130.0 - 135.0	135.0 - 150.0	150.0 - 195.0	195.0 - 200.0	Integral
tot. err.	1.88	4.18	2.35	2.40	2.79	2.85	3.15	3.82	3.52	2.66	2.14	2.05	1.89	1.42	2.86	2.94	0.90	
change/%	15.05	0.00	0.00	1.69	0.00	0.01	0.00	0.01	0.00	0.23	0.33	0.40	0.43	0.91	0.92	0.02	9.65	
ttH_tt																		
ttH_other	0.00	0.00	0.00	0.00	0.00	0.00	0.00	0.00	0.00	0.00	0.00	0.00	0.00	0.00	0.00		0.00	0.00
ttH_WW																		
ggHWW																		0.48
ggH																	0.03	1.09
ZttQCD																		36.58
ZttEWK												0.06		0.06			0.11	8.20
ZllQCD	1.07			0.44	0.03				0.01	0.17	0.17	0.17	0.17	0.17	0.39		0.39	2.09
ZllEWK	0.01	0.01	0.01	0.02		0.04		0.05		0.05	0.01	0.01	0.01	0.05		0.05	0.01	0.17
ZH																		
WH																		
VV																		2.46
VBFHWW																		6.72
VBFH																		16.55
Top																		8.14
Fake																		5.90

Mass / GeV

Figure D.1: Overview of all processes in all $m_{\tau\tau}^{\text{MMC}}$ bins in the $\tau_e\tau_\mu$ vbf_1 signal region. Bins with an entry correspond to templates with zero yield. The entry shows an estimate of the neglected uncertainty for the empty bin. No entry for the total integral corresponds to a negligible total yield. The relative change of the total uncertainty per bin is shown when including the uncertainty estimate of empty bins.

To quantify the impact of the missing uncertainty component on the measurement's result Asimov fits were conducted including only the $\tau_e\tau_\mu$ regions in the VBFH phase space. Since the uncertainty change is most significant in the first bin as shown in Figure D.1 and most events over the whole mass range are either signal events or $Z \to \tau\tau$ events[1] the uncertainty change was propagated to the $Z \to \tau\tau$ events. This is motivated by the signal events being located at larger $m_{\tau\tau}^{\text{MMC}}$ values. First, a reference value of the sensitivity for this specific fit model has to be found. Thus, an Asimov fit similar to the actual fit model but only including the regions described before is performed, resulting in an uncertainty on the VBFH POI of $^{+0.834806}_{-0.809118}$. Following the argumentation of applying the missing uncertainty on the $Z \to \tau\tau$ events, its normalisation factor was replaced by a nuisance parameter whose prior was taken from the fit result of this first fit setup. This modified fit configuration results in a VBFH POI uncertainty of $^{+0.833177}_{-0.807817}$. Finally, the effect of the missing uncertainty due to empty bins is propagated to the fit by inflating the prior of the $Z \to \tau\tau$ normalisation NP by 15%. The final fit setup yields a VBFH POI uncertainty of $^{+0.833409}_{-0.807998}$, showing only a deviation of 0.03% with respect to the fit without the inflated prior. It has to be noted that the overall effect of the missing uncertainty is overestimated in this test by inflating the prior over the whole $m_{\tau\tau}^{\text{MMC}}$ range and not just the first bin.

Hence, the overall impact of this effect on the measurement is found to be negligible.

[1] As can be deducted from the total integrals.

D.1.2 Binning Algorithm Parameters

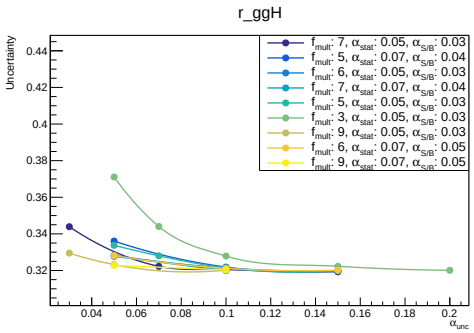

(a) POI targeting the inclusive ggH production.

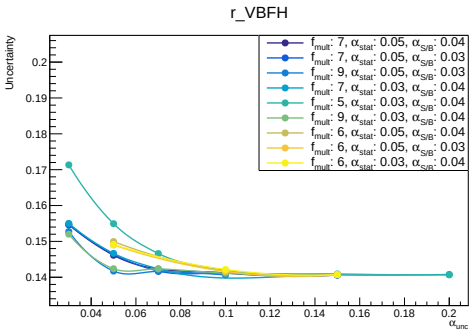

(b) POI targeting the inclusive VBFH production.

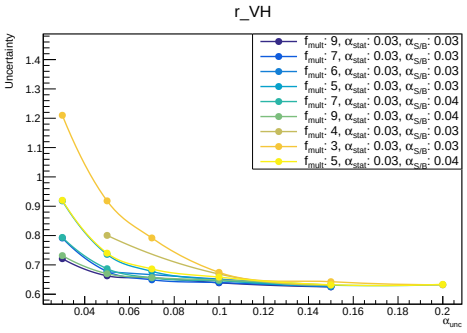

(c) POI targeting the inclusive VH production.

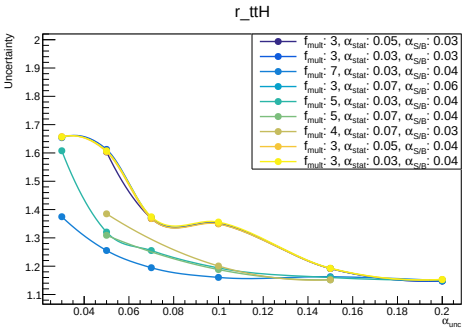

(d) POI targeting the inclusive $t\bar{t}H$ production.

Figure D.2: Uncertainty on all POIs of the measurement as a function of the binning algorithm's α_{unc}. Smaller uncertainties correspond to a higher sensitivity of the measurement. The best nine parameter combinations for the respective POI are shown.

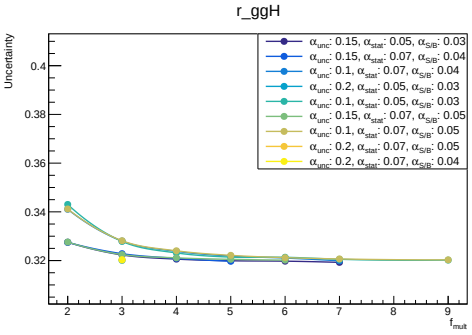

(a) POI targeting the inclusive ggH production.

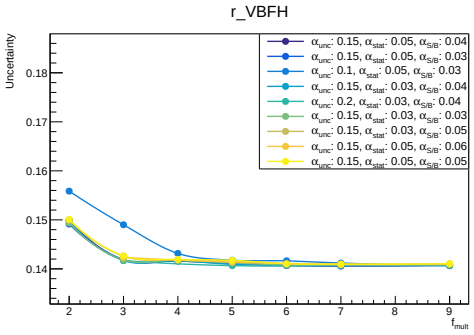

(b) POI targeting the inclusive VBFH production.

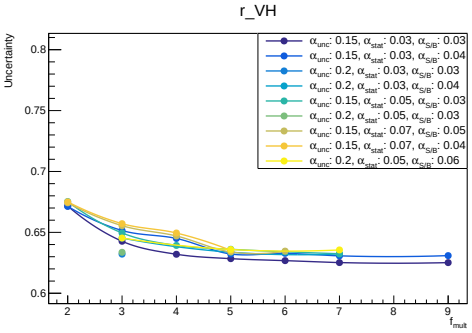

(c) POI targeting the inclusive VH production.

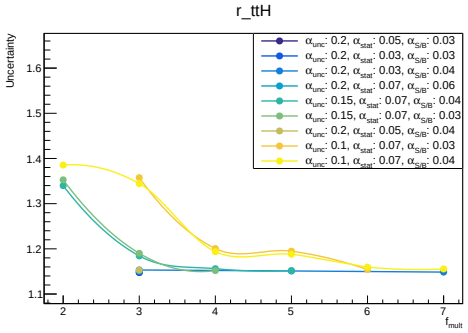

(d) POI targeting the inclusive $t\bar{t}H$ production.

Figure D.3: Uncertainty on all POIs of the measurement as a function of the binning algorithm's f_{mult}. Smaller uncertainties correspond to a higher sensitivity of the measurement. The best nine parameter combinations for the respective POI are shown.

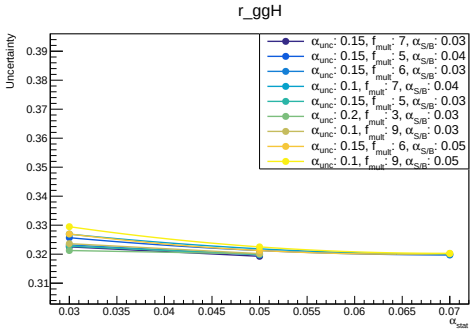

(a) POI targeting the inclusive ggH production.

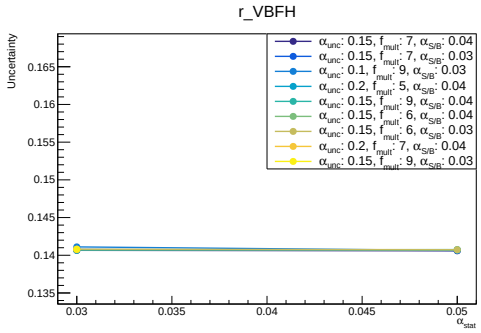

(b) POI targeting the inclusive VBFH production.

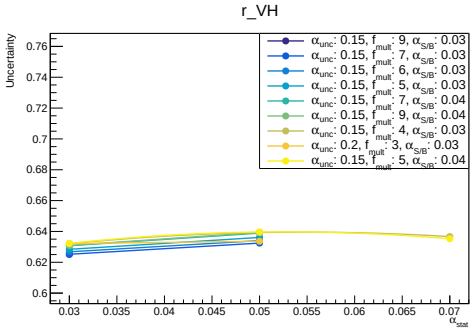

(c) POI targeting the inclusive VH production.

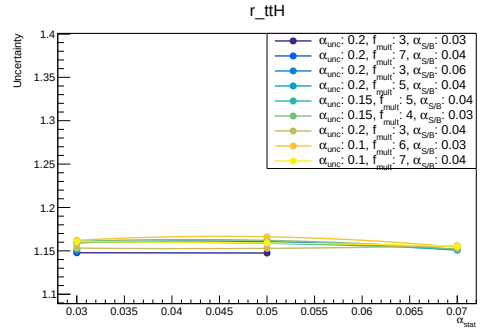

(d) POI targeting the inclusive $t\bar{t}H$ production.

Figure D.4: Uncertainty on all POIs of the measurement as a function of the binning algorithm's α_{stat}. Smaller uncertainties correspond to a higher sensitivity of the measurement. The best nine parameter combinations for the respective POI are shown.

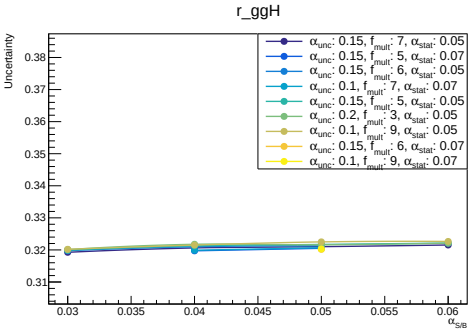

(a) POI targeting the inclusive ggH production.

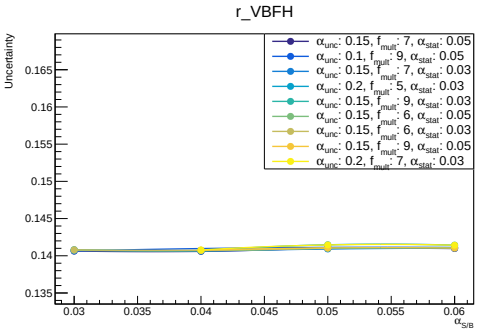

(b) POI targeting the inclusive VBFH production.

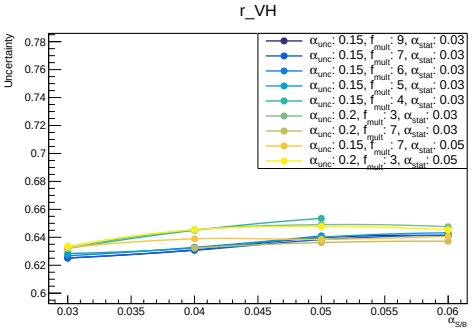

(c) POI targeting the inclusive VH production.

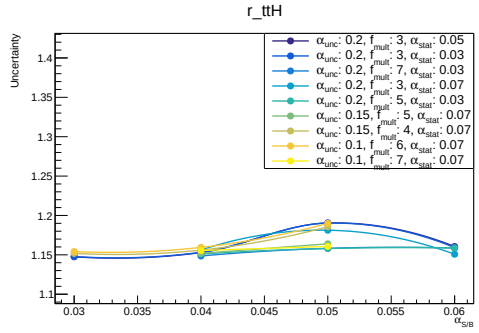

(d) POI targeting the inclusive $t\bar{t}H$ production.

Figure D.5: Uncertainty on all POIs of the measurement as a function of the binning algorithm's $\alpha_{S/B}$. Smaller uncertainties correspond to a higher sensitivity of the measurement. The best nine parameter combinations for the respective POI are shown.

D.2 Asimov Fit Studies

The intention of this appendix is to document studies conducted using Asimov pseudodata related to Section 6.3. Asimov fit results using the final fit model are documented in Appendix D.2.2.

D.2.1 $Z \to \tau\tau$ Normalisation Factor Model

Since the fit model introduced in Figure 6.1 includes pairings of 32 signal regions and, finally, 31 $Z \to \tau\tau$ normalisation factors alternative setups with a reduced number of NFs were studied. This is motivated by NFs being allowed to float freely in the likelihood minimisation. Reducing the number of freely floating parameters, or alternatively imposing constraints by replacing NFs with NPs, could possibly increase the sensitivity of the measurement. Thus, three alternative NF models were studied where the $Z \to \tau\tau$ NF in the $t\bar{t}H$ phase space is not altered as it is not paired with a dedicated Z + jets control regions. Effectively, the alternative models correlate different regions of phase space, thus reducing the overall number of NFs. It has to be noted, though, that a final model based on one of these alternatives would have to introduce new NPs accounting for migration uncertainties between the correlated regions as it was done in Reference [7].

The alternative $Z \to \tau\tau$ NF schemes are the following (always including the additional $t\bar{t}H$ $Z \to \tau\tau$ NF in the fit model but not counting it in the naming schemes):

3 NFs One inclusive NF per boosted, VBFH and VH phase space.

9 NFs One inclusive NF per boosted, VBFH and VH phase space and per di-τ decay channel.

10 NFs One NF per signal region phase space but inclusive in the di-τ decay channel.

By correlating individual phase space regions the available statistics to determine the $Z \to \tau\tau$ NF value increases and, thus, the uncertainty on the combined NFs decreases, as shown in Figure D.6. Normalisation factors for the Top processes remain unchanged when correlating $Z \to \tau\tau$ NF indicating a small correlation between them. The effect of the different setups on the parameters of interest and NPs related to the Z + jets normalisation are shown in Figure D.7 and D.8. While the NPs related to τ_{had} are effectively unchanged the Z + jets theory NPs tend to get more constrained. This is likely caused by the aforementioned missing NPs accounting for migrations between different correlated regions. The sensitivity of the measurement, i.e. the uncertainty on the POIs, is stable with respect to the alternative NF models. Most variations are at the level of numerical precision while the sensitivity of one ggH POI (ggF, ≥ 1 jet, 60 GeV $< p_{\text{T}}$(H) $<$ 120 GeV) slightly increases when correlating all boosted signal regions. However, including the additional migration uncertainties possibly mitigates this slight improvement. Thus, the NF scheme with 31 $Z \to \tau\tau$ NF introduced in Figure 6.1 is used in the final fit model.

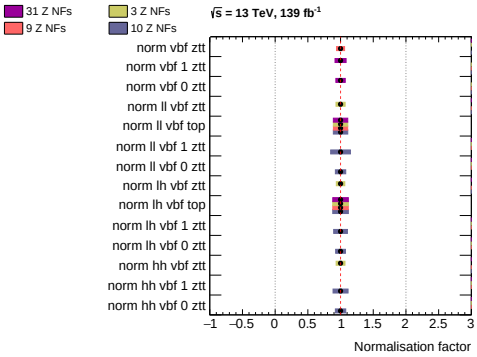

(a) NFs in the VBFH-like phase space.

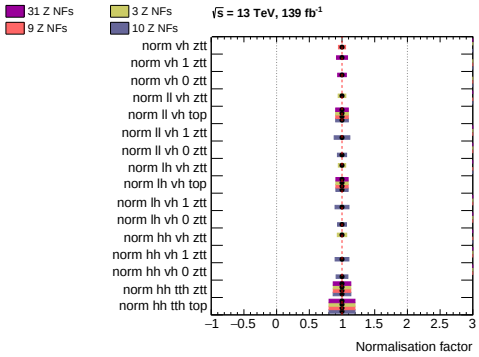

(b) NFs in the VH-like and $t\bar{t}H$-like phase space.

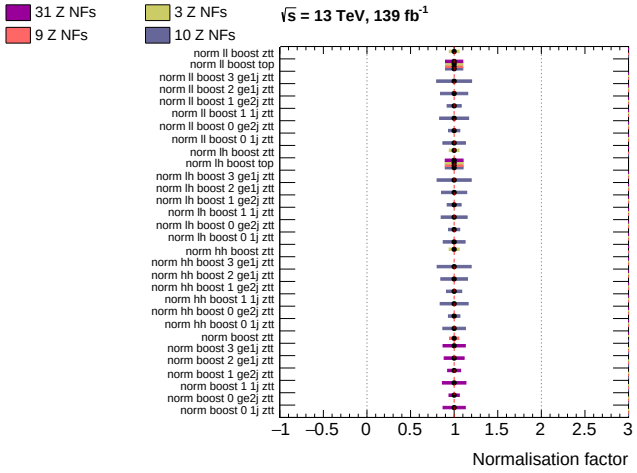

(c) NFs in the ggH-like phase space.

Figure D.6: Normalisation factors in a fit with Asimov pseudodata for different $Z \to \tau\tau$ normalisation factor models.

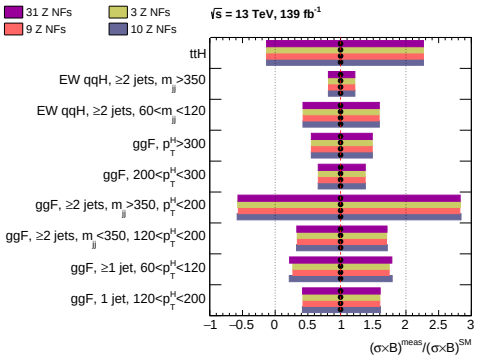

(a) Parameters of interest.

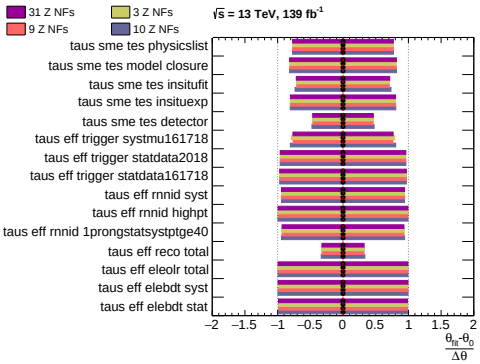

(b) Nuisance parameters related to τ_{had}.

Figure D.7: Pulls and constraints of the POIs and τ_{had} related NPs in a fit with Asimov pseudodata for different $Z \to \tau\tau$ normalisation factor models. The units (GeV) in the naming of the POIs have been omitted.

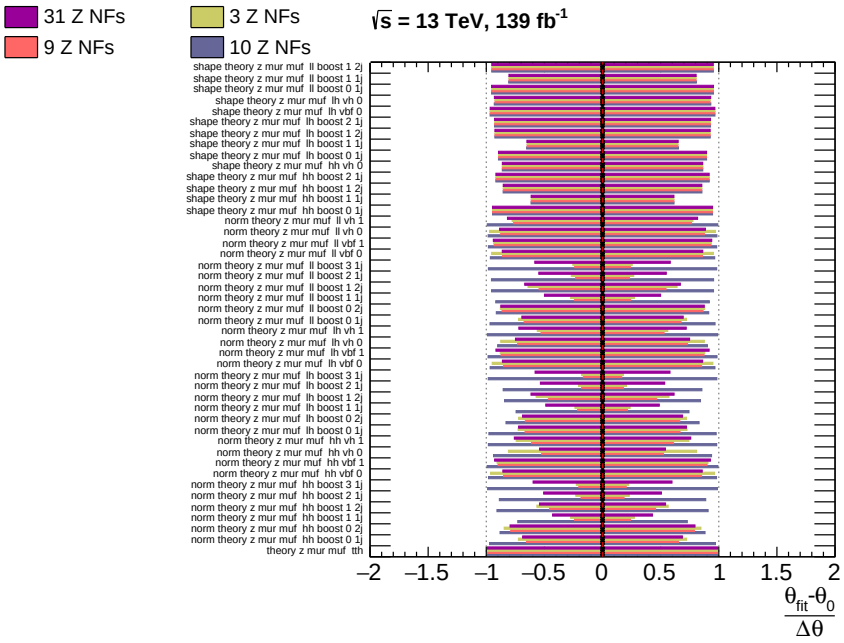

(a) Nuisance parameters related to Z + jets $\mu_R\mu_F$.

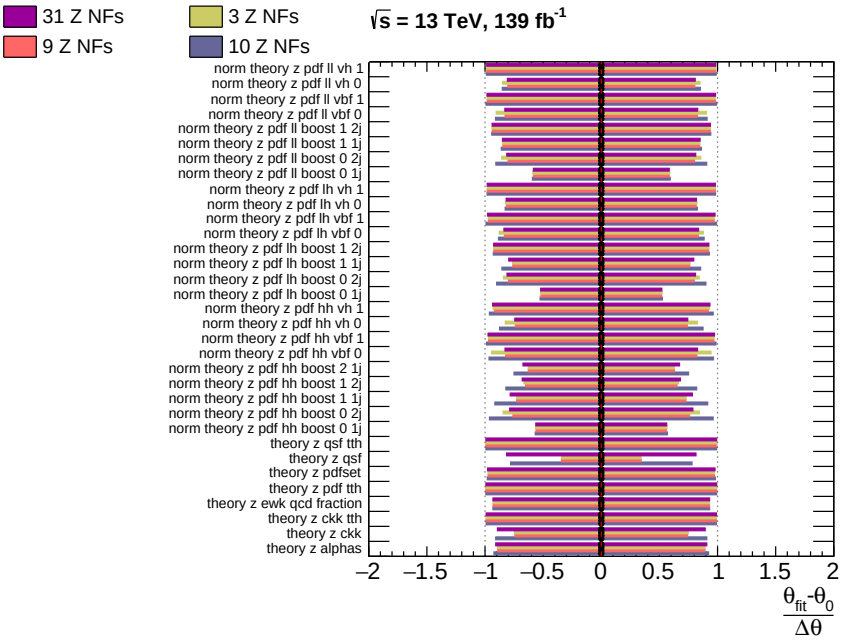

(b) Nuisance parameters related to Z + jets PDF.

Figure D.8: Pulls and constraints of Z + jets theory related NPs in a fit with Asimov pseudodata for different $Z \to \tau\tau$ normalisation factor models.

D.2.2 Pulls & Constraints of the Final Model Using Asimov Pseudodata

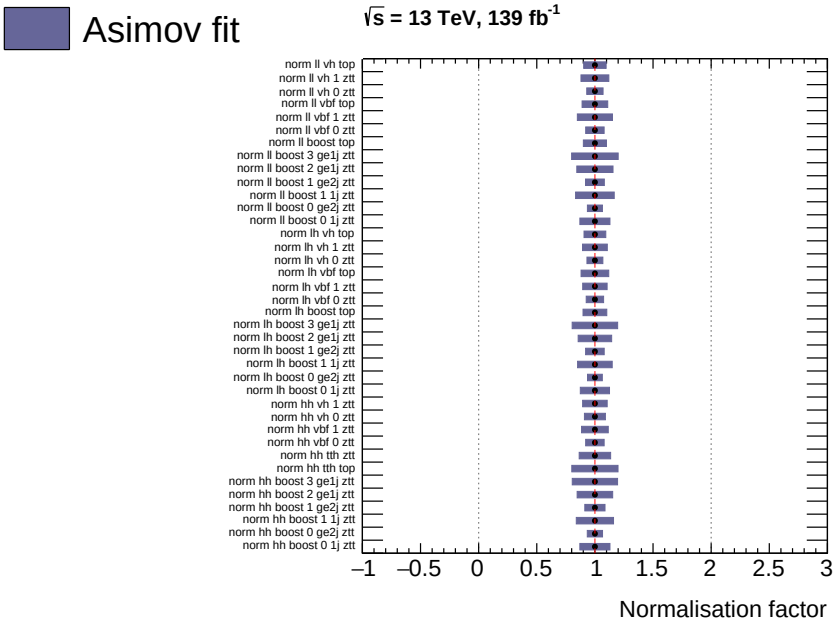

(a) Normalisation factors.

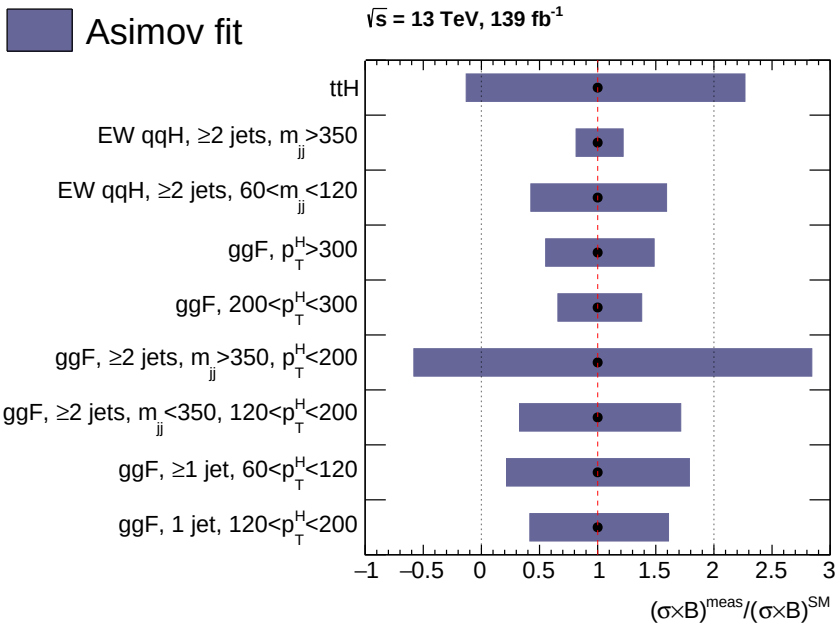

(b) Parameters of interest.

Figure D.9: Pulls and constraints of the NFs and POIs in a fit with Asimov pseudodata. The units (GeV) in the naming of the POIs have been omitted.

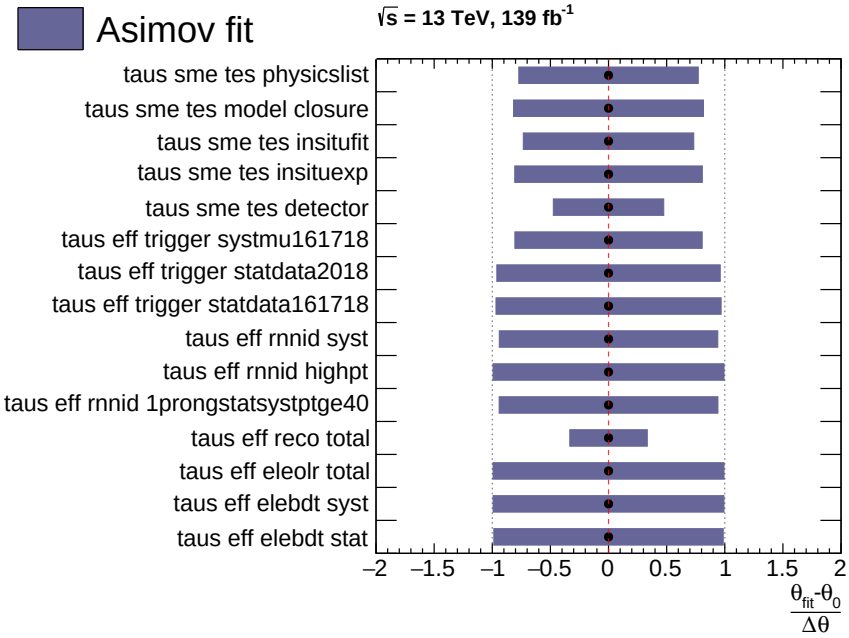

(a) Nuisance parameters related to τ_{had}.

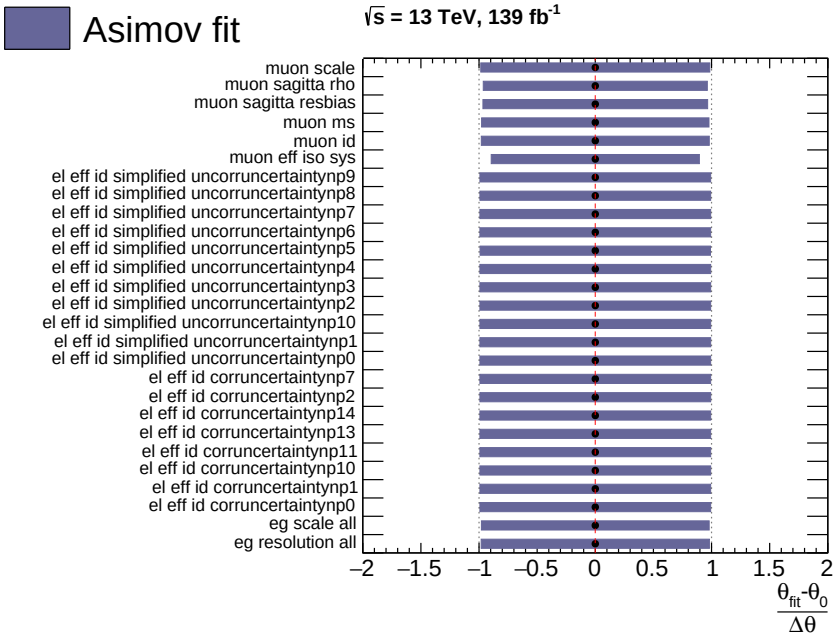

(b) Nuisance parameters related to electrons and muons.

Figure D.10: Pulls and constraints of the τ_{had} and electron/muon related NPs in a fit with Asimov pseudodata.

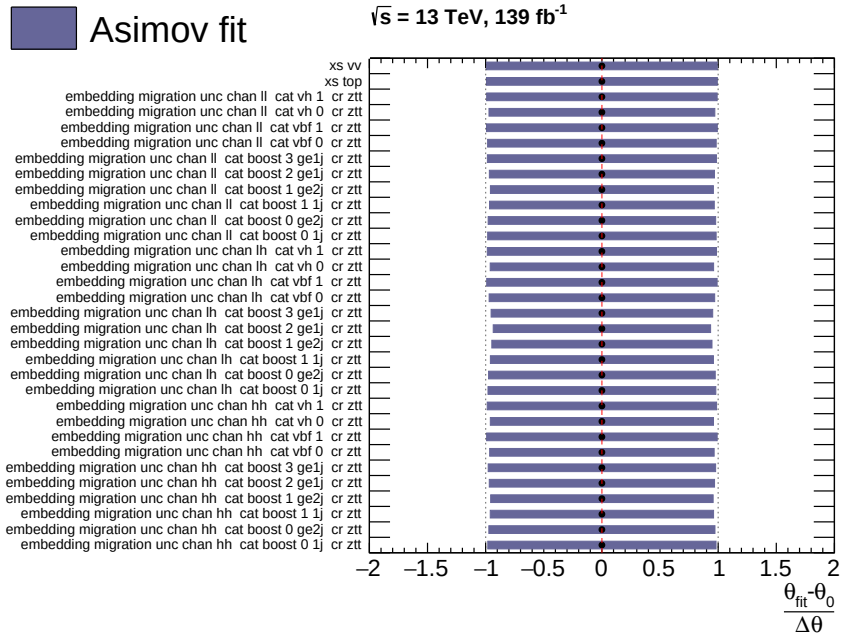

(a) Nuisance parameters related to the simplified embedding.

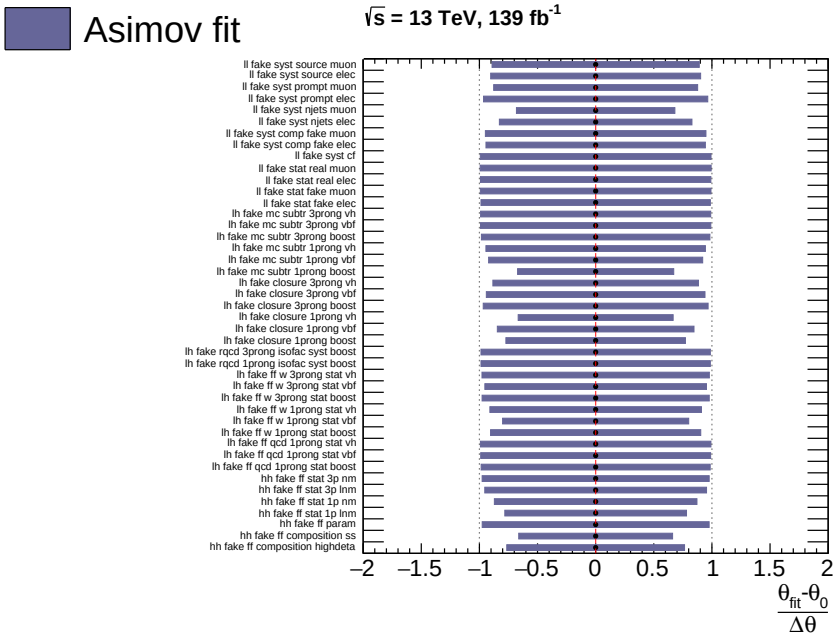

(b) Nuisance parameters related to misidentified τ-lepton estimation.

Figure D.11: Pulls and constraints of the simplified embedding and misidentified τ-lepton estimation related NPs in a fit with Asimov pseudodata.

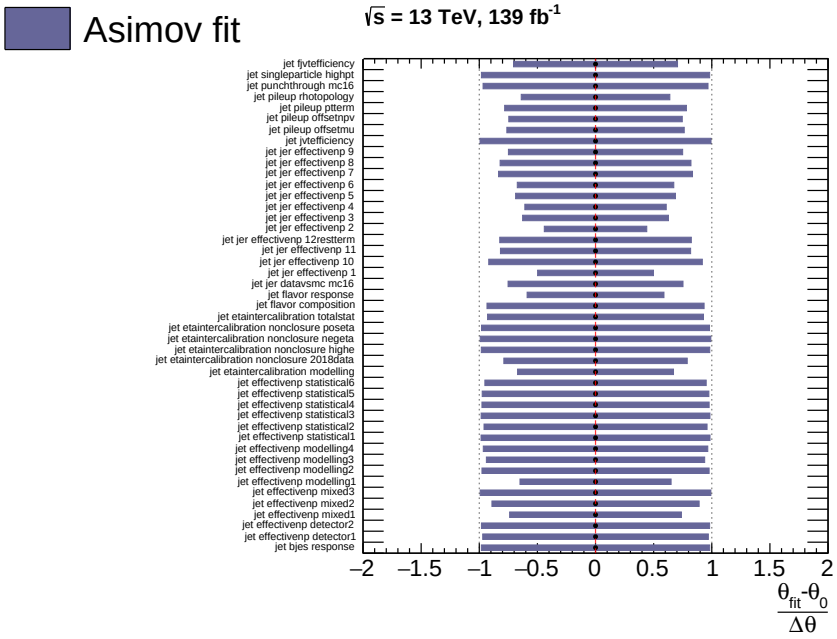

(a) Nuisance parameters related to jets.

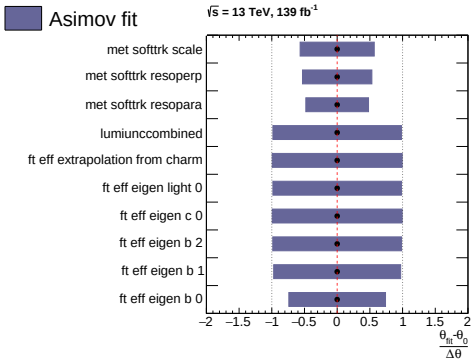

(b) Nuisance parameters related to flavour tagging and $E_{\mathrm{T}}^{\mathrm{miss}}$.

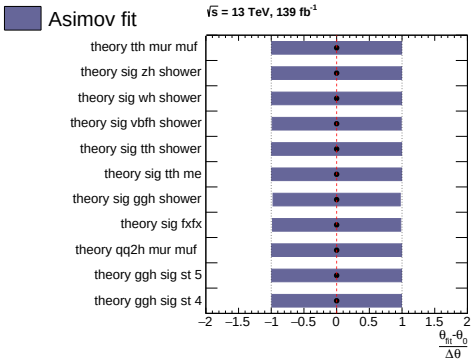

(c) Nuisance parameters related to signal theory.

Figure D.12: Pulls and constraints of the jet, flavour tagging, $E_{\mathrm{T}}^{\mathrm{miss}}$ and signal theory related NPs in a fit with Asimov pseudodata.

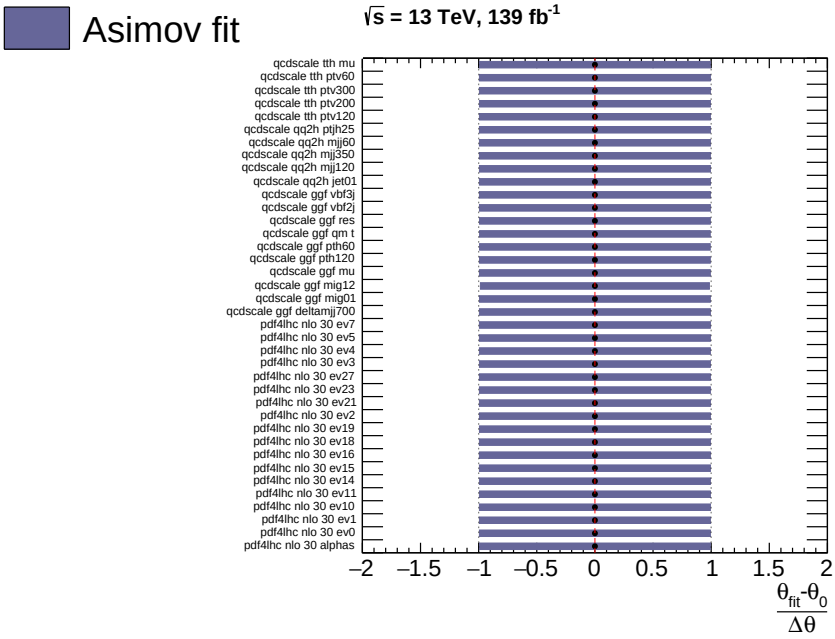

(a) Nuisance parameters related to signal theory QCD and PDF.

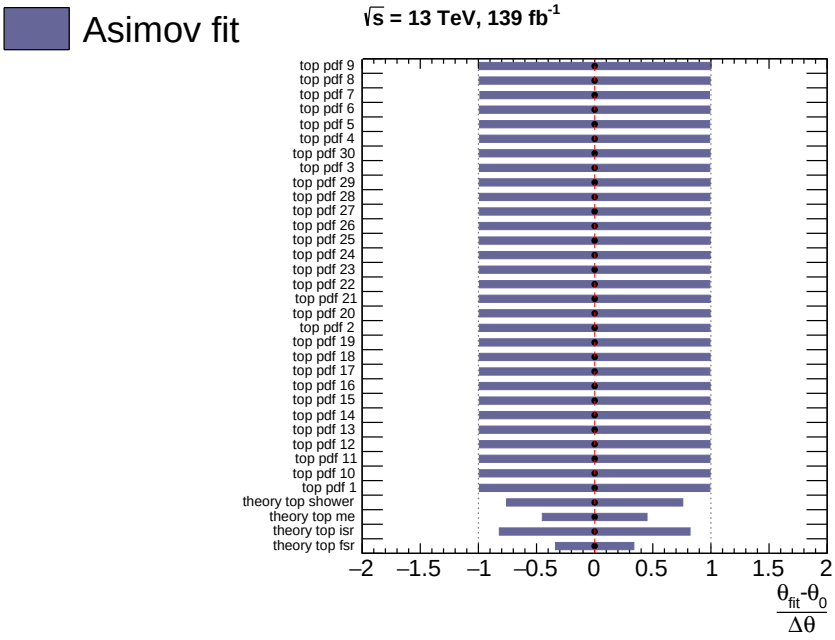

(b) Nuisance parameters related to Top theory.

Figure D.13: Pulls and constraints of the signal theory QCD and PDF as well as Top theory related NPs in a fit with Asimov pseudodata.

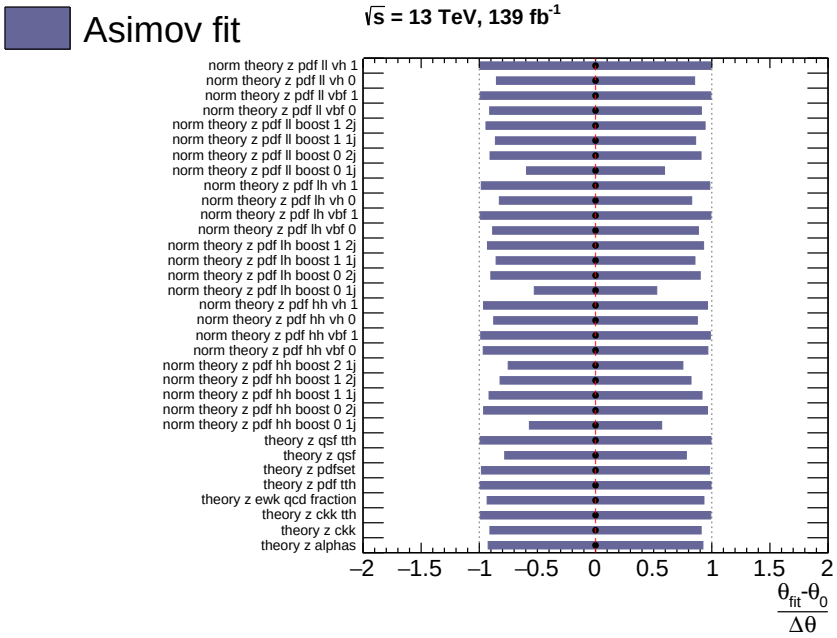

(a) Nuisance parameters related to Z + jets PDF and other theory uncertainties.

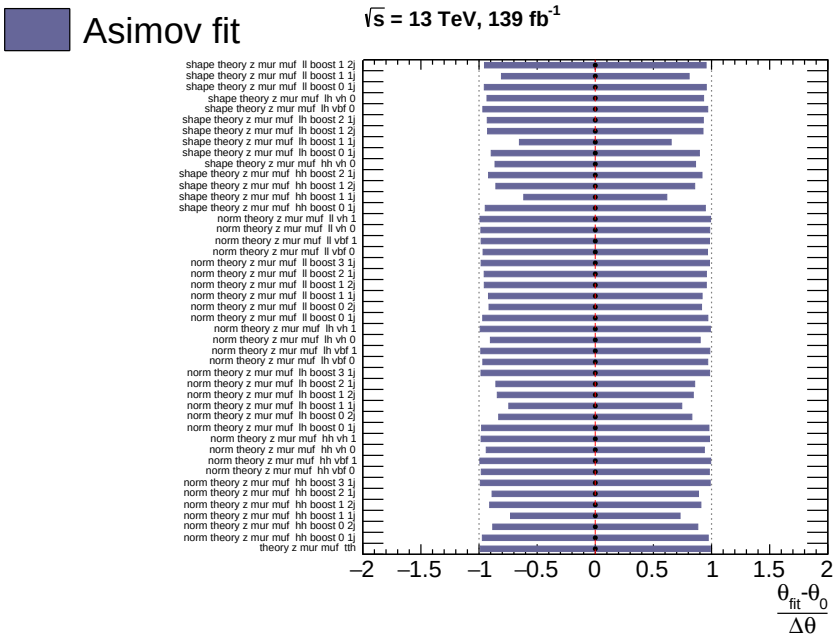

(b) Nuisance parameters related to Z + jets $\mu_R\mu_F$.

Figure D.14: Pulls and constraints of the Z + jets theory uncertainty related NPs in a fit with Asimov pseudodata.

D.3 Partially Unblinded Fit Studies

D.3.1 Pulls & Constraints of the Final Model in the Partially Unblinded Fits

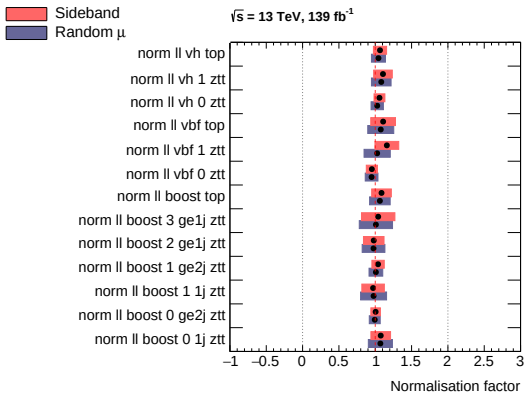

(a) NFs in the $\tau_e\tau_\mu$ channel.

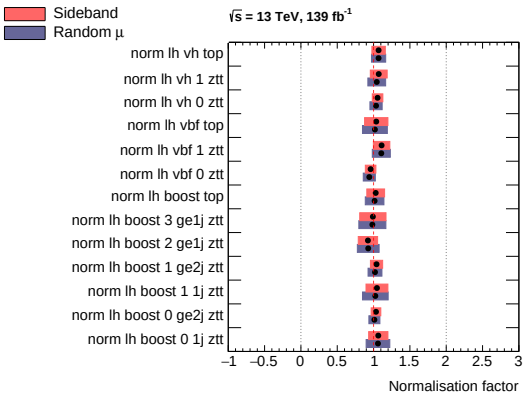

(b) NFs in the $\tau_{\text{lep}}\tau_{\text{had}}$ channel.

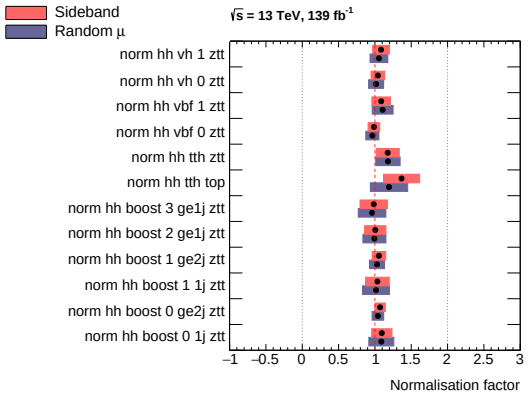

(c) NFs in the $\tau_{\text{had}}\tau_{\text{had}}$ channel.

Figure D.15: Pulls and constraints of the normalisation factors in the sideband fit (light red) and random signal strength fit (dark blue).

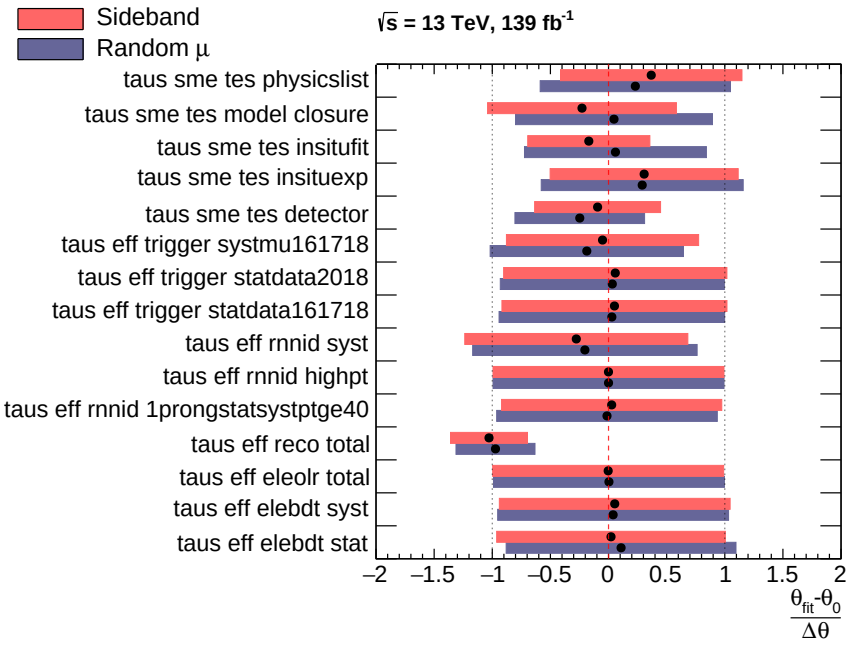

(a) Nuisance parameters related to τ_{had}.

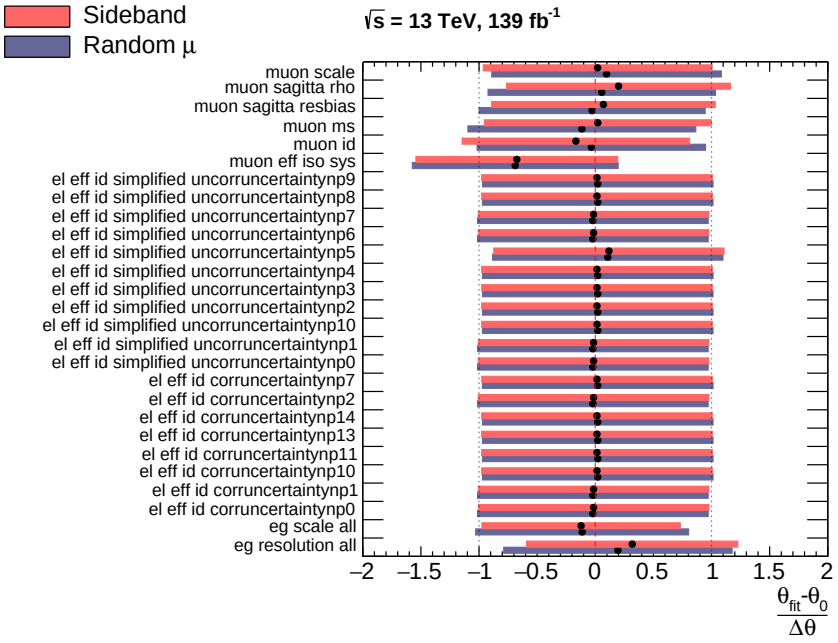

(b) Nuisance parameters related to electrons and muons.

Figure D.16: Pulls and constraints of the τ_{had} and electron/muon related NPs in the sideband fit (light red) and random signal strength fit (dark blue).

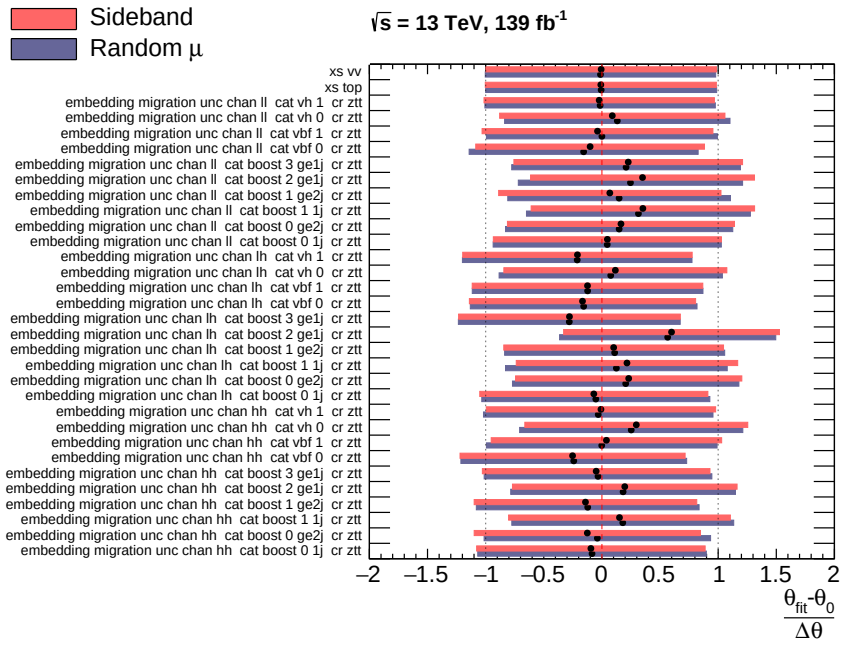

(a) Nuisance parameters related to the simplified embedding.

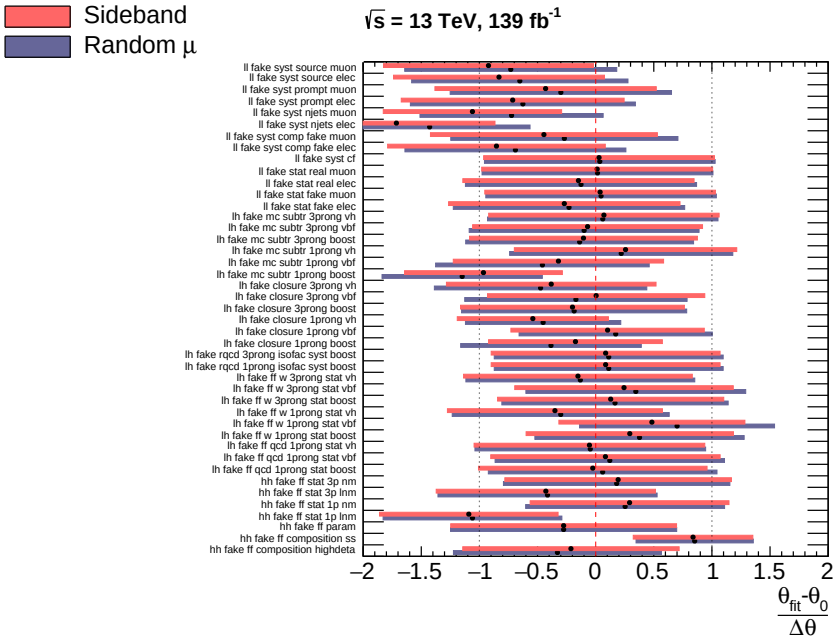

(b) Nuisance parameters related to misidentified τ-lepton estimation.

Figure D.17: Pulls and constraints of the simplified embedding and misidentified τ-lepton estimation related NPs in the sideband fit (light red) and random signal strength fit (dark blue).

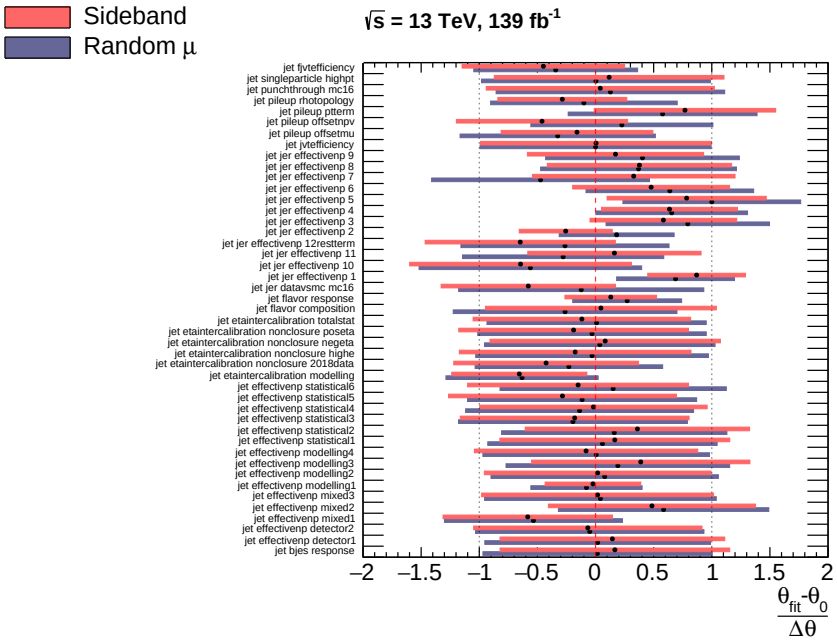

(a) Nuisance parameters related to jets.

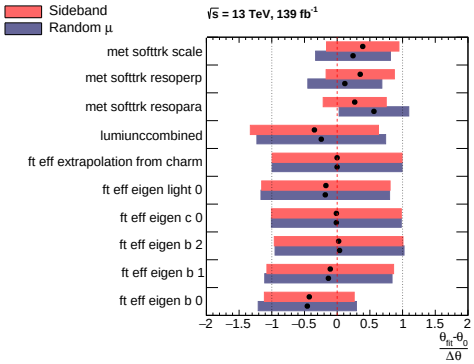

(b) Nuisance parameters related to flavour tagging and $E_{\mathrm{T}}^{\mathrm{miss}}$.

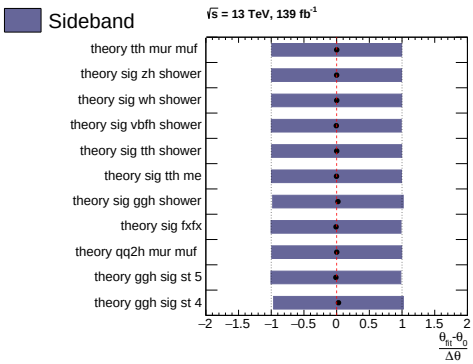

(c) Nuisance parameters related to signal theory.

Figure D.18: Pulls and constraints of the jet, flavour tagging, $E_{\mathrm{T}}^{\mathrm{miss}}$ and signal theory related NPs in the sideband fit (light red) and random signal strength fit (dark blue).

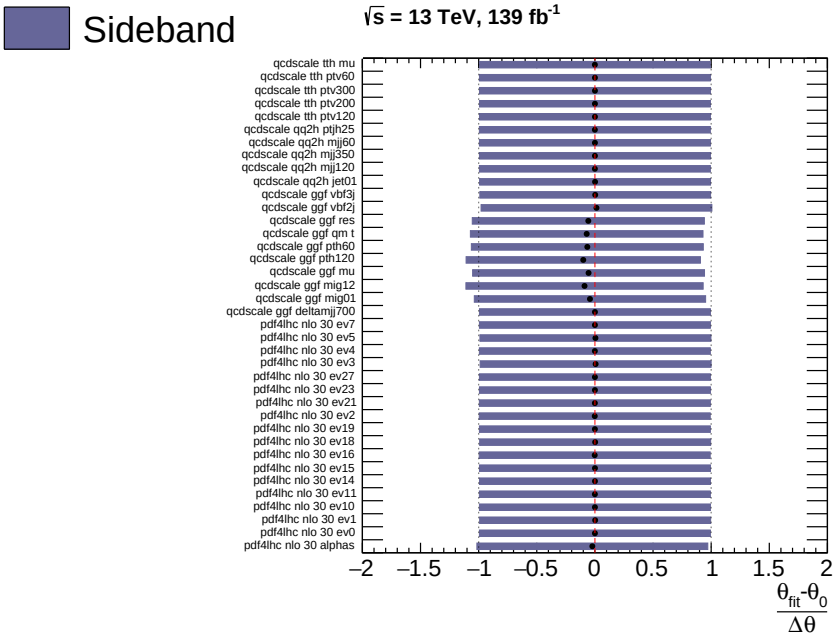

(a) Nuisance parameters related to signal theory QCD and PDF.

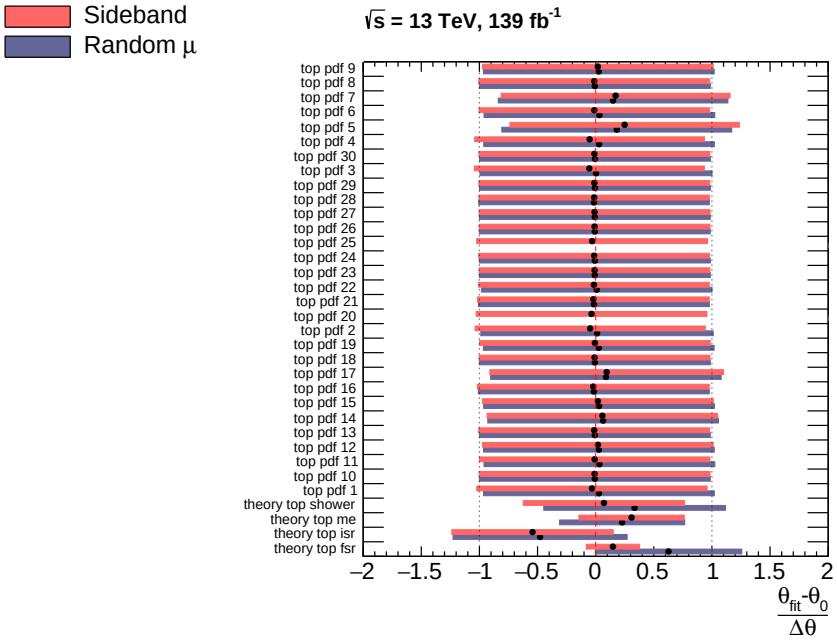

(b) Nuisance parameters related to Top theory.

Figure D.19: Pulls and constraints of the signal theory QCD and PDF as well as Top theory related NPs in the sideband fit (light red) and random signal strength fit (dark blue).

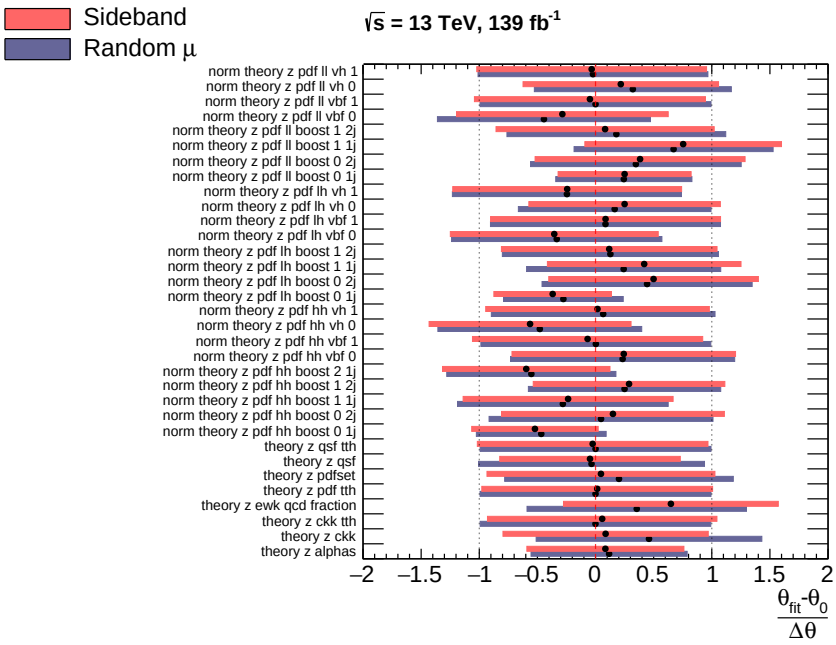

(a) Nuisance parameters related to Z + jets PDF and other theory uncertainties.

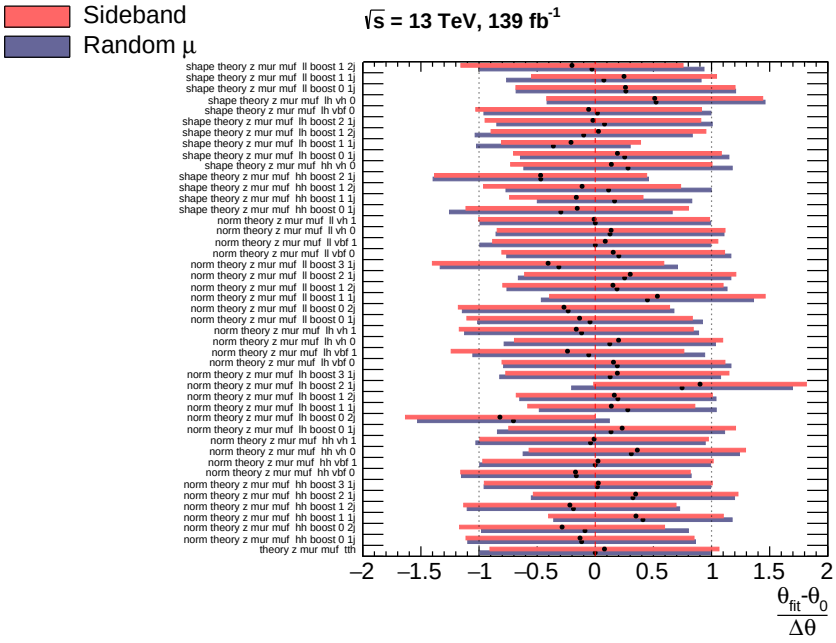

(b) Nuisance parameters related to Z + jets $\mu_R\mu_F$.

Figure D.20: Pulls and constraints of the Z + jets theory uncertainty related NPs in the sideband fit (light red) and random signal strength fit (dark blue).

D.3.2 τ_{had} Reconstruction Efficiency Studies

In addition to the studies regarding the τ_{had} reconstruction efficiency uncertainty presented in Section 6.3.1 this appendix summarises additional information on the observed effect. Since the track reconstruction in ATLAS is very well understood the pull of this NP is more likely to be caused by a mismodelling of the track classification in the τ_{had} reconstruction. By splitting the NP into components only affecting hadronically decaying τ-leptons with one charged track and decays with three charged tracks it can be studied whether this affects τ-leptons with more tracks more heavily. As shown in Figure D.21, the effect is of a similar magnitude in both cases. The constraints of the split NP reflect that the regions in the fit contain more τ_{had} decays with one track compared to τ_{had} decays with three tracks.

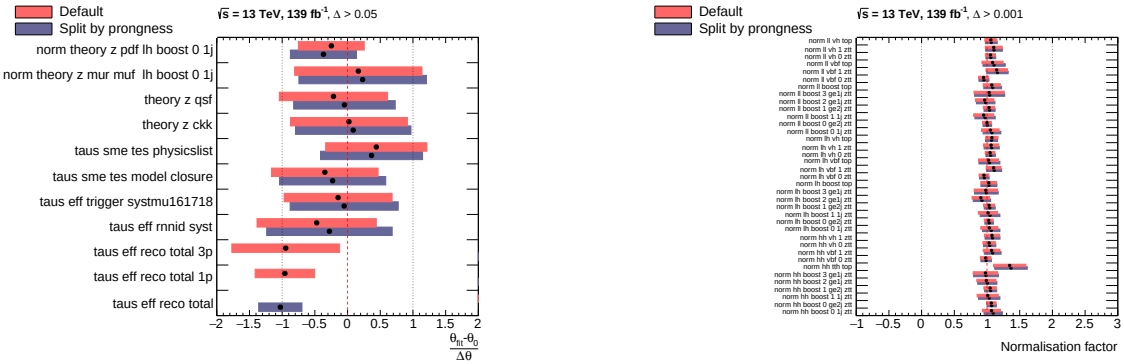

(a) Nuisance parameters.

(b) Normalisation factors.

Figure D.21: Pulls and constraints of the nuisance parameters and normalisation factors in the random signal strength fit with a difference greater than 0.05 and 0.001, respectively. The default fit model (light red) is compared to a fit model with the τ_{had} reconstruction efficiency NP split by the number of charged tracks in hadronic τ-lepton decays (dark blue), i.e. one track or three tracks.

Studying the pull separately for $\tau_{\text{lep}}\tau_{\text{had}}$ decays and $\tau_{\text{had}}\tau_{\text{had}}$ decays indicates whether the effect scales with the number of hadronically decaying τ-leptons in the di-τ channel as expected. The pull is of similar size for both decay channels as shown in Figure D.22. This resembles the expected behaviour due to the implementation of uncertainties in HistFactory. Additionally to the "nominal" template, up and down variations are provided defining the $\pm1\sigma$ variations of the uncertainty. These variation templates already incorporate the scaling by the number of τ_{had}, i.e. the $\tau_{\text{had}}\tau_{\text{had}}$ variations roughly increase quadratically compared to the original size of the $\tau_{\text{lep}}\tau_{\text{had}}$ variations.

As HistFactory only requires $\pm1\sigma$ variation templates and the likelihood evaluation is continuous, it implements different interpolation and extrapolation functions. Typically, the interpolation function is a polynomial of 6^{th} order and the extrapolation function is an exponential. For small uncertainties at the order of percent these functions effectively show linear behaviour. Their advantage lies in the smooth transition between interpolation and extrapolation, also with respect to their derivatives, see Reference [154]. Since the τ_{had} reconstruction efficiency scales with the number of τ_{had} as previously discussed, an alternative set of functions was studied for the $\tau_{\text{had}}\tau_{\text{had}}$ channel. This set of functions interpolates using a parabola and extrapolates with a linear function, motivated by the quadratic scaling in the $\tau_{\text{had}}\tau_{\text{had}}$ channel. The functions for the $\tau_{\text{lep}}\tau_{\text{had}}$ channel were not modified. Resulting changes are shown for a preliminary fit model in the sideband fit in Figure D.23. The

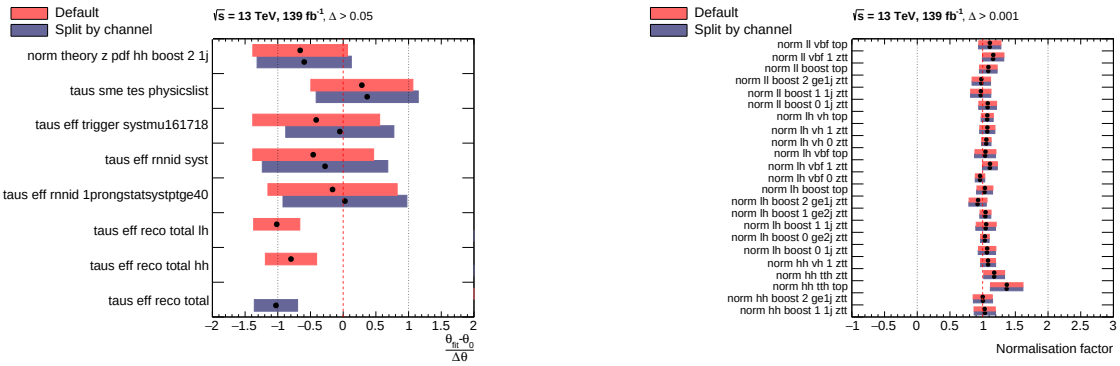

(a) Nuisance parameters.

(b) Normalisation factors.

Figure D.22: Pulls and constraints of the nuisance parameters and normalisation factors in the random signal strength fit with a difference greater than 0.05 and 0.001, respectively. The default fit model (light red) is compared to a fit model with the τ_{had} reconstruction efficiency NP split by di-τ decay channel (dark blue), i.e. into $\tau_{\text{lep}}\tau_{\text{had}}$ and $\tau_{\text{had}}\tau_{\text{had}}$.

τ_{had} reconstruction efficiency NP does not fulfill the required minimum pull difference in the figure, meaning the alternative interpolation does not yield a different pull. However, a few other NPs affecting the τ_{had} normalisation show slight deviations due to the modified interpolation. The largest deviation is observed for the di-τ trigger scale factor uncertainty as it only affects the $\tau_{\text{had}}\tau_{\text{had}}$ channel. This also hints towards a scaling with the number of τ_{had}. Overall, the fit can be considered stable with respect to the choice of interpolation and extrapolation and, thus, the defaults are used in the final fit.

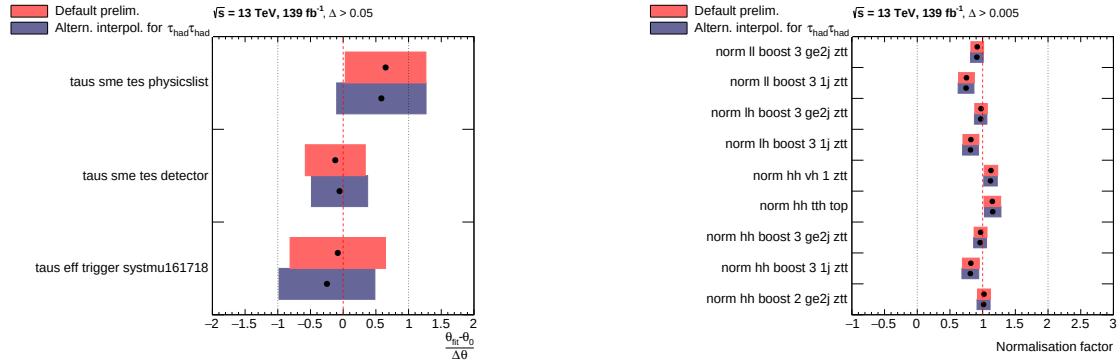

(a) Nuisance parameters.

(b) Normalisation factors.

Figure D.23: Pulls and constraints of the nuisance parameters and normalisation factors in the sideband fit with a difference greater than 0.05 and 0.005, respectively. The default interpolation (light red) used for all NPs is compared to an alternative interpolation for the τ_{had} reconstruction efficiency NP in the $\tau_{\text{had}}\tau_{\text{had}}$ channel (dark blue).

D.3.3 Z + Jets Theory Uncertainty Model

As motivated in Section 6.3.2, the Z + jets theory uncertainties are decorrrelated across all kinematic regions as well as their normalisation and shape variation components. The resulting pulls and constraints of the decorrrelated Z + jets theory NPs are summarised in Figure D.24. With respect to the fully correlated NP scheme the pulls and constraints could be alleviated in most kinematic regions.

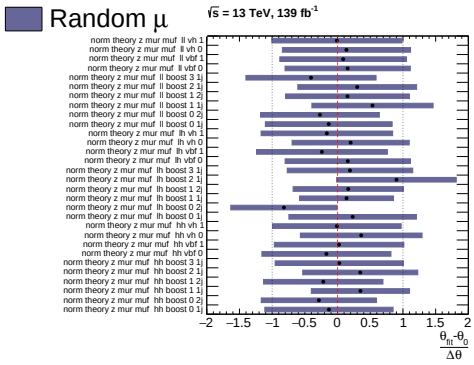

(a) Normalisation components of the $\mu_R\mu_F$ uncertainty.

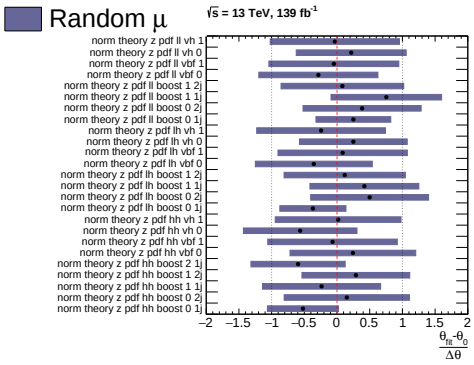

(b) Normalisation components of the PDF uncertainty.

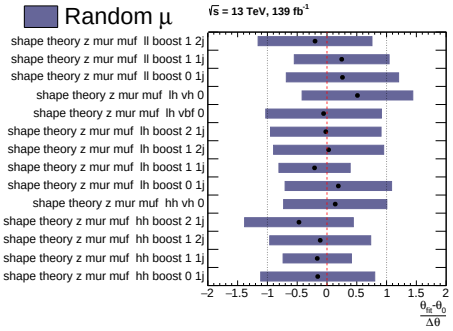

(c) Shape components of the $\mu_R\mu_F$ uncertainty.

Figure D.24: Pulls and constraints of the decorrrelated Z + jets theory NPs in the random signal strength fit. The final NP scheme is shown.

Since the decorrrelated NP scheme allows for a more finely granulated variation of the Z + jets normalisation the influence of the chosen NP scheme on the pulls of other NPs is studied in Figure D.25. Only NPs changing by at least 0.05 in their pull are considered in order to exclude numerically caused deviations. Most of these NPs have a direct impact on the Z + jets normalisation, thus causing correlations to the theory uncertainties and ultimately resulting in the observed changes. Only a few misidentified τ-lepton related NPs pass the criterion of a change greater than 0.05 caused by indirect correlations of a changing Z + jets normalisation that is likely compensated by the observed misidentified τ-lepton varitions. Finally, the impact of the chosen Z + jets theory uncertainty scheme on the sensitivity of the measurement has been assessed using Asimov fits. The resulting uncertainties on the POIs in the most complex setup measuring the STXS cross-sections are shown in Figure D.26. Some uncertainties slightly increase which to some degree is expected because the decorrelation alleviates the original Z + jets theory NP constraints that are propagated to the final POI uncertainties.

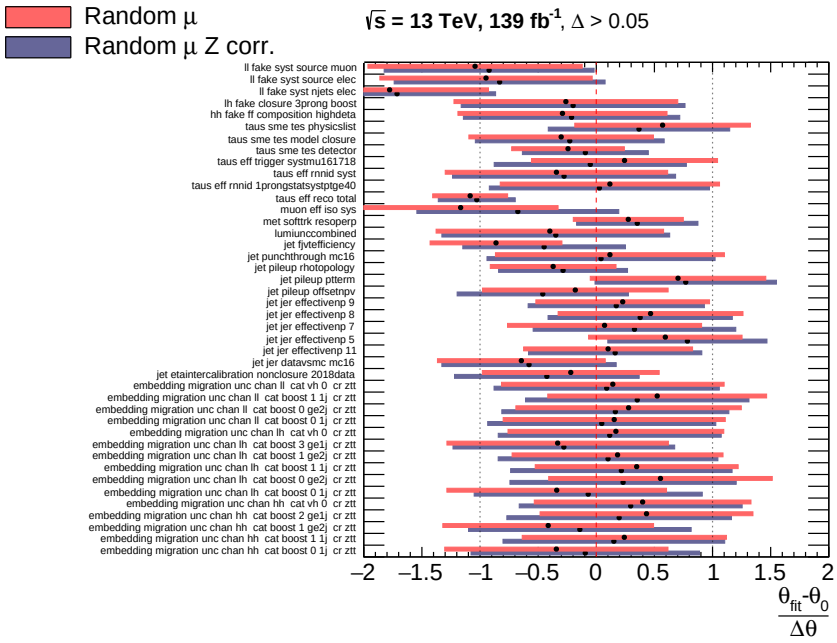

Figure D.25: Pulls and constraints in the random signal strength fit with a difference greater than 0.05 in their mean comparing the fully correlated (dark blue) and the final Z + jets theory NP scheme (light red).

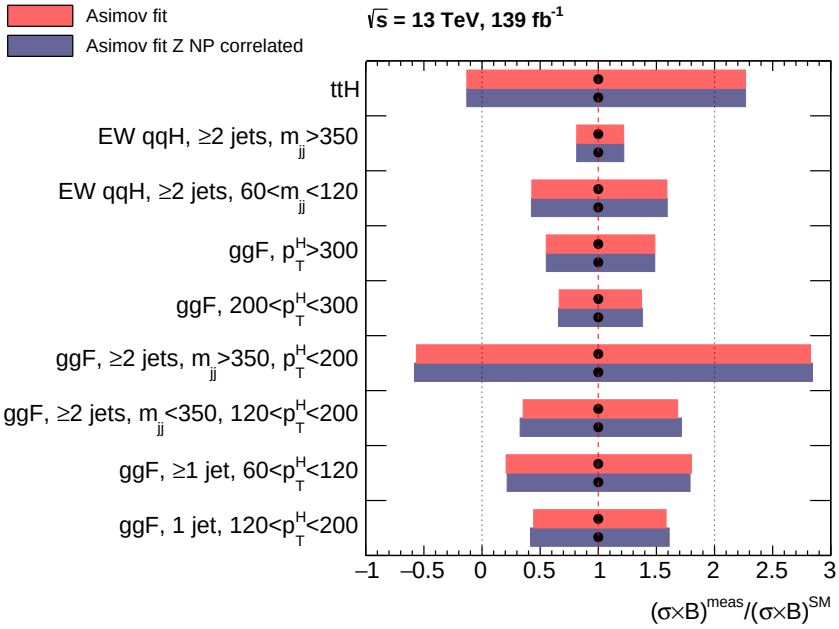

Figure D.26: Effect of decorrelating the PDF and $\mu_R\mu_F$ Z+jets theory uncertainties (light red) on the parameters of interest in Asimov fits in comparison to a fully correlated NP scheme (dark blue). The decorrrelated NP scheme is used in the final fit model. The units (GeV) in the naming of the POIs have been omitted.

D.4 Pulls, Constraints & Toy Based Categorisation of the Final Model in the Unblinded Fit

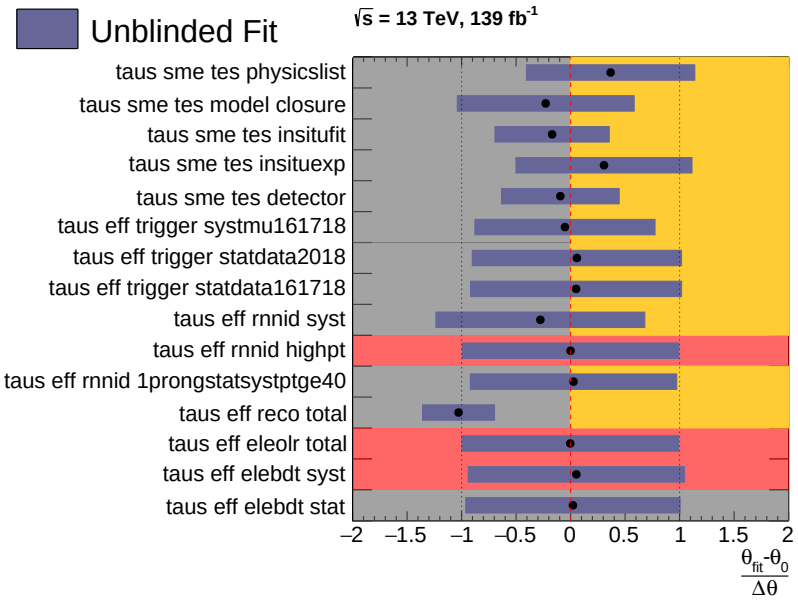

(a) Nuisance parameters related to τ_{had}.

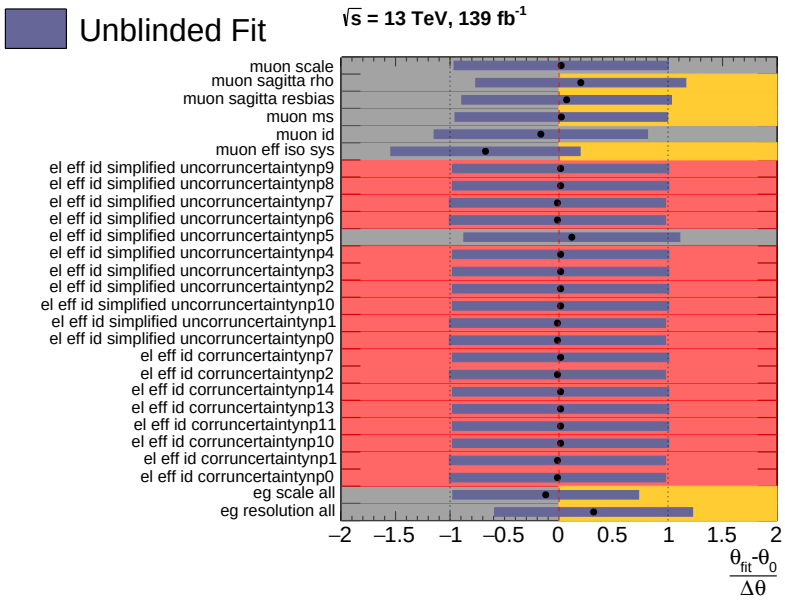

(b) Nuisance parameters related to electrons and muons.

Figure D.27: Pulls and constraints of the τ_{had} and electron/muon related NPs in the unblinded fit. The background colours indicate whether the nuisance parameter is expected to be pulled or constrained. More details on the categorisation are given in Section 7.2.

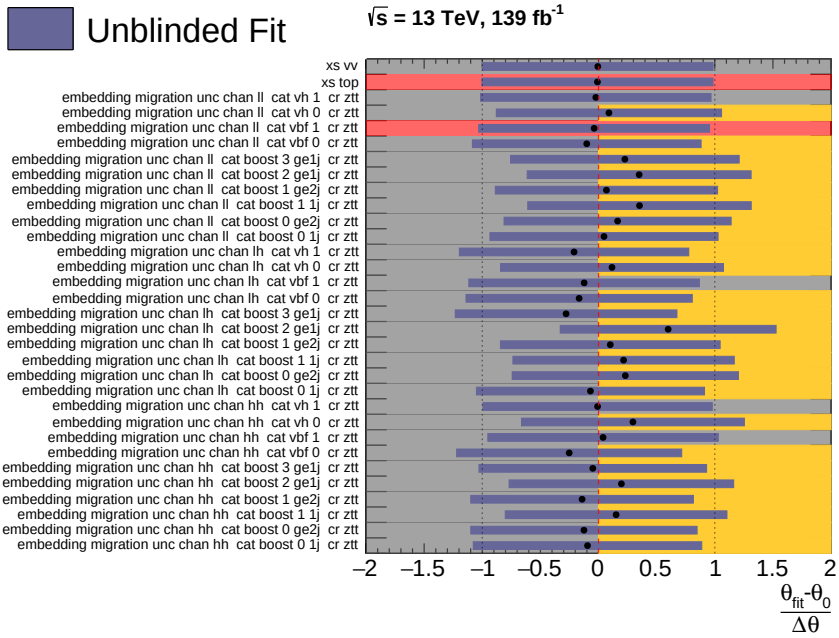

(a) Nuisance parameters related to the simplified embedding.

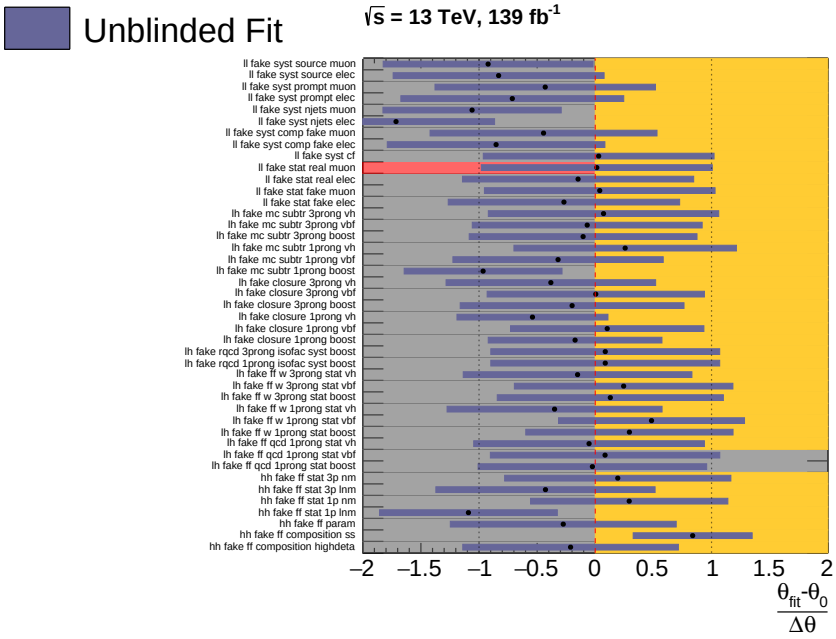

(b) Nuisance parameters related to misidentified τ-lepton estimation.

Figure D.28: Pulls and constraints of the simplified embedding and misidentified τ-lepton estimation related NPs in the unblinded fit. The background colours indicate whether the nuisance parameter is expected to be pulled or constrained. More details on the categorisation are given in Section 7.2.

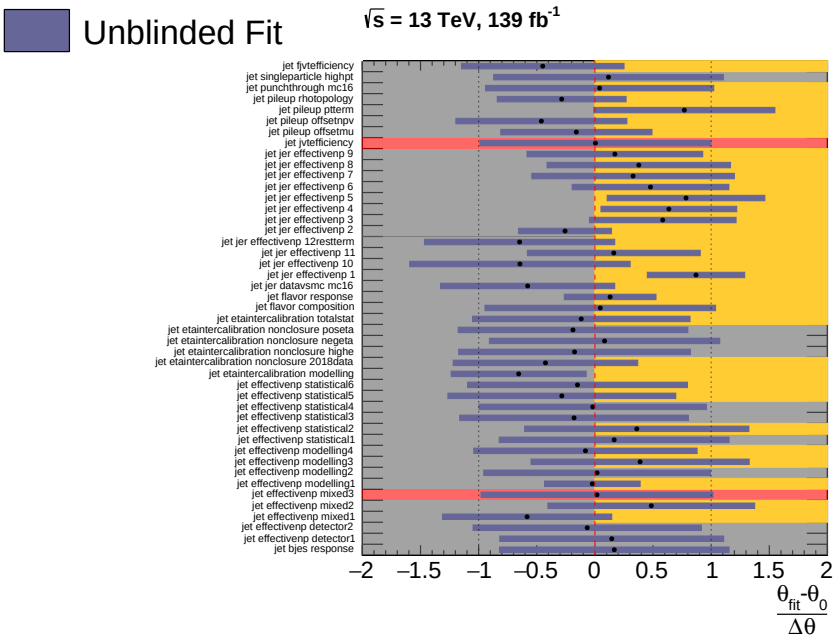

(a) Nuisance parameters related to jets.

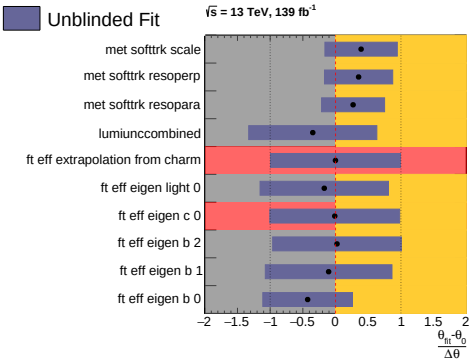

(b) Nuisance parameters related to flavour tagging and $E_{\mathrm{T}}^{\mathrm{miss}}$.

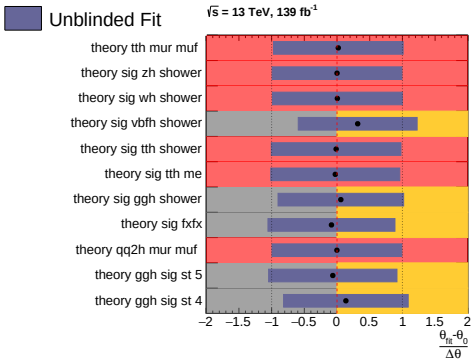

(c) Nuisance parameters related to signal theory.

Figure D.29: Pulls and constraints of the jet, flavour tagging, $E_{\mathrm{T}}^{\mathrm{miss}}$ and signal theory related NPs in the unblinded fit. The background colours indicate whether the nuisance parameter is expected to be pulled or constrained. More details on the categorisation are given in Section 7.2.

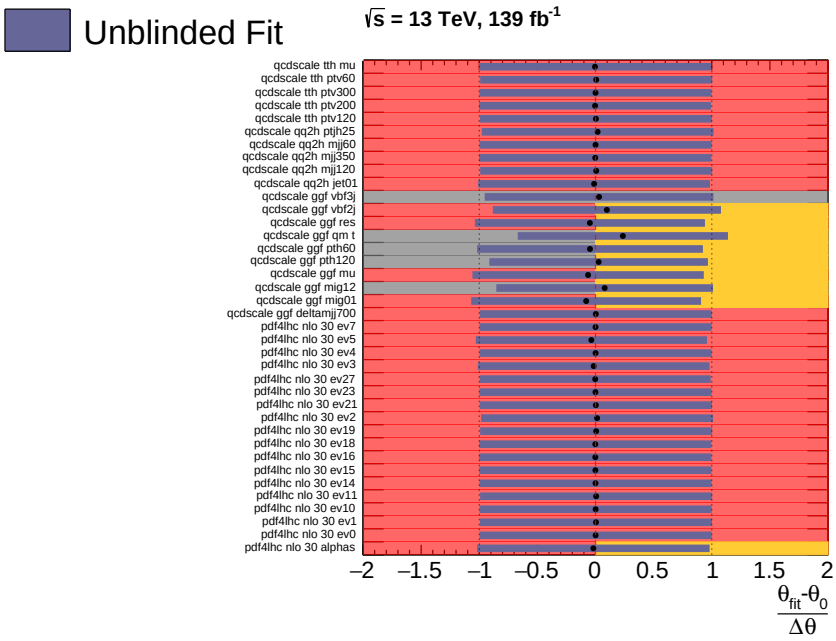

(a) Nuisance parameters related to signal theory QCD and PDF.

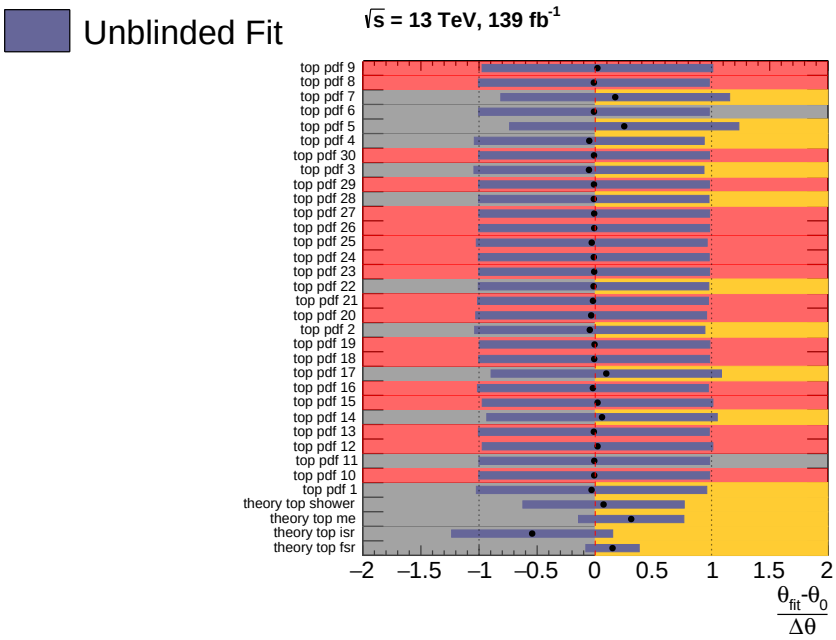

(b) Nuisance parameters related to Top theory.

Figure D.30: Pulls and constraints of the signal theory QCD and PDF as well as Top theory related NPs in the unblinded fit. The background colours indicate whether the nuisance parameter is expected to be pulled or constrained. More details on the categorisation are given in Section 7.2.

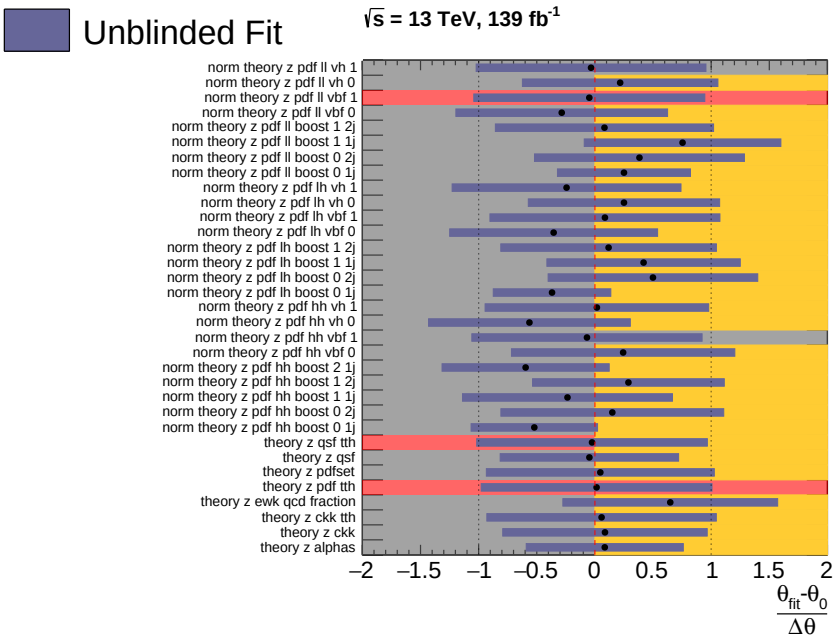

(a) Nuisance parameters related to Z + jets PDF and other theory uncertainties.

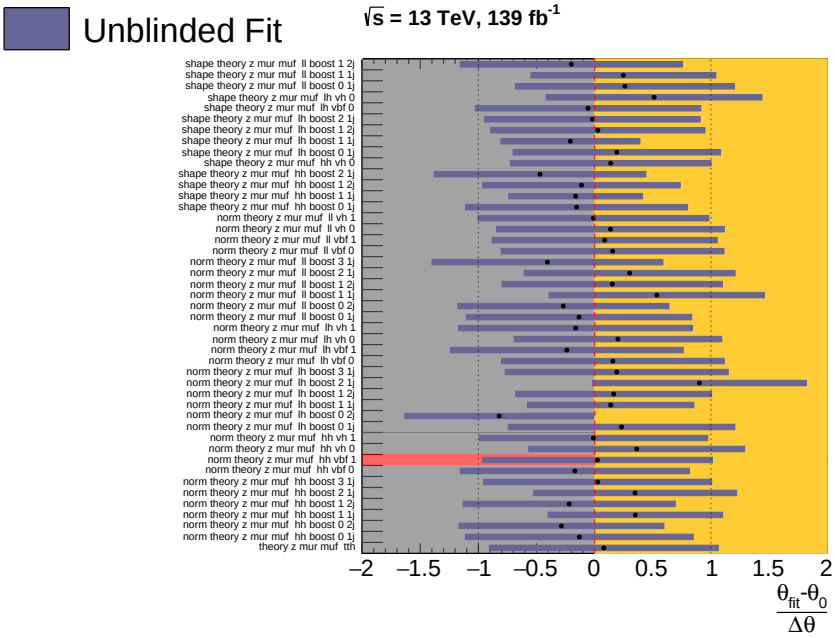

(b) Nuisance parameters related to Z + jets $\mu_R\mu_F$.

Figure D.31: Pulls and constraints of the Z + jets theory uncertainty related NPs in the unblinded fit. The background colours indicate whether the nuisance parameter is expected to be pulled or constrained. More details on the categorisation are given in Section 7.2.

APPENDIX E

Distributions of $m_{\tau\tau}^{\text{MMC}}$

E.1 Prefit & Blinded

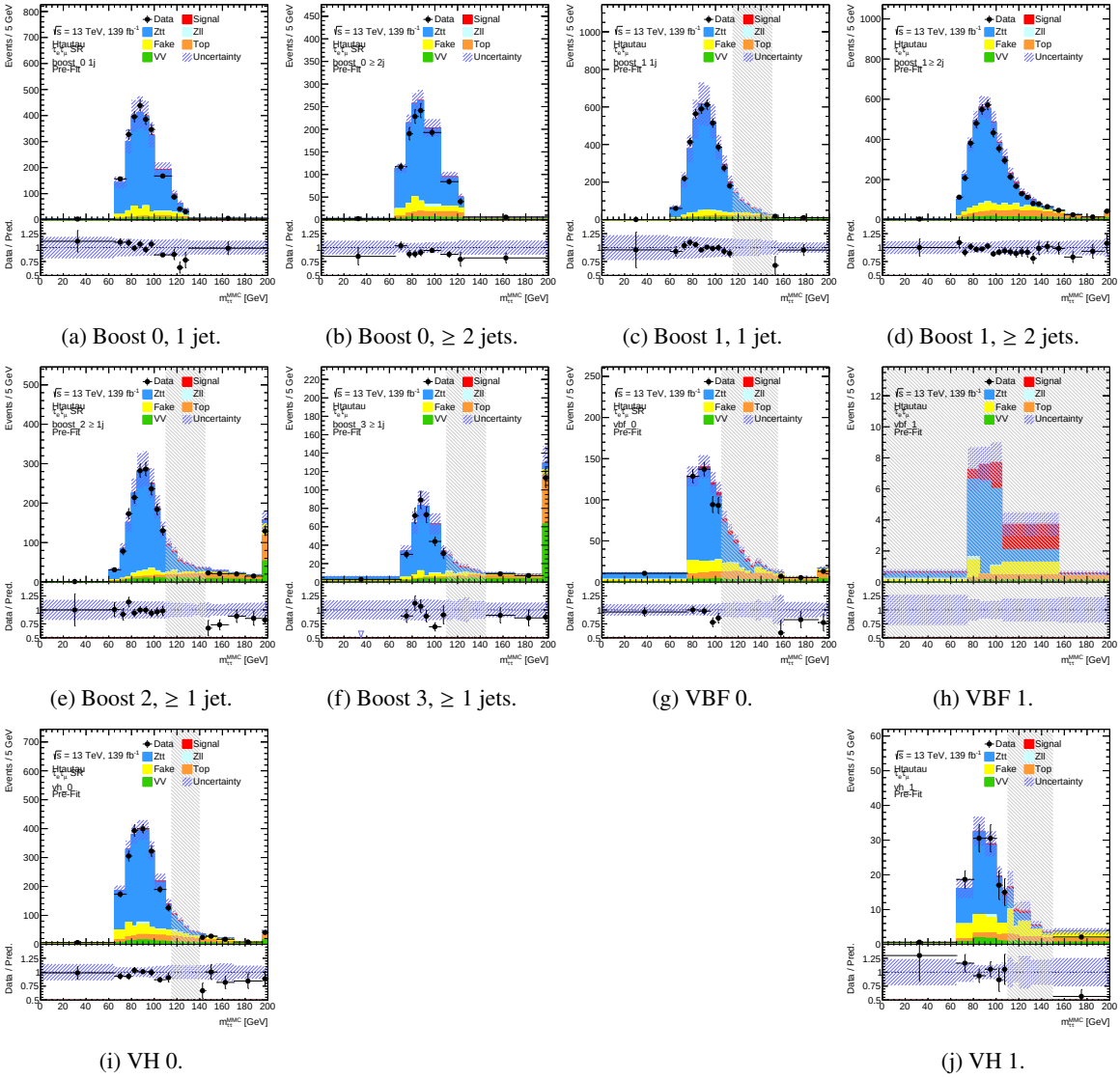

(a) Boost 0, 1 jet. (b) Boost 0, ≥ 2 jets. (c) Boost 1, 1 jet. (d) Boost 1, ≥ 2 jets.

(e) Boost 2, ≥ 1 jet. (f) Boost 3, ≥ 1 jets. (g) VBF 0. (h) VBF 1.

(i) VH 0. (j) VH 1.

Figure E.1: Prefit and blinded mass distributions in the final binning used in the likelihood fit. All signal regions in the $\tau_e\tau_\mu$ channel are shown.

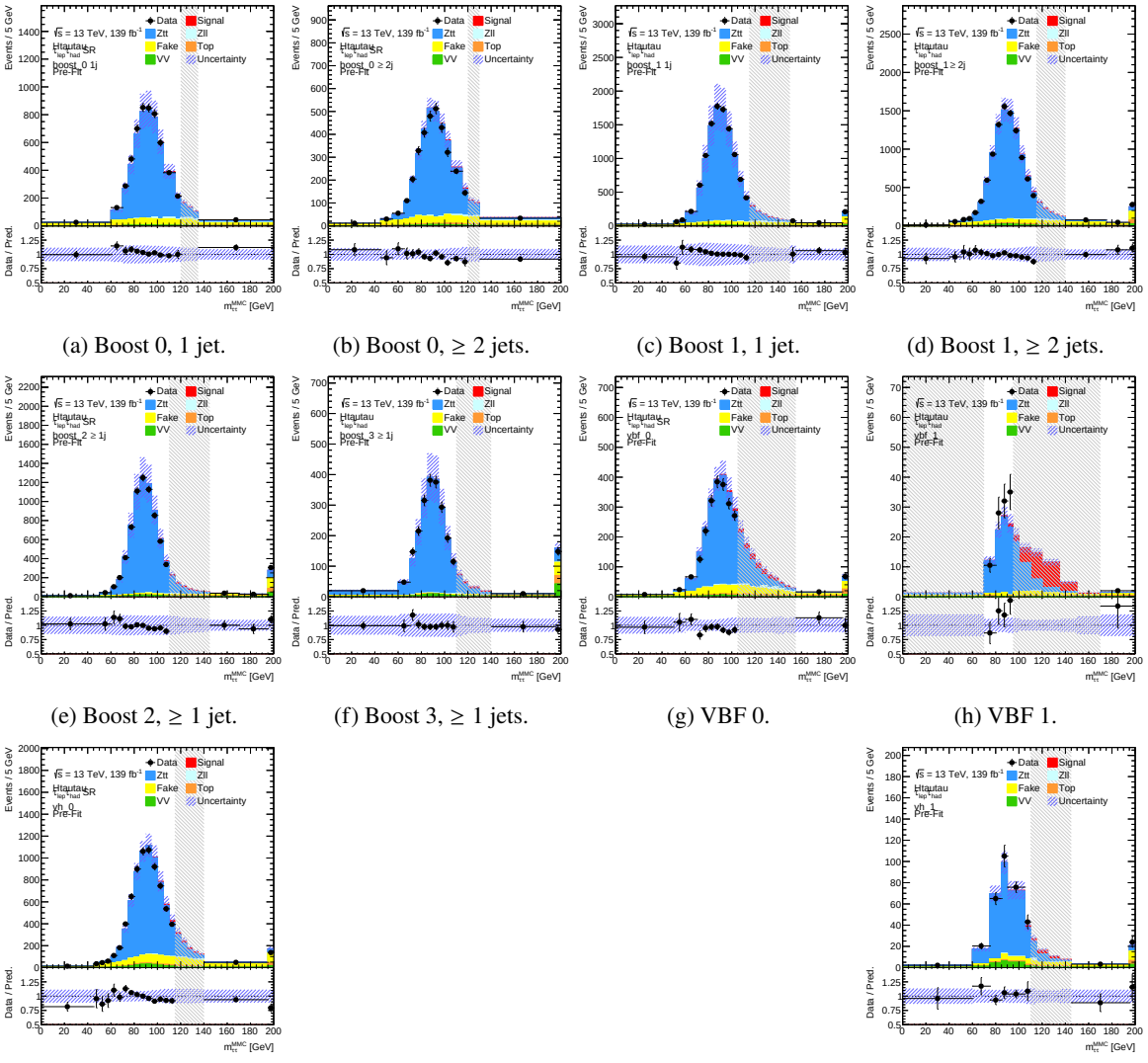

(a) Boost 0, 1 jet. (b) Boost 0, ≥ 2 jets. (c) Boost 1, 1 jet. (d) Boost 1, ≥ 2 jets.

(e) Boost 2, ≥ 1 jet. (f) Boost 3, ≥ 1 jets. (g) VBF 0. (h) VBF 1.

(i) VH 0. (j) VH 1.

Figure E.2: Prefit and blinded mass distributions in the final binning used in the likelihood fit. All signal regions in the $\tau_{\text{lep}}\tau_{\text{had}}$ channel are shown.

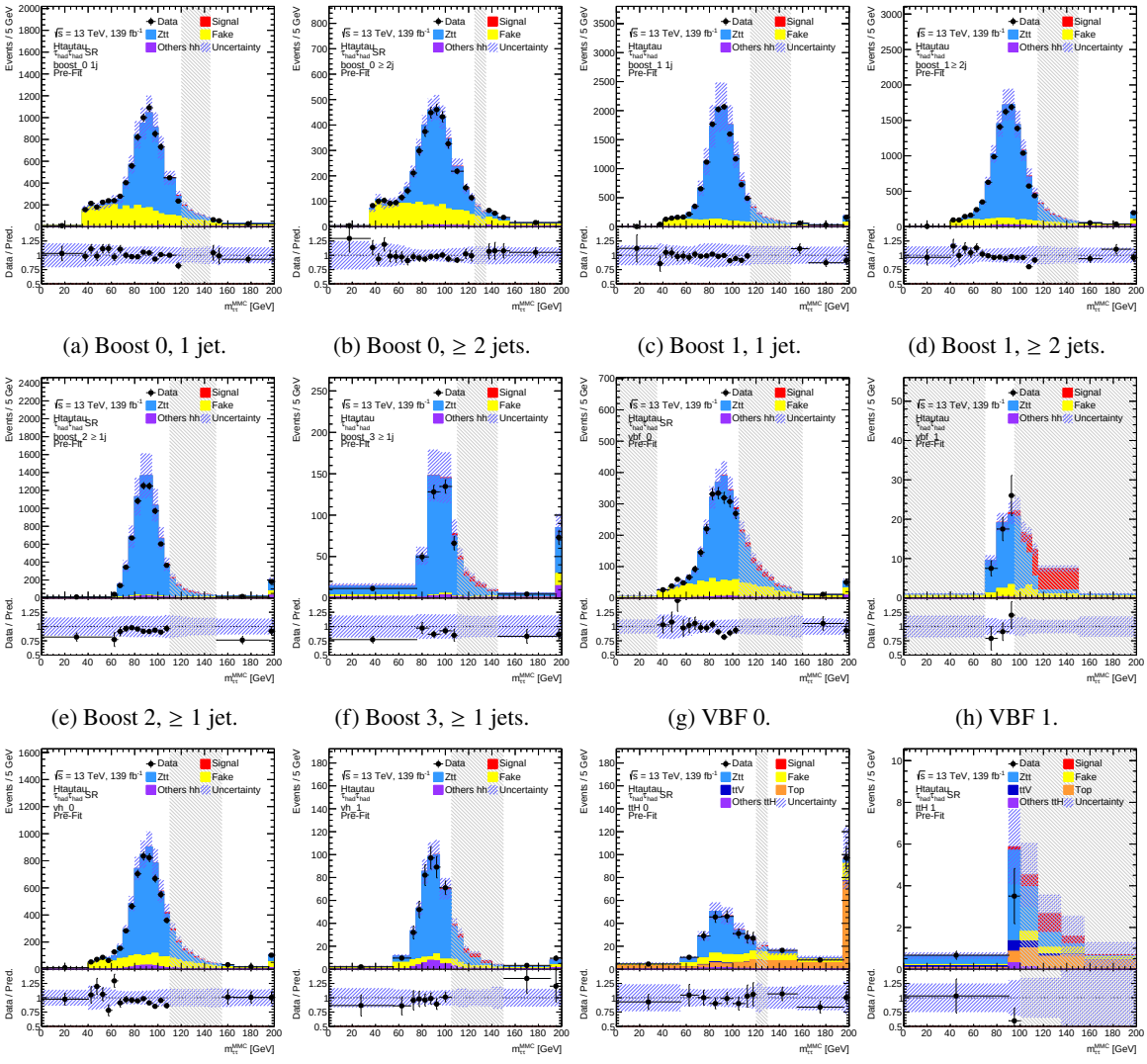

(a) Boost 0, 1 jet. (b) Boost 0, ≥ 2 jets. (c) Boost 1, 1 jet. (d) Boost 1, ≥ 2 jets.

(e) Boost 2, ≥ 1 jet. (f) Boost 3, ≥ 1 jets. (g) VBF 0. (h) VBF 1.

(i) VH 0. (j) VH 1. (k) ttH 0. (l) ttH 1.

Figure E.3: Prefit and blinded mass distributions in the final binning used in the likelihood fit. All signal regions in the $\tau_{\text{had}}\tau_{\text{had}}$ channel are shown.

E.2 Postfit & Unblinded

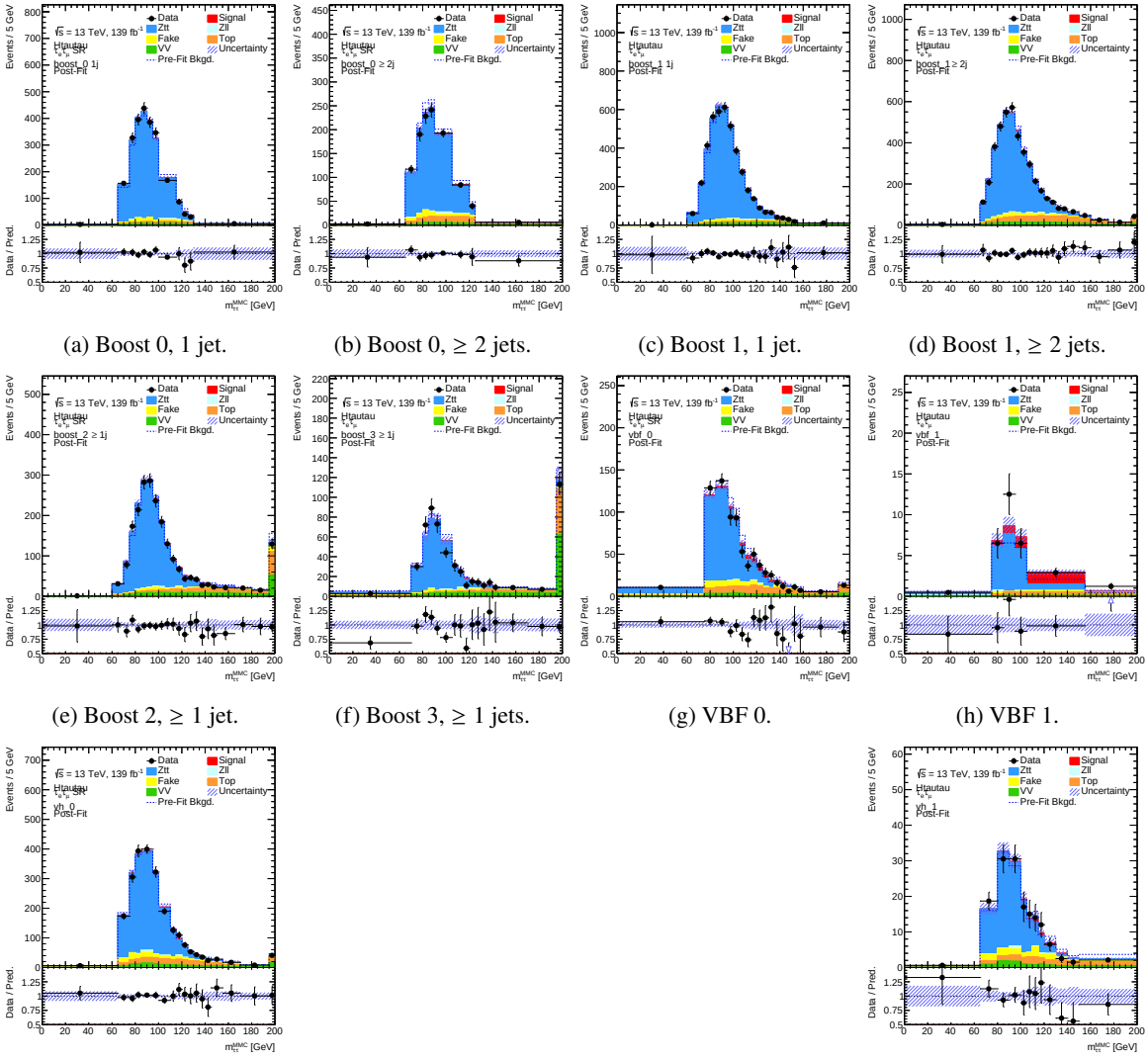

(a) Boost 0, 1 jet. (b) Boost 0, ≥ 2 jets. (c) Boost 1, 1 jet. (d) Boost 1, ≥ 2 jets.

(e) Boost 2, ≥ 1 jet. (f) Boost 3, ≥ 1 jets. (g) VBF 0. (h) VBF 1.

(i) VH 0. (j) VH 1.

Figure E.4: Postfit and unblinded mass distributions in the final binning used in the likelihood fit. All signal regions in the $\tau_e\tau_\mu$ channel are shown.

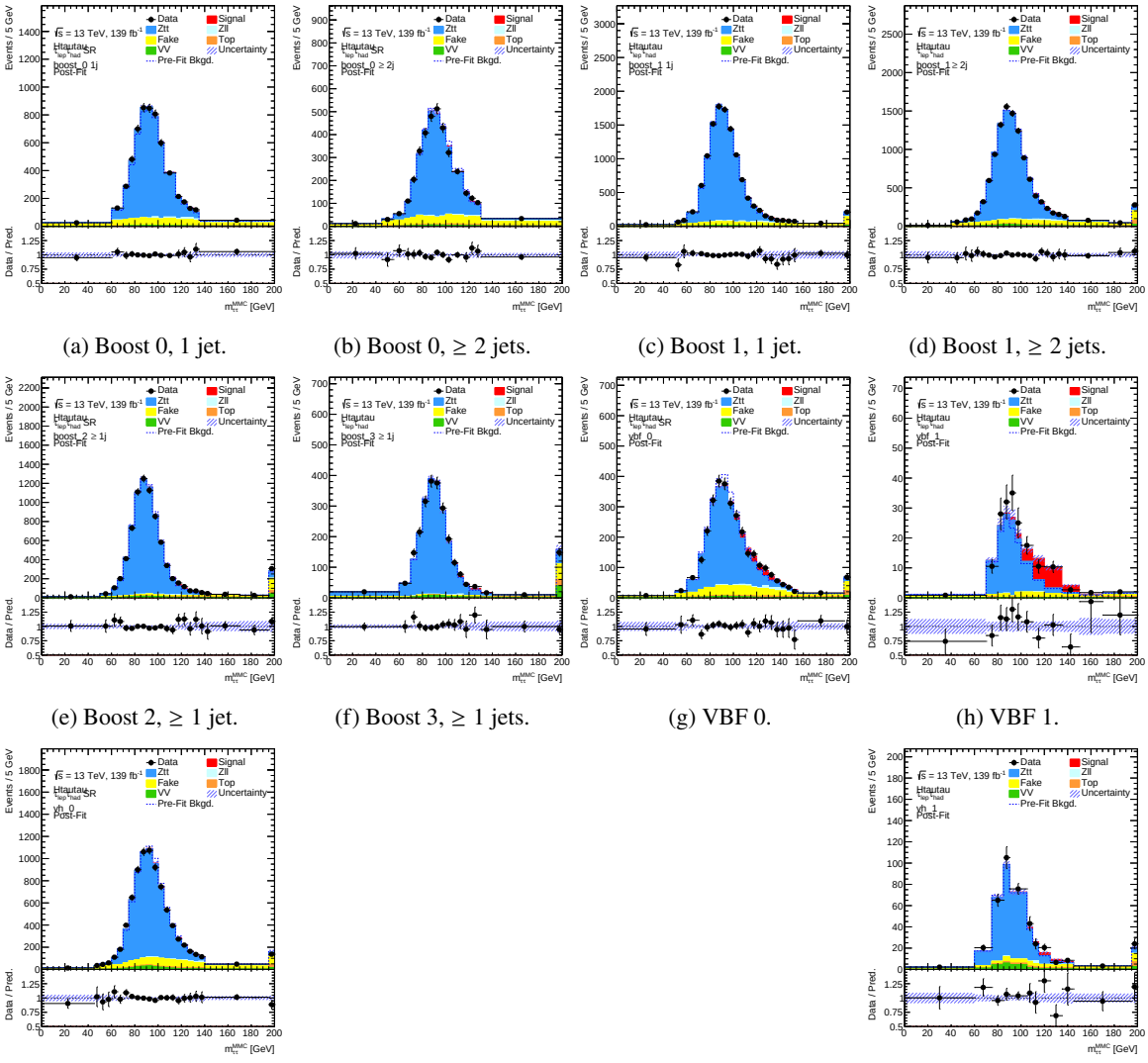

(a) Boost 0, 1 jet. (b) Boost 0, ≥ 2 jets. (c) Boost 1, 1 jet. (d) Boost 1, ≥ 2 jets.

(e) Boost 2, ≥ 1 jet. (f) Boost 3, ≥ 1 jets. (g) VBF 0. (h) VBF 1.

(i) VH 0. (j) VH 1.

Figure E.5: Postfit and unblinded mass distributions in the final binning used in the likelihood fit. All signal regions in the $\tau_{\text{lep}}\tau_{\text{had}}$ channel are shown.

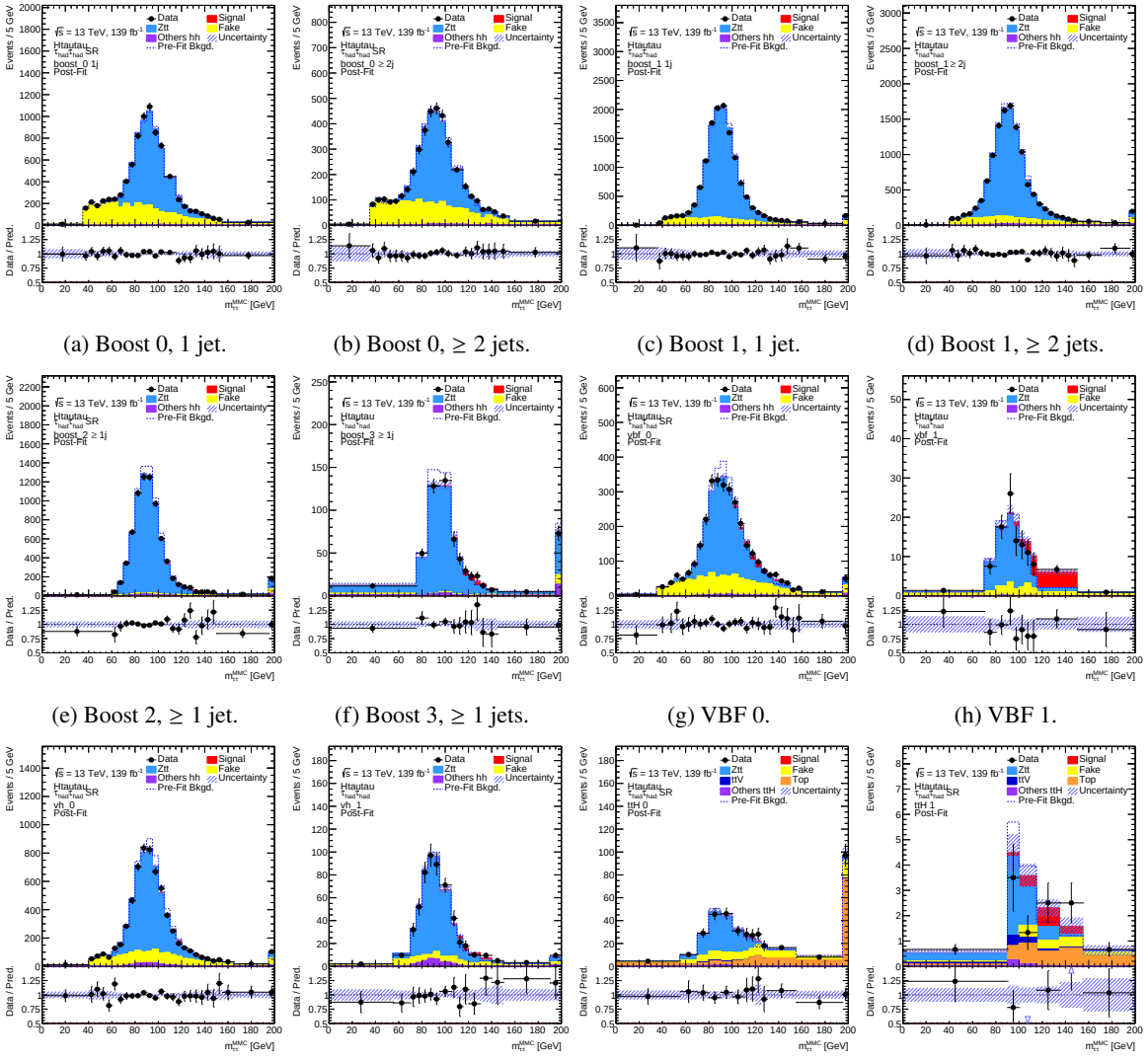

(a) Boost 0, 1 jet. (b) Boost 0, ≥ 2 jets. (c) Boost 1, 1 jet. (d) Boost 1, ≥ 2 jets.

(e) Boost 2, ≥ 1 jet. (f) Boost 3, ≥ 1 jets. (g) VBF 0. (h) VBF 1.

(i) VH 0. (j) VH 1. (k) ttH 0. (l) ttH 1.

Figure E.6: Postfit and unblinded mass distributions in the final binning used in the likelihood fit. All signal regions in the $\tau_{\text{had}}\tau_{\text{had}}$ channel are shown.

List of Figures

List of Tables

List of Algorithms

Acknowledgements

First and foremost, I would like to thank my family for equipping me with the necessary tools to tackle a project like my PhD. I want to express my gratitude towards my mother, my brother and my grandma; without their continuous support and encouragment I would not have been able to reach this point.

I would like to thank Klaus Desch for a multitude of things, ranging from providing me with the opportunity to do my PhD in his group, to the scientific discussions and supporting me whenever needed. Similarly, for his insight and support I especially would like to thank Philip Bechtle. My thanks goes to Christian Grefe for showing me the various peculiarities of ATLAS software and for the discussions we had working together in the Tau working group. I also thank Peter Wagner for his ideas and expertise.

Thank you also to all the people that have shaped the working group over the years and with whom I had the pleasure of working (or drinking coffee). Former and present colleagues and friends like Florian Beisiegel, Philipp König, Oliver Ricken, Martin Werres, Tobias Klingl, Maike Hansen, Lara Schildgen, Basti Schmidt, Florian Hinterkeuser, Rico Caprilles Diaz (the list goes on) have created a great atmosphere in the group facilitating scientific exchange and distractions from science when necessary. I especially would like to mention Philipp König, as we motivated each other to keep going no matter what obstacle either of us faced. For enduring my ideas during their Bachelor's and Master's theses I would like to thank Kevin Bass, Lena Hermann, Ramy Hmaid, Alina Manthei, Hoang Ngyuen and Martin Werres. For the chance to work in outreach projects and our conversations I am grateful to Barbara Valeriani-Kaminski. I also thank Philipp, Christian, Philip, Florian and Tascha for proof-reading my thesis.

Over the years I had the pleasure of working with a lot of different people from all over the world, too many to name all of them. I very much enjoyed meeting and working with them in various workshops, conferences and on other occasions.

Every physics measurement like this thesis needs a well-working IT infrastructure for which I especially thank Oliver Freyermuth and Peter Wienemann. I was lucky enough to be able to work with them in the IT department on several projects for which I am truly grateful.

Finally, I have to thank my family and friends for their support and getting my mind off physics every once in a while. For her support and patience I especially would like to thank my fiancée Tascha Benayas Delgado.